

Regulatory Mechanisms that Govern Membrane Deformation and Scission
in the ESCRT-Mediated Endocytic Pathway

By

Amber L. Schuh

A dissertation submitted in partial fulfillment of
the requirements for the degree of

Doctor of Philosophy

(Biochemistry)

at the

UNIVERSITY OF WISCONSIN-MADISON

2013

Date of final oral examination: 11/7/13

The dissertation is approved by the following members of the Final Oral Committee:

Anjon Audhya, Assistant Professor, Biomolecular Chemistry

Edwin R. Chapman, Professor, Neuroscience

James L. Keck, Professor, Biomolecular Chemistry

Jeffrey D. Hardin, Professor, Zoology

John L. Markley, Professor, Biochemistry

ACKNOWLEDGEMENTS

I would like to begin by thanking my advisor, Dr. Jon Audhya. Jon has been a great mentor during my graduate school career. During our discussions of science, he always reminded me of the big picture when I would get caught up in the individual details of a specific experiment. He has been extremely patient with me, especially during those moments when I felt that all of my experiments were failing and I found it hard to stay optimistic. I have learned a great deal from my time in his lab, and I will forever be grateful for all of his help over the years.

I also want to thank the rest of my committee: Drs: Ed Chapman, Jeff Hardin, Jim Keck, and John Markley for all of their helpful advice and experimental suggestions. I would also like to thank past and present members of the Chapman lab who taught me a great deal of experimental techniques. I also need to extend sincere gratitude to the Keck lab for being a second lab home I could go to for almost anything. In particular, Dr. Nick George taught me many experimental techniques and during the process became a great friend. Also, Basu Bhattacharyya has been a classmate, a collaborator, and a close friend. I owe him huge thanks for all of the help he has extended to me.

I will forever be grateful for the amazing lab mates I have had the pleasure to work with in the Audhya lab. Each of you has made this an enjoyable place to come to work every day, and I cannot thank you enough for that. I'm especially grateful for having the opportunity to work with Dr. Jon Mayers, Kylee Morrison, and Erin McMillan who have become great friends over the years. I also would like to thank all the amazing friends that I have made here in Madison.

Your friendships have gotten me through all the rough times of graduate school, plus we have made some really fun memories that I will cherish forever.

There are a special group of friends that go back a very long time that I have to thank: Wendy, Mandy, Krystal, A.J, Nichole, Ashley, and Heather. You girls have been my friends for over a decade and some have been my friends for over twenty years. I would not be the person I am today without having you girls in my life. Each of us had our ups and downs throughout the years, but our friendships have always prevailed. I look forward to all the years of friendship to come.

Most of all I have to thank my family, especially my mom and dad. You two work harder than anyone I know, and I cannot thank you enough for instilling that work ethic in me. Both of you have been very supportive in my education, and I would not be where I am today without you. I also need to thank my two older brothers, Chad and Chris who have been terrific big brothers. During all the times I tagged along with you both, I thank you for teaching me that I can accomplish more than I sometimes realize and for never letting me take the easy way out. Those lessons have been essential in graduate school. I also want to thank my sister-in-laws, Julie and Lindsey who are wonderful additions to the family. I also have to acknowledge my niece and nephew, Eve and Wyatt, who have a very special place in my heart. There is nothing better than spending the day with them and I look forward to many more fun days together. I also need to thank my Grandma Court and my Aunt Vicki who have been there for every milestone in my life, and have done so many extra things for me along the way. Lastly, I want to thank my boyfriend Dan who has been a huge part of my life for the past seven years. Thank you for your patience and understanding when I had to cancel plans for experiments or work late.

You have always been extremely supportive and encouraged me when I needed it most. Most of all, thank you for reminding me there is more to life than just school because I have needed this lesson the most. I look forward to what our future has in store for us.

ABSTRACT

Cells are able to respond to external stimuli and sense the surrounding environment by varying the lipid and protein composition of the plasma membrane. One way this is achieved is through receptor downregulation via the endocytic pathway. Once receptors are at the early endosome, the endosomal sorting complexes required for transport (ESCRT) machinery identifies and clusters ubiquitinated receptors, induces membrane deformation, and drives vesicle scission. This intricate process generates intraluminal vesicles (ILVs) within an endosome, known as a multivesicular endosome (MVE). Upon ILV formation, receptors are sequestered from cytoplasmic effectors. A MVE fuses with the lysosome where the contents are degraded. A great deal of emphasis has been placed on understanding how the ESCRT machinery carries out this membrane deformation and scission process, but a cohesive mechanism remains unknown. In this thesis, I demonstrate that ESCRT-II and Vps20 generate a curvature sensing supercomplex that restricts Vps32 filament formation to highly curved membranes. Membrane remodeling is observed through this filament formation. I also show that ESCRT-II and Vps20 interact in solution, which raises the possibility that a curvature sensing supercomplex may exist within the cytoplasm. Furthermore, I demonstrate that Vps20 is in an open conformation in solution unlike the downstream ESCRT-III subunit, Vps24. This crucial finding suggests that all ESCRT-III subunits are not in the same conformation, which could help explain the distinct function of each ESCRT-III protein. Finally, I show that unmodified Vps32 can self-assemble independent of upstream ESCRT components and characterize a mechanism of Vps32 filament assembly, *in vitro*.

Table of Contents

Acknowledgments	i
Abstract	iv
Table of Contents	v
List of Tables and Figures	vii
List of Abbreviations	xii
Chapter 1: Introduction	1
The Endocytic Pathway: a Mechanism for Receptor Downregulation	2
The ESCRT Machinery	3
Characterization of the ESCRT-III Filament	9
ESCRT-III Disassembly by the Vps4-Vta1 Complex	11
Proposed Models of ESCRT Function	15
Additional Cellular Functions of the ESCRTs	18
ESCRT Machinery and Disease	20
Research Focus	22
Figures	24
References	34
Chapter 2: Association of ESCRT-II with Vps20 Generates a Curvature Sensitive Protein Complex Capable of Nucleating Filaments of ESCRT-III.....	44
Abstract	45
Introduction	46
Results	48
Discussion	55
Materials and Methods	58
Acknowledgements and Experimental Contributions	62
Figures	63
References	84

Chapter 3: The Open Conformation of the ESCRT-III Subunit Vps20 is Independent of ESCRT-II Binding	88
Abstract	89
Introduction	90
Results	93
Discussion	99
Materials and Methods	102
Acknowledgements and Experimental Contributions	105
Figures	106
References	129
Chapter 4: Mechanisms of ESCRT-III Spiral Filament Assembly	132
Abstract	133
Introduction	134
Results and Discussion	135
Materials and Methods	140
Acknowledgements and Experimental Contributions	149
Figures	150
References	188
Chapter 5: Discussion and Future Directions	192
A supercomplex of ESCRT-II and Vps20 senses membrane curvature...	
What is next?	194
Conformational variation within the ESCRT-III subunits	196
Characterization of the Vps32 filament	197
Final Perspective	199
Figure	200
References	202

Appendix A: Mechanisms by which TFG Functions in Protein Secretion and Oncogenesis	204
Abstract	205
Introduction	206
Results	208
Discussion	220
Materials and Methods	224
Acknowledgements and Contributions	232
Figures	233
References	266
Appendix B: Phosphoinositide Signaling During Membrane Transport in <i>Saccharomyces cerevisiae</i>	271
Abstract	272
Phosphoinositide metabolism in the yeast <i>Saccharomyces cerevisiae</i>	273
Binding domains and effector proteins of PI3P	277
The FYVE domain	278
The Phox homology (PX) domain	281
Effectors of PI3,5P ₂ and their roles in membrane trafficking	285
Roles for PI4P in membrane transport	287
Functions of PI4P synthesized by Pik1p in the Golgi	288
Functions of PI4P synthesized by Stt4p at the plasma membrane	294
Roles for PI4,5P ₂ in membrane transport	297
Perspectives and Conclusions	304
Figures	305
References	309

List of Tables and Figures

- Figure 1.1: The endocytic pathway. (p. 24)
- Figure 1.2: Components of the ESCRT machinery (p. 26)
- Table 1.1: Proteins of the ESCRT machinery and their interacting partners. (p. 28)
- Figure 1.3: Structures of ESCRT-III subunits. (p. 30)
- Figure 1.4: The ESCRT machinery plays defined roles in membrane scission for MVE biogenesis, cytokinesis, and viral budding. (p. 32)
- Figure 2.1: ESCRT-II bound to Vps20 binds preferentially to liposomes of higher curvature. (p. 63)
- Figure 2.2: A complex of ESCRT-II bound to Vps20 senses membrane curvature. (p. 65)
- Figure 2.3: Vps20 targets ESCRT-II to membranes of high curvature. (p. 68)
- Figure 2.4: ESCRT-II and Vps20 nucleate a strand of Vps32 monomers that bind specifically to highly curved bilayers. (p. 70)
- Figure 2.5: ESCRT-III filaments alter the dynamics of highly curved membranes. (p. 72)
- Figure 2.S1: *C. elegans* ESCRT-II and Vps20 exhibit similar hydrodynamic properties to their human counterparts and do not sense elevated membrane curvature individually. (p. 74)
- Figure 2.S2: Membrane binding of ESCRT-II/Vps20 increases as the square of the membrane curvature and association of Vps20 with ESCRT-II lowers the affinity of ESCRT-II for flat membranes. (p. 76)
- Figure 2.S3: ESCRT-III filaments form specifically on highly curved membranes. (p. 79)
- Figure 2.S4: ESCRT-III assembly promotes membrane remodeling and bilayer sealing on a mica surface. (p. 82)
- Figure 3.1: Vps20 and ESCRT-II interact in solution. (p. 106)
- Figure 3.2: SAXS analysis of Vps24. (p. 108)
- Figure 3.2: SAXS analysis of Vps24. (p. 110)
- Figure 3.4: SAXS analysis of Vps20 Δ C. (p. 112)

- Figure 3.5: Overlay of open and closed crystal structures of hVps24 onto Vps20 Δ C SAXS envelope. (p. 114)
- Figure 3.6: Overlay of open and closed crystal structures of hVps24 onto Vps24 SAXS envelope. (p. 116)
- Figure 3.7: Overlay of open and closed crystal structures of hVps24 onto Vps20 SAXS envelope. (p. 118)
- Table 3.S1: Identification of ESCRT-II interacting partners using immunoprecipitation followed by solution mass spectrometry. (p. 120)
- Figure 3.S1: Sequence alignment of *C. elegans* Vps24 and Vps20 (p. 121)
- Figure 3.S2: Concentration comparison for Vps24. (p. 123)
- Figure 3.S3: Concentration comparison for Vps20. (p. 125)
- Figure 3.S4: Raw data for Vps20 Δ C. (p. 127)
- Figure 4.1: Vps32 polymerizes to form curved, single-stranded filaments. (p. 150)
- Figure 4.2: Stable interactions between neighboring α 2 helices drive head-to-tail assembly of Vps32 filaments. (p. 152)
- Figure 4.3: Spiral assembly of Vps32 filaments harnesses intrinsic free energy. (p. 154)
- Figure 4.4: The carboxyl-terminus of Vps32 inhibits the lateral association of filaments within spirals. (p. 156)
- Figure 4.S1: *C. elegans* Vps32 is evolutionarily conserved. (p. 158)
- Figure 4.S2: *C. elegans* Vps32 forms an exchangeable pool of monomers and oligomers in solution. (p. 160)
- Figure 4.S3: Vps32 polymers form single-stranded, circular filaments following negative straining electron microscopy. (p. 162)
- Figure 4.S4: Vps32 polymers form spiral filaments in vitreous ice. (p. 164)
- Figure 4.S5: Vitrified Vps32 polymers exhibit a range of lengths. (p. 166)
- Figure 4.S6: Creation of a GUI system to track filament trajectories. (p. 168)
- Figure 4.S7: Vps32 filaments are composed of distinct, globular densities joined by thin connections. (p. 170)

- Figure 4.S8: A pseudo-atomic model of *C. elegans* Vps32 exhibits a similar conformation to human CHMP3 and CHMP4B. (p. 172)
- Figure 4.S9: Only a single orientation of Vps32 is compatible with the EM density map. (p. 174)
- Figure 4.S10: Identification of a common interface between monomers within ESCRT-III filaments. (p. 176)
- Figure 4.S11: Human CHMP3 exhibits similar flexibility as compared to *C. elegans* Vps32. (p. 178)
- Figure 4.S12: Increasing the rigidity of the Vps32 helical hairpin inhibits spiral filament assembly. (p. 180)
- Figure 4.S13: An unbiased approach to determining the distance between adjacent filaments within Vps32 spirals. (p. 182)
- Figure 4.S14: The carboxyl-terminus of Vps32 functions as a spacer between filaments within spirals. (p. 184)
- Figure 4.S15: A speculative model illustrating ESCRT-III spiral constriction during membrane scission. (p. 186)
- Figure 5.1: SAXS analysis of Did2 (p. 200)
- Figure A.1: *C. elegans* TFG-1 interacts with the ER exit site component SEC-16. (p. 233)
- Figure A.2: TFG-1 localizes to ER exit sites that are juxtaposed to the Golgi. (p. 235)
- Figure A.3: TFG-1 regulates SEC-16 levels on ER exit sites. (p. 238)
- Figure A.4: The amino-terminus of TFG-1 mediates its oligomerization. (p. 241)
- Figure A.5: TFG-1 is required for COPII recruitment and protein secretion. (p. 243)
- Figure A.6: Human TFG functions at ER exit sites and binds to Sec16. (p. 245)
- Figure A.7: Targeting of the NTRK1 kinase domain to ER exit sites is sufficient to activate NTRK1-mediated downstream signaling. (p. 248)
- Figure A.S1: TFG-1 functions with SEC-16 at ER exit sites. (p. 250)
- Figure A.S2: TFG-1 is required for secretion and normal localization of RAB-6. (p. 253)
- Figure A.S3: Human TFG is a conserved protein required for VSVG(ts045)-GFP secretion. (p. 256)

Figure A.S4: The region of Sec16B necessary for its targeting to ER exit sites forms a homo oligomer and targeting of NTRK1 to ER exit sites is necessary for cell transformation. (p. 258)

Figure A.S5: TFG-1 localizes to ER exit sites in several distinct tissues. (p. 260)

Figure A.S6: Full scan data of immunoblots and Coomassie stained gels. (p. 262)

Table A.S1: Essential SEC-16 interacting proteins identified by mass spectrometry. (p. 264)

Figure B.1: Phosphoinositide metabolism in yeast. (p. 305)

Figure B.1: Phosphoinositide metabolism in yeast. (p. 307)

List of Abbreviations

AFM:	Atomic Force Microscopy
ALS:	Amyotrophic Lateral Sclerosis
ATP:	Adenosine Triphosphate
CPS:	Carboxypeptidase S
Cryo-EM:	Cryogenic Electron Microscopy
DUB:	Deubiquitinating Enzyme
EGFR:	Epidermal Growth Factor Receptor
EM:	Electron Microscopy
ESCRT:	Endosomal Sorting Complex Required for Transport
FFT:	Fast Fourier Transform
GLUE:	Gram-Like Ubiquitin-Binding in Eap-45
GST:	Glutathione Agarose Beads
GUV:	Giant Unilamellar Vesicles
HIV-1:	Human Immunodeficiency Virus
ILV:	Intralumenal Vesicle
MALS:	Multiangle Light Scattering
MD:	Molecular Dynamics
MIM:	MIT-Domain-Interacting Motifs
MIT:	Microtubule Interacting and Transport
MudPIT:	Multidimensional Protein Identification Technology
MVE:	Multivesicular Endosome
NSD:	Nominal Spatial Discrepancy
NZF:	Np14-Type Zinc Finger

PC:	Phosphatidylcholine
PE:	Phosphatidylethanolamine
PEG:	Polyethylene Glycol
PH:	Pleckstrin Homology
PI3P:	Phosphatidylinositol 3-Phosphate
PI3,5P ₂ :	Phosphatidylinositol 3,5-Bisphosphate
PS:	Phosphatidylserine
RMSD:	Root Mean Squared Deviation
SAXS:	Small-Angle X-Ray Scattering
SEC:	Size-Exclusion Chromatography
SLB:	Supported lipid bilayer
UBD:	Ubiquitin Binding Domains
UEV:	Ubiquitin E2 Variant
VSL:	Vps4, SBP1, LIP5
WH:	Winged Helix

Chapter One

Introduction

The Endocytic Pathway: a Mechanism for Receptor Downregulation

For a cell to properly function and survive, it must sense the surrounding environment and respond to external stimuli. Cellular communication with the environment is largely dependent upon the composition of the outer leaflet of the plasma membrane. Changes in protein and lipid composition within the plasma membrane can affect signaling pathways, cell-cell contact, surface recognition, and cytoskeleton contacts (1). Endocytosis is one mechanism that the cell uses to regulate the contents of its plasma membrane through internalization of cell surface receptors, solutes, and cell surface lipids by invagination and scission (2). In the first step, these extracellular contents are contained in a vesicle that fuses with the early endosome. The early endosome acts as a sorting hub in response to the needs of the cell. Contents can be recycled back to the plasma membrane, transported to the trans-Golgi network, or trafficked for degradation through endosomal maturation and fusion with the lysosome (**Figure 1.1**) (3,4).

Many active cell surface receptors, herein referred to as cargoes, are regulated via the degradative pathway. This process involves the formation of endosomes with cargo laden intraluminal vesicles known as multivesicular endosomes (MVEs). Once cargo is moved from the limiting membrane of the endosome into the lumen, cytoplasmic signaling domains are sequestered away from the cytosol, blocking any downstream signaling effects. MVEs fuse with lysosomes allowing their vesicular contents to be degraded by hydrolases (3,5). Defects in the formation of MVEs prevent termination of signaling cascades and reduce delivery of cargo to the lysosome. The resulting persistent receptor signaling can lead to cancer, diabetes, immune deficiencies, and cardiovascular disease (5).

The ESCRT Machinery

Cargoes that are to be trafficked to the lysosome are modified with ubiquitin on their cytoplasmic tails (4,6,7). Ubiquitylation occurs at the cell surface and/or at the endosomal limiting membrane, and this modification is recognized by a set of proteins known as the ESCRT machinery. A single ubiquitin moiety is capable of identifying a cargo molecule for internalization and degradation (4,7). The majority of ubiquitin is removed from cargo by deubiquitinating enzymes (DUBs) which are recruited by interactions with components of the ESCRT machinery prior to intraluminal vesicle (ILV) formation (4,8).

The ESCRT machinery was initially discovered in yeast where its function is required for hydrolase delivery to the vacuole, a lysosome-like structure. Deletions of genes expressing ESCRT proteins cause aberrant endosomal morphology that has come to be known as the class E compartment (9-11). The ESCRT machinery is responsible for clustering of ubiquitylated cargo, membrane deformation, and vesicle scission during ILV formation (12). Though the protein complexes and many of their interacting partners have been well characterized, the exact mechanism for each of these steps is poorly defined. The ESCRT machinery consists of five complexes: ESCRT-0, I, II, III, Vps4-Vta1, in addition to several accessory proteins (13,14). Because there is a lack of uniformity in nomenclature of the ESCRT proteins, they will be denoted by the yeast names, except for a few well-characterized metazoan proteins: Hrs, Stam, Tsg101, and Alix. (See **Figure 1.2** and **Table 1.1** for an overview of ESCRT proteins). Biochemical characterization of the components of each ESCRT complex, a discussion of their roles in diverse cellular processes including: MVE biogenesis, cytokinesis, viral budding and autophagy, and postulated models of ESCRT function are discussed in detail below.

ESCRT-0

In solution, ESCRT-0 functions as a 1:1 complex consisting of the two subunits Hrs and Stam (15). Both of these subunits contain clathrin binding domains (16,17) and multiple ubiquitin binding domains (UBDs) (18). Disruption of ESCRT-0's interaction with UBDs causes defects in the downregulation of ubiquitinated cargo, such as epidermal growth factor receptor (EGFR) (19). Hrs contains a PSAP amino acid sequence located within a proline-rich region near the center of the protein sequence, which is important for interaction with the downstream ESCRT-I complex (20). ESCRT-0 constitutively associates with endosomes through the FYVE zinc-finger domain in HRS, which binds specifically to phosphatidylinositol 3-phosphate (PI3P), a lipid enriched in the endosomal membrane (21-23). This FYVE domain is capable of penetrating into the lipid bilayer, resulting in a high affinity interaction, with a K_d near 10 nM (24). An additional study using atomic force microscopy (AFM), has shown that in the presence of membranes, ESCRT-0 can form a heterotetramer consisting of two Hrs subunits as well as two subunits of Stam (25). This is consistent with a crystal structure of the metazoan Hrs FYVE domain that revealed a dimer interface (26). This strong interaction between PI3P and the FYVE domain of Hrs provides both membrane recruitment and membrane specificity for the ESCRT-0 complex, setting the stage for downstream ESCRT assembly (18,23).

ESCRT-I

ESCRT-I is a heterotetramer in solution with a 1:1:1:1 ratio of the following subunits: Tsg101, Vps28, Vps37 and Mvb12 (27-29). Crystallographic studies have solved the complete structure of the yeast ESCRT-I complex revealing a 176 Å long, highly-asymmetric complex that contains a core and a stalk portion. The core, also known as the headpiece, is made of three

helical hairpins which encompasses a portion of all four subunits. The stalk extends from the core 130 Å and is made of Tsg101, Vps37, and Mvb12 (28). The Tsg101 subunit contains an N-terminal ubiquitin E2 variant domain (UEV) that binds ubiquitylated cargo and PSAP motifs similar to those found in Hrs and select viral proteins, such as the Gag protein from human immunodeficiency virus (HIV-1) (20,27,30). ESCRT-I binds weakly to acidic phospholipids but does not have binding specificity for PI3P, *in vitro* (28). This weak membrane association is unlikely to recruit ESCRT-I to endosomal membranes; however, it has been proposed that ESCRT-I's association with ESCRT-0 and ubiquitylated cargo could drive localization of ESCRT-I (20). It has been demonstrated that yeast Vps28 contains a C-terminal four helix bundle that interacts with Vps36, a subunit of ESCRT-II (31).

ESCRT-II

ESCRT-II forms a stable heterotetramer composed of two Vps25 subunits and one subunit each of Vps22 and Vps36 (32). The core complex of yeast ESCRT-II has been crystallized, revealing a trilobal structure, in which two lobes each contain a single Vps25 subunit and the third branch is formed by a heterodimer between Vps22 and Vps36. It should be noted that the N-terminal portion of Vps36 is omitted from these structures (33-35). The core contains eight winged helix (WH) domains; two per subunit that superimpose on one another despite no identifiable sequence similarity between subunits. Common features of WH domains are hydrophobic patches that facilitate protein-protein interactions. These hydrophobic regions of Vps22 and Vps36 are mostly occupied by their interaction with one another, as well as with Vps25. Vps22 contains a basic N-terminal helix that interacts nonspecifically with acidic

phospholipids (35). Vps25, on the other hand, has exposed hydrophobic patches that likely interact with Vps20 of ESCRT-III (34).

The N-terminus of Vps36 contains a Gram-like ubiquitin-binding in Eap-45 (GLUE) domain that varies in structural architecture between yeast and other metazoans. Despite slight differences, the GLUE domain of Vps36 appears to act ubiquitously as a split pleckstrin homology (PH) domain that is capable of binding PI3P as well as other phosphoinositides (36,37). Unlike the metazoan GLUE domain, the GLUE domain of yeast contains the insertion of two Np14-type zinc finger (NZF) domains that are each crucial for protein-protein interactions (36). The NZF1 domain binds to the C-terminus of Vps28 (from the ESCRT-I complex (31)), while NZF2 domain binds directly to ubiquitin (38). Although metazoan Vps36 does not contain NZF domains, the GLUE domain itself is capable of binding to ubiquitin (37). The exact binding site between ESCRT-II and ESCRT-I has yet to be characterized in metazoans, but yeast two-hybrid experiments have confirmed this interaction (39).

Because there are two copies of Vps25 present in ESCRT-II, several studies have investigated whether it is necessary for both Vps25 subunits to be present for ESCRT-II to function properly in receptor downregulation (33,40). A study conducted in yeast utilized a fluorescently tagged cargo molecule, carboxypeptidase S (CPS), to monitor proper lysosome trafficking via the endocytic pathway. When yeast contained only a mutated ESCRT-II complex with a single Vps25 subunit, CPS accumulated on the lumen of aberrant class E compartments (33). In another study, it was shown that in these same mutants ESCRT-III can interact with a single Vps25 subunit, but a defect in sorting still occurred suggesting that both Vps25 subunits are required for proper sequestration of cargo (40).

ESCRT-III

Unlike the other ESCRT complexes, ESCRT-III subunits contain no known UBDs and are individual subunits in the cytoplasm capable of assembling into a complex only at the surface of membranes (41). Once assembled, the core complex is made up of the following proteins, which are recruited to the endosomal membrane in the following respective order: Vps20, Vps32, Vps24, and Vps2 (42). Did2, Ist1, and Vps60 are three additional ESCRT-III subunits that function during the late steps of MVE formation, and unlike the core ESCRT-III proteins, are not essential for function (43-45).

ESCRT-III proteins have all been proposed to have a similar core architecture that includes a basic N-terminus, crucial for membrane targeting, and an acidic C-terminus, which is important for protein-protein interactions (46-48). Human Vps24 (residues 9-183) has been crystallized and reveals a 70 Å long helical hairpin ($\alpha 1$ and $\alpha 2$) that forms an asymmetric four-helix bundle with two short helices ($\alpha 3$ and $\alpha 5$) that pack at the open end of the hairpin. A fifth helix ($\alpha 5$) is connected to the four-helix bundle via a 20 amino acid long disordered linker (**Figure 1.3A**) (46). In addition, the N-terminus of Ist1 (residues 1-189) has been crystallized (**Figure 1.3B**) and has a similar four-helix bundle that overlays with the four-helix bundle of Vps24 with a root mean squared deviation (RMSD) of 2.4 Å for the alpha carbon positions (47). However, one striking difference between the two structures is how helix five is connected. In Ist1, helix five packs against the closed end of the hairpin. In contrast, helix 5 of Vps24 is positioned near the open end of the hairpin (46,47). Based on these structures and secondary structure prediction models, all ESCRT-III subunits are likely to have an asymmetric four-helix bundle with a fifth helix connected by a very flexible region.

It has been proposed that the C-terminus of the ESCRT-III subunits, which includes helix five, acts as an auto-inhibitory domain that prevents interaction between individual ESCRT-III subunits from occurring in the cytoplasm (48-53). A study using human Vps24 has shown that the N-terminal region of Vps24 can pull down C-terminal fragments of Vps24 but not full-length Vps24, suggesting that full-length Vps24 is auto-inhibited from assembly via a blocked binding interface (50). Another study placed environmentally-sensitive probes within the $\alpha 5$ - $\alpha 6$ loop of Vps20 and Vps32 and observed significant fluorescence changes upon addition of liposomes. This suggests that conformational changes occur in the auto-inhibitory region of early ESCRT-III subunits upon membrane binding indicating that this interaction could assist in the release of auto-inhibition necessary for ESCRT-III assembly (53). Furthermore, small-angle X-ray scattering (SAXS) studies have produced a model of an open conformation of human Vps24 under high salt concentrations, which likely disrupt the electrostatics present in the closed conformation (51). In addition to the autoinhibitory domain, the C-terminus of ESCRT-III proteins contains MIT-domain-interacting motifs (MIM) that bind with varying affinities to the microtubule interacting and transport (MIT) domain of Vps4, an ATPase that disassembles the ESCRT-III complex (54-56).

Vps20 is N-terminally myristoylated which helps target it to the endosomal membrane where it acts as a nucleator for ESCRT-III assembly (41,42). Vps20 binds to each Vps25 subunit of ESCRT-II. It is proposed that through the combination of interaction with membranes and ESCRT-II a conformational change in Vps20 is induced, which in turn relieves autoinhibition (34,53). Recently, AFM experiments have shown that a complex consisting of Vps20 and ESCRT-II preferentially binds to membranes of high curvature and could spatially regulate

ESCRT-III assembly to the highly curved vesicle bud necks (57). Vps32, the most abundant ESCRT-III subunit, is recruited to the endosomal membrane by direct interaction with Vps20. The C-terminus of Vps32 binds to Alix, which is an ESCRT-associated protein predicted to stabilize Snf7 oligomers and recruit DUBs (14,54). In addition, Vps32 homo-oligomerizes to form filaments that are essential for membrane scission activity and are capped by Vps24 subunits, blocking further oligomerization (42,53). *In vitro* studies have shown that mammalian Vps24 preferentially binds to phosphatidylinositol 3,5-bisphosphate (PI3,5P₂), a lipid synthesized late on endosomal membranes. This lipid interaction may provide some regulation of Vps24 recruitment in order to act as the cap, although further studies are necessary to better understand this potential mechanism (58). Vps24 recruits Vps2, which is essential for the proper localization of Vps4 (42). The recruitment and activity of Vps4 is further regulated by Did2, Ist1 and Vps60 (12,44). Although the order of ESCRT-III assembly has been well characterized, the exact stoichiometry of each of the subunits at the endosomal membrane remains unknown.

Characterization of the ESCRT-III Filament

A great deal of attention has been focused on understanding how ESCRT-III filaments assemble due to the critical role these filaments have in the scission of membrane necks with negative curvature. Specifically, electron microscopy (EM) has been utilized to visualize ESCRT-III filaments, which has significantly advanced this area of research (52,59-62). ESCRT-III filaments were first visualized upon overexpression of human Snf7 in Cos7 cells, which caused Snf7 to accumulate in protein patches on the plasma membrane, as well as on endosomal compartments. EM images of the plasma membrane depict highly-curved, circular filaments. Upon co-expression of a mutant Vps4 protein that is unable to hydrolyze adenosine

triphosphate (ATP) (Vps4EQ) these filaments were able to morph into buds and occasional tubules that extend away from the cell. This was the first visualization of ESCRT filaments distorting membranes (60). Similarly, overexpression of human Vps2 in HeLa cells resulted in tubes protruding from the cell surface (62). Concentrated, recombinant yeast Vps24 also formed filaments, and single-particle reconstruction was applied to the negative stain EM images of these filaments (61). The crystal structure of human Vps24 (46) was modeled onto the reconstructed filaments of yeast Vps24 to produce a 25 Å helical reconstruction of a two-stranded Vps24 filament. Based upon this reconstruction, inter-strand contacts were made via the $\alpha 1/\alpha 2$ hairpin. A Vps24 variant, K55S, which encodes a mutation in this loop region prevented filament formation *in vitro*, and also had CPS-sorting defects *in vivo*, suggesting the closed end of the hairpin may play a crucial role in protein-protein interactions that occur during filament formation (61). In a recent study, a mutation that relieved auto-inhibition in recombinant yeast, Vps32-R52E, promoted filament formation. These filaments were examined by EM, and long proto-filaments made of two intertwining subfilaments; approximately 4 nm in diameter, were visualized. When Vps32-R52E was incubated with lipid monolayers, spirals were visualized with an outer diameter of ~50 nm. Interestingly, addition of Vps24 and Vps2 to Vps32 protofilaments generated coiled helices. This remodeling event could provide energy for the membrane bending and scission required for ILV formation (52). Taken together, these findings strongly support a model in which ESCRT-III filaments assemble into a structure capable of deforming the membrane to promote ILV formation. However, further characterization is necessary to better understand which structures the filaments adopt *in vivo*.

ESCRT-III Disassembly by the Vps4-Vta1 Complex

Energy in the form of ATP is required to disassemble the ESCRT-III complex from the endosomal membrane to replenish the cytosolic pool of ESCRT-III subunits for further rounds of MVE formation (9,41,63). This process is carried out by Vps4, the only known enzyme in the ESCRT machinery, which is regulated by late acting ESCRT-III subunits: Ist1, Did2, and Vps60 (43-45). Subcellular fractionation experiments in yeast have shown that deletion of Vps4 causes a shift in ESCRT-III distribution from the cytoplasm to the endosomal membrane, confirming that Vps4 is essential for removing ESCRT-III from the endosomal membrane (41,63).

Vps4-Vta1

Vps4 contains a single ATPase cassette and is classified as a Type 1 ATPase that typically function as oligomeric rings (9). The crystal structure of human Vps4 reveals an N-terminal ESCRT-III binding MIT domain, a flexible linker, a large AAA-ATPase α/β domain, a small AAA-ATPase four-helix bundle, a unique β domain, and a final helix. Consistent with other Type 1 AAA-ATPases, Vps4 binds ATP using Walker A/B motifs in the large AAA-ATPase domain as well as portions of the small AAA-ATPase domain (64). Vps4EQ, encoded by a mutation in the Walker B magnesium binding motif, allows ATP binding but inhibits hydrolysis and has been shown to inhibit lysosome protein sorting (63,64).

In vitro studies have shown that Vps4 exists either as a monomer or dimer in the absence of ATP, and upon nucleotide binding, it assembles into stacked oligomeric rings (63-65). A great deal of emphasis has been placed on understanding the stoichiometry of these stacked rings by using Vps4EQ to block ATP hydrolysis and maintain complex assembly. Analytical ultracentrifugation (64,66), multi-angle light scattering (MALS) (67), size-exclusion

chromatography (SEC) (68,69), cross-linking experiments (63), and cryo-EM techniques (66-68) have all been utilized on Vps4EQ with ATP in attempts to characterize the nucleotide bound oligomeric state. The most frequent complex observed has been a stacked structure of two hexameric rings (67-69), although alternative oligomers of 10 (63) and 14 (66) subunits have also been observed. Regardless of the observed stoichiometry, the rings stack with a central pore that passes through the complex (64,65). A current model proposes that disassembly occurs by movement of ESCRT-III through this central pore (64); however, further experiments are necessary to confirm this. Sub-cellular fractionation experiments in yeast show that Vps4 is mostly cytosolic whereas Vps4EQ appears in membrane-associated fractions, suggesting that ATP hydrolysis drives Vps4 oligomer disassembly from the membrane (64,70). In addition, the flexible linker between the MIT domain and the ATPase region has been suggested to play a role in the regulation of self-assembly and ATPase activity (71), which adds further to the complexity of Vps4.

Vta1 is an ESCRT protein that contains three distinct regions: two N-terminally located MIT domains, a random coil linker, and a C-terminal Vps4, SBP1, LIP5 (VSL) domain. The VSL domain directly binds the β -domain of Vps4 (64,72-75) and is also responsible for homo-dimerization (73,75). Deletion of Vta1 causes an intermediate phenotype with mild sorting defects of CPS and partial redistribution of ESCRT-III subunits to endosomal membranes. These phenotypes are not as severe as deletion of Vps4, but they do suggest that Vta1 may regulate Vps4 by stimulating ESCRT-III release (73,76). Addition of Vta1 to Vps4 significantly stimulates the ATPase activity of Vps4 and also stabilizes Vps4EQ complex assembly in the presence of ATP (70,72,73,76). The full complex of Vps4-Vta1 has been a subject of extensive

research, and two different models based on low-resolution structures have been proposed. One model suggests that a Vta1 dimer contacts two Vps4 subunits, one from each hexameric ring, providing stabilization within the dodecameric structure (75). A cryo-EM reconstruction of a Vps4-Vta1 complex argues for three dimer pairs of Vta1 that would interact with only one hexameric ring of Vps4. This model was based in part on the asymmetry seen between the two hexameric rings (68). Higher resolution structures will be needed to fully elucidate the mechanisms of how Vta1 stabilizes Vps4 assembly as well as stimulates its ATPase activity.

MIT-MIM Interaction

The N-terminal MIT domain of Vps4 is a compact antiparallel three-helix bundle capable of interactions with MIM domains found in the C-terminus of ESCRT-III proteins (77). ESCRT-III proteins contain either MIM1 motifs that bind between $\alpha 1$ and $\alpha 2$ of Vps4 (54,55) or MIM2 motifs that bind between $\alpha 1$ and $\alpha 3$ of Vps4 (56). Vps2, Did2, Vps24, and Ist1 all contain MIM1 domains. A Vps4 variant, L64D, is capable of blocking interactions with MIM1 domains resulting in impaired CPS sorting (55). Vps20, Vps32, and Ist1 all contain MIM2 domains, and blocking these interactions with Vps4 similarly cause sorting defects (56). Vps60 contains a unique MIM domain that has not been well characterized but has been shown to directly bind the C-terminus of Vps4 (70). All of the ESCRT-III MIM domains, except the MIM domains of Ist1, have been shown to stimulate ATP hydrolysis, *in vitro* (78). Based on structural analysis, the MIT domain of Vps4 is capable of interacting simultaneously with both MIM1 and MIM2-containing proteins (54-56). The Vps2 MIM motif has a high affinity for the Vps4 MIT motif, and *in vitro* reconstitution assays have shown that this interaction is essential for ESCRT-III disassembly (59,79). The interaction between Vps4 and the MIM domains of ESCRT-III are

complex, and further experiments are needed in order to determine how these interactions interplay during ESCRT-III complex disassembly.

Vps60, Did2, and Ist1: Regulators of the Vps4-Vta1 complex

Ist1 is an ESCRT-III protein that is slightly larger than the other ESCRT-III proteins and forms an elongated monomer in solution (44,80). Ist1 directly binds to and acts as a negative regulator of Vps4 in solution (70,80). When Ist1 is mixed in equimolar concentrations with Vps4EQ in the presence of ATP, Vps4EQ complex assembly was inhibited. In fact, a heterodimer between Ist1 and Vps4EQ forms. Furthermore, Ist1 inhibits ATPase activity of yeast Vps4 and blocks Vta1's stimulation of Vps4 activity (80). Ist1 also binds directly to Did2 allowing for localization of Ist1 to MVEs (44,80). Ist1 has also been suggested to play a positive role in facilitating Vps4 recruitment to the membrane surface, despite inhibiting ATPase activity in solution (80). This dual regulatory role of Ist1 on Vps4 requires further studies to fully appreciate how Ist1 regulates disassembly of ESCRT-III subunits.

Did2 localizes to the endosomal membrane through interaction with Vps24. Sub-cellular fractionation studies have revealed a redistribution of Vps32 and Vps24 to the pellet fraction upon deletion of Did2, which suggests that Did2 plays a role in ESCRT-III disassembly (43). Did2 has also been shown to interact with the MIT2 domain of Vta1. This same region of Vta1 can directly bind to Vps60, which depends on this interaction for endosomal localization (81). Yeast genetics have been extensively utilized to try to elucidate specific roles for these regulatory proteins but many questions remain. Observations about how Ist1 plays a negative role in solution but has a positive effect at the endosomal membrane will have to be reconciled. Also it will be important to determine the temporal order of Did2 associations with Vps4, Vta1

and Ist1 as well as the specific role each of these interactions has on regulating ESCRT-III disassembly. Furthermore, it will be important to discover any differences that may exist between metazoan and yeast regulation of Vps4.

Proposed Models of ESCRT Function

Since the ESCRT machinery was first discovered, an abundance of models have been proposed for ESCRT function. One model, which observed the role each complex has in MVE formation, was generated based on budding in giant unilamellar vesicles (GUVs). These experiments showed that high concentrations of ESCRT-III alone were sufficient to bud and release ILVs, but physiological concentrations were insufficient to release ILVs (79,82). In these same assays, ESCRT-0 formed regions of clustered ubiquitylated cargo, ESCRT-I and ESCRT-II deformed the membrane, and ESCRT-III induced scission for ILV formation. Overall, this led to a model in which ESCRT-0 forms large regions of clustered cargo followed by the recruitment of ESCRT-I and ESCRT-II, which would induce membrane deformation. In this model, it is proposed that ESCRT-I and ESCRT-II use their multiple membrane interactions to act as the foundation for the forming bud necks, where ESCRT-III would be recruited and restricted to the membrane buds for scission to take place (82). However, this model does not provide mechanistic details of how ESCRT-I/ESCRT-II would induce membrane deformation or how membrane scission by ESCRT-III would occur.

To specifically address membrane scission by ESCRT-III filaments several different models have been generated to mechanistically explain this process. In the “dome” model, Vps32 would form flat, inward-spiraling filaments that would isolate a membrane patch and initiate a bud. Binding of the filament to lipid head groups would prevent lipid exchange with

the surrounding membrane and could sequester cargo within these initial buds. Vps24-Vps2 would then polymerize as a tube that narrows at the end of the forming vesicle, generating a hemi-spherical dome-like shape that occupies the original bud. This would result in the formation of a very thin membrane neck connecting the dome to the nascent vesicle. As the protein dome thickens, the neck would narrow until a point was reached in which membrane scission became energetically favorable, and an unattached vesicle and a membrane cap would remain (18,83,84). EM images of Vps24-Vps2 revealed helical tubes with their membrane binding sites on the outside of the tubes (59). This provides strong experimental data to support this computational based “dome” model. This model explains why ESCRT-III filaments escape sequestration within the ILV. However, it fails to address why Vps24 and Vps2 proteins were not necessary for ILV budding in the GUV based assay mentioned above (82).

The recently proposed “whorl” model is based upon a solution structure of an ESCRT-I/ESCRT-II supercomplex. It is a slight variation of the dome model that adds the upstream ESCRT proteins. It begins with ESCRT-0 recruiting ESCRT-I, which in turn recruits ESCRT-II, generating a supercomplex that stabilizes the initial membrane bud. In this model, 6-10 copies of ESCRT-I/ESCRT-II would fit in the bud neck, and ubiquitinated cargo could be passed from ESCRT-0 to this supercomplex. The solution structures revealed a variety of conformations, suggesting that a change from an open to a closed state is possible. This model proposes that ESCRT-0 dissociation would cause the supercomplex to close, dragging cargo into the neck. ESCRT-III filaments would extend from ESCRT-II into the neck, generating a whorl arrangement that could constrict the membrane. Vps4 assembly could organize central locations where the filaments meet. Each of these filaments would interact with membranes and, through

the binding energy generated from filament formation, would eventually promote scission (84,85). However, the passing of ubiquitinated cargo is difficult to imagine because ESCRT-0 contains multiple UBDs whereas ESCRT-I and ESCRT-II only have one each, and the UBDs have similar binding affinities for ubiquitin (4,86). Also the “whorl” model is not as adaptable as the “dome” model in regard to scission of the various sized necks in which the ESCRT machinery is capable of acting upon (84).

Similar to the dome model, the “purse string” model depicts Vps20 activating Vps32, allowing it to oligomerize into a spiral on the membrane. This spiral would surround the ubiquitinated cargo, inducing membrane deformation. Vps32 would be capped by Vps24-Vps2, which would help to recruit the Vps4-Vta1 complex to the site of ESCRT-III formation. However, unlike other ESCRT-III scission models, the “purse string” model describes Vps4-Vta1 as playing an essential role in membrane scission, as well as recycling ESCRT-III to the cytoplasm. This model proposes that through ATP hydrolysis, the Vps4-Vta1 complex would act as a mechanical motor and generate a force by shrinking the spiral rings through the removal of ESCRT-III subunits. This would generate a tighter spiral around cargo, similar to a purse string, until scission occurred (18,53). Future experiments will be necessary to determine if Vps4 participates in scission or merely recycles the ESCRT-III complex. *In vitro* studies utilizing the GUV assay described budding in the absence of Vps4 (79,82). On the other hand, live cell imaging of cytokinesis and HIV-budding has shown that Vps4 is recruited to these sites with ESCRT-III, prior to membrane scission, suggesting that Vps4 participates in this process (87-89). Overall, more conclusive data will be needed to determine the mechanistic role, if any, that Vps4 has in membrane scission. The past decade has seen an explosion in understanding the

ESCRT machinery. However, the field will need to fill in the unknown areas to build a cohesive model of how this intricate group of proteins functions.

Additional Cellular Functions of the ESCRTs

Although the ESCRT machinery was initially identified in MVE formation, more recent work has elucidated additional roles in cytokinesis, viral budding, and autophagy. Cytokinesis and viral budding induce membrane invaginations that extend away from the cytoplasm requiring a final scission event that utilize proteins from the ESCRT machinery (**Figure 1.4**). The specific role of the ESCRT machinery in autophagy is less clear.

Cytokinesis

Cytokinesis is the process that separates two daughter cells from one another during the final stage of mitosis. During this process, an actin-myosin ring constricts resulting in two daughter cells connected by a membrane tube known as the intracellular bridge. During abscission, the final step of cytokinesis, select ESCRT proteins play a crucial role in cleavage of the intracellular bridge (90,91). In animal cells, Tsg101 (from the ESCRT-I complex) and Alix both localize to the cellular mid-body through interaction with Cep55, a centrosomal protein that is found during the late stages of cytokinesis (92-95). Depleting either Alix or Tsg101 results in a significant increase in multinucleated cells, which further confirms their role in cytokinesis (92). ESCRT-III and Vps4 are also required for abscission and the current model suggests that Cep55's interaction with ESCRT-I and Alix recruits ESCRT-III to the mid-body through a direct interaction between Vps32 and Alix. This assembly of ESCRT-III leads to cleavage of the membrane neck and requires Vps4 for disassembly (93,95). A combination of live cell imaging and EM during abscission in human cells has revealed a 17 nm diameter filament that narrowed

the bridge during a time course of the experiment. ESCRT-III localized within this region and was essential for filament assembly (96). This suggests that ESCRT-III utilizes a similar mechanism in its role in abscission to MVE biogenesis, but further studies will be necessary to understand how the ESCRT-III machinery is activated. In addition, it remains unclear if other proteins required for abscission interact with ESCRT complexes to complete this cleavage event.

Viral Budding

Membrane-enveloped viruses complete their replication in the cytoplasm of their host cell and then exit the cell by budding from the plasma membrane. Many of these viruses will hijack the host cell's ESCRT machinery to carry out scission of the virus bud (97). Specifically, HIV-1 can be used as a model because its exploitation of ESCRT machinery for release from the cell has been well-characterized (98). Alix, ESCRT-I, ESCRT-III and Vps4 have a direct role in viral budding, and the Gag protein is responsible for directing ESCRTs to viral bud necks. It is worth noting that Vps20, unlike the other ESCRT-III subunits, is not required for HIV particle release (39). The viral Gag protein can drive bud formation independent of ESCRT but requires their assembly for scission of the neck connecting the viral bud to the plasma membrane (99). The PSAP motif within the late domain of the Gag protein binds to the UEV domain of Tsg101 and drives ESCRT localization to the site of viral budding (30,98). However, it remains unclear as to how ESCRT-I recruits and activates Vps32 to begin ESCRT-III assembly. Alix has been hypothesized to act as the bridge between these two complexes because it localizes to viral buds and also interacts with ESCRT-I and Vps32 (100). Confirmatory experiments are still needed to directly demonstrate Alix's role in viral budding.

Autophagy

Autophagy is a cellular pathway in which portions of the plasma membrane self-engulf to degrade proteins and/or organelles. This process is dependent upon the nutritional needs of the cell and serves to replenish biosynthetic molecules, clear damaged organelles, or turn over proteins and lipids. Autophagy requires the progression of a double membrane compartment that starts as a preautophagosomal structure that matures into an isolated membrane known as phagophore. This phagophore closes to produce an autophagosome, which eventually fuses with the lysosome for degradation of its contents. An autophagosome is equivalent in structure to an MVE with a single large ILV, and closure of the autophagosome is equivalent to the scission event that occurs in MVE formation (101-104). Recent EM work has shown that depletion of ESCRT proteins inhibits autophagosome degradation, suggesting a role for the ESCRT machinery in autophagy (105-107). Future studies will be needed to determine if ESCRT machinery is directly involved in the scission of membranes for autophagosome formation or if aberrant ESCRT function triggers signals to inhibit autophagy in a more indirect role.

ESCRT Machinery and Disease

Receptor attenuation is essential for cellular homeostasis and is accomplished through the endocytic pathway. The ESCRT machinery plays a vital role in the downregulation of these receptors. Dysfunction of ESCRT components are associated with cancer and can be linked to persistent cell signaling from improperly-trafficked receptors (5). As mentioned above, EGFR depends on the ESCRT pathway for down regulation, and continual signaling of EGFR has been linked to mammary carcinomas, squamous cell carcinomas and glioblastomas (108). Depletion of Hrs, Tsg101 or Vps25 have all been linked to defects in EGFR degradation (109-111), and

components of ESCRT-I may function as tumor suppressor genes (5). Also, aberrant Tsg101 transcripts from alternative splice sites have been observed at a high frequency in some cases of cancer (5,112). Many details of how the ESCRT machinery functions as tumor suppressors have not been well characterized and as the mechanisms of the pathway begin to be elucidated; this likely will become an important focus of the ESCRT field.

Proper lysosomal function in neurons is crucial to protect cells from protein aggregates that can lead to neurodegenerative diseases such as Alzheimer's, Huntington's, and Parkinson's disease. Since the ESCRT machinery is necessary for MVE formation and has been linked to autophagy (two pathways that are directly linked to the lysosome) these proteins play a vital role in lysosomal maintenance (113). Impaired ESCRT function has been associated with a host of neurodegenerative diseases. The most highly-studied are mutations in Vps2 that are found in a subset of patients with frontotemporal dementia and amyotrophic lateral sclerosis (ALS) (114,115). It has been suggested that mutations in Vps2 lead to the accumulation and improper clearing of ubiquitin-positive protein aggregates that may normally rely on autophagy (106,107). Like Vps2, many of the neurodegenerative diseases involving ESCRT machinery also involve the autophagy pathway (113). To better understand the role the ESCRT machinery plays in maintaining neuron health, the intersection between the ESCRT pathway and autophagy will need to be closely studied, which is an area that is currently lagging in the ESCRT field. Furthermore, understanding the mechanistic details of how the ESCRT machinery function will be essential for the development of treatments for diseases caused by aberrant ESCRT function.

Research Focus

Despite great advances that have been made in the ESCRT field in the past decade, regulation of the ESCRT machinery remains poorly understood. My thesis work has sought out to address how later acting ESCRT-II and ESCRT-III complexes are regulated within MVE biogenesis. Specifically Chapter Two describes the use of various assays to observe interactions between several of the later acting ESCRT proteins and lipids. Through these studies we discovered that a supercomplex between ESCRT-II and Vps20 preferentially binds to highly curved membranes, restricting Vps32 oligomerization to regions of high curvature. This supports a model in which this supercomplex binds to bud necks during MVE biogenesis. This would spatially and temporarily regulate assembly of downstream ESCRT-III to provide precise control over scission events within the cell.

Chapter Three describes the use of SAXS to characterize the conformational states of Vps24 and Vps20. We demonstrate that Vps20 is in open conformation in solution, unlike Vps24 which is in a closed state. In addition, SEC studies show that Vps20 interacts directly with the ESCRT-II complex independent of liposomes. Added to the conclusions of Chapter Two, this raises the possibility that a curvature-sensing supercomplex of ESCRT-II and Vps20 exists within the cytoplasm where Vps20 is already in an open state. This suggests that ESCRT-III subunits may not all be in the same auto-inhibited conformation within solution and that a potentially more complicated mechanism than the simple open-closed model currently accepted by the field is required to explain their assembly.

Chapter Four describes EM experiments used to characterize the overall architecture of a Vps32 filament. Through these characterizations we discovered that monomers in the filament

are flexible and can accommodate a range of bending angles. Also, the C-terminus of Vps32 restricts the spacing of the spiral in the lateral direction. This study defines a new mechanism of ESCRT-III assembly.

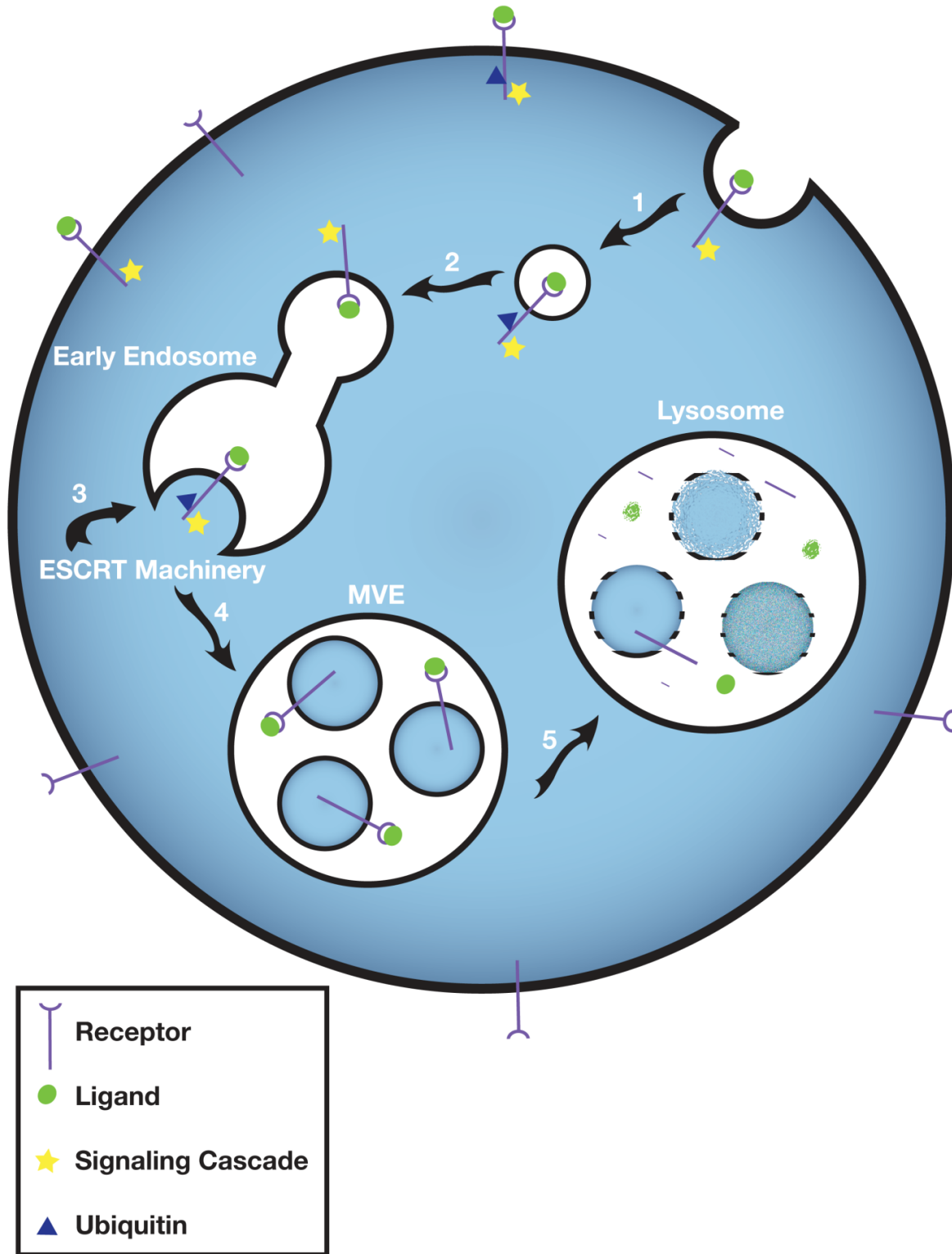


Figure 1.1: The Endocytic Pathway and the ESCRT Machinery.

Figure 1.1: The Endocytic Pathway.

Steps of the endocytic pathway. Step 1: Proteins, solutes, and cell surface lipids are internalized and brought to the early endosome. Step 2: The early endosome acts as a sorting hub where cargo can be transported to the plasma membrane, trans-Golgi complex, or lysosomes. Step 3: Cargo destined for degradation is ubiquitinated. The ESCRT machinery identifies and clusters ubiquitinated receptors, induces membrane deformation, and drives vesicle scission to generate a MVE. Step 4: At the MVE, receptors are internalized within the lumen of an endosome and are unable to interact with downstream signaling effectors within the cytoplasm. Step 5: The MVE fuses with the lysosome where the contents are degraded by hydrolases.

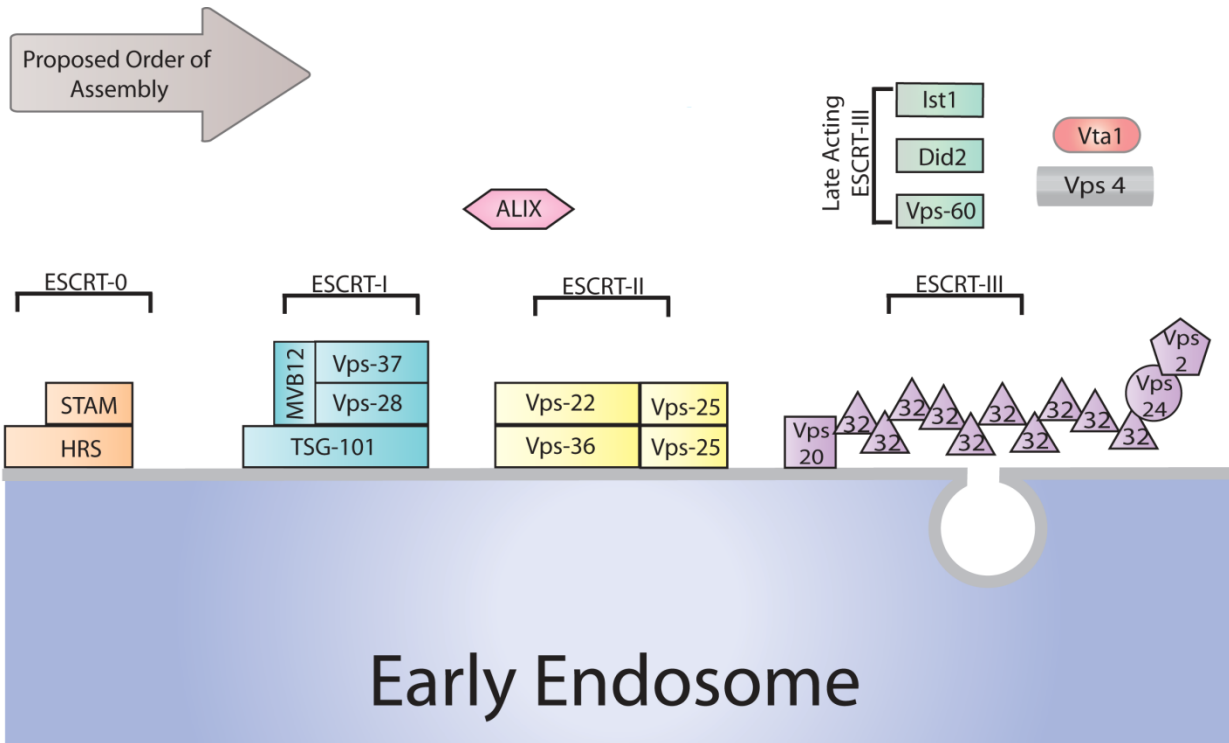


Figure 1.2: Components of the ESCRT Machinery.

Figure 1.2: Components of the ESCRT Machinery

Individual subunits of each of the ESCRT complexes are shown. The sequential order that the ESCRT machinery has been proposed to follow goes from left to right. Vps32 is shown as a filament near the site of ILV formation due to its proposed role in membrane scission. Late acting ESCRT-III subunits may play a role in regulating Vps4 function and are thus shown near the Vps4-Vta1 complex. Alix has been suggested to play a role in stabilizing the filament of Vps32. Figure modified from (113).

Protein	Interacting Partners
ESCRT-0	
HRS (Vps27)	PI3P, Ubiquitin, TSG-101, STAM, Clathrin, Cep55
STAM (Hse1)	Ubiquitin, HRS, Clathrin
ESCRT-I	
TSG-101 (Vps23)	Ubiquitin, HRS, ALIX, MVB12, Vps28, Vps37
Vps28	Vps36, Vps20, TSG-101
Vps37	MVB12, TSG-101
MVB12	TSG-101, Vps37
ESCRT-II	
Vps22 (EAP30)	Vps25
Vps25 (EAP20)	Vps20, Vps22, Vps36
Vps36 (EAP45)	Ubiquitin, PI3P, Vps25, Vps28
ESCRT-III	
Vps20 (CHMP6)	Vps28, Vps32, Vps4
Vps32 (Snf7, CHMP4)	Vps20, Vps24, Vps4, ALIX
Vps24 (CHMP3)	Vps32, Vps2, Vps4, Did2
Vps2 (CHMP2)	Vps24, Vps4
Late Acting ESCRT-III	
Did2 (CHMP1)	Ist1, Vps4, Vta1, Vps24
Ist1	Vps4, Did2
Vps60 (CHMP5)	Vta1
Accessory/Other	
Vta1 (Lip5)	Vps4, Vps60, Did2
Vps4	ALIX, Vps20, Vps32, Vps24, Vps2, Did2, Vta1, Ist1
ALIX (Bro1)	TSG-101, Vps32, Cep55

Table 1.1: Proteins of the ESCRT machinery and their interacting partners.

Table 1.1: Proteins of the ESCRT machinery and their interacting partners.

Table of the relevant ESCRT proteins and crucial interacting protein partners are listed.

Alternative names found in the literature are given in parenthesis. (3,12,116).

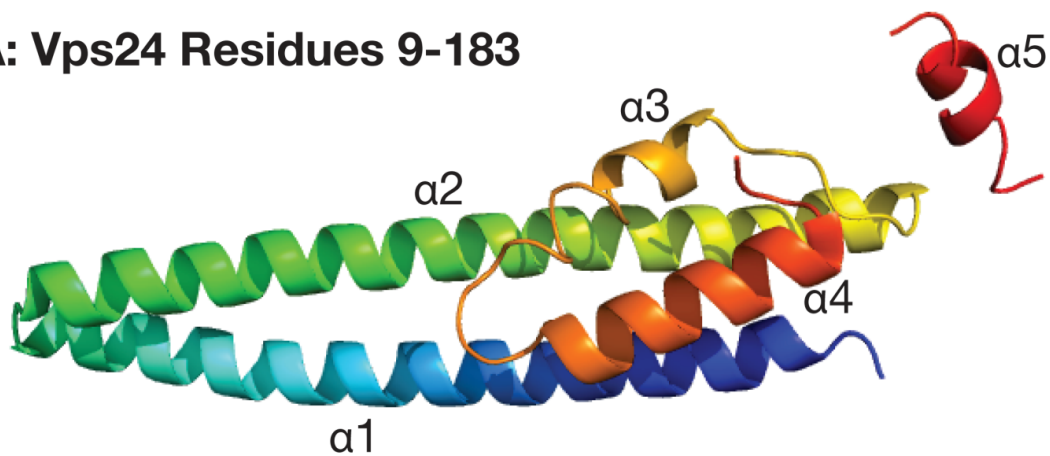
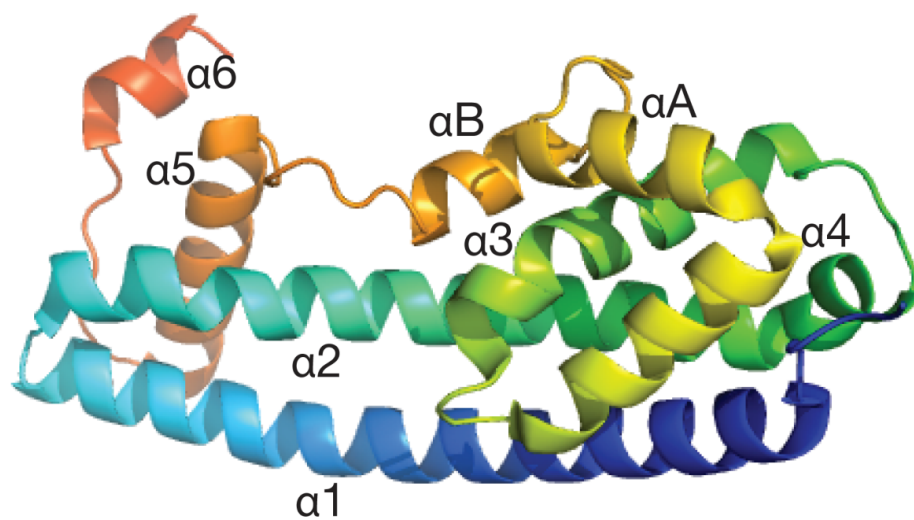
A: Vps24 Residues 9-183**B: Ist1 Residues 1-189**

Figure 1.3: Structures of ESCRT-III subunits.

Figure 1.3: Structures of ESCRT-III subunits.

Both crystal structures are colored in a blue to red gradient from the N-to-C terminus.

Figure 1.3A represents the crystal structure of human Vps24 (PDB: 2GD5) amino acids 9-183.

Helices are labeled 1-5 and act as the model for all ESCRT-III subunits. In this structure the position of helix 5 is near the four-helix bundle representing the open conformation (46). **Figure**

1.3B represents the crystal structure of human Ist1 (PDB: 3FRR) amino acids 1-183. Helices are labeled 1-5 to correspond to the helices of the human Vps24 structure. Two additional helices αA and αB are inserted to maintain the core ESCRT-III helix nomenclature. The auto-inhibitory domain is packed against the loop of the helical hairpin; representing the closed conformation (47).

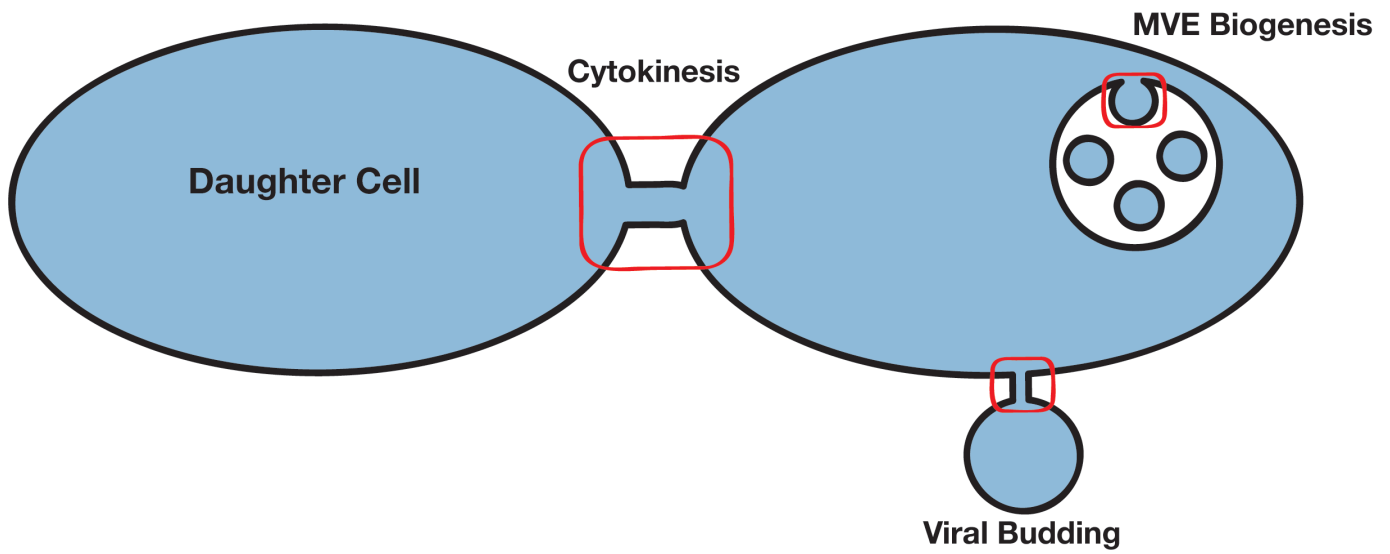


Figure 1.4: The ESCRT machinery plays defined roles in membrane scission for MVE biogenesis, cytokinesis, and viral budding.

Figure 1.4: The ESCRT machinery plays defined roles in membrane scission for MVE biogenesis, cytokinesis, and viral budding.

ESCRT machinery is required for diverse cellular processes. Red boxes highlight cellular locations where the ESCRT machinery is recruited and functions in membrane scission activity.

This image is modified from (117).

REFERENCES

1. Doherty, G. J., and McMahon, H. T. (2009) Mechanisms of endocytosis. *Annu Rev Biochem* **78**, 857-902
2. Falguières, T., Luyet, P. P., and Gruenberg, J. (2009) Molecular assemblies and membrane domains in multivesicular endosome dynamics. *Exp Cell Res* **315**, 1567-1573
3. Williams, R. L., and Urbé, S. (2007) The emerging shape of the ESCRT machinery. *Nat Rev Mol Cell Biol* **8**, 355-368
4. Piper, R. C., and Katzmann, D. J. (2007) Biogenesis and function of multivesicular bodies. *Annu Rev Cell Dev Biol* **23**, 519-547
5. Saksena, S., and Emr, S. D. (2009) ESCRTs and human disease. *Biochem Soc Trans* **37**, 167-172
6. Katzmann, D. J., Odorizzi, G., and Emr, S. D. (2002) Receptor downregulation and multivesicular-body sorting. *Nat Rev Mol Cell Biol* **3**, 893-905
7. Hicke, L., and Dunn, R. (2003) Regulation of membrane protein transport by ubiquitin and ubiquitin-binding proteins. *Annu Rev Cell Dev Biol* **19**, 141-172
8. Clague, M. J., and Urbé, S. (2006) Endocytosis: the DUB version. *Trends Cell Biol* **16**, 551-559
9. Babst, M., Sato, T. K., Banta, L. M., and Emr, S. D. (1997) Endosomal transport function in yeast requires a novel AAA-type ATPase, Vps4p. *EMBO J* **16**, 1820-1831
10. Rieder, S. E., Banta, L. M., Köhrer, K., McCaffery, J. M., and Emr, S. D. (1996) Multilamellar endosome-like compartment accumulates in the yeast vps28 vacuolar protein sorting mutant. *Mol Biol Cell* **7**, 985-999
11. Odorizzi, G., Babst, M., and Emr, S. D. (1998) Fab1p PtdIns(3)P 5-kinase function essential for protein sorting in the multivesicular body. *Cell* **95**, 847-858
12. Raiborg, C., and Stenmark, H. (2009) The ESCRT machinery in endosomal sorting of ubiquitylated membrane proteins. *Nature* **458**, 445-452
13. Mayers, J. R., and Audhya, A. (2012) Vesicle formation within endosomes: An ESCRT marks the spot. *Commun Integr Biol* **5**, 50-56
14. Wollert, T., Yang, D., Ren, X., Lee, H. H., Im, Y. J., and Hurley, J. H. (2009) The ESCRT machinery at a glance. *J Cell Sci* **122**, 2163-2166

15. Ren, X., Kloer, D. P., Kim, Y. C., Ghirlando, R., Saidi, L. F., Hummer, G., and Hurley, J. H. (2009) Hybrid structural model of the complete human ESCRT-0 complex. *Structure* **17**, 406-416
16. Raiborg, C., Bache, K. G., Mehlum, A., Stang, E., and Stenmark, H. (2001) Hrs recruits clathrin to early endosomes. *EMBO J* **20**, 5008-5021
17. McCullough, J., Row, P. E., Lorenzo, O., Doherty, M., Beynon, R., Clague, M. J., and Urbé, S. (2006) Activation of the endosome-associated ubiquitin isopeptidase AMSH by STAM, a component of the multivesicular body-sorting machinery. *Curr Biol* **16**, 160-165
18. Henne, W. M., Buchkovich, N. J., and Emr, S. D. (2011) The ESCRT pathway. *Dev Cell* **21**, 77-91
19. Hirano, S., Kawasaki, M., Ura, H., Kato, R., Raiborg, C., Stenmark, H., and Wakatsuki, S. (2006) Double-sided ubiquitin binding of Hrs-UIM in endosomal protein sorting. *Nat Struct Mol Biol* **13**, 272-277
20. Bache, K. G., Brech, A., Mehlum, A., and Stenmark, H. (2003) Hrs regulates multivesicular body formation via ESCRT recruitment to endosomes. *J Cell Biol* **162**, 435-442
21. Burd, C. G., and Emr, S. D. (1998) Phosphatidylinositol(3)-phosphate signaling mediated by specific binding to RING FYVE domains. *Mol Cell* **2**, 157-162
22. Katzmann, D. J., Stefan, C. J., Babst, M., and Emr, S. D. (2003) Vps27 recruits ESCRT machinery to endosomes during MVB sorting. *J Cell Biol* **162**, 413-423
23. Raiborg, C., Bremnes, B., Mehlum, A., Gillooly, D. J., D'Arrigo, A., Stang, E., and Stenmark, H. (2001) FYVE and coiled-coil domains determine the specific localisation of Hrs to early endosomes. *J Cell Sci* **114**, 2255-2263
24. Stahelin, R. V., Long, F., Diraviyam, K., Bruzik, K. S., Murray, D., and Cho, W. (2002) Phosphatidylinositol 3-phosphate induces the membrane penetration of the FYVE domains of Vps27p and Hrs. *J Biol Chem* **277**, 26379-26388
25. Mayers, J. R., Fyfe, I., Schuh, A. L., Chapman, E. R., Edwardson, J. M., and Audhya, A. (2011) ESCRT-0 assembles as a heterotetrameric complex on membranes and binds multiple ubiquitylated cargoes simultaneously. *J Biol Chem* **286**, 9636-9645
26. Mao, Y., Nickitenko, A., Duan, X., Lloyd, T. E., Wu, M. N., Bellen, H., and Quioco, F. A. (2000) Crystal structure of the VHS and FYVE tandem domains of Hrs, a protein involved in membrane trafficking and signal transduction. *Cell* **100**, 447-456

27. Katzmann, D. J., Babst, M., and Emr, S. D. (2001) Ubiquitin-dependent sorting into the multivesicular body pathway requires the function of a conserved endosomal protein sorting complex, ESCRT-I. *Cell* **106**, 145-155
28. Kostelansky, M. S., Schluter, C., Tam, Y. Y., Lee, S., Ghirlando, R., Beach, B., Conibear, E., and Hurley, J. H. (2007) Molecular architecture and functional model of the complete yeast ESCRT-I heterotetramer. *Cell* **129**, 485-498
29. Audhya, A., McLeod, I. X., Yates, J. R., and Oegema, K. (2007) MVB-12, a fourth subunit of metazoan ESCRT-I, functions in receptor downregulation. *PLoS One* **2**, e956
30. Pornillos, O., Higginson, D. S., Stray, K. M., Fisher, R. D., Garrus, J. E., Payne, M., He, G. P., Wang, H. E., Morham, S. G., and Sundquist, W. I. (2003) HIV Gag mimics the Tsg101-recruiting activity of the human Hrs protein. *J Cell Biol* **162**, 425-434
31. Gill, D. J., Teo, H., Sun, J., Perisic, O., Veprintsev, D. B., Emr, S. D., and Williams, R. L. (2007) Structural insight into the ESCRT-I/-II link and its role in MVB trafficking. *EMBO J* **26**, 600-612
32. Babst, M., Katzmann, D. J., Snyder, W. B., Wendland, B., and Emr, S. D. (2002) Endosome-associated complex, ESCRT-II, recruits transport machinery for protein sorting at the multivesicular body. *Dev Cell* **3**, 283-289
33. Hierro, A., Sun, J., Rusnak, A. S., Kim, J., Prag, G., Emr, S. D., and Hurley, J. H. (2004) Structure of the ESCRT-II endosomal trafficking complex. *Nature* **431**, 221-225
34. Teo, H., Perisic, O., González, B., and Williams, R. L. (2004) ESCRT-II, an endosome-associated complex required for protein sorting: crystal structure and interactions with ESCRT-III and membranes. *Dev Cell* **7**, 559-569
35. Im, Y. J., and Hurley, J. H. (2008) Integrated structural model and membrane targeting mechanism of the human ESCRT-II complex. *Dev Cell* **14**, 902-913
36. Teo, H., Gill, D. J., Sun, J., Perisic, O., Veprintsev, D. B., Vallis, Y., Emr, S. D., and Williams, R. L. (2006) ESCRT-I core and ESCRT-II GLUE domain structures reveal role for GLUE in linking to ESCRT-I and membranes. *Cell* **125**, 99-111
37. Slagsvold, T., Aasland, R., Hirano, S., Bache, K. G., Raiborg, C., Trambaiolo, D., Wakatsuki, S., and Stenmark, H. (2005) Eap45 in mammalian ESCRT-II binds ubiquitin via a phosphoinositide-interacting GLUE domain. *J Biol Chem* **280**, 19600-19606
38. Alam, S. L., Sun, J., Payne, M., Welch, B. D., Blake, B. K., Davis, D. R., Meyer, H. H., Emr, S. D., and Sundquist, W. I. (2004) Ubiquitin interactions of NZF zinc fingers. *EMBO J* **23**, 1411-1421

39. Langelier, C., von Schwedler, U. K., Fisher, R. D., De Domenico, I., White, P. L., Hill, C. P., Kaplan, J., Ward, D., and Sundquist, W. I. (2006) Human ESCRT-II complex and its role in human immunodeficiency virus type 1 release. *J Virol* **80**, 9465-9480
40. Teis, D., Saksena, S., Judson, B. L., and Emr, S. D. (2010) ESCRT-II coordinates the assembly of ESCRT-III filaments for cargo sorting and multivesicular body vesicle formation. *EMBO J* **29**, 871-883
41. Babst, M., Katzmann, D. J., Estepa-Sabal, E. J., Meerloo, T., and Emr, S. D. (2002) Escrt-III: an endosome-associated heterooligomeric protein complex required for mvb sorting. *Dev Cell* **3**, 271-282
42. Teis, D., Saksena, S., and Emr, S. D. (2008) Ordered assembly of the ESCRT-III complex on endosomes is required to sequester cargo during MVB formation. *Dev Cell* **15**, 578-589
43. Nickerson, D. P., West, M., and Odorizzi, G. (2006) Did2 coordinates Vps4-mediated dissociation of ESCRT-III from endosomes. *J Cell Biol* **175**, 715-720
44. Rue, S. M., Mattei, S., Saksena, S., and Emr, S. D. (2008) Novel Ist1-Did2 complex functions at a late step in multivesicular body sorting. *Mol Biol Cell* **19**, 475-484
45. Bowers, K., Lottridge, J., Helliwell, S. B., Goldthwaite, L. M., Luzio, J. P., and Stevens, T. H. (2004) Protein-protein interactions of ESCRT complexes in the yeast *Saccharomyces cerevisiae*. *Traffic* **5**, 194-210
46. Muzioł, T., Pineda-Molina, E., Ravelli, R. B., Zamborlini, A., Usami, Y., Göttlinger, H., and Weissenhorn, W. (2006) Structural basis for budding by the ESCRT-III factor CHMP3. *Dev Cell* **10**, 821-830
47. Bajorek, M., Schubert, H. L., McCullough, J., Langelier, C., Eckert, D. M., Stubblefield, W. M., Uter, N. T., Myszka, D. G., Hill, C. P., and Sundquist, W. I. (2009) Structural basis for ESCRT-III protein autoinhibition. *Nat Struct Mol Biol* **16**, 754-762
48. Lin, Y., Kimpler, L. A., Naismith, T. V., Lauer, J. M., and Hanson, P. I. (2005) Interaction of the mammalian endosomal sorting complex required for transport (ESCRT) III protein hSnf7-1 with itself, membranes, and the AAA+ ATPase SKD1. *J Biol Chem* **280**, 12799-12809
49. Shim, S., Kimpler, L. A., and Hanson, P. I. (2007) Structure/function analysis of four core ESCRT-III proteins reveals common regulatory role for extreme C-terminal domain. *Traffic* **8**, 1068-1079
50. Zamborlini, A., Usami, Y., Radoshitzky, S. R., Popova, E., Palu, G., and Göttlinger, H. (2006) Release of autoinhibition converts ESCRT-III components into potent inhibitors of HIV-1 budding. *Proc Natl Acad Sci U S A* **103**, 19140-19145

51. Lata, S., Roessle, M., Solomons, J., Jamin, M., Gottlinger, H. G., Svergun, D. I., and Weissenhorn, W. (2008) Structural basis for autoinhibition of ESCRT-III CHMP3. *J Mol Biol* **378**, 818-827
52. Henne, W. M., Buchkovich, N. J., Zhao, Y., and Emr, S. D. (2012) The endosomal sorting complex ESCRT-II mediates the assembly and architecture of ESCRT-III helices. *Cell* **151**, 356-371
53. Saksena, S., Wahlman, J., Teis, D., Johnson, A. E., and Emr, S. D. (2009) Functional reconstitution of ESCRT-III assembly and disassembly. *Cell* **136**, 97-109
54. Obita, T., Saksena, S., Ghazi-Tabatabai, S., Gill, D. J., Perisic, O., Emr, S. D., and Williams, R. L. (2007) Structural basis for selective recognition of ESCRT-III by the AAA ATPase Vps4. *Nature* **449**, 735-739
55. Stuchell-Brereton, M. D., Skalicky, J. J., Kieffer, C., Karren, M. A., Ghaffarian, S., and Sundquist, W. I. (2007) ESCRT-III recognition by VPS4 ATPases. *Nature* **449**, 740-744
56. Kieffer, C., Skalicky, J. J., Morita, E., De Domenico, I., Ward, D. M., Kaplan, J., and Sundquist, W. I. (2008) Two distinct modes of ESCRT-III recognition are required for VPS4 functions in lysosomal protein targeting and HIV-1 budding. *Dev Cell* **15**, 62-73
57. Fyfe, I., Schuh, A. L., Edwardson, J. M., and Audhya, A. (2011) Association of the endosomal sorting complex ESCRT-II with the Vps20 subunit of ESCRT-III generates a curvature-sensitive complex capable of nucleating ESCRT-III filaments. *J Biol Chem* **286**, 34262-34270
58. Whitley, P., Reaves, B. J., Hashimoto, M., Riley, A. M., Potter, B. V., and Holman, G. D. (2003) Identification of mammalian Vps24p as an effector of phosphatidylinositol 3,5-bisphosphate-dependent endosome compartmentalization. *J Biol Chem* **278**, 38786-38795
59. Lata, S., Schoehn, G., Jain, A., Pires, R., Piehler, J., Gottlinger, H. G., and Weissenhorn, W. (2008) Helical structures of ESCRT-III are disassembled by VPS4. *Science* **321**, 1354-1357
60. Hanson, P. I., Roth, R., Lin, Y., and Heuser, J. E. (2008) Plasma membrane deformation by circular arrays of ESCRT-III protein filaments. *J Cell Biol* **180**, 389-402
61. Ghazi-Tabatabai, S., Saksena, S., Short, J. M., Pobbati, A. V., Veprintsev, D. B., Crowther, R. A., Emr, S. D., Egelman, E. H., and Williams, R. L. (2008) Structure and disassembly of filaments formed by the ESCRT-III subunit Vps24. *Structure* **16**, 1345-1356
62. Bodon, G., Chassefeyre, R., Pernet-Gallay, K., Martinelli, N., Effantin, G., Hulsik, D. L., Belly, A., Goldberg, Y., Chatellard-Causse, C., Blot, B., Schoehn, G., Weissenhorn, W., and Sadoul, R. (2011) Charged multivesicular body protein 2B (CHMP2B) of the

- endosomal sorting complex required for transport-III (ESCRT-III) polymerizes into helical structures deforming the plasma membrane. *J Biol Chem* **286**, 40276-40286
63. Babst, M., Wendland, B., Estepa, E. J., and Emr, S. D. (1998) The Vps4p AAA ATPase regulates membrane association of a Vps protein complex required for normal endosome function. *EMBO J* **17**, 2982-2993
 64. Scott, A., Chung, H. Y., Gonciarz-Swiatek, M., Hill, G. C., Whitby, F. G., Gaspar, J., Holton, J. M., Viswanathan, R., Ghaffarian, S., Hill, C. P., and Sundquist, W. I. (2005) Structural and mechanistic studies of VPS4 proteins. *EMBO J* **24**, 3658-3669
 65. Gonciarz, M. D., Whitby, F. G., Eckert, D. M., Kieffer, C., Heroux, A., Sundquist, W. I., and Hill, C. P. (2008) Biochemical and structural studies of yeast Vps4 oligomerization. *J Mol Biol* **384**, 878-895
 66. Hartmann, C., Chami, M., Zachariae, U., de Groot, B. L., Engel, A., and Grütter, M. G. (2008) Vacuolar protein sorting: two different functional states of the AAA-ATPase Vps4p. *J Mol Biol* **377**, 352-363
 67. Landsberg, M. J., Vajjhala, P. R., Rothnagel, R., Munn, A. L., and Hankamer, B. (2009) Three-dimensional structure of AAA ATPase Vps4: advancing structural insights into the mechanisms of endosomal sorting and enveloped virus budding. *Structure* **17**, 427-437
 68. Yu, Z., Gonciarz, M. D., Sundquist, W. I., Hill, C. P., and Jensen, G. J. (2008) Cryo-EM structure of dodecameric Vps4p and its 2:1 complex with Vta1p. *J Mol Biol* **377**, 364-377
 69. Inoue, M., Kamikubo, H., Kataoka, M., Kato, R., Yoshimori, T., Wakatsuki, S., and Kawasaki, M. (2008) Nucleotide-dependent conformational changes and assembly of the AAA ATPase SKD1/VPS4B. *Traffic* **9**, 2180-2189
 70. Lottridge, J. M., Flannery, A. R., Vincelli, J. L., and Stevens, T. H. (2006) Vta1p and Vps46p regulate the membrane association and ATPase activity of Vps4p at the yeast multivesicular body. *Proc Natl Acad Sci U S A* **103**, 6202-6207
 71. Shestakova, A., Curtiss, M., Davies, B. A., Katzmann, D. J., and Babst, M. (2013) The Linker Region Plays a Regulatory Role in Assembly and Activity of the Vps4 AAA ATPase. *J Biol Chem*
 72. Yeo, S. C., Xu, L., Ren, J., Boulton, V. J., Wagle, M. D., Liu, C., Ren, G., Wong, P., Zahn, R., Sasajala, P., Yang, H., Piper, R. C., and Munn, A. L. (2003) Vps20p and Vta1p interact with Vps4p and function in multivesicular body sorting and endosomal transport in *Saccharomyces cerevisiae*. *J Cell Sci* **116**, 3957-3970
 73. Azmi, I., Davies, B., Dimaano, C., Payne, J., Eckert, D., Babst, M., and Katzmann, D. J. (2006) Recycling of ESCRTs by the AAA-ATPase Vps4 is regulated by a conserved VSL region in Vta1. *J Cell Biol* **172**, 705-717

74. Yang, D., and Hurley, J. H. (2010) Structural role of the Vps4-Vta1 interface in ESCRT-III recycling. *Structure* **18**, 976-984
75. Xiao, J., Xia, H., Zhou, J., Azmi, I. F., Davies, B. A., Katzmann, D. J., and Xu, Z. (2008) Structural basis of Vta1 function in the multivesicular body sorting pathway. *Dev Cell* **14**, 37-49
76. Shiflett, S. L., Ward, D. M., Huynh, D., Vaughn, M. B., Simmons, J. C., and Kaplan, J. (2004) Characterization of Vta1p, a class E Vps protein in *Saccharomyces cerevisiae*. *J Biol Chem* **279**, 10982-10990
77. Scott, A., Gaspar, J., Stuchell-Brereton, M. D., Alam, S. L., Skalicky, J. J., and Sundquist, W. I. (2005) Structure and ESCRT-III protein interactions of the MIT domain of human VPS4A. *Proc Natl Acad Sci U S A* **102**, 13813-13818
78. Merrill, S. A., and Hanson, P. I. (2010) Activation of human VPS4A by ESCRT-III proteins reveals ability of substrates to relieve enzyme autoinhibition. *J Biol Chem* **285**, 35428-35438
79. Wollert, T., Wunder, C., Lippincott-Schwartz, J., and Hurley, J. H. (2009) Membrane scission by the ESCRT-III complex. *Nature* **458**, 172-177
80. Dimaano, C., Jones, C. B., Hanono, A., Curtiss, M., and Babst, M. (2008) Ist1 regulates Vps4 localization and assembly. *Mol Biol Cell* **19**, 465-474
81. Azmi, I. F., Davies, B. A., Xiao, J., Babst, M., Xu, Z., and Katzmann, D. J. (2008) ESCRT-III family members stimulate Vps4 ATPase activity directly or via Vta1. *Dev Cell* **14**, 50-61
82. Wollert, T., and Hurley, J. H. (2010) Molecular mechanism of multivesicular body biogenesis by ESCRT complexes. *Nature* **464**, 864-869
83. Fabrikant, G., Lata, S., Riches, J. D., Briggs, J. A., Weissenhorn, W., and Kozlov, M. M. (2009) Computational model of membrane fission catalyzed by ESCRT-III. *PLoS Comput Biol* **5**, e1000575
84. McCullough, J., Colf, L. A., and Sundquist, W. I. (2013) Membrane fission reactions of the mammalian ESCRT pathway. *Annu Rev Biochem* **82**, 663-692
85. Boura, E., Rózycki, B., Chung, H. S., Herrick, D. Z., Canagarajah, B., Cafiso, D. S., Eaton, W. A., Hummer, G., and Hurley, J. H. (2012) Solution structure of the ESCRT-I and -II supercomplex: implications for membrane budding and scission. *Structure* **20**, 874-886
86. Nickerson, D. P., Russell, M. R., and Odorizzi, G. (2007) A concentric circle model of multivesicular body cargo sorting. *EMBO Rep* **8**, 644-650

87. Jouvenet, N., Zhadina, M., Bieniasz, P. D., and Simon, S. M. (2011) Dynamics of ESCRT protein recruitment during retroviral assembly. *Nat Cell Biol* **13**, 394-401
88. Baumgärtel, V., Ivanchenko, S., Dupont, A., Sergeev, M., Wiseman, P. W., Kräusslich, H. G., Bräuchle, C., Müller, B., and Lamb, D. C. (2011) Live-cell visualization of dynamics of HIV budding site interactions with an ESCRT component. *Nat Cell Biol* **13**, 469-474
89. Elia, N., Sougrat, R., Spurlin, T. A., Hurley, J. H., and Lippincott-Schwartz, J. (2011) Dynamics of endosomal sorting complex required for transport (ESCRT) machinery during cytokinesis and its role in abscission. *Proc Natl Acad Sci U S A* **108**, 4846-4851
90. Guizetti, J., and Gerlich, D. W. (2012) ESCRT-III polymers in membrane neck constriction. *Trends Cell Biol* **22**, 133-140
91. Eggert, U. S., Mitchison, T. J., and Field, C. M. (2006) Animal cytokinesis: from parts list to mechanisms. *Annu Rev Biochem* **75**, 543-566
92. Carlton, J. G., and Martin-Serrano, J. (2007) Parallels between cytokinesis and retroviral budding: a role for the ESCRT machinery. *Science* **316**, 1908-1912
93. Morita, E., Sandrin, V., Chung, H. Y., Morham, S. G., Gygi, S. P., Rodesch, C. K., and Sundquist, W. I. (2007) Human ESCRT and ALIX proteins interact with proteins of the midbody and function in cytokinesis. *EMBO J* **26**, 4215-4227
94. Lee, H. H., Elia, N., Ghirlando, R., Lippincott-Schwartz, J., and Hurley, J. H. (2008) Midbody targeting of the ESCRT machinery by a noncanonical coiled coil in CEP55. *Science* **322**, 576-580
95. Carlton, J. G., Agromayor, M., and Martin-Serrano, J. (2008) Differential requirements for Alix and ESCRT-III in cytokinesis and HIV-1 release. *Proc Natl Acad Sci U S A* **105**, 10541-10546
96. Guizetti, J., Schermelleh, L., Mäntler, J., Maar, S., Poser, I., Leonhardt, H., Müller-Reichert, T., and Gerlich, D. W. (2011) Cortical constriction during abscission involves helices of ESCRT-III-dependent filaments. *Science* **331**, 1616-1620
97. Demirov, D. G., and Freed, E. O. (2004) Retrovirus budding. *Virus Res* **106**, 87-102
98. Garrus, J. E., von Schwedler, U. K., Pornillos, O. W., Morham, S. G., Zavitz, K. H., Wang, H. E., Wettstein, D. A., Stray, K. M., Côté, M., Rich, R. L., Myszka, D. G., and Sundquist, W. I. (2001) Tsg101 and the vacuolar protein sorting pathway are essential for HIV-1 budding. *Cell* **107**, 55-65

99. Ivanchenko, S., Godinez, W. J., Lampe, M., Kräusslich, H. G., Eils, R., Rohr, K., Bräuchle, C., Müller, B., and Lamb, D. C. (2009) Dynamics of HIV-1 assembly and release. *PLoS Pathog* **5**, e1000652
100. Odorizzi, G., Katzmann, D. J., Babst, M., Audhya, A., and Emr, S. D. (2003) Bro1 is an endosome-associated protein that functions in the MVB pathway in *Saccharomyces cerevisiae*. *J Cell Sci* **116**, 1893-1903
101. Hurley, J. H. (2010) The ESCRT complexes. *Crit Rev Biochem Mol Biol* **45**, 463-487
102. Mizushima, N., Levine, B., Cuervo, A. M., and Klionsky, D. J. (2008) Autophagy fights disease through cellular self-digestion. *Nature* **451**, 1069-1075
103. Nakatogawa, H., Suzuki, K., Kamada, Y., and Ohsumi, Y. (2009) Dynamics and diversity in autophagy mechanisms: lessons from yeast. *Nat Rev Mol Cell Biol* **10**, 458-467
104. Hurley, J. H., and Hanson, P. I. (2010) Membrane budding and scission by the ESCRT machinery: it's all in the neck. *Nat Rev Mol Cell Biol* **11**, 556-566
105. Rusten, T. E., Vaccari, T., Lindmo, K., Rodahl, L. M., Nezis, I. P., Sem-Jacobsen, C., Wendler, F., Vincent, J. P., Brech, A., Bilder, D., and Stenmark, H. (2007) ESCRTs and Fab1 regulate distinct steps of autophagy. *Curr Biol* **17**, 1817-1825
106. Filimonenko, M., Stuffers, S., Raiborg, C., Yamamoto, A., Malerød, L., Fisher, E. M., Isaacs, A., Brech, A., Stenmark, H., and Simonsen, A. (2007) Functional multivesicular bodies are required for autophagic clearance of protein aggregates associated with neurodegenerative disease. *J Cell Biol* **179**, 485-500
107. Lee, J. A., Beigneux, A., Ahmad, S. T., Young, S. G., and Gao, F. B. (2007) ESCRT-III dysfunction causes autophagosome accumulation and neurodegeneration. *Curr Biol* **17**, 1561-1567
108. Blume-Jensen, P., and Hunter, T. (2001) Oncogenic kinase signalling. *Nature* **411**, 355-365
109. Thompson, B. J., Mathieu, J., Sung, H. H., Loeser, E., Rørth, P., and Cohen, S. M. (2005) Tumor suppressor properties of the ESCRT-II complex component Vps25 in *Drosophila*. *Dev Cell* **9**, 711-720
110. Vaccari, T., and Bilder, D. (2005) The *Drosophila* tumor suppressor vps25 prevents nonautonomous overproliferation by regulating notch trafficking. *Dev Cell* **9**, 687-698
111. Moberg, K. H., Schelble, S., Burdick, S. K., and Hariharan, I. K. (2005) Mutations in *erupted*, the *Drosophila* ortholog of mammalian tumor susceptibility gene 101, elicit non-cell-autonomous overgrowth. *Dev Cell* **9**, 699-710

112. Kameyama, T., Suzuki, H., and Mayeda, A. (2012) Re-splicing of mature mRNA in cancer cells promotes activation of distant weak alternative splice sites. *Nucleic Acids Res* **40**, 7896-7906
113. Stuffers, S., Brech, A., and Stenmark, H. (2009) ESCRT proteins in physiology and disease. *Exp Cell Res* **315**, 1619-1626
114. Parkinson, N., Ince, P. G., Smith, M. O., Highley, R., Skibinski, G., Andersen, P. M., Morrison, K. E., Pall, H. S., Hardiman, O., Collinge, J., Shaw, P. J., Fisher, E. M., Study, M. P. i. A., and Consortium, F. (2006) ALS phenotypes with mutations in CHMP2B (charged multivesicular body protein 2B). *Neurology* **67**, 1074-1077
115. Skibinski, G., Parkinson, N. J., Brown, J. M., Chakrabarti, L., Lloyd, S. L., Hummerich, H., Nielsen, J. E., Hodges, J. R., Spillantini, M. G., Thusgaard, T., Brandner, S., Brun, A., Rossor, M. N., Gade, A., Johannsen, P., Sørensen, S. A., Gydesen, S., Fisher, E. M., and Collinge, J. (2005) Mutations in the endosomal ESCRTIII-complex subunit CHMP2B in frontotemporal dementia. *Nat Genet* **37**, 806-808
116. Saksena, S., Sun, J., Chu, T., and Emr, S. D. (2007) ESCRTing proteins in the endocytic pathway. *Trends Biochem Sci* **32**, 561-573
117. Martin-Serrano, J., and Neil, S. J. (2011) Host factors involved in retroviral budding and release. *Nat Rev Microbiol* **9**, 519-531

Chapter 2

Association of ESCRT-II with Vps20 Generates a Curvature Sensitive Protein Complex Capable
of Nucleating Filaments of ESCRT-III

The work presented in this chapter has been published:

Fyfe I*, Schuh AL*, Edwardson M, Audhya A.
(2011) *J Biol Chem.* 39:34262-34270.

*Denotes Equal Contribution

ABSTRACT

The scission of membranes necessary for vesicle biogenesis and cytokinesis is mediated by cytoplasmic proteins, which include members of the ESCRT (endosomal sorting complex required for transport) machinery. During the formation of intraluminal vesicles that bud into multivesicular endosomes, the ESCRT-II complex initiates polymerization of ESCRT-III subunits essential for membrane fission. However, mechanisms underlying the spatial and temporal regulation of this process remain unclear. Here, we show that purified ESCRT-II binds to the ESCRT-III subunit Vps20 on chemically-defined membranes in a curvature dependent manner. Using a combination of liposome co-flotation assays, fluorescence-based liposome interaction studies and high-resolution atomic force microscopy, we find that the interaction between ESCRT-II and Vps20 increases their affinity for lipid bilayers of elevated curvature. We additionally demonstrate that ESCRT-II and Vps20 nucleate flexible filaments of Vps32 that polymerize specifically along highly curved membranes as a single string of monomers. Strikingly, Vps32 filaments are shown to modulate membrane dynamics *in vitro*, a prerequisite for membrane scission events in cells. We propose that a curvature-dependent assembly pathway provides the spatial regulation of ESCRT-III to fuse juxtaposed bilayers of elevated curvature.

INTRODUCTION

Formation of multivesicular endosomes (MVEs), which is mediated by a set of protein complexes collectively known as the ESCRT machinery, is critical for the downregulation of activated cell surface receptors and thereby exhibits properties of a tumor suppressor pathway (1,2). Although endocytosis from the plasma membrane restricts receptors from further access to ligands, most activated receptors continue signaling from internal membrane compartments (3). However, sequestration of receptors within endosomes terminates their signaling potential by prohibiting access to cytoplasmic effector molecules. Unlike endocytosis, ESCRT-mediated vesicle biogenesis involves a budding event away from the cytoplasm. In a topologically similar fashion, components of the ESCRT machinery also function in the budding of several enveloped viruses from the plasma membrane, and in cytokinesis (4,5).

Early acting ESCRT complexes (ESCRT-0, -I, and -II) function in cargo recognition (6). Each complex contains one or more ubiquitin-interacting domains that can recruit and concentrate ubiquitinated cargoes of the MVE pathway. Additionally, each complex exhibits membrane-binding activity. ESCRT-0 associates avidly with the endosomally enriched lipid phosphatidylinositol 3-phosphate (PI3P), and under steady state conditions, the majority of ESCRT-0 localizes to endosomes (7). In contrast, ESCRT-I and ESCRT-II are predominantly cytoplasmic in most cell types, and are transiently recruited onto the membrane during MVE biogenesis (8,9). Recent studies have implicated both complexes in membrane deformation and the generation of nascent buds on giant unilamellar vesicles (GUVs). Addition of the ESCRT-III subunits Vps20 and Vps32 was sufficient to release nascent vesicles into the GUV lumen, indicating a specific role for ESCRT-III in membrane cleavage (10,11). Surprisingly, in the

absence of other ESCRT machinery, Vps32 together with an activated form of Vps20 (lacking its regulatory carboxyl-terminus) were also sufficient to generate luminal vesicles in the GUV-based assay (11). Although high concentrations of Vps32 were necessary, these studies suggest that ESCRT-III may also function in vesicle formation. Consistent with this idea, overexpression of human Vps32 in mammalian cells results in the formation of tubules that extend away from the cytoplasm, and the yeast ESCRT-III subunits mediate the formation of inward invaginations on small unilamellar vesicles (12,13).

The ESCRT-III subunits exist in an auto-inhibited state in solution (14). ESCRT-III assembly requires Vps20 activation, which is mediated by ESCRT-II in the case of MVE biogenesis (15). Fluorescence spectroscopy measurements suggest that Vps20 undergoes a conformational change when bound to ESCRT-II on liposomes, which may foster an interaction between Vps20 and Vps32 that takes place only on membranes (13). Additionally, when mixed together, ESCRT-II and Vps20 associate with liposomes more tightly than either alone (16). Although this phenomenon has not been mechanistically explained, a molecular model predicts that ESCRT-II bound to Vps20 would exhibit a convex membrane-binding surface (17), which may explain their increased binding to the curved surfaces of liposomes. Here, we demonstrate that association of ESCRT-II with Vps20 generates a curvature sensitive complex that is capable of nucleating 2 filaments of Vps32. Our data further indicate that Vps32 filaments assemble specifically on membranes of high curvature and enable membrane remodeling necessary for scission. By sensing membrane curvature, ESCRT-III function is both spatially and temporally restricted to fission events during vesicle biogenesis and cytokinesis.

RESULTS

A complex of ESCRT-II bound to Vps20 binds preferentially to membranes of high curvature.

To study the role of membrane curvature in the regulation of ESCRT assembly, we first examined the binding properties of ESCRT-II and Vps20 to synthetic liposomes of two different diameters (**Figure 2.S1A**). We used recombinant *C. elegans* proteins, due to their robust expression in *E. coli* and high degree of purity following affinity and size exclusion chromatography (**Figures 2.1A and 2.1B**). The hydrodynamic properties of *C. elegans* ESCRT-II and Vps20 were nearly identical to that of human ESCRT-II and CHMP6 respectively, consistent with their high level of amino acid sequence similarity (**Figures 2.1A, 2.1B, 2.S1B, and 2.S1C**; (18)). Using an assay in which proteins are mixed with liposomes and then floated through a gradient (**Figure 2.S1D**), we found that ESCRT-II and Vps20 individually exhibited a preference for 183 nm vesicles as compared to 95 nm vesicles (**Figures 2.1C and 2.1D**). In contrast, a mixture of ESCRT-II and Vps20 bound significantly more tightly to the smaller, more highly curved vesicles (by approximately 2-fold), suggesting that the assembled ESCRT-II/Vps20 “supercomplex” senses elevated membrane curvature (**Figure 2.1E**).

To confirm a curvature-sensitive association between membranes and ESCRT-II/Vps20, we used a fluorescence-based assay. We labeled the only endogenous cysteine residue in Vps20 with BODIPY-FL and measured its binding to liposomes of various sizes that contained rhodamine-labeled phosphatidyl-ethanolamine (Rhodamine-PE) in the presence of unlabeled ESCRT-II (**Figures 2.2A, 2.2B, and 2.S2A**). The BODIPY-FL modification did not affect the interaction between Vps20 and ESCRT-II (**Figure 2.2C**). Ratiometric confocal imaging showed

a reciprocal relationship between the intensities of the fluorophores (**Figure 2.2D**), indicating that ESCRT-II/Vps20 binds more avidly to smaller liposomes of higher curvature. The best-fit curve through the data was essentially described by a power series in the form of $y \propto x^{-1}$, demonstrating that membrane binding of ESCRT-II/Vps20 varied as the multiplicative inverse of the liposome surface area (**Figure 2.S2B**; see Experimental Procedures for additional details). Thus, ESCRT-II/Vps20 membrane binding is proportional to the square of the membrane curvature. Based on these findings, we conclude that ESCRT-II bound to Vps20 senses the curvature of lipid bilayers. In contrast, we were unable to detect the association of BODIPY-FL labeled Vps20 with liposomes in the absence of ESCRT-II (**Figure 2.S2C**), consistent with a necessity to perform immunoblot analysis to detect Vps20 in co-floitation assays (see **Figure 2.1D**).

Vps20 regulates ESCRT-II distribution on supported lipid bilayers.

Methodology to visualize ESCRT complex assembly *in vitro* is currently limited. Although the development of a fluorescence microscopy-based assay using GUVs has been instrumental in defining distinct roles for each ESCRT complex, the relatively low resolution of the light microscope prohibits the acquisition of nanometer scale structural information regarding ESCRT complex assembly on the membrane surface (10,11). Moreover, we have found GUVs to be highly dynamic, capable of undergoing spontaneous membrane deformations, including luminal vesicle formation, in a protein-independent manner. Although the addition of ESCRT proteins increases the frequency at which luminal vesicles form within GUVs, these caveats have prevented us from reproducibly interpreting data acquired using this assay. To study the assembly of ESCRT components on membranes, we took advantage of an alternative approach

that uses atomic force microscopy (AFM). With this method, components of the ESCRT machinery can be visualized at nanometer resolution on supported lipid bilayers (SLBs) that exhibit a thickness of approximately 4 nm, using label-free, recombinant proteins. During assembly of SLBs, we observed that several gaps formed throughout the surface, where the underlying mica could be visualized (**Figure 2.S2D**). Based on molecular dynamics simulations, the edges of SLBs are predicted to be highly curved surfaces (**Figure 2.S2E**; (19)) with a radius (~2 nm) comparable to that of a constricted vesicle bud neck (~10-15 nm; (20-24)). Although direct experimental data to describe the bilayer edge is lacking, the energy cost to maintain exposed hydrocarbon tails in an aqueous solution greatly exceeds the energy necessary for migration of polar headgroups around a bilayer edge (25-29). Thus, the use SLBs afforded us the unique opportunity to study the association of ESCRT components with both flat and highly curved membrane surfaces simultaneously.

To validate the system, we examined the well-characterized, curvature sensitive F-BAR domain derived from FCHo (30) on SLBs. Although particles corresponding to the F-BAR domain varied in size, the majority (89.9% of particles within the volume range of a F-BAR homodimer) associated with edges of SLBs, consistent with its elevated affinity for curved membranes (**Figures 2.2E and 2.2F**). In contrast, the curvature insensitive ESCRT-0 complex, composed of Hrs and STAM, exhibited a uniform distribution throughout the bilayer (**Figure 2.2G**; (31)). Together, these data illustrate the utility of our SLB system in characterizing the membrane-binding properties of proteins.

ESCRT-II bound to membranes as individual particles that were distributed evenly across the bilayer (**Figure 2.3A**). Analysis of the particles produced a volume distribution with a peak

in the region of 100-200 nm³, similar to that expected of a single ESCRT-II complex (140.3 nm³) based on amino acid composition (**Figures 2.3B and 2.3C**). We conclude that ESCRT-II on membranes behaves as an individual heterotetrameric complex that lacks curvature sensitivity.

When ESCRT-II and Vps20 were co-incubated with liposomes at a 1:1 molar ratio and analyzed by AFM, the total number of particles observed on the membrane was decreased by approximately 4-fold compared to ESCRT-II alone (**Figure 2.S2F**). Specifically, we observed a decrease in particle association with flat regions of the SLB. These data suggested that a complex of ESCRT-II bound to Vps20 binds less efficiently to flat lipid bilayers. Additionally, the particles were no longer distributed evenly across the membrane. Instead, ~30% were concentrated at the periphery of the gaps that had formed during bilayer assembly (**Figure 2.3D**). Since Vps20 can associate with both copies of Vps25 present in ESCRT-II (15), we increased the molar ratio of ESCRT-II:Vps20 to 1:2. Under these conditions, we observed a further shift in particle distribution, with ~50% at the edges of gaps (**Figure 2.3D**). Although binding of Vps20 to ESCRT-II does not sufficiently alter the volume of particles observed by AFM, we suspected that the remaining particles that bound throughout the bilayer were ESCRT-II complexes that were not bound to Vps20. We therefore added a 3-fold molar excess of Vps20 to increase the likelihood of ESCRT-II/Vps20 supercomplex formation. Under these conditions, we found that a clear majority (~65%) of particles targeted to the highly curved edges of SLBs (**Figures 2.3D and 2.3E**). Similar results were obtained using SLBs that lacked phosphatidylinositol 3-phosphate (PI3P), indicating that recruitment of ESCRT-II/Vps20 to bilayer edges was independent of phosphoinositides (**Figure 2.S2G**). We conclude that the association of ESCRT-II with Vps20 dramatically increases the affinity of the proteins for highly curved surfaces,

providing a mechanism for spatially restricting Vps20-mediated ESCRT-III assembly to the neck of nascent, inward-budding vesicles.

The ESCRT-II/Vps20 complex directs ESCRT-III filament assembly specifically on highly curved membranes.

To directly examine ESCRT-III polymer formation, we first purified recombinant Vps32, an ESCRT-III subunit known to function downstream of Vps20. Based on gel filtration and glycerol gradient studies, Vps32 exists in a monomeric conformation in solution, exhibiting nearly identical hydrodynamic properties to carbonic anhydrase, a well-characterized globular monomer (**Figures 2.S3A and 2.S3B**). In contrast to Vps20, which failed to detectably associate with SLBs, Vps32 bound to membranes as individual particles that were scattered throughout the bilayer (**Figures 2.S3C and 2.S3D**). However, when Vps32 was co-incubated with ESCRT-II and Vps20, we observed the formation of flexible filaments that lined the edges of the bilayer gaps (**Figure 2.4A**). The size and shape of the gap made no significant impact on filament assembly; nor did the addition of Vps24 and Vps2. To further define how the Vps32 filaments associate with the bilayer, we modulated the amount of force applied by the AFM tip (**Figure 2.S3E**). With force that is sufficient to compress or penetrate the bilayer, we were able to clearly visualize the filaments bordering the gap. However, when the force exerted by the AFM tip was lowered, filaments were no longer visible, suggesting that the filament height was equal to or below the surface of the bilayer (**Figures 2.4B and 2.4C**). Based on these findings, we conclude that Vps32 filaments bind specifically to the edges of highly curved membranes. In agreement with this idea, we failed to observe cases in which ESCRT-III filaments extended onto the flat

surface of the SLB, suggesting that similar to ESCRT-II/Vps20, Vps32 filaments are also curvature sensitive during polymerization.

The Vps32 filaments emerged from one or both sides of a central particle of ESCRT-II/Vps20 (**Figures 2.S3F and 2.S3G**). Using the height and width of each filament, we calculated the volume of a spherical, monomeric subunit to range from 20-40 nm³, similar to the volume of a single Vps32 molecule (29.9 nm³) based on its amino acid composition (**Figure 2.S3H**). Furthermore, based on the hydrodynamic properties of Vps32 (**Figures 2.S3A and 2.S3B**) and volume calculations using AFM, we determined that each 100 nm filament (in length) contains approximately 8 subunits of Vps32 arranged in an end-to-end configuration and is on average 13.4 (+/- 2.5) nm wide, similar to the diameter of endogenous ESCRT-III filaments that assemble during abscission (32).

ESCRT-III promotes membrane remodeling.

Imaging of SLBs in the absence of protein by AFM revealed that some gaps fill with membrane over time, indicating that the bilayer is mobile on the mica surface (**Figure 2.5A**). We took advantage of this phenomenon to study the effect of Vps32 filament assembly on membrane dynamics and found that membrane closure occurred more rapidly and uniformly in the presence of ESCRT proteins (**Figures 2.5A-2.5C and 2.S4**). In the majority of cases, we found that Vps32 filaments remained associated with the bilayer surface after membrane closure (**Figures 2.5B and 2.5C**). These data indicate that the filaments permit the passive movement of membrane but cannot disassemble spontaneously, consistent with previous work demonstrating that ESCRT-III removal from membranes requires an energy-dependent step that involves the

Vps4 ATPase (33). Together, these data demonstrate that individual ESCRT-III filaments are sufficient to drive the remodeling of lipid bilayers.

DISCUSSION

Viral budding, cytokinesis, and luminal vesicle formation within endosomes all share a common requirement for ESCRT-mediated membrane fission, which necessitates a significant input of free energy. This barrier is overcome by electrostatic interactions between components of the ESCRT machinery and the membrane (34). ESCRT-III subunits are ideally suited to mediate membrane fission, as each component harbors an electrically polarized core that contains amino-terminal basic residues that bind strongly to acidic phospholipids. In contrast, upstream ESCRT complexes are unlikely to participate in the scission process, but instead function as adaptors to target ESCRT-III to various cellular locations. In the case of HIV-1 infection, virally encoded Gag binds two upstream ESCRT factors, Tsg101 and Alix, to drive ESCRT-III polymerization on the plasma membrane (35). Although HIV-1 bud formation is ESCRT-independent, bud release strictly requires ESCRT function. Similarly during cytokinesis, the midbody-associated protein Cep55 recruits Tsg101 and Alix to allow the assembly of ESCRT-III on the intracellular bridge (5,36).

The ESCRT complexes possess distinct activities during MVE biogenesis.

ESCRT-III activity enables membrane scission and daughter cell separation, but initial steps of cleavage furrow formation do not require the ESCRT machinery. At the endosome, ESCRT-0, -I, and -II cooperate to properly localize ESCRT-III to act at the final scission step of luminal vesicle formation (1,6). However, the formation of nascent buds does not appear to require ESCRT-III (10). Together, these findings strongly support a model in which ESCRT-III functions after the membrane bending steps that occur prior to fission. Consistent with this idea, we found that ESCRT-III polymerizes specifically on highly curved membranes. By sensing

curvature, ESCRT-III function is spatially restricted to unique areas of a lipid bilayer, and may thereby prevent nonspecific ESCRT-mediated membrane remodeling. Importantly, we also demonstrate that ESCRT-II/Vps20 membrane binding is proportional to the square of the curvature, which is directly related to the bending energy of a membrane. Thus, as membrane bending increases, so does the membrane binding of ESCRT-II/Vps20, which may ultimately trigger a conformational switch enabling Vps32 filament assembly. Based on our data, we speculate that Vps20 associates with ESCRT-II to generate a mechanosensitive complex, which specifically nucleates ESCRT-III polymerization subsequent to membrane bending events (**Figure 2.5D**).

Requirements for ESCRT-mediated membrane scission.

Several models that share common features currently exist to explain ESCRT-mediated membrane scission. The “purse-string” model suggests that the AAA-ATPase Vps4 mediates disassembly of ESCRT-III circular arrays to draw opposing membranes together and allow fission (13). Although Vps4 is required for ESCRT-III disassembly and recycling, recent evidence indicates that the ATPase is dispensable for vesicle budding (10,11,37). Consistent with this idea, we find that ESCRT-III disassembly is not required to alter membrane dynamics, which would be necessary during fission. Alternative models suggest that ESCRT-III spirals or dome-like structures are sufficient to draw opposing membranes together (11,12,34,37). Although our data do not preclude the possibility that such polymers are actually generated *in vivo*, we found no evidence for their formation using purified, recombinant proteins. A limitation of our study is the use of SLBs assembled on a mica surface, which may not be conducive to the formation of Vps32 flat spirals. Nevertheless, our data indicate that the binding of single

ESCRT-III filaments to membranes can generate sufficient energy to modulate membrane dynamics. In the future, it will be essential to establish tractable assays *in vivo*, which permit high-resolution analysis of normal ESCRT assembly on endosomes, to validate our findings and those obtained from other artificial systems that are currently in use.

Based on our data examining ESCRT-III assembly on a lipid bilayer that closely resembles a constricting bud neck, we offer a new model for ESCRT-mediated fission (**Figure 2.5D**). We propose that ESCRT-III filaments assemble specifically on highly curved membrane surfaces, contributing sufficient binding energy to promote membrane fission. Such a model is consistent with the wide range of ESCRT-mediated fission events, including the release of nascent vesicles (~40-50 nm in diameter) and sealing of the relatively large intracellular bridge during cytokinesis (~200 nm in diameter).

MATERIALS and METHODS

Protein purification and hydrodynamic studies

Recombinant protein expression was performed using BL21 (DE3) *E. coli*. For ESCRT-II, all subunits were cloned into the polycistronic expression vector pST39 (38), and a single tag was appended onto Vps25 to enable purification (described briefly below). Purifications were conducted using glutathione agarose beads (for GST-Vps20) or nickel affinity resin (for intact ESCRT-II and monomeric Vps32). The GST moiety was removed from Vps20 using Prescission protease. For size exclusion chromatography, samples (2 mL) were applied to a Superose 6 gel filtration column (GE Healthcare), and 1 mL fractions were collected. The Stokes radius of each protein or protein complex was calculated from its elution volume based on the elution profiles of characterized globular standards (39). 4 mL glycerol gradients (10-30%) were poured using a Gradient Master and fractionated (200 mL) from the top by hand. Sedimentation values were calculated by comparing the position of the peak with that of characterized standards run on a separate gradient in parallel (31). To fluorescently label Vps20, a 20-fold molar excess of BODIPY-FL-maleimide was incubated with Vps20 overnight with rotation. The reaction was quenched using an excess of glutathione. Unbound dye was removed by gel filtration chromatography. Based on the amount of protein recovered and its absorbance, stoichiometry (BODIPY-FL:Vps20) was determined to be ~1:1.

Production of liposomes and co-flotation assays

Liposomes (36.5% phosphatidylcholine (PC), 30% phosphatidylethanolamine (PE), 30% phosphatidylserine (PS), 3% phosphatidylinositol 3-phosphate (PI3P), and 0.5% Rhodamine-labeled PE) were prepared by extrusion through polycarbonate filters with pore sizes of 30 and

200 nm (Avanti Polar Lipids). Dynamic light scattering measurements were conducted to determine the actual size of liposomes generated. For co-flotation assays, liposomes were incubated with protein in buffer (50 mM Hepes, pH 7.6 and 100 mM NaCl) prior to mixing with Accudenz density medium. Mixtures were overlaid with decreasing concentrations of Accudenz (0-40%) and centrifuged for 2 hours at 280,000 x g. During this period, liposomes and associated proteins floated to the buffer/Accudenz interface and were harvested by hand. Recovery of liposomes was normalized based on the fluorescence intensity of the sample, and equivalent fractions (when comparing flotation experiments that use liposomes of differing sizes) were separated by SDS-PAGE and stained with Coomassie to determine the relative amount of protein that bound (40). Similar results were obtained with liposomes composed of 51.5% PC, 30% PE, 15% PS, 3% PI3P and 0.5% Rhodamine-PE.

Fluorescence confocal microscopy and analysis

Fluorescent images of BODIPY-FL-Vps20 and Rhodamine-labeled liposomes were acquired on a swept field confocal microscope (Nikon Ti-E) equipped with a Roper CoolSnap HQ2 CCD camera using a Nikon 60X, 1.4NA Planapo oil objective lens. Acquisition parameters were controlled by Nikon Elements software. To image immobilized liposomes, coverslips were first cleaned and coated with a solution of polyethylene glycol (PEG) and biotin-PEG (40:1 ratio). The PEG-coated glass was then incubated with 1 mM avidin for 10 minutes and washed several times with buffer (50 mM Hepes, pH 7.6 and 100 mM NaCl). 100 μ L of liposomes (15 mM; 35.9% PC, 30% PE, 30% PS, 3% PI3P, 1% Biotinyl-PE, and 0.1% Rhodamine-PE) were mixed with ESCRT-II (250 nM) and BODIPY-FL-Vps20 (250 nM) and incubated on avidin-coated coverslips for 30 min. Unbound liposomes and protein were aspirated and replaced with 3 μ L of

50 mM Hepes, pH 7.6 and 100 mM NaCl, prior to inversion onto a depression slide for imaging. Image analysis was conducted using Metamorph software. Based on the plausible assumptions that the fluorescence intensity of each liposome is proportional to its surface area and the ratio of BODIPY-FL:Rhodamine fluorescence is proportional to the concentration of labeled Vps20 bound to each liposome, we were able to determine the relationship between Vps20 membrane binding and membrane curvature in the presence of ESCRT-II. Specifically, we plotted the fluorescence intensity of each liposome (following background subtraction) on the x-axis and the relative concentration of Vps20 that bound to each liposome on the y-axis and determined the best fit curve to be a power series described by:

$$y = kx^{-0.993}$$

Since the surface area of a liposome is proportional to the square of its radius,

$$[\text{Vps20}]_{\text{bound}} \propto 1/\text{Radius}^2$$

Furthermore, since the curvature of a membrane is defined as the inverse of its radius,

$$[\text{Vps20}]_{\text{bound}} \propto \text{Curvature}^2$$

Atomic force microscopy

AFM imaging was performed using a Veeco Digital Instruments Multimode instrument, controlled by a Nanoscope IIIa controller. All imaging was conducted under fluid using NSC-18 cantilevers with a Cr-Au coating (Mikromasch). Their resonant frequencies were 30-35 kHz, and the actual scanning frequencies were ~5% below the maximal resonance peak. The root-mean-square voltage was maintained at 2 V. Lipid mixtures containing PC (54%), PE (30%), PS (15%) and PI3P (1%) were dried under nitrogen and hydrated in water overnight. Suspensions were probe-sonicated at an amplitude of 10 mA until the mixture became transparent.

Liposomes were incubated in the presence or absence of proteins for 30 min and then placed on freshly cleaved mica. In each case, 40 mL of the liposome mixture and an equal volume of Hepes-buffered saline (HBS; 50 mM Hepes pH 7.6, 150 mM NaCl, 1 mM Ca²⁺) was applied to the mica surface. The mica was washed twice with HBS and placed in the fluid cell of the AFM. The assembled lipid bilayer was immersed in 150 mL of HBS, and all imaging was performed at room temperature. AFM images were plane-fitted to remove tilt, and each scan line was fitted to a first-order equation. Particles were identified and their dimensions were measured manually using the section tool. The height and radius of each particle were used to calculate its molecular volume using the following equation: $V_m = (\pi h/6)(3r^2 + h^2)$, where h is the particle height and r is the radius (31,41). Each particle was measured twice in both dimensions and an average was taken for the calculation. Widths and heights of filaments were determined by taking cross sections at three points along the filaments and taking the average.

ACKNOWLEDGEMENTS

We thank E. Chapman, M. Jackson, C. Johnson, and E. Hui for advice and helpful discussions, R. Murphy for use of dynamic light scattering instrumentation, N. George for technical assistance, and members of the Audhya lab for critically reading this manuscript. The work was supported by the NIH (grant 1R01GM088151-01A1 to A.A.). I.F. is supported by a Biotechnology and Biological Sciences Research Council Doctoral Training Award.

EXPERIMENTAL CONTRIBUTIONS

A.S. purified proteins, conducted protein-liposome binding assays, and protein hydrodynamic studies. I.F. performed AFM experiments.

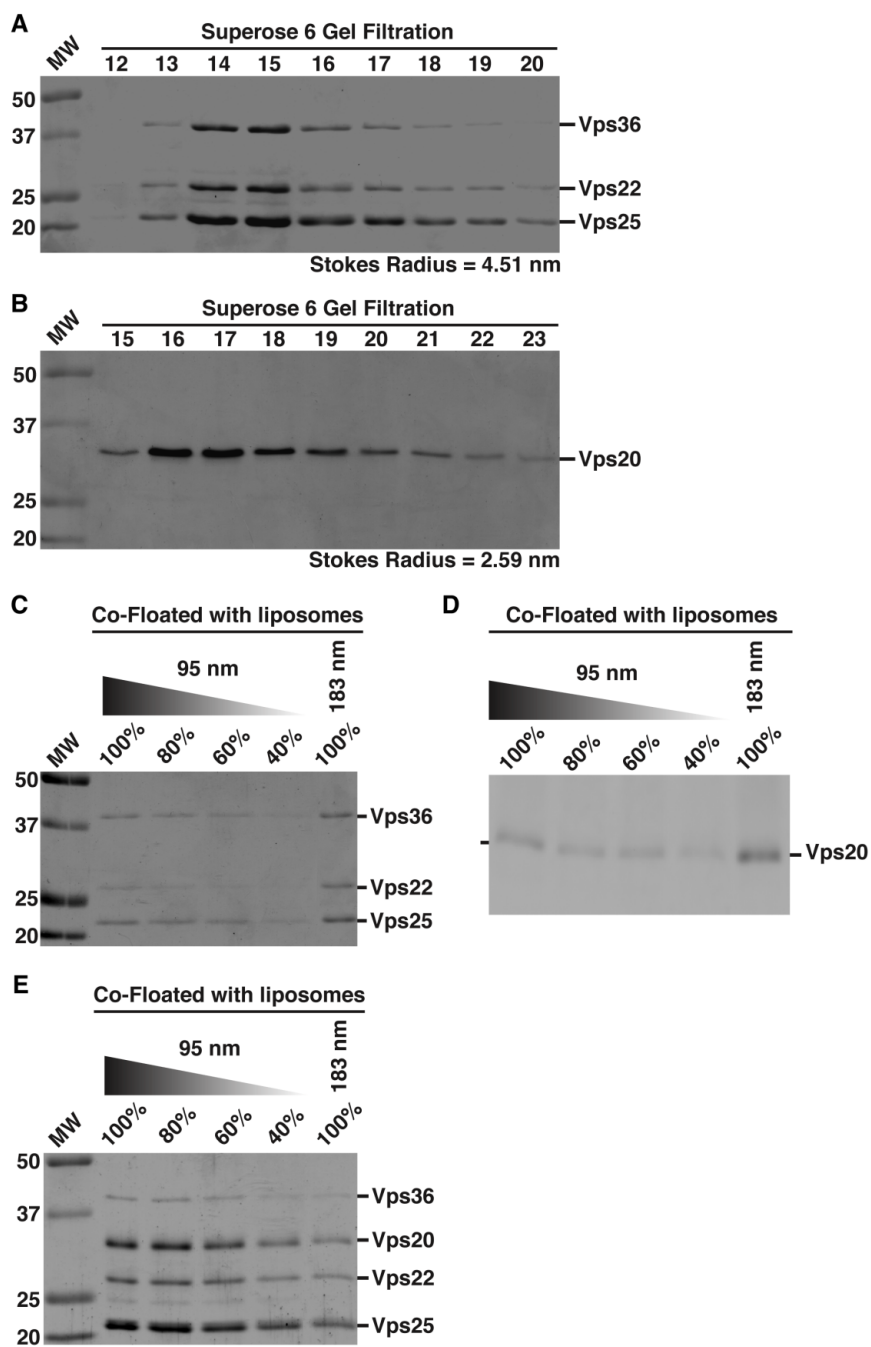


Figure 2.1. ESCRT-II bound to Vps20 binds preferentially to liposomes of higher curvature.

Figure 2.1. ESCRT-II bound to Vps20 binds preferentially to liposomes of higher curvature.

(Figure 2.1A) ESCRT-II initially purified using nickel affinity chromatography was subjected to size exclusion chromatography, and the peak fractions eluted were separated by SDS-PAGE and stained using Coomassie. A Stokes radius was calculated based on the elution profile of characterized standards. Data shown are representative of at least 3 independent experiments.

(Figure 2.1B) Vps20 was purified initially as a GST-fusion protein on glutathione agarose. The GST moiety was removed using Prescission protease and untagged Vps20 was analyzed as in A. Data shown are representative of at least 3 independent experiments. **(Figures 2.1C-2.1E)** A co-floitation assay was used to analyze the binding of ESCRT-II, Vps20 or a mixture of ESCRT-II and Vps20 to liposomes of different diameters (95 nm and 183 nm). Fractions were resolved by SDS-PAGE and stained using Coomassie **(Figures 2.1C and 2.1E)** or immunoblotted using Vps20 antibodies **(Figure 2.1D)**. A dilution series of each protein or protein mixture that co-floated with 95 nm liposomes was loaded to quantify the relative amount that co-floated with 183 nm vesicles. Data shown are representative of at least 3 independent experiments.. Based on densitometry measurements, 101.7% (+/- 17.7%) of the ESCRT-II complex co-floated with 183 nm vesicles relative to 95 nm vesicles. For Vps20, 107.7% (+/- 13.5%) of the protein co-floated with 183 nm vesicles relative to 95 nm vesicles. For a mixture of ESCRT-II and Vps20, 45.0% (+/- 13.1%) of the complex co-floated with 183 nm vesicles as compared to 95 nm vesicles.

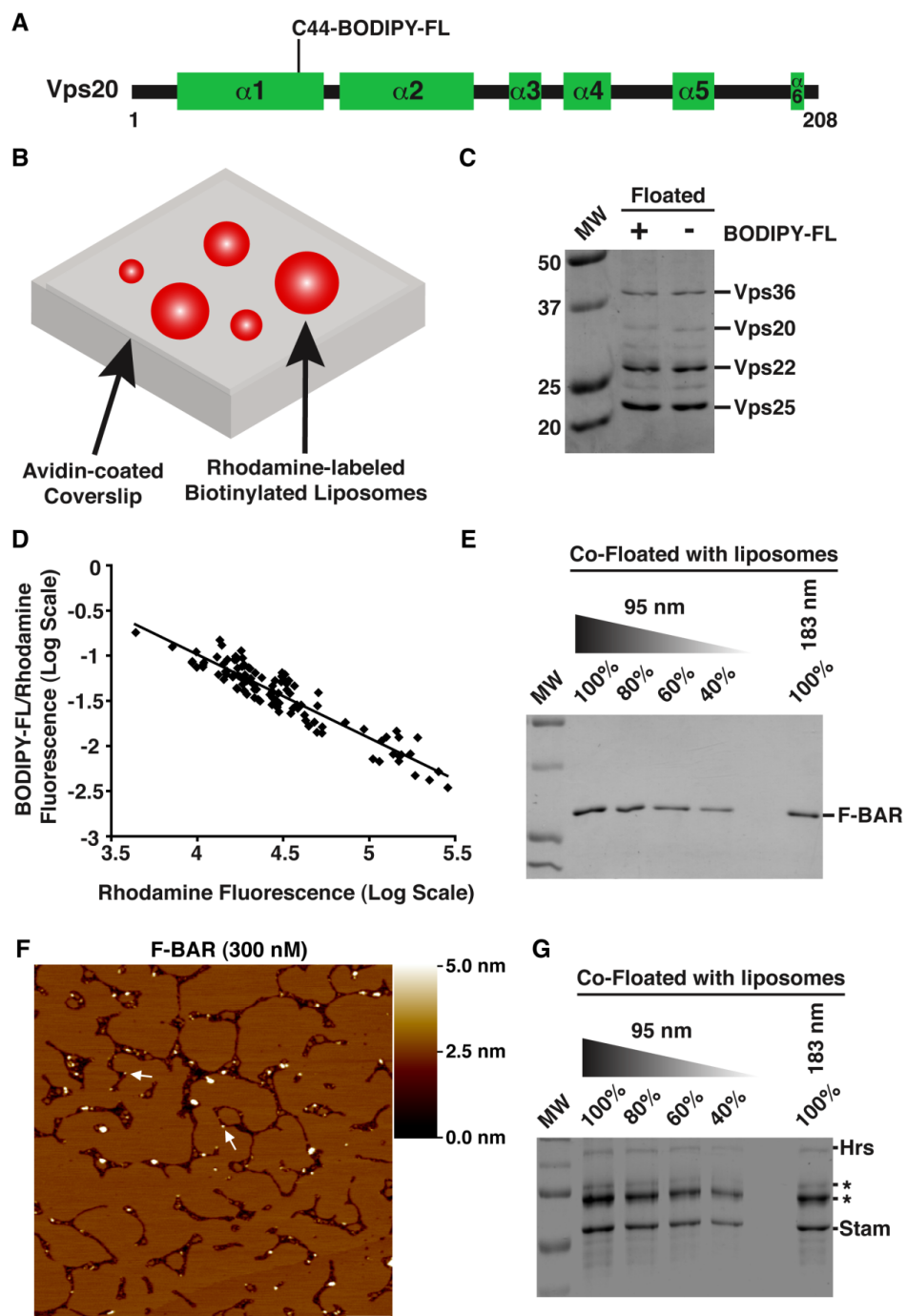


Figure 2.2. A complex of ESCRT-II bound to Vps20 senses membrane curvature.

Figure 2.2. A complex of ESCRT-II bound to Vps20 senses membrane curvature.

(**Figure 2.2A**) Cartoon illustrating the secondary structure organization of Vps20, highlighting the position of the BODIPY-FL modification. Alpha-helical domains are predicted based on sequence alignment with CHMP6. (**Figure 2.2B**) A schematic representation of a fluorescence-based liposome binding assay. (**Figure 2.2C**) A co-floitation assay was used to analyze the association of ESCRT-II with either unlabeled Vps20 or Vps20 conjugated to BODIPY-FL. Labeled Vps20 exhibits a slightly reduced mobility during SDS-PAGE as compared to unlabeled Vps20. (**Figure 2.2D**) The log of the BODIPY-FL:Rhodamine fluorescence ratio for individual liposomes was plotted against the log of liposome fluorescence intensity. More than 200 immobilized liposomes were analyzed in 3 independent experiments. (**Figure 2.2E**) The FCHo F-BAR domain was analyzed using the co-floitation assay described in **Figure 2.1**. Data shown are representative of at least 3 independent experiments. Based on densitometry measurements, 80.0% (+/- 3.5%) of the FCHo F-BAR domain co-floated with 183 nm vesicles relative to 95 nm vesicles. (**Figure 2.2F**) Representative AFM images of bilayers assembled in the presence of the FCHo F-BAR domain (300 nM). Arrows highlight the presence of F-BAR particles at the bilayer edges. Based on hydrodynamic studies, the F-BAR domain forms a homodimer in solution. A shade-height scale bar is shown on the right of each image. White scale bar, 500 nm. (**Figure 2.2G**) The ESCRT-0 complex was analyzed using the co-floitation assay. Since Hrs stability during flotation was compromised (asterisks highlight breakdown products of Hrs based on immunoblot analysis, which co-migrate with bacterial heat shock proteins that co-purify with recombinant ESCRT-0 during SDS-PAGE), the intensity of STAM was used to determine that ESCRT-0 binds to liposomes in a curvature-independent fashion. Data shown are representative

of at least 3 independent experiments. Based on densitometry measurements, 94.5% (+/- 13.4%) of ESCRT-0 co-floated with 183 nm vesicles relative to 95 nm vesicles.

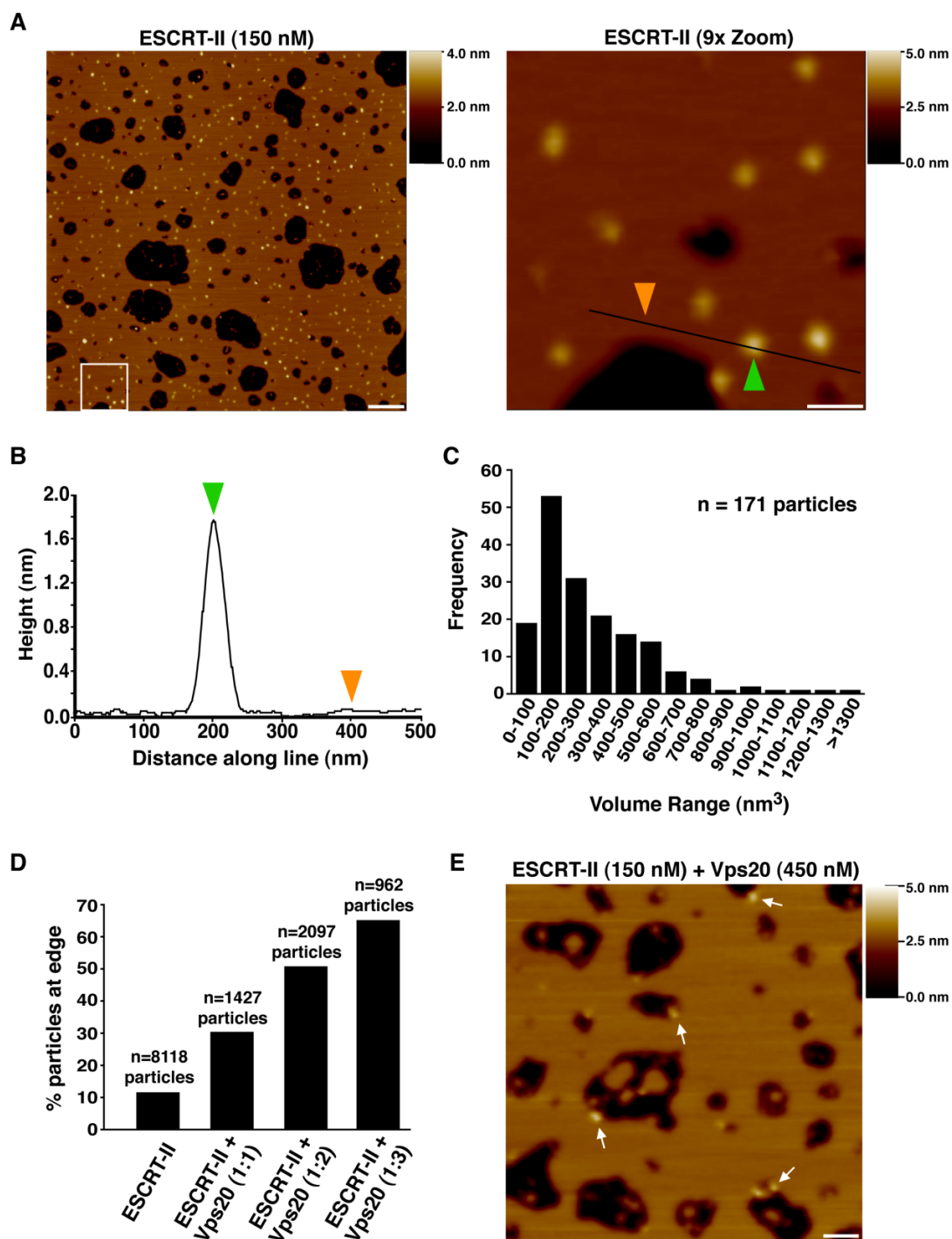


Figure 2.3. Vps20 targets ESCRT-II to membranes of high curvature.

Figure 2.3. Vps20 targets ESCRT-II to membranes of high curvature.

(Figure 2.3A) Representative AFM images of bilayers assembled in the presence of ESCRT-II (150 nM). A 9-fold magnification of the boxed region is shown on the right. A shade-height scale bar is shown on the right of each image. White scale bar (left), 500 nm and white scale bar (right), 100 nm. **(Figure 2.3B)** Analysis of the height distribution along the line drawn on the right panel of A. Colored arrowheads highlight the heights at two positions along the line as shown in A. **(Figure 2.3C)** Frequency distribution of molecular volumes for the ESCRT-II complex bound to the bilayer surface. Total number of particles analyzed is indicated. **(Figure 2.3D)** Bar graph showing the percentage of particles that appear at the edges of bilayers following the addition of various amounts of Vps20 to ESCRT-II. The total number of particles analyzed is indicated above each bar. **(Figure 2.3E)** Representative AFM image of a bilayer with an identical composition as described in A assembled in the presence of ESCRT-II (150 nM) and Vps20 (450 nM). Arrows highlight the presence of ESCRT-II/Vps20 particles at the bilayer edges. A shade-height scale bar is shown on the right. White scale bar, 125 nm.

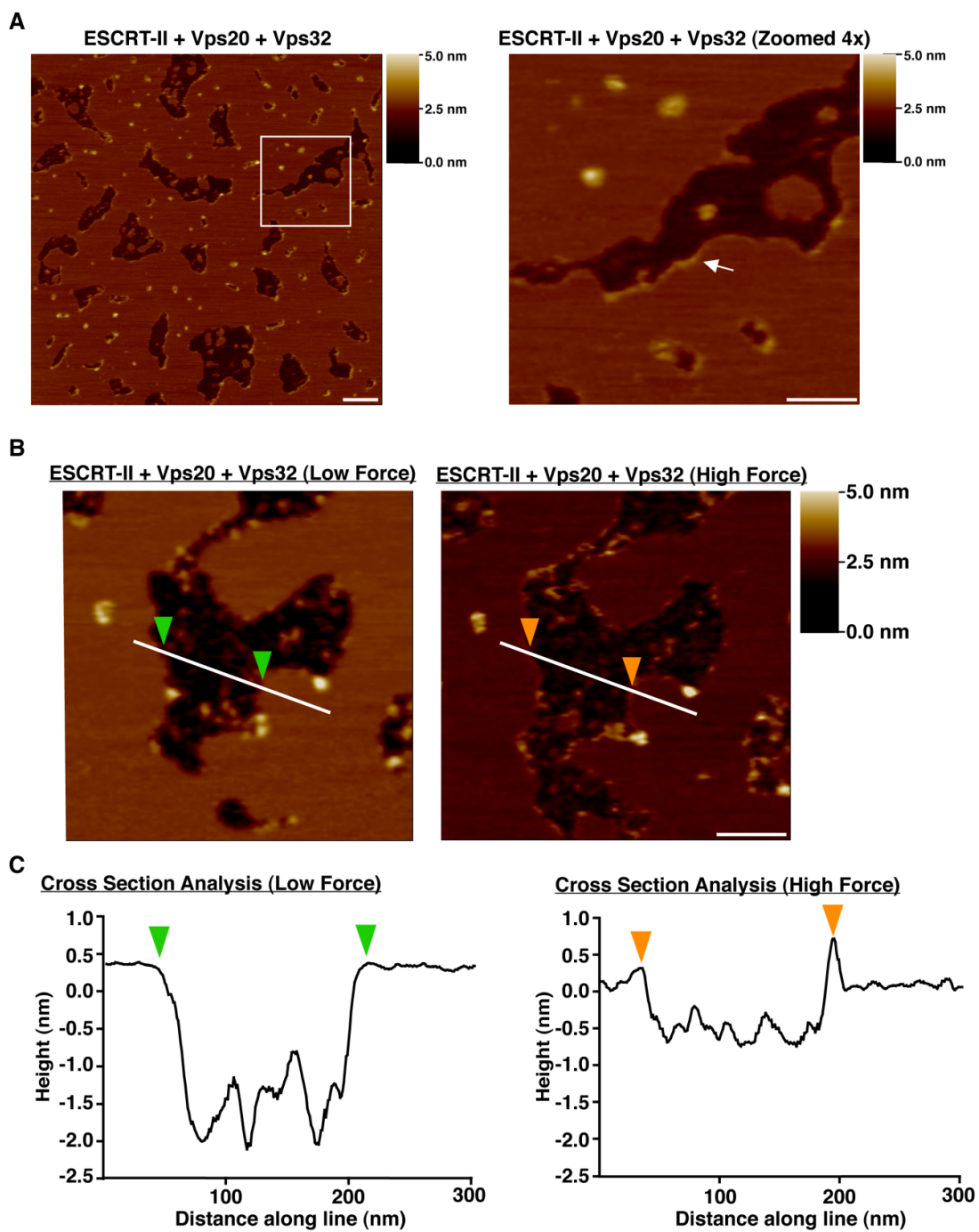


Figure 2.4. ESCRT-II and Vps20 nucleate a strand of Vps32 monomers that bind specifically to highly curved bilayers.

Figure 2.4. ESCRT-II and Vps20 nucleate a strand of Vps32 monomers that bind specifically to highly curved bilayers.

(**Figure 2.4A**) Representative AFM images of a bilayer assembled in the presence of ESCRT-II (100 nM), Vps20 (150 nM), and Vps32 (450 nM). A 4-fold magnification of the boxed region is shown on the right. The arrow highlights the presence of a filament along the bilayer edge. A shade-height scale bar is shown on the right of each image. White scale bar (left), 200 nm and white scale bar (right), 100 nm. (**Figure 2.4B**) Representative AFM images of an identical region of a bilayer formed in the presence of ESCRT-II (100 nM), Vps20 (150 nM), and Vps32 (450 nM) following the application of low force (left) and high force (right) with the AFM tip. A shade-height bar is shown on the right. White scale bar, 100 nm. (**Figure 2.4C**) The height relative to the bilayer is plotted along the lines shown in B. Color-coded arrowheads highlight the bilayer edges.

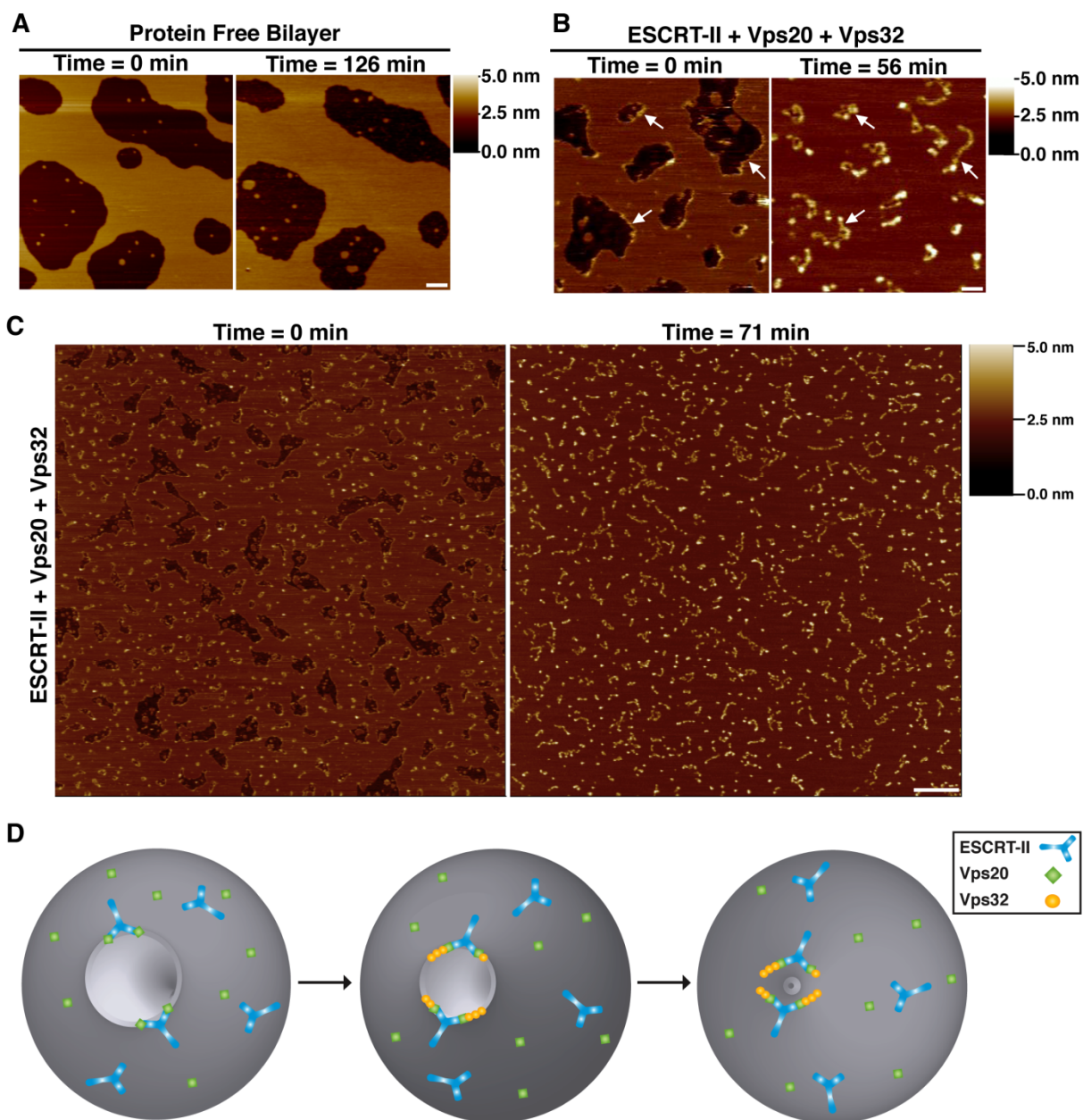


Figure 2.5. ESCRT-III filaments alter the dynamics of highly curved membranes.

Figure 2.5. ESCRT-III filaments alter the dynamics of highly curved membranes.

(**Figure 2.5A**) Representative AFM images of protein-free bilayers taken 126 minutes apart. A shade-height scale bar is shown on the right. White scale bar, 200 nm. (**Figure 2.5B**) Representative AFM images of bilayers assembled in the presence of ESCRT-II (150 nM), Vps20 (150 nM) and Vps32 (450 nM) taken 56 minutes apart. Arrows highlight the presence of the same filaments at each timepoint. A shade-height scale bar is shown on the right. White scale bar, 200 nm. (**Figure 2.5C**) Representative AFM images of a bilayer formed in the presence of ESCRT-II (100 nM), Vps20 (150 nM), and Vps32 (450 nM) taken 71 minutes apart. A shade-height bar is shown on the right. White scale bar, 500 nm. (**Figure 2.5D**) A diagram illustrating a model for ESCRT-III mediated membrane scission. The association of ESCRT-II and Vps20 (Step 1) generates a curvature sensitive protein assembly that is capable of nucleating strings of Vps32 monomers (Step 2) that bind to the highly curved surface of a vesicle bud neck. The binding energy between polymerized ESCRT-III and the membrane is sufficient to overcome the energy barrier to membrane fusion (Step 3). The presence of free ESCRT-II and Vps20 is also shown on the membrane surface, which do not exhibit enhanced binding to regions of elevated curvature.

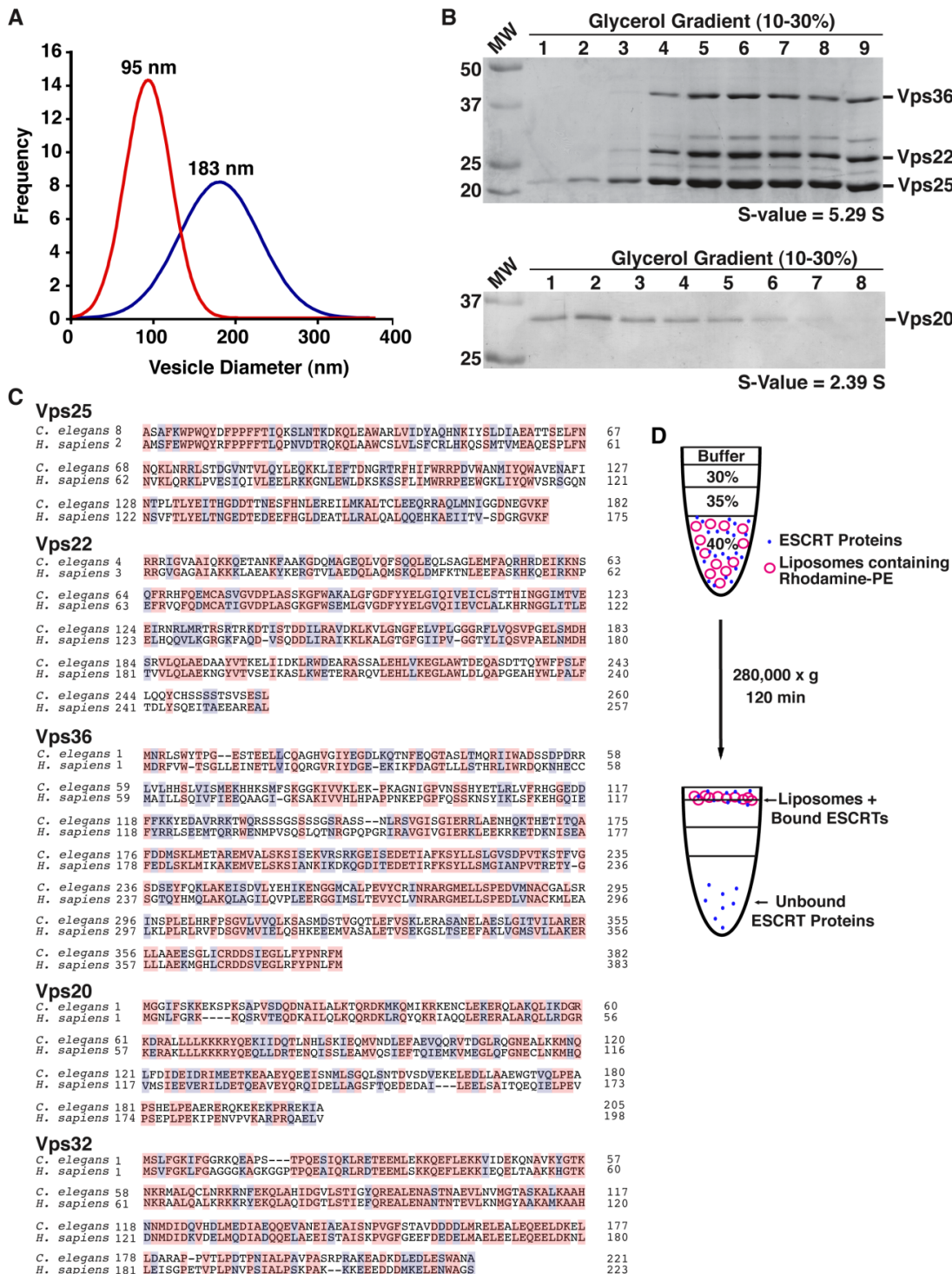


Figure 2.S1. *C. elegans* ESCRT-II and Vps20 exhibit similar hydrodynamic properties to their human counterparts and do not sense elevated membrane curvature individually.

Figure 2.S1. *C. elegans* ESCRT-II and Vps20 exhibit similar hydrodynamic properties to their human counterparts and do not sense elevated membrane curvature individually.

(Figure 2.S1A) Graphical representation of the results from dynamic light scattering measurements, which define the sizes of liposomes that form following extrusion through membranes harboring 30 nm (red line) and 200 nm (blue line) pores (n=2 independent experiments). **(Figure 2.S1B)** Purified *C. elegans* ESCRT-II (top) and Vps20 (bottom) were fractionated over glycerol gradients (10-30%), and their sedimentation values were calculated based on the mobility of characterized standards separated on parallel gradients (n=3). **(Figure 2.S1C)** Sequence alignments between *C. elegans* and human ESCRT-II and Vps20 proteins. Identical (red) and similar (blue) residues are highlighted. *C. elegans* Vps25 is encoded by W02A11.2, Vps22 by C27F2.5, Vps36 by F17C11.8, Vps20 by Y65B4A.3, and Vps32 (essential isoform) by C56C10.3. **(Figure 2.S1D)** Schematic representation of a co-flotation assay used to determine whether proteins associate with liposomes.

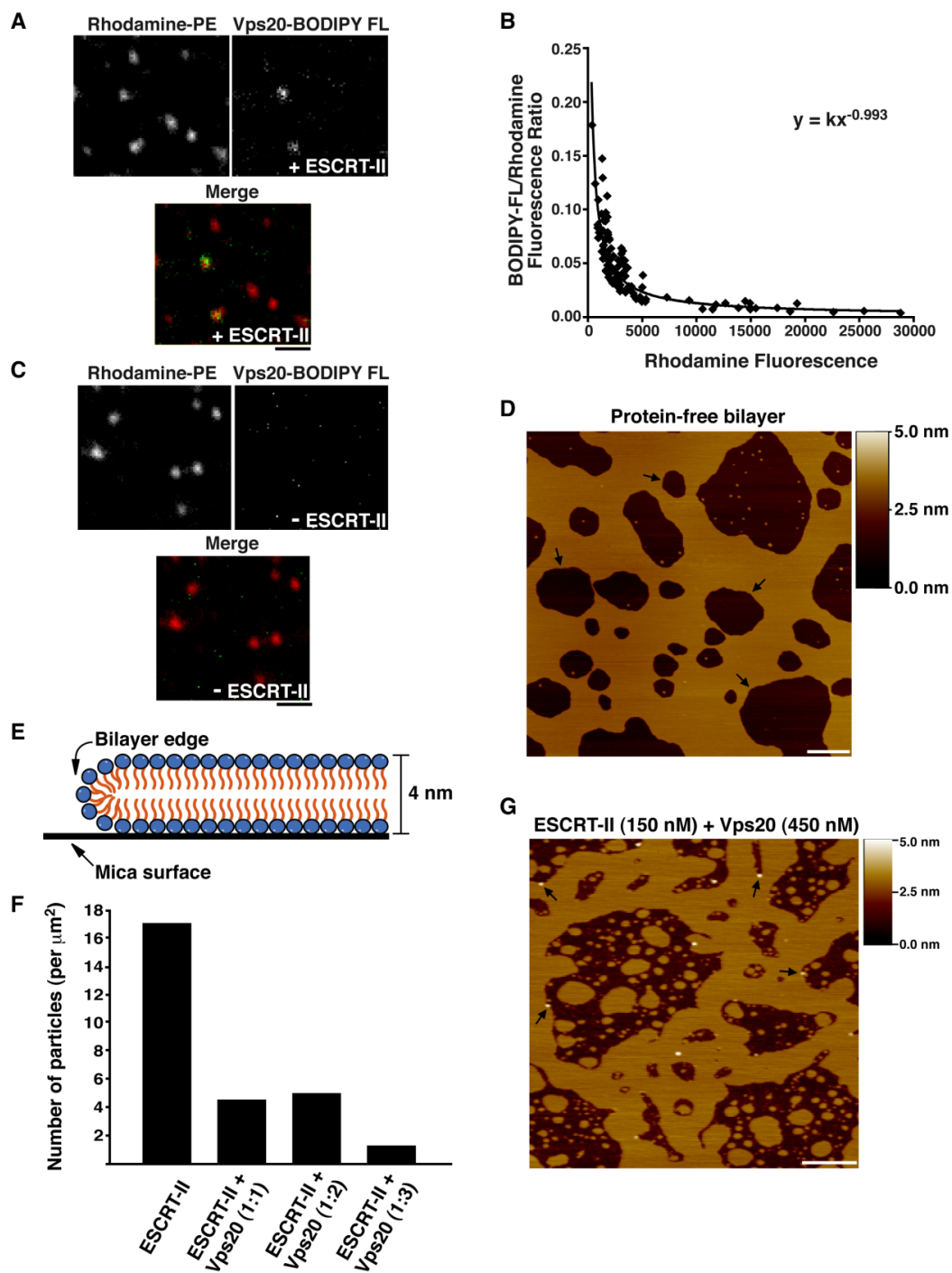


Figure 2.S2. Membrane binding of ESCRT-II/Vps20 increases as the square of the membrane curvature and association of Vps20 with ESCRT-II lowers the affinity of ESCRT-II for flat membranes.

Figure 2.S2. Membrane binding of ESCRT-II/Vps20 increases as the square of the membrane curvature and association of Vps20 with ESCRT-II lowers the affinity of ESCRT-II for flat membranes.

(**Figure 2.S2A**) BODIPY-FL-labeled Vps20 (right) and ESCRT-II were mixed and incubated with immobilized liposomes containing Rhodamine-PE (left) on a coverslip prior to imaging using confocal microscopy. A merged panel showing the localization of Vps20 (green) relative to Rhodamine-PE liposomes (red) is shown below. Bar, 2 μm . (**Figure 2.S2B**) The fluorescence intensity of individual liposomes was measured. Rhodamine intensity was plotted against the fluorescence intensity of BODIPY-FL divided by the fluorescence intensity of rhodamine. Data are representative of at least 3 independent experiments. A best fit curve was generated that is described by the following equation: $y = kx^{-0.993}$, where k is a constant (R^2 value = 0.95).

(**Figure 2.S2C**) BODIPY-FL-labeled Vps20 (right) was incubated with immobilized liposomes containing Rhodamine-PE (left) on a coverslip prior to imaging using confocal microscopy. A merged panel showing the localization of Vps20 (green) relative to Rhodamine-PE liposomes (red) is shown below. Bar, 2 μm . (**Figure 2.S2D**) Representative AFM image of a bilayer formed in the absence of proteins. Arrows highlight gaps in the bilayer, where the exposed mica surface can be visualized. A shade-height scale bar is shown on the right. White scale bar, 500 nm. (**Figure 2.S2E**) A schematic diagram illustrating the likely topology of the membrane at the edges of supported lipid bilayers. The typical height of a bilayer formed on a mica surface is approximately 4 nm, although the measured thickness is usually less because of partial penetration of the bilayer by the probe. (**Figure 2.S2F**) Using AFM, the total number of ESCRT-II particles bound to the bilayer was counted in the presence of varying concentrations

of Vps20 (0-450 nM). In each case, the concentration of ESCRT-II used remained constant (150 nM). Each experiment was conducted at least 2 times, and an area of at least 450 μm^2 was analyzed for each replicate. **(Figure 2.S2G)** A representative AFM image of a bilayer composed of phosphatidylcholine (55%), phosphatidylethanolamine (30%), and phosphatidylserine (15%) assembled in the presence of ESCRT-II (150 nM) and Vps20 (450 nM). Arrows highlight ESCRT-II/Vps20 particles bound to the edges of bilayers, which is independent of phosphoinositides. A shade-height scale bar is shown on the right. White scale bar, 500 nm.

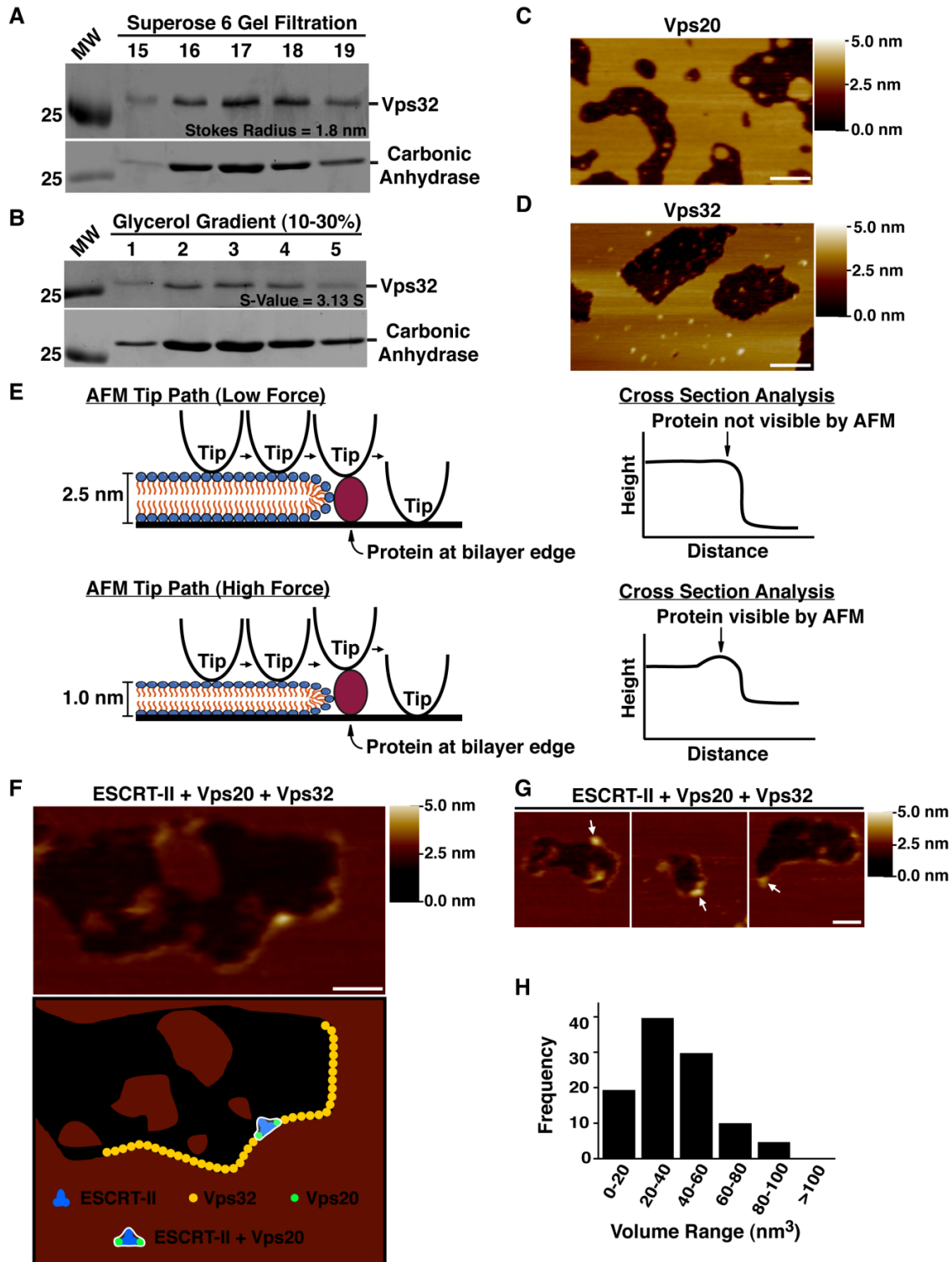


Figure 2.S3. ESCRT-III filaments form specifically on highly curved membranes.

Figure 2.S3. ESCRT-III filaments form specifically on highly curved membranes.

(**Figure 2.S3A**) Vps32 initially purified using nickel affinity chromatography was subjected to size exclusion chromatography, and the peak fractions eluted were separated by SDS-PAGE and stained using Coomassie blue (top). For comparison, the elution profile of carbonic anhydrase, a globular, monomeric protein of a similar molecular weight is shown (bottom). A Stokes radius for Vps32 was calculated based on the elution profile of characterized standards (n=3). (**Figure 2.S3B**) Purified Vps32 was fractionated over a glycerol gradient (10-30%), and its sedimentation value was calculated based on the mobility of characterized standards separated on parallel gradients (n=3). For comparison, the fractionation profile of carbonic anhydrase is shown (bottom). (**Figure 2.S3C**) A representative AFM image of a bilayer formed in the presence of Vps20 (150 nM). A shade-height bar is shown on the right. White scale bar, 250 nm. (**Figure 2.S3D**) A representative AFM image of a bilayer formed in the presence of Vps32 (450 nM). A shade-height bar is shown on the right. White scale bar, 250 nm. (**Figure 2.S3E**) A schematic diagram showing that proteins bound to the edges of bilayers are not visible unless additional force is applied by the AFM tip to compress the bilayer. Apparent heights of the bilayer are shown. (**Figure 2.S3F**) The top panel shows a representative AFM image of a bilayer formed in the presence of ESCRT-II (100 nM), Vps20 (150 nM), and Vps32 (450 nM). A shade-height bar is shown on the right. White scale bar, 100 nm. The bottom panel is a schematic representation of the top panel, highlighting the spatial distribution of ESCRT-II (blue), Vps20 (green), and Vps32 (yellow). The ESCRT-II/Vps20 complex (encircled in white) is also shown. (**Figure 2.S3G**) Additional representative AFM images of bilayers formed as in F at high magnification. Arrows highlight ESCRT-II/Vps20 nucleation complexes. A shade-height bar is shown on the

right. White scale bar, 50 nm. (**Figure 2.S3H**) Frequency distribution of molecular volumes for Vps32 monomers within filaments bound to the edges of lipid bilayers. More than 20 filaments were analyzed in 3 independent experiments.

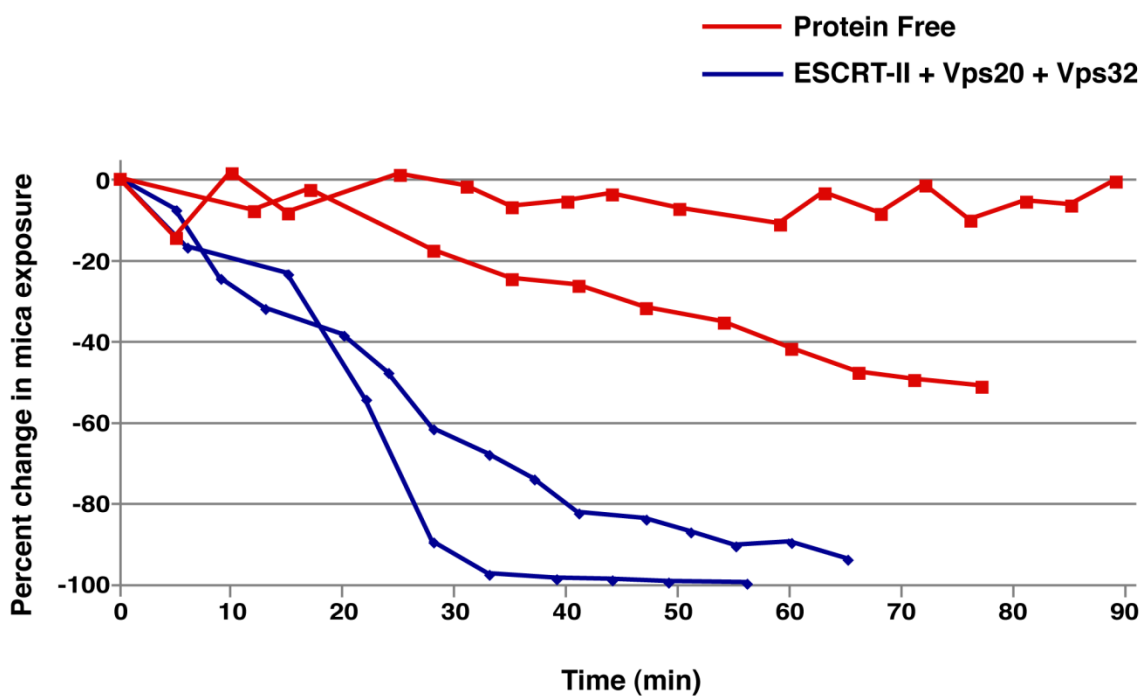


Figure 2.S4. ESCRT-III assembly promotes membrane remodeling and bilayer sealing on a mica surface.

Figure 2.S4. ESCRT-III assembly promotes membrane remodeling and bilayer sealing on a mica surface. Using AFM, the surface area of mica that remained exposed following SLB assembly was calculated over a region greater than $2.25 \mu\text{m}^2$ at different time intervals, both in the presence (blue) and absence (red) of ESCRT-II (150 nM), Vps20 (150 nM), and Vps32 (450 nM). Four independent experiments are shown as a percent change in the area of exposed mica over time.

REFERENCES

1. Raiborg, C., and Stenmark, H. (2009) The ESCRT machinery in endosomal sorting of ubiquitylated membrane proteins. *Nature* **458**, 445-452
2. Saksena, S., and Emr, S. D. (2009) ESCRTs and human disease. *Biochem Soc Trans* **37**, 167-172
3. Sorkin, A., and Von Zastrow, M. (2002) Signal transduction and endocytosis: close encounters of many kinds. *Nat Rev Mol Cell Biol* **3**, 600-614
4. Garrus, J. E., von Schwedler, U. K., Pornillos, O. W., Morham, S. G., Zavitz, K. H., Wang, H. E., Wettstein, D. A., Stray, K. M., Côté, M., Rich, R. L., Myszka, D. G., and Sundquist, W. I. (2001) Tsg101 and the vacuolar protein sorting pathway are essential for HIV-1 budding. *Cell* **107**, 55-65
5. Carlton, J. G., and Martin-Serrano, J. (2007) Parallels between cytokinesis and retroviral budding: a role for the ESCRT machinery. *Science* **316**, 1908-1912
6. Hurley, J. H., and Emr, S. D. (2006) The ESCRT complexes: structure and mechanism of a membrane-trafficking network. *Annu Rev Biophys Biomol Struct* **35**, 277-298
7. Gaullier, J. M., Simonsen, A., D'Arrigo, A., Bremnes, B., Stenmark, H., and Aasland, R. (1998) FYVE fingers bind PtdIns(3)P. *Nature* **394**, 432-433
8. Xie, W., Li, L., and Cohen, S. N. (1998) Cell cycle-dependent subcellular localization of the TSG101 protein and mitotic and nuclear abnormalities associated with TSG101 deficiency. *Proc Natl Acad Sci U S A* **95**, 1595-1600
9. Langelier, C., von Schwedler, U. K., Fisher, R. D., De Domenico, I., White, P. L., Hill, C. P., Kaplan, J., Ward, D., and Sundquist, W. I. (2006) Human ESCRT-II complex and its role in human immunodeficiency virus type 1 release. *J Virol* **80**, 9465-9480
10. Wollert, T., and Hurley, J. H. (2010) Molecular mechanism of multivesicular body biogenesis by ESCRT complexes. *Nature* **464**, 864-869
11. Wollert, T., Wunder, C., Lippincott-Schwartz, J., and Hurley, J. H. (2009) Membrane scission by the ESCRT-III complex. *Nature* **458**, 172-177
12. Hanson, P. I., Roth, R., Lin, Y., and Heuser, J. E. (2008) Plasma membrane deformation by circular arrays of ESCRT-III protein filaments. *J Cell Biol* **180**, 389-402
13. Saksena, S., Wahlman, J., Teis, D., Johnson, A. E., and Emr, S. D. (2009) Functional reconstitution of ESCRT-III assembly and disassembly. *Cell* **136**, 97-109

14. Zamborlini, A., Usami, Y., Radoshitzky, S. R., Popova, E., Palu, G., and Göttlinger, H. (2006) Release of autoinhibition converts ESCRT-III components into potent inhibitors of HIV-1 budding. *Proc Natl Acad Sci U S A* **103**, 19140-19145
15. Teis, D., Saksena, S., Judson, B. L., and Emr, S. D. (2010) ESCRT-II coordinates the assembly of ESCRT-III filaments for cargo sorting and multivesicular body vesicle formation. *EMBO J* **29**, 871-883
16. Teo, H., Perisic, O., González, B., and Williams, R. L. (2004) ESCRT-II, an endosome-associated complex required for protein sorting: crystal structure and interactions with ESCRT-III and membranes. *Dev Cell* **7**, 559-569
17. Im, Y. J., Wollert, T., Boura, E., and Hurley, J. H. (2009) Structure and function of the ESCRT-II-III interface in multivesicular body biogenesis. *Dev Cell* **17**, 234-243
18. Im, Y. J., and Hurley, J. H. (2008) Integrated structural model and membrane targeting mechanism of the human ESCRT-II complex. *Dev Cell* **14**, 902-913
19. Kasson, P. M., and Pande, V. S. (2004) Molecular dynamics simulation of lipid reorientation at bilayer edges. *Biophys J* **86**, 3744-3749
20. Kozlovsky, Y., and Kozlov, M. M. (2003) Membrane fission: model for intermediate structures. *Biophys J* **85**, 85-96
21. Jackson, M. B. (2009) Minimum membrane bending energies of fusion pores. *J Membr Biol* **231**, 101-115
22. Lee, M. C., and Schekman, R. (2004) Cell biology. BAR domains go on a bender. *Science* **303**, 479-480
23. Liu, J., Kaksonen, M., Drubin, D. G., and Oster, G. (2006) Endocytic vesicle scission by lipid phase boundary forces. *Proc Natl Acad Sci U S A* **103**, 10277-10282
24. Liu, J., Sun, Y., Oster, G. F., and Drubin, D. G. (2010) Mechanochemical crosstalk during endocytic vesicle formation. *Curr Opin Cell Biol* **22**, 36-43
25. Litster, J. D. (1975) Stability of lipid bilayers and red blood cell membranes. *Physics Letters A* **53**, 193-194
26. Wang, H., de Joannis, J., Jiang, Y., Gaulding, J. C., Albrecht, B., Yin, F., Khanna, K., and Kindt, J. T. (2008) Bilayer edge and curvature effects on partitioning of lipids by tail length: atomistic simulations. *Biophys J* **95**, 2647-2657
27. Jiang, F. Y., Bouret, Y., and Kindt, J. T. (2004) Molecular dynamics simulations of the lipid bilayer edge. *Biophys J* **87**, 182-192

28. de Joannis, J., Jiang, F. Y., and Kindt, J. T. (2006) Coarse-grained model simulations of mixed-lipid systems: composition and line tension of a stabilized bilayer edge. *Langmuir* **22**, 998-1005
29. Jiang, Y., and Kindt, J. T. (2007) Simulations of edge behavior in a mixed-lipid bilayer: fluctuation analysis. *J Chem Phys* **126**, 045105
30. Henne, W. M., Kent, H. M., Ford, M. G., Hegde, B. G., Daumke, O., Butler, P. J., Mittal, R., Langen, R., Evans, P. R., and McMahon, H. T. (2007) Structure and analysis of FCHO2 F-BAR domain: a dimerizing and membrane recruitment module that effects membrane curvature. *Structure* **15**, 839-852
31. Mayers, J. R., Fyfe, I., Schuh, A. L., Chapman, E. R., Edwardson, J. M., and Audhya, A. (2011) ESCRT-0 assembles as a heterotetrameric complex on membranes and binds multiple ubiquitylated cargoes simultaneously. *J Biol Chem* **286**, 9636-9645
32. Guizetti, J., Schermelleh, L., Mäntler, J., Maar, S., Poser, I., Leonhardt, H., Müller-Reichert, T., and Gerlich, D. W. (2011) Cortical constriction during abscission involves helices of ESCRT-III-dependent filaments. *Science* **331**, 1616-1620
33. Babst, M., Wendland, B., Estepa, E. J., and Emr, S. D. (1998) The Vps4p AAA ATPase regulates membrane association of a Vps protein complex required for normal endosome function. *EMBO J* **17**, 2982-2993
34. Fabrikant, G., Lata, S., Riches, J. D., Briggs, J. A., Weissenhorn, W., and Kozlov, M. M. (2009) Computational model of membrane fission catalyzed by ESCRT-III. *PLoS Comput Biol* **5**, e1000575
35. Fujii, K., Hurley, J. H., and Freed, E. O. (2007) Beyond Tsg101: the role of Alix in 'ESCRTing' HIV-1. *Nat Rev Microbiol* **5**, 912-916
36. Lee, H. H., Elia, N., Ghirlando, R., Lippincott-Schwartz, J., and Hurley, J. H. (2008) Midbody targeting of the ESCRT machinery by a noncanonical coiled coil in CEP55. *Science* **322**, 576-580
37. Lata, S., Schoehn, G., Jain, A., Pires, R., Piehler, J., Gottlinger, H. G., and Weissenhorn, W. (2008) Helical structures of ESCRT-III are disassembled by VPS4. *Science* **321**, 1354-1357
38. Tan, S. (2001) A modular polycistronic expression system for overexpressing protein complexes in Escherichia coli. *Protein Expr Purif* **21**, 224-234
39. Audhya, A., McLeod, I. X., Yates, J. R., and Oegema, K. (2007) MVB-12, a fourth subunit of metazoan ESCRT-I, functions in receptor downregulation. *PLoS One* **2**, e956

40. Tucker, W. C., Weber, T., and Chapman, E. R. (2004) Reconstitution of Ca²⁺-regulated membrane fusion by synaptotagmin and SNAREs. *Science* **304**, 435-438
41. Barrera, N. P., Ormond, S. J., Henderson, R. M., Murrell-Lagnado, R. D., and Edwardson, J. M. (2005) Atomic force microscopy imaging demonstrates that P2X₂ receptors are trimers but that P2X₆ receptor subunits do not oligomerize. *J Biol Chem* **280**, 10759-10765

Chapter 3

The Open Conformation of the ESCRT-III Subunit Vps20 is Independent of ESCRT-II Binding

This chapter represents a manuscript in preparation for publication:

Schuh AL and Audhya A

ABSTRACT

Members of the endosomal sorting complex required for transport (ESCRT) machinery function in membrane remodeling processes during multivesicular endosome (MVE) biogenesis, cytokinesis, and retroviral budding. In MVE biogenesis, ESCRT-II and the ESCRT-III subunit Vps20 play a specific role in regulating downstream assembly of the ESCRT-III complex. Previous work suggests that Vps20, like other ESCRT-III subunits, exhibits an autoinhibited, closed conformation in solution. Its activation has been proposed to depend on an association with ESCRT-II specifically at endosomes membranes. However, we show here that ESCRT-II and Vps20 interact directly in solution, both in cytosolic *C. elegans* extracts and using recombinant proteins *in vitro*. Moreover, we demonstrate that purified Vps20 exhibits an open, extended conformation, irrespective of ESCRT-II binding, in contrast with the closed, autoinhibited architecture of another ESCRT-III subunit, Vps24. Our data argue that individual ESCRT-III subunits exhibit distinct configurations in the cytoplasm, which are tailored for their specific functions during ESCRT-mediated membrane reorganization events.

INTRODUCTION

Activated cell surface receptors undergo downregulation through the generation of multivesicular endosomes (MVEs), which sequester cargoes within the lumen of the endosome and block interactions with cytoplasmic effectors (1,2). Biogenesis of MVEs is dependent upon a collection of proteins known as the ESCRT machinery, which functions in the identification of cargo for internalization, membrane deformation to generate nascent vesicles that bud away from the cytoplasm, and the scission event that releases these vesicles into the endosome lumen (3). Receptors destined for degradation are modified by ubiquitin conjugation, which acts as a sorting signal recognized by early-acting components of the ESCRT machinery (4). In addition to MVE biogenesis, subsets of the ESCRT machinery also play roles in cytokinesis and the budding of several enveloped viruses, including HIV-1. These three processes are topologically equivalent, suggesting a specialized function for the ESCRT machinery in promoting scission events from the cytoplasmic surface of membranes (5,6).

The ESCRT machinery is made of five complexes (ESCRT-0, ESCRT-I, ESCRT-II, ESCRT-III, and Vps4-Vta1), and a set of regulatory factors. ESCRT-0, ESCRT-I, and ESCRT-II form stable, heteropolymeric complexes in the cytoplasm, which contain ubiquitin binding domains that directly interact with cargo (7). *In vitro* studies have shown that ESCRT-I and ESCRT-II can contribute to membrane deformation on the surface of giant unilamellar vesicles (GUVs), and upon addition of the ESCRT-III subunits, Vps20 and Vps32, release nascent vesicles into the lumen of GUVs. This suggests that ESCRT-III has a direct role in membrane scission (8). Unlike upstream ESCRT complexes, ESCRT-III only assembles at a membrane surface and requires the Vps4-Vta1 complex for disassembly from the endosomal membrane for additional rounds of MVE biogenesis (7,9).

The core ESCRT-III subunits are recruited in a sequential fashion to the site of MVE formation and include: Vps20, Vps32, Vps24 and Vps2, respectively (10). Vps20 binds to each of the two Vps25 subunits of ESCRT-II (11). *In vitro* experiments suggest that conformational changes may occur in Vps20 when mixed with ESCRT-II and liposomes, and these structural changes are associated with the recruitment and subsequent activation of Vps32 (12). Vps32 is the most abundant ESCRT-III subunit and polymerizes to form filaments, which play a direct role in membrane scission (10,12). Additionally, a supercomplex of ESCRT-II and Vps20 preferentially binds to regions of high curvature, spatially regulating Vps32 filament formation (13). Vps24 acts as a cap for the forming filament and also binds to Vps2, which plays an important role in the Vps4-dependent disassembly of the ESCRT-III complex (10).

The ESCRT-III proteins possess a similar overall architecture, with a basic amino-terminus and an acidic carboxyl-terminus. Crystallographic data on the helical core of human Vps24 (CHMP3) revealed a 70 Å helical hairpin (composed of helices 1 and 2) that forms an asymmetric four-helix bundle with two short helices (helices 3 and 4) (14). The carboxyl-terminal portions (including helix 5) of the ESCRT-III proteins have been proposed to act as autoinhibitory domains, which prevent interaction between individual ESCRT-III subunits within the cytoplasm (12,15-18). Two structures of human Vps24 have placed helix 5 in different positions. One shows helix 5 in a closed conformation, where it is packed against the helical hairpin loop (19); the other structure represents an open conformation where helix 5 lies perpendicular to the four helix bundle (14). Based on a crystal structure of the binding interface between Vps20 and ESCRT-II, the positioning of helix 5 would not be impacted by their association (20), suggesting that ESCRT-II binding to Vps20 would not promote its transition to

a more open, active conformation. Here, we take advantage of small angle X-ray scattering (SAXS) to demonstrate that Vps20, unlike Vps24, is constitutively in an extended, open conformation, independently of ESCRT-II. Our findings indicate that free ESCRT-III subunits exhibit distinct conformations in solution, and additionally suggest that autoinhibition does not represent a general mechanism to prevent cytosolic assembly of ESCRT-III polymers *in vivo*.

RESULTS

ESCRT-II and Vps20 interact in solution

ESCRT-II and Vps20 have been shown previously to associate only at endosomal membranes in yeast. A mechanism underlying this specificity is lacking, and structural studies fail to support the idea that these factors would be unable to bind in solution. We used polyclonal antibodies directed against ESCRT-II to conduct a series of immunoprecipitations from *C. elegans* embryo extracts. Multidimensional protein identification technology (MudPIT) was used to identify interacting partners. A directed search for all components of the ESCRT machinery revealed the presence of only the three characterized ESCRT-II subunits and the ESCRT-III protein Vps20 (**Table 3.S1**). To confirm this finding, we immunoprecipitated ESCRT-II and Vps20 separately from *C. elegans* extracts, and conducted a set of immunoblot analyses. Consistent with our unbiased mass spectrometry-based approach, we found that ESCRT-II and Vps20 bind to one another in solution, but neither interacts with the upstream ESCRT-0 subunit STAM (**Figures 3.1A and 3.1B**). To determine whether this interaction was direct, we purified recombinant forms of ESCRT-II and Vps20 and measured their association using size exclusion chromatography. Independently, ESCRT-II and Vps20 exhibit Stokes radii of ~4.9 nm and ~3.0 nm, respectively (Figure 3.1C). However, when combined at a molar ratio of 1:2 (to account for the presence of two Vps20 binding sites in ESCRT-II), a new complex containing both components of the ESCRT machinery forms in solution, with an enlarged Stokes radius of ~5.5 nm. These data indicate that ESCRT-II and Vps20 interact directly in solution.

Small angle X-ray scattering reveals differences in the conformations of two ESCRT-III subunits

The interface between ESCRT-II and ESCRT-III has been determined crystallographically and identifies an amino-terminal helix in Vps20 (part of an asymmetric four-helix bundle), which mediates its association with ESCRT-II. This interaction is not predicted to alter the autoinhibitory conformation that is observed in other ESCRT-III subunits, including human Vps24 and the ESCRT-related regulatory factor Ist1. Combined with our findings that ESCRT-II and Vps20 interact in solution, we questioned the proposed role for ESCRT-II in relieving Vps20 from an autoinhibited state to nucleate ESCRT-III polymerization (See **Figure 3.S1** for secondary structure organization). To explore the structures of full-length ESCRT-III subunits, none of which are amenable to X-ray crystallography, we took advantage of small angle X-ray scattering (SAXS), a low-resolution structural approach that permits *ab initio* modeling to determine the conformations of proteins in solution. Previous studies using SAXS demonstrated that full-length human Vps24 exhibits a closed conformation. To validate this approach using *C. elegans* ESCRT-III proteins, we conducted SAXS on purified, recombinant *C. elegans* Vps24. Our analysis produced consistent and interpretable scattering profiles across three protein concentrations (**Figure 3.S2B**). From these data, we determined the radius of gyration (R_g) and maximal protein distances (D_{max}) to range from 23.3-25.2 Å and 73.5-74.5 Å, respectively (**Figures 3.2A and 3.S2A**). We generated a merged data set between two concentrations, which produced an R_g of 23.2 Å and a D_{max} of 74.0 Å (**Figure 3.2B**). The Porod volume was used to estimate the molecular weight to be 21 kD, consistent with its predicted

molecular weight of 23.6 kD, based on amino acid composition. These data indicate that *C. elegans* Vps24 is monodispersed and monomeric in solution.

An overall protein envelope was determined *ab initio* from the scattering profile (21). 15 independent models of Vps24 were aligned and averaged (22), with a nominal spatial discrepancy (NSD) of 0.67 (**Figure 3.2C**). The overall envelope of Vps24 reveals a compact structure in agreement with the previously published SAXS envelope of human Vps24, which exhibited a D_{\max} of 75 Å (17). Together, our findings demonstrate that *C. elegans* Vps24 possesses a similar conformation as compared to human Vps24 and validates our use of SAXS to study ESCRT-III structure.

To determine the conformation of Vps20 in solution, we purified a recombinant form of the full-length, untagged protein to homogeneity. A combination of size exclusion chromatography and multi-angle light scattering (MALS) analysis demonstrated that Vps20 elutes in a single peak with a molecular mass of 25.5 kD (**Figure 3.S3C**). These data indicate that Vps20 is monomeric in solution. SAXS analysis produced consistent and interpretable scattering profiles across three unique protein concentrations (**Figure 3.S3B**). In contrast to our findings using Vps24, our analysis of Vps20 revealed R_g and D_{\max} values ranging from 27.4-28.8 Å and 93.0-95.0 Å, respectively (**Figures 3.3A and 3.S3A**). We generated a merged data set between two concentrations, producing an overall R_g of 27.3 Å and a D_{\max} of 94.0 Å (**Figure 3.3B**). The Porod volume estimated the molecular weight to be 25 kD, consistent with the predicted molecular weight of a Vps20 monomer, 24.1 kD.

An overall protein envelope for Vps20 was obtained using *ab initio* modeling. 15 independent models produced an average envelope with a NSD value of 0.69 (**Figure 3.3C**). In

contrast to the conformation of Vps24, the overall shape of Vps20 in solution revealed an elongated conformation. To verify that the limited concentration of salt (100 mM) used in our experiments was not affecting the shape of Vps20, we conducted SAXS analysis on Vps20 in the absence of salt, which yielded a similar D_{\max} of 99.5 Å (**Figure 3.S3D**). Together, these data indicate that Vps20 and Vps24 do not share a similar conformation in solution.

Vps20 exhibits an open conformation independent of ESCRT-II in solution

Although the SAXS envelope for Vps20 indicates an extended conformation in solution, the orientation of the protein is difficult to assign. We therefore generated a truncated form of *C. elegans* Vps20 containing its asymmetric helical core (Vps20 Δ C, helices 1-5 encoded by amino acids 1-170), which we studied using SAXS. Our analysis produced an interpretable scattering profile (**Figure 3.S4A**) and revealed that Vps20 Δ C possesses an R_g of 22.8 Å and a D_{\max} of 86.0 Å (**Figure 3.4A**). The Porod volume determined the molecular weight to be 20.2 kD, nearly identical to that of a monomeric form of Vps20 Δ C (19.7 kD). 15 independent models produced an envelope with a NSD value of 0.77 (**Figure 3.4B**).

Although the positioning of carboxyl-terminal helices within ESCRT-III subunits varies, depending on whether they exhibit an open or a closed conformation, the helical core domain is structurally stable (19,23). For example, two crystallographic structures for Vps24 have been determined. One of these structures utilizes a carboxyl-terminal truncation, which displaces helix 5 away from the helical hairpin and represents an open conformation (14). The alternative structure of Vps24 represents a closed conformation, in which helix 5 is packed against the helical hairpin loop (19). Unbiased *in silico* methods were used to align both crystal structures within the SAXS envelope of Vps20 Δ C. While the open form of Vps24 fits well into the SAXS

envelope of Vps20 Δ C in all orientations (**Figure 3.5A**), the closed form could not be fit into the envelope without helix 5 extending beyond its boundaries (**Figure 3.5B**). These data suggest that Vps20 Δ C represents the open conformation of Vps20.

We also overlaid the closed and open Vps24 structures onto our full-length *C. elegans* Vps24 SAXS envelope (**Figures 3.6A and 3.6B** respectively). In the open conformation, we found that helix 5 extends beyond the SAXS model using an unbiased modeling program. We additionally attempted to manually fit the open structure, but still encountered difficulty in accommodating helix 5 within the boundaries of the SAXS envelope (**Figure 3.6C**). In contrast, we were able to easily fit the closed Vps24 conformation onto the SAXS structure, confirming that in solution, Vps24 exhibits an autoinhibited, closed state in which helix 5 is folded onto the helical hairpin loop.

Informed by the orientation of the Vps24 crystal structure on the SAXS envelope generated by truncated Vps20, we performed similar docking studies using our SAXS model for full-length Vps20. Similar to Vps20 Δ C, we found that the open configuration of Vps24 fit nicely into the envelope (**Figure 3.7A**). Additionally, we identified a density in our SAXS envelope below helix 5, which may account for the remaining carboxyl-terminal residues of Vps20, which were too unstructured to be modeled using crystallographic data obtained for Vps24. In contrast, when the structure representing the closed conformation of Vps24 was docked, we failed to identify a satisfactory conformation that did not leave substantial density both above and below the crystal structure (**Figure 3.7B**). Since Vps20 adopts an elongated conformation in solution, with a diameter of 94 Å, the crystal structure in which helix 5 is displaced from the helical hairpin loop helps to account for this increase in diameter that extends

beyond the helical hairpin. Collectively, our data strongly suggest that Vps20 adopts an open conformation in solution unlike the downstream ESCRT-III subunit Vps24, which remains in an autoinhibited, closed state until activation.

DISCUSSION

ESCRT-mediated membrane fission is dependent upon the ESCRT-III complex. However, the mechanisms by which ESCRT-III subunits function cooperatively to mediate membrane scission are unknown. Recently, several models have been postulated to describe this process. In the “dome model,” Vps32 forms flat, inward-spiraling filaments that bind and initiate polymerization of Vps24 and Vps2, which generate a tube-like structure with a narrowing diameter that ultimately facilitates membrane cleavage (24). Another scenario commonly referred to as the “purse string model” asserts that Vps32 filaments are capped by Vps24 and its binding partner Vps2 to promote Vps4-Vta1 complex recruitment. In this case, Vps4-mediated disassembly of ESCRT-III filaments alters its structure to promote membrane scission (12). Despite mechanistic differences within these models, all require ESCRT-III subunits to possess discrete functions during the membrane fission process. However, until now, it has been difficult to structurally distinguish components of the core ESCRT-III complex, even though each acts in a non-redundant manner.

To define potential structural differences among the ESCRT-III subunits, we focused our attention on Vps20, a key factor linking the actions of ESCRT-II and ESCRT-III in MVE biogenesis (10). Although mechanisms underlying Vps20-mediated initiation of Vps32 polymerization remain unclear, the binding interface between Vps20 and the Vps25 subunit of ESCRT-II has been crystallized, revealing a specific association with the amino-terminal portion of helix one within Vps20 (20). This binding surface is not precluded in either the open or closed conformations of other ESCRT-III subunits (14,19), challenging the idea that ESCRT-II activates Vps20 by altering its conformation (12). Although ESCRT-II modulates the fluorescence properties of Vps20, interpretation of these data is challenging in the absence of

structural information. Moreover, our data demonstrate that ESCRT-II and Vps20 bind avidly in solution, a finding that is inconsistent with the model that ESCRT-II mediates Vps20 activation specifically on the endosomal membrane. Instead, Vps20 may interact directly with ESCRT-II in the cytoplasm, generating a curvature-sensing supercomplex that binds to curved membranes and stimulates Vps32 polymerization at nascent vesicle bud necks (13). In this revised model, an alteration in Vps20 conformation by ESCRT-II becomes unnecessary, as curvature sensing spatially restricts assembly of ESCRT-III polymers.

Although high-resolution structures have been determined for the majority of the early-acting ESCRT machinery, the architectures of individual ESCRT-III subunits have been challenging to define using crystallographic methods. SAXS represents an attractive, alternative approach that provides complimentary information of the conformation and overall shape of a protein, albeit at low resolution. An additional advantage of SAXS is that experiments are performed in solution without the need to incorporate artificial fluorescent dyes or tags, which can introduce structural artifacts (25). Indeed, previous SAXS analysis of human Vps24 showed it to exist in a closed conformation in solution, consistent with models in which ESCRT-III subunits remain autoinhibited in the cytoplasm. In the presence of non-physiological concentrations of salt, Vps24 can undergo a conformational change to an elongated state (17), suggesting that SAXS analysis of ESCRT-III subunits is capable of determining their conformation. Our studies on *C. elegans* Vps24 confirmed previous results. However, analysis of full-length Vps20 indicated it to be in an extended conformation, irrespective of salt concentration or the presence of ESCRT-II. These findings again argue against a role for ESCRT-II in promoting a conformational change in Vps20.

Based on our data, we propose that the conformations of individual ESCRT-III subunits vary, potentially tailoring each to a specific function during membrane scission. Additionally, our findings demonstrate that current models, which suggest all ESCRT-III proteins undergo structural rearrangement to enable complex assembly, are overly simplistic. Only through a systematic structural characterization of each ESCRT-III subunit will the full complexity of ESCRT-III complex assembly be ultimately revealed.

MATERIALS and METHODS

Immunoprecipitation

Adult hermaphrodites were grown synchronously in liquid culture following previously described protocol (26). For mass spectrometry, proteins were precipitated using TCA and processed for MudPIT analysis (26). The spectra were searched with the SEQUEST™ algorithm (27) or ProLuCID (28) against the WormBase *C. elegans* (version 2.11 created on 01-10-2010) database. Immunoprecipitations were also conducted as previously described (29).

Protein purification and size exclusion chromatography studies

Recombinant protein expression was performed using BL21-T1R (DE3) *E. coli*. All proteins utilized in this study were *C. elegans*. For ESCRT-II, all subunits were cloned into the polycistronic expression vector pST39 (30) with a single tag appended to Vps25 to enable purification. Vps24 and Vps20 Δ C (amino acids 1-170) were cloned into pGEX6P-1, which encodes a cleavable, amino-terminal GST tag. Vps20 was cloned into His-Sumo-pET28d with a cleavable, amino-terminal His-Sumo tag. Protein purifications were conducted using glutathione agarose beads (for GST-Vps24 and GST-Vps20 Δ C) or nickel affinity resin (for intact ESCRT-II and His-Sumo-Vps20). The GST moiety was removed from bound Vps24 and Vps20 Δ C proteins supplemented with Prescission protease. The His-Sumo tag was removed with Sumo protease and after cleavage the sample was incubated with fresh nickel to isolate Vps20. Following affinity purification, all proteins (1 mL) were applied to a S200 size exclusion column (GE Healthcare) equilibrated in either SAXS buffer (50 mM Tris (pH 8.0), 10 mM DTT, 100 mM NaCl) or ESCRT-II/Vps20 interaction buffer (50 mM Hepes (pH 7.6), 1 mM DTT, 100 mM NaCl). Samples for SAXS were dialyzed overnight into the SAXS buffer to ensure proper buffer

matching (Vps20 sample without salt was dialyzed into SAXS buffer without NaCl). For ESCRT-II/Vps20 interaction study both proteins were independently reran over the S200 size exclusion column along with a 1:2 molar ratio (ESCRT-II:Vps20). 1 mL fractions were collected for each run and analyzed by SDS-PAGE analysis. Densitometry of each band was used to calculate peak elution volumes. Stokes radii were determined as previously described (26). Light-scattering data were collected using a Wyatt mini-DAWN TREOS three-angle light scattering detector coupled to a high-resolution size-exclusion column. Data were collected at a flow rate of 0.5 mL/min and analyzed with the ASTRA software to determine molecular weight of protein (31).

Small angle X-ray scattering data collection

SAXS data were collected at the National Magnetic Resonance Facility at Madison (NMRFAM) using a Bruker Nanostar. The Bruker Nanostar had a wavelength of 1.54 Å with a sample-detector distance set to 67.7 cm resulting in a momentum transfer range of $0.01 < q < 0.40 \text{ \AA}^{-1}$. Data for SAXS buffer and protein were collected at 25°C for 2-4 hours. To account for excluded volume of the protein, buffer was subtracted. For optimal data, merged data sets were generated from two different concentrations using the lowest angles from one dataset and the highest angles from another. An overlapping region of at least 60 points was utilized for the merging process. This was conducted in accordance with the Primus analysis guide. Guinier analysis was conducted to determine the R_g value through the use of the Primus software package (ATSAS) (25,32). A comparison of concentrations was conducted to detect overall quality of data.

SAXS analysis and modeling

Processing of SAXS data was performed with Gnom software (ATSAS) (32) to determine the D_{\max} of the protein and the Porod volume. An approximate MW can be determined by using the Porod volume in the following equation: $MW = (\text{Porod volume} \times 1.2)/2$. Specifically, the Gnom software generates the pair distance distribution function (PDDF) for each sample, which describes the probability of finding two atoms a select distance apart. D_{\max} refers to the distance where the probability is zero to find two atoms said distance apart. This distance defines the maximum dimension and governs the overall shape of the SAXS envelope. The D_{\max} was adjusted (1-2 Å increments) until the following criteria were met: there was a smooth drop to zero probability at D_{\max} , agreement between the R_g from the Guiner transform and the R_g from the PDDF was achieved, and agreement between the experimental scatter data and the regularized scattering from the PDDF was reached. To avoid over-smoothing the regularization parameter, alpha, was kept below 5. The scattering amplitudes of the PDDF were used to calculate 15 replicate ab initio dummy atom models using DAMMIF (21). The DAMAVER program was used to determine an averaged model, which report a mean NSD value to describe the uniqueness of the overall model (33). Models generated from DAMAVER were superimposed with crystal structures (2GD5 and 3FRT) using the Supcomb20 algorithm (33).

ACKNOWLEDGEMENTS

We thank S. Butcher, J. Burke, B. Bhattacharyya for advice and helpful discussions, M. Anderson and J. Burke for technical assistance with the Bruker Nanostar, and members of the Audhya lab for critically reading this manuscript. This study made use of the National Magnetic Resonance Facility at Madison, which is supported by NIH grants P41RR02301 (BRTP/ NCRN) and P41GM66326 (NIGMS). Additional equipment was purchased with funds from the University of Wisconsin, the NIH (RR02781, RR08438), the NSF (DMB-8415048, OIA-9977486, BIR-9214394), and the USDA. The work was supported by the NIH (grant 1R01GM088151-01A1 to A.A.).

EXPERIMENTAL CONTRIBUTIONS

A.S. performed experiments.

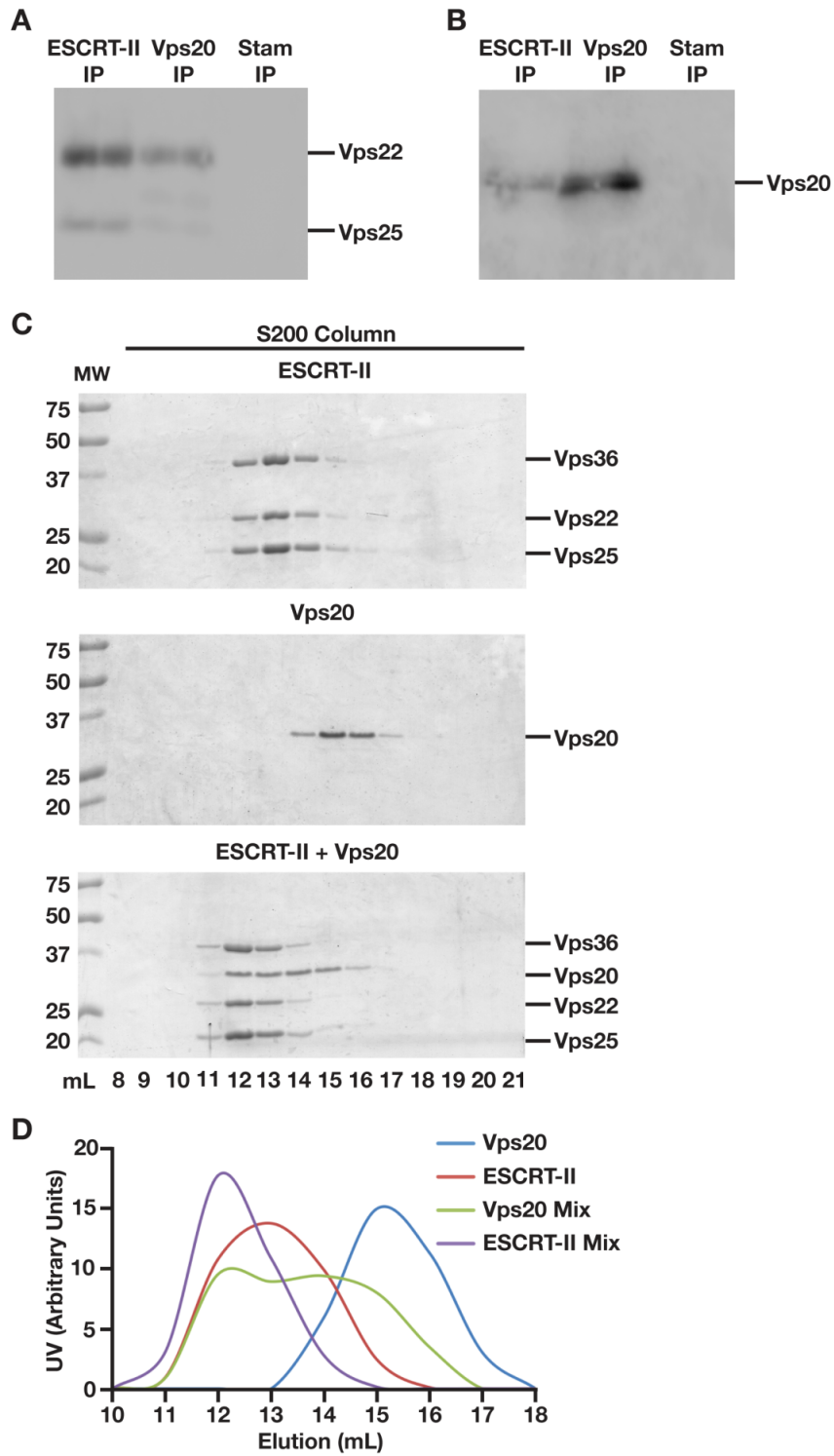


Figure 3.1: Vps20 and ESCRT-II interact in solution.

Figure 3.1: Vps20 and ESCRT-II interact in solution.

(**Figures 3.1A and 3.1B**) ESCRT-II, Vps20, and STAM were immunoprecipitated from *C. elegans* embryo extracts and blotted with an ESCRT-II antibody (**Figure 3.1A**) and a Vps20 antibody (**Figure 3.1B**). The STAM IP was conducted as negative control. (**Figure 3.1C**) ESCRT-II and Vps20 were initially purified using nickel affinity chromatography and subjected to size exclusion chromatography. ESCRT-II and Vps20 were mixed in a 1:2 molar ratio for one hour at 4° C, and this mix was also subjected to size exclusion chromatography. The peak fractions of each run were separated by SDS-PAGE and stained using Coomassie. (**Figure 3.1D**) A graphical representation of the densitometry measurements conducted on each gel shown in C. Based on this graph, peak elution volumes and Stokes radii were determined to be the following: 12.9 mL (4.9 nm) for ESCRT-II alone, 15.1 mL (3 nm) for Vps20 alone, 12.1 mL (5.6 nm) for ESCRT-II within mix, 12.2 and 14 mL (5.5 and 4 nm, respectively) for Vps20 within mix.

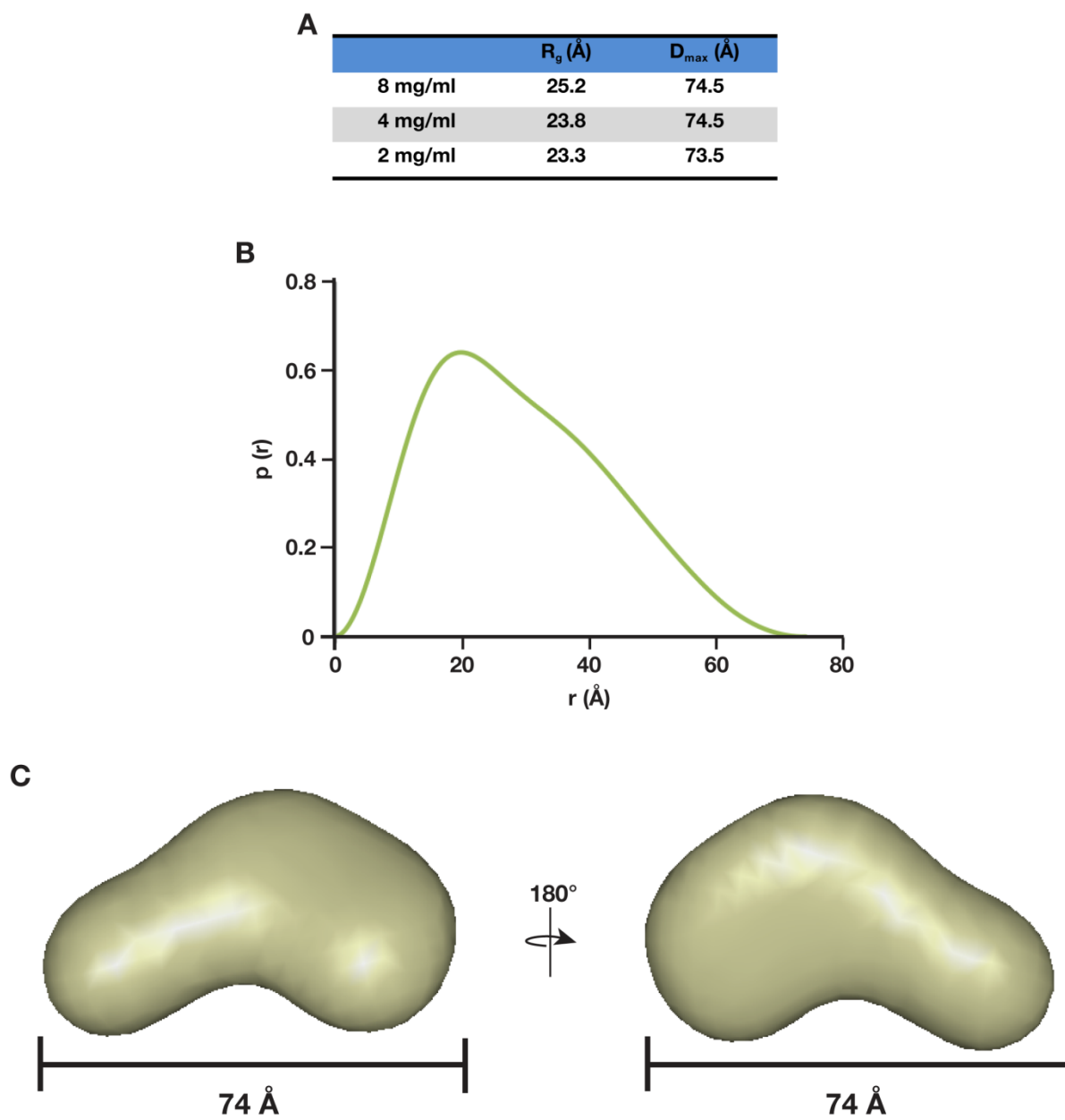


Figure 3.2: SAXS analysis of Vps24.

Figure 3.2: SAXS analysis of Vps24.

(**Figure 3.2A**) Shows the R_g and D_{max} values for the three concentrations of *C. elegans* Vps24 tested; 8 mg/mL, 4 mg/mL, and 2 mg/mL. (**Figure 3.2B**) Pair wise distance distribution function plot of the merge data set generated from 8mg/mL and 2mg/mL determined a D_{max} of 74 Å.

(**Figure 3.2C**) *Ab initio* structure of Vps24. Fifteen structures were generated using the program DAMMIF and averaged with DAMAVER, resulting in a NSD value of 0.67.

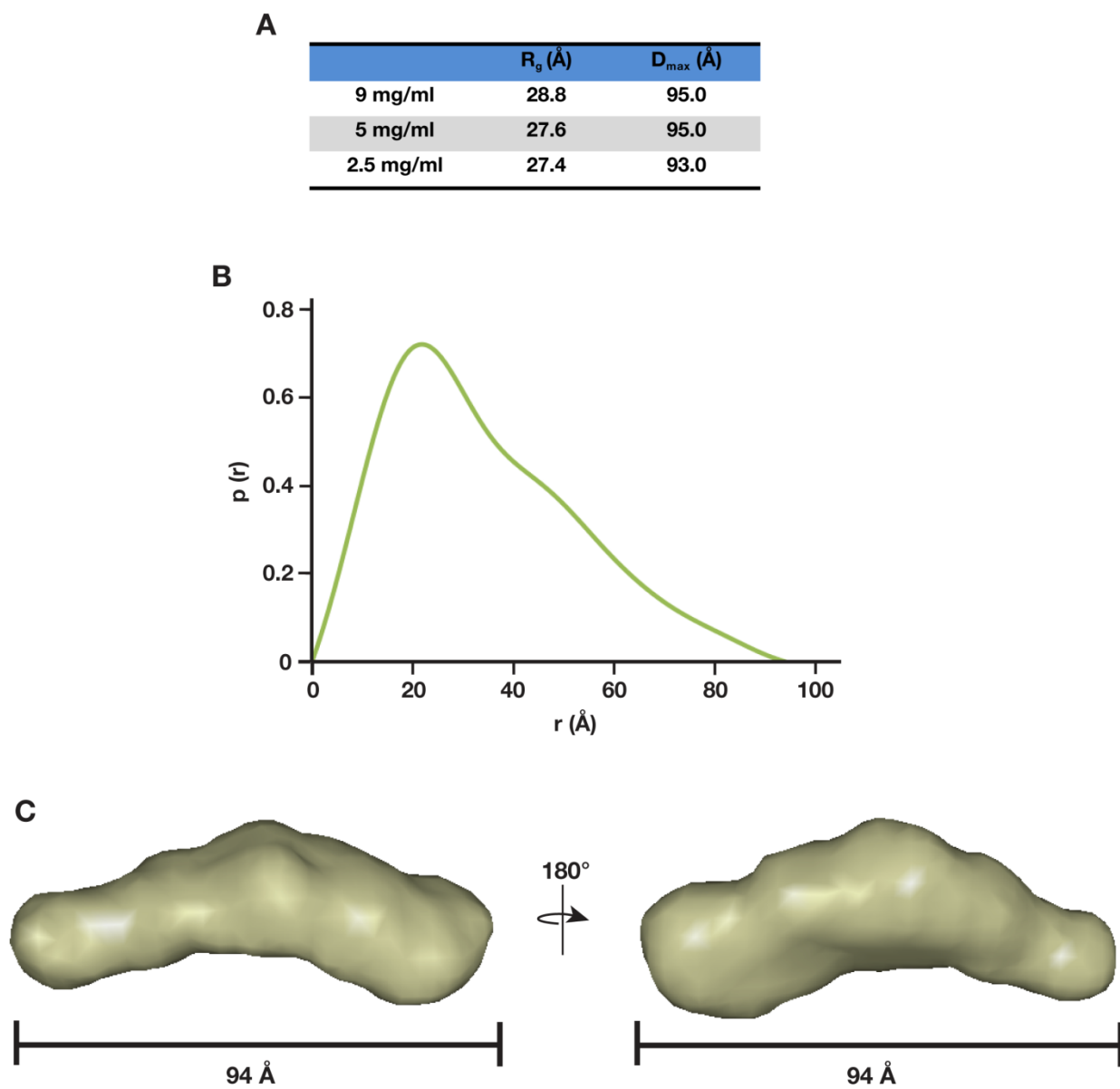


Figure 3.3: SAXS analysis of Vps20.

Figure 3.3: SAXS analysis of Vps20

(**Figure 3.3A**) Shows the R_g and D_{max} values for the three concentrations of *C. elegans* Vps20 tested; 9 mg/mL, 5 mg/mL, and 2.5 mg/mL. (**Figure 3.3B**) Pair wise distance distribution function plot of the merge data set generated from 5mg/mL and 2.5mg/mL determined a D_{max} of 94 Å. (**Figure 3.3C**) *Ab initio* structure of Vps20. Fifteen structures were generated using the program DAMMIF and averaged with DAMAVER, resulting in a NSD value of 0.69.

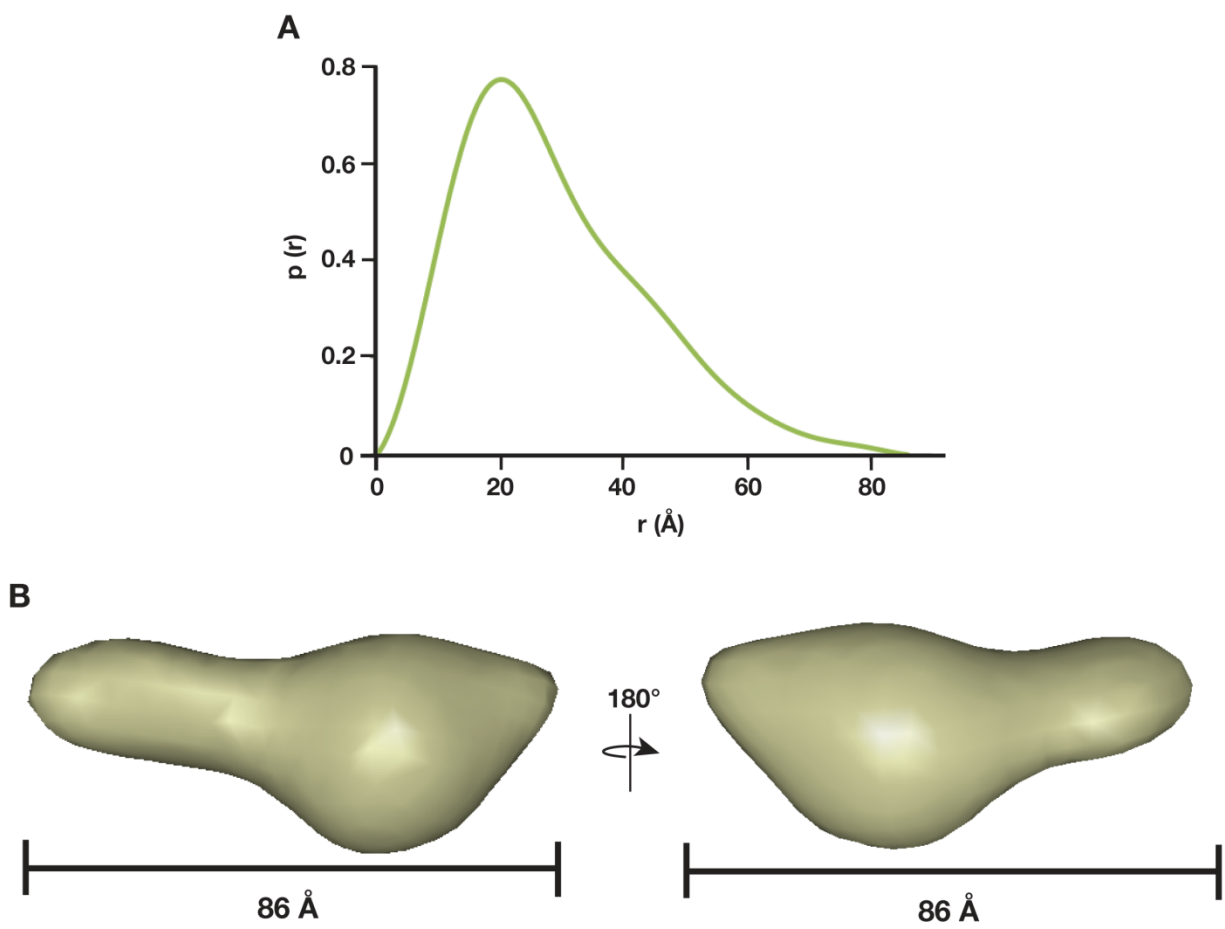


Figure 3.4: SAXS analysis of Vps20 Δ C.

Figure 3.4: SAXS analysis of Vps20 Δ C.

(**Figure 3.4A**) Pair wise distance distribution function plot generated from 9mg/mL Vps20 Δ C data determined a D_{\max} of 86 Å. (**Figure 3.4B**) *Ab initio* structure of Vps20 Δ C. Fifteen structures were generated using the program DAMMIF and averaged with DAMAVER, resulting in a NSD value of 0.77.

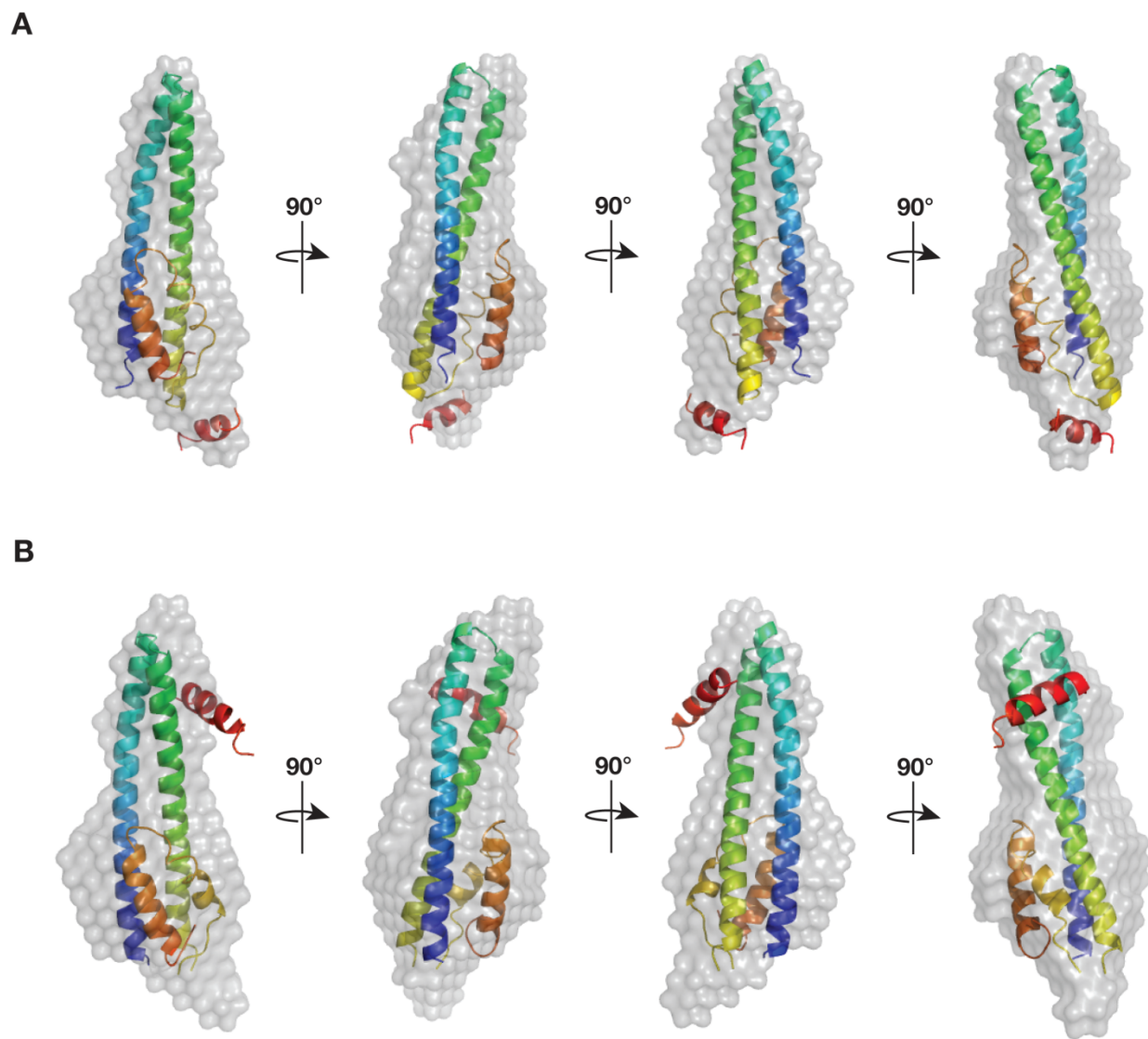


Figure 3.5: Overlay of open and closed crystal structures of hVps24 onto Vps20 Δ C SAXS envelope.

Figure 3.5: Overlay of open and closed crystal structures of hVps24 onto Vps20 Δ C SAXS envelope.

(Figure 3.5A) Supcomb20 program was used to align hVps24 structure (PDB: 2GD5 representing the open conformation) with the SAXS model for Vps20 Δ C. **(Figure 3.5B)**

Supcomb20 program was used to align hVps24 structure (PDB: 3FRT representing the closed conformation) with the SAXS model for Vps20 Δ C.

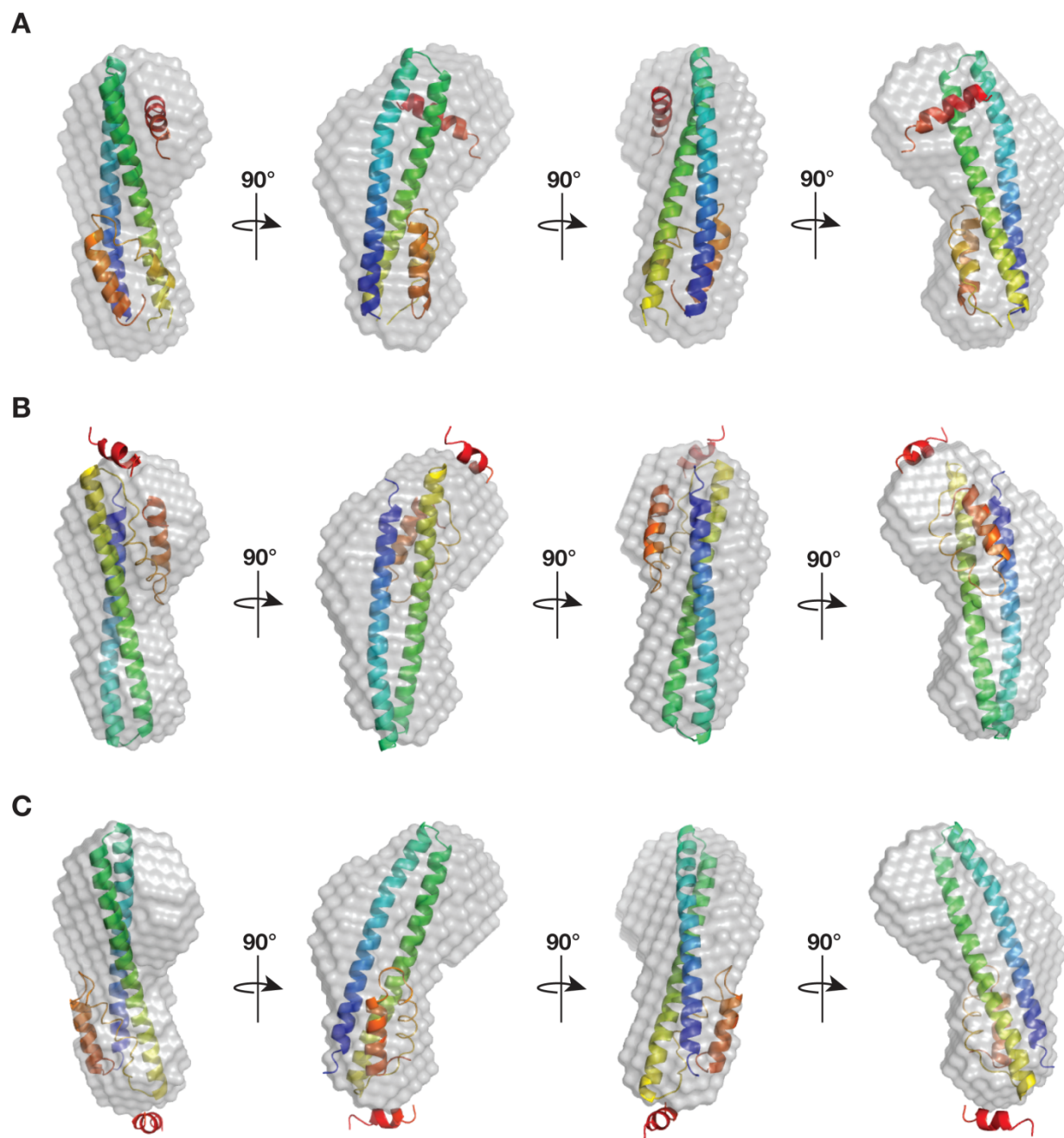


Figure 3.6: Overlay of open and closed crystal structures of hVps24 onto Vps24 SAXS envelope.

Figure 3.6: Overlay of open and closed crystal structures of hVps24 onto Vps24 SAXS envelope.

(**Figure 3.6A**) Supcomb20 program was used to align hVps24 structure (PDB: 3FRT representing the closed conformation) with the SAXS model for Vps24. (**Figure 3.6B**) Supcomb program was used to align hVps24 structure (PDB: 2GD5 representing the open conformation) with SAXS model for Vps24. (**Figure 3.6C**) Manual refinement of the hVps24 structure (PDB: 2GD5 representing the open conformation) was performed in an attempt to optimize alignment within the SAXS model for Vps24.

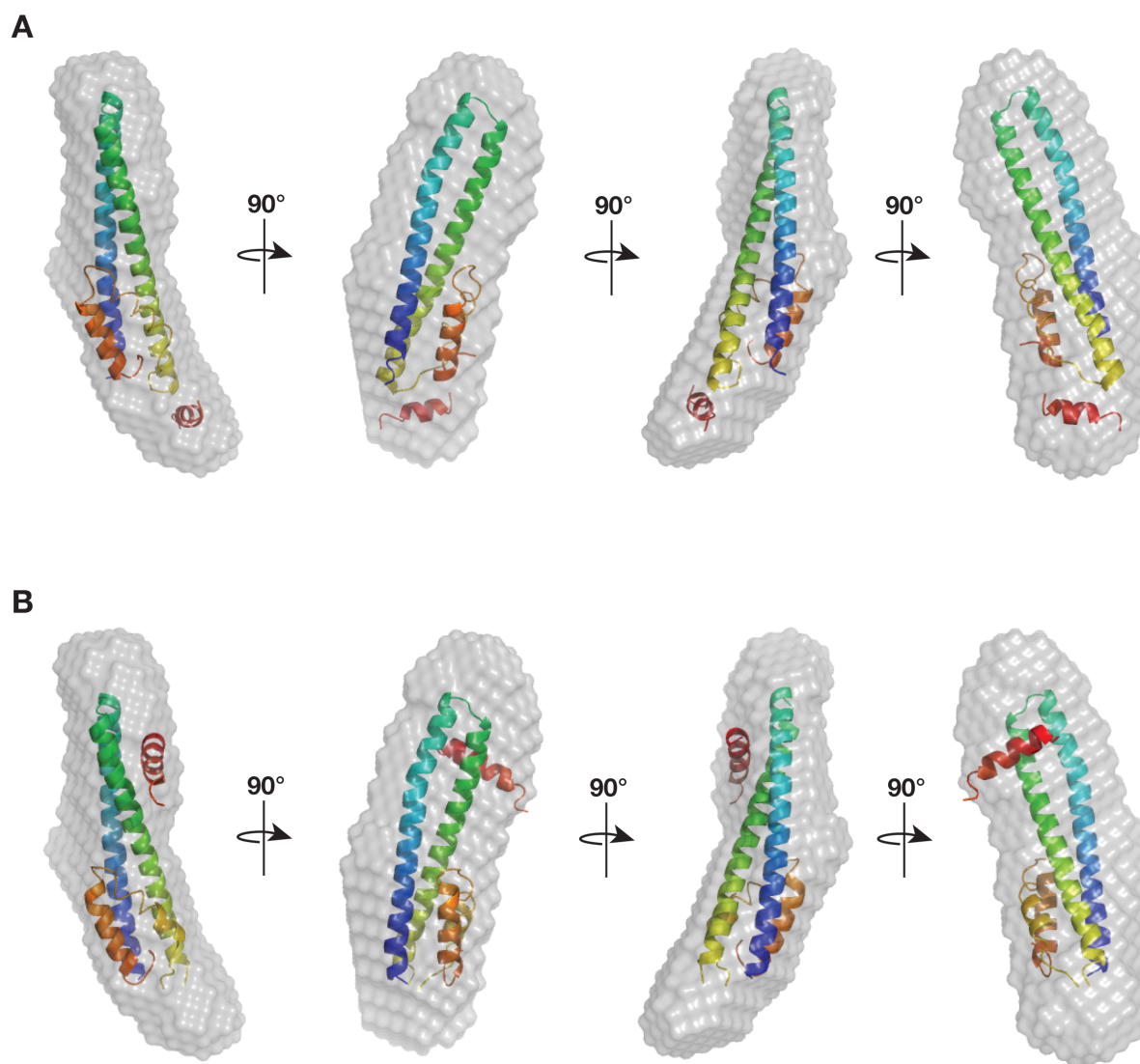


Figure 3.7: Overlay of open and closed crystal structures of hVps24 onto Vps20 SAXS envelope.

Figure 3.7: Overlay of open and closed crystal structures of hVps24 onto Vps20 SAXS envelope.

(**Figure 3.7A**) Supcomb20 program was used to align hVps24 structure (PDB: 2GD5 representing the open conformation) with the SAXS model for Vps20. (**Figure 3.7B**)

Supcomb20 program was used to align hVps24 structure (PDB: 3FRT representing the closed conformation) with the SAXS model for Vps20.

Protein	% Sequence Coverage	Predicted Size (kD)
Vps-22 (C27F2.5)	59.1	30.3
Vps-25 (W02A11.2)	72.1	21.5
Vps-36 (F17C11.8)	77.4	42.7
Vps20 (Y65B4A.3)	43.4	24.1

Table 3.S1: Identification of ESCRT-II interacting partners using immunoprecipitation followed by solution mass spectrometry.

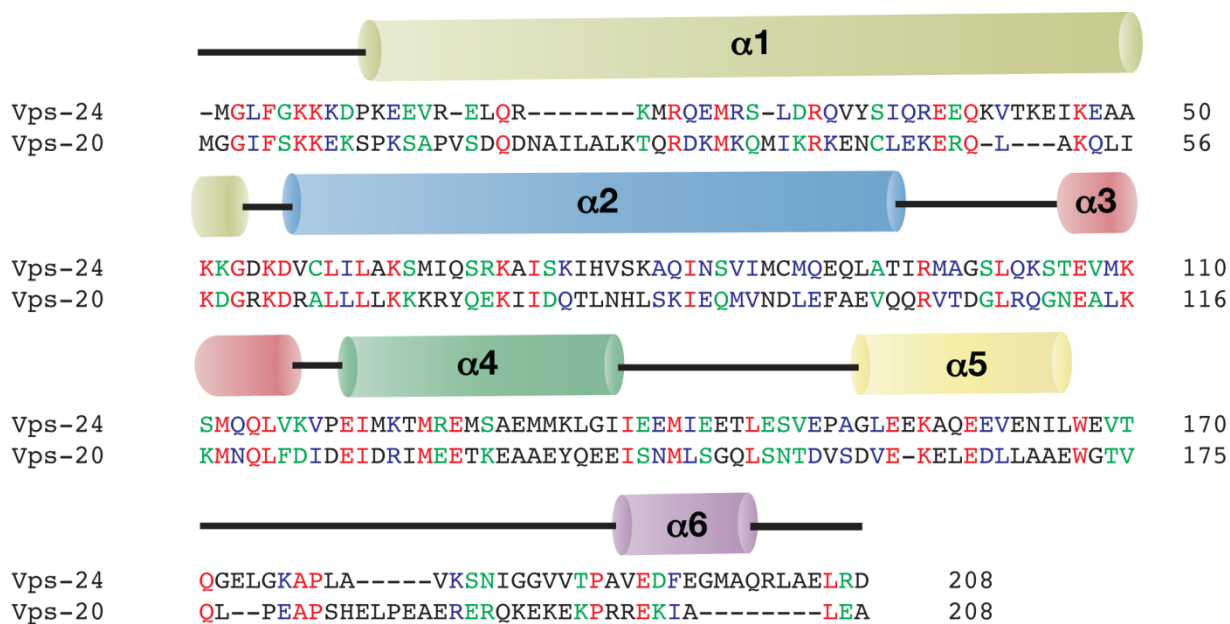


Figure 3.S1: Sequence alignment of *C. elegans* Vps24 and Vps20

Figure 3.S1: Sequence alignment of *C. elegans* Vps24 and Vps20

Sequence alignment of *C. elegans* Vps24 and Vps20 was performed with Clustal Omega alignment program (34). Red indicates positions with fully conserved residues, blue indicates positions with strongly similar properties, green indicates positions with weakly similar properties, and black indicates positions with no similarities. Alpha-helical domain placements are based on the secondary structure predictions made by the software PELE.

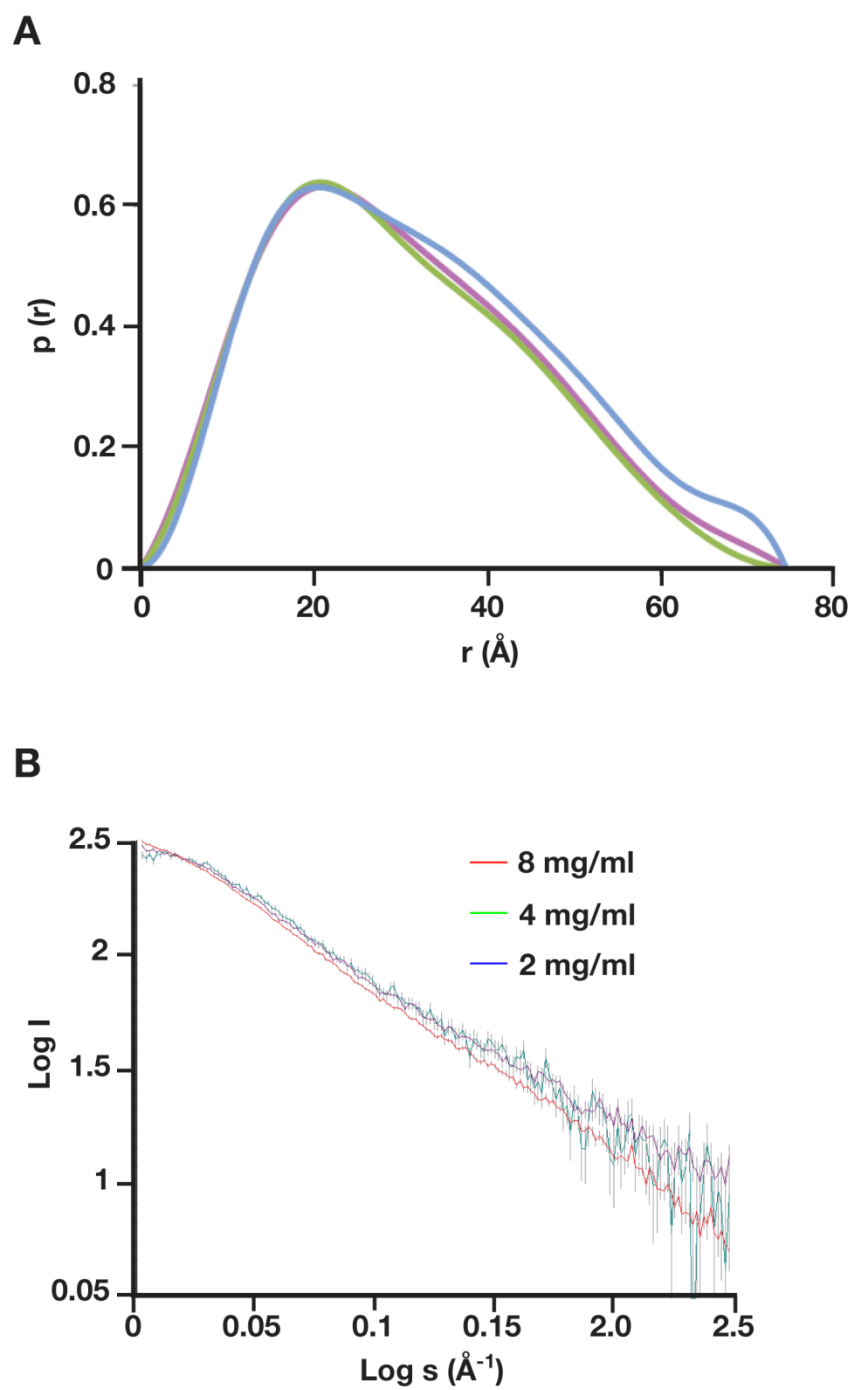


Figure 3.S2: Concentration comparison for Vps24.

Figure 3.S2: Concentration comparison for Vps24.

(**Figure 3.S2A**) Pair distance distribution function plot comparing the three concentrations of Vps24 used in SAXS experiments (8,4 and 2 mg/mL). (**Figure 3.S2B**) Log of scattered intensity vs. log of s is shown across the three concentrations of Vps24 used in SAXS experiments (8,4 and 2mg/mL). S is defined as: $s = 4\pi\sin(\theta)/\lambda$ (λ = wavelength and 2θ = scattering angle).

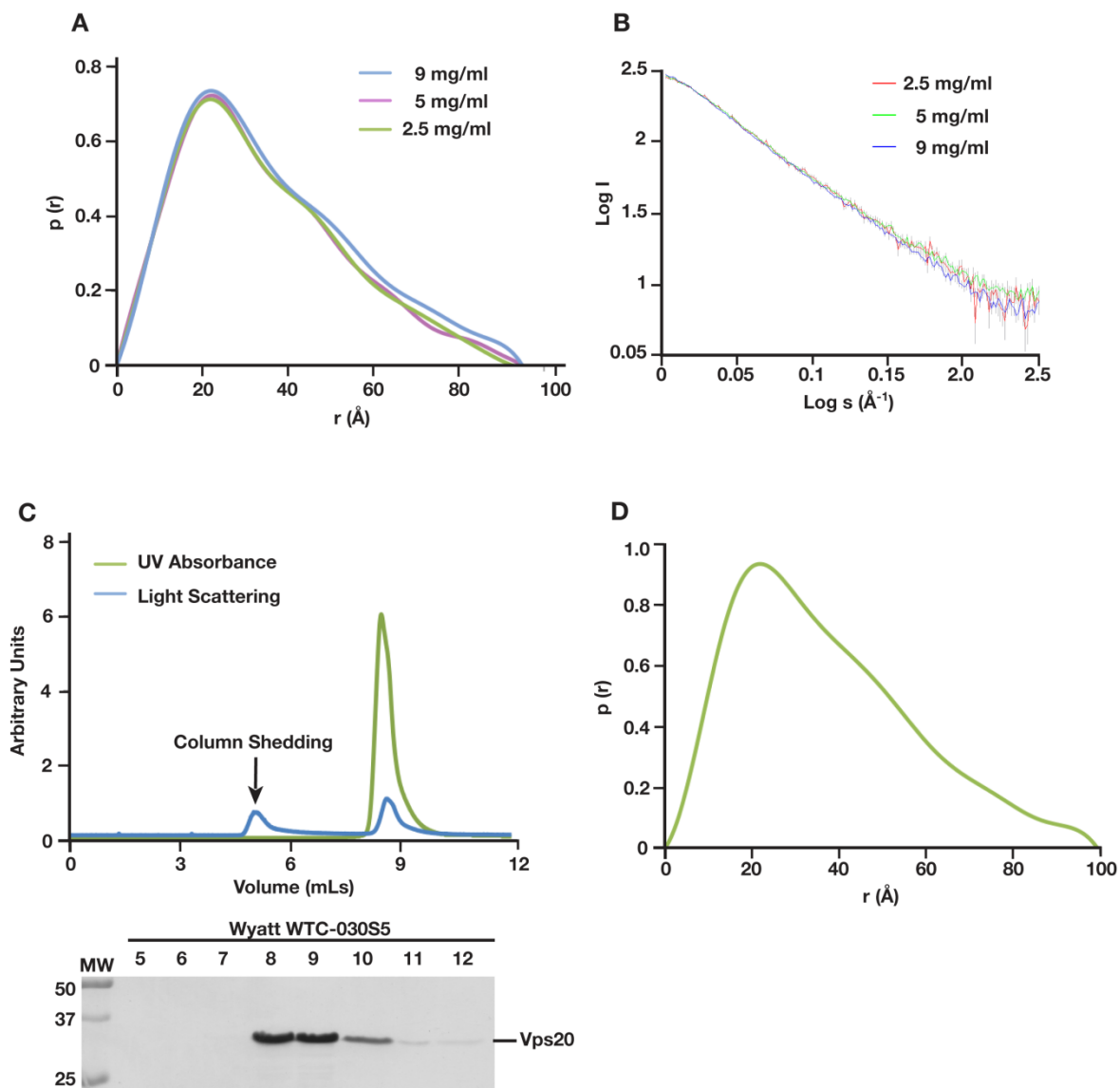


Figure 3.S3: Concentration comparison for Vps20.

Figure 3.S3: Concentration comparison for Vps20.

(**Figure 3.S3A**) Pair distance distribution function plot comparing the three concentrations of Vps20 used in SAXS experiments (9,5 and 2.5 mg/mL). (**Figure 3.S3B**) Log of scattered intensity vs. log of s is shown across the three concentrations of Vps20 used in SAXS experiments (9,5 and 2.5mg/mL). S is defined as: $s = 4\pi\sin(\theta)/\lambda$ (λ = wavelength and 2θ = scattering angle). (**Figure 3.S3C**) Vps20 was purified and examined by light scattering following size-exclusion chromatography. (**Figure 3.S3D**) Pair distance distribution function plot for Vps20 in SAXS buffer without salt at a concentration of 6mg/mL. D_{\max} was determined to be 99.5 Å.

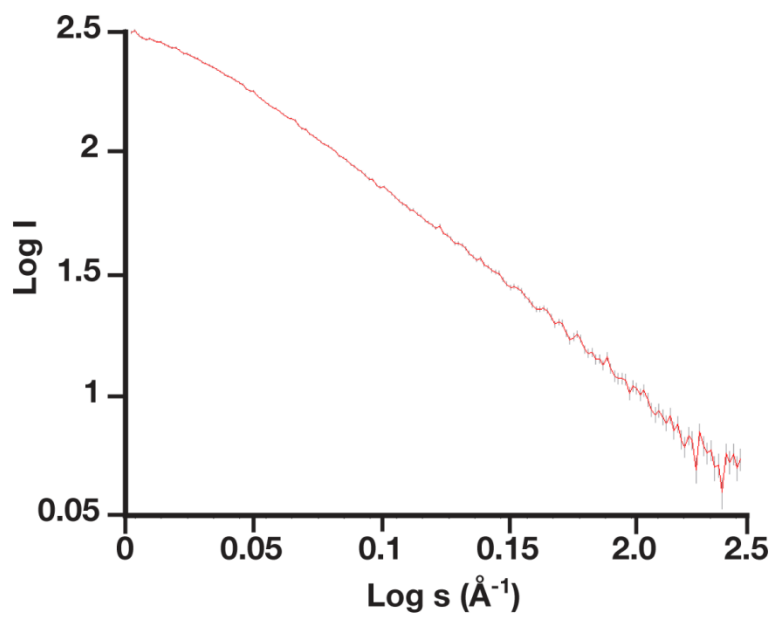


Figure 3.S4: Raw data for Vps20ΔC.

Figure 3.S4: Raw data for Vps20ΔC.

Log of scattered intensity vs. log of s is shown for Vps20ΔC used in a SAXS experiment (9 mg/mL). S is defined as: $s = 4\pi\sin(\theta)/\lambda$ (λ = wavelength and 2θ = scattering angle).

REFERENCES

1. Williams, R. L., and Urbé, S. (2007) The emerging shape of the ESCRT machinery. *Nat Rev Mol Cell Biol* **8**, 355-368
2. Saksena, S., and Emr, S. D. (2009) ESCRTs and human disease. *Biochem Soc Trans* **37**, 167-172
3. Raiborg, C., and Stenmark, H. (2009) The ESCRT machinery in endosomal sorting of ubiquitylated membrane proteins. *Nature* **458**, 445-452
4. Katzmann, D. J., Odorizzi, G., and Emr, S. D. (2002) Receptor downregulation and multivesicular-body sorting. *Nat Rev Mol Cell Biol* **3**, 893-905
5. Carlton, J. G., and Martin-Serrano, J. (2007) Parallels between cytokinesis and retroviral budding: a role for the ESCRT machinery. *Science* **316**, 1908-1912
6. Martin-Serrano, J., and Neil, S. J. (2011) Host factors involved in retroviral budding and release. *Nat Rev Microbiol* **9**, 519-531
7. Henne, W. M., Buchkovich, N. J., and Emr, S. D. (2011) The ESCRT pathway. *Dev Cell* **21**, 77-91
8. Wollert, T., and Hurley, J. H. (2010) Molecular mechanism of multivesicular body biogenesis by ESCRT complexes. *Nature* **464**, 864-869
9. Babst, M., Katzmann, D. J., Estepa-Sabal, E. J., Meerloo, T., and Emr, S. D. (2002) Escrt-III: an endosome-associated heterooligomeric protein complex required for mvb sorting. *Dev Cell* **3**, 271-282
10. Teis, D., Saksena, S., and Emr, S. D. (2008) Ordered assembly of the ESCRT-III complex on endosomes is required to sequester cargo during MVB formation. *Dev Cell* **15**, 578-589
11. Teis, D., Saksena, S., Judson, B. L., and Emr, S. D. (2010) ESCRT-II coordinates the assembly of ESCRT-III filaments for cargo sorting and multivesicular body vesicle formation. *EMBO J* **29**, 871-883
12. Saksena, S., Wahlman, J., Teis, D., Johnson, A. E., and Emr, S. D. (2009) Functional reconstitution of ESCRT-III assembly and disassembly. *Cell* **136**, 97-109
13. Fyfe, I., Schuh, A. L., Edwardson, J. M., and Audhya, A. (2011) Association of the endosomal sorting complex ESCRT-II with the Vps20 subunit of ESCRT-III generates a curvature-sensitive complex capable of nucleating ESCRT-III filaments. *J Biol Chem* **286**, 34262-34270

14. Muzioł, T., Pineda-Molina, E., Ravelli, R. B., Zamborlini, A., Usami, Y., Göttlinger, H., and Weissenhorn, W. (2006) Structural basis for budding by the ESCRT-III factor CHMP3. *Dev Cell* **10**, 821-830
15. Lin, Y., Kimpler, L. A., Naismith, T. V., Lauer, J. M., and Hanson, P. I. (2005) Interaction of the mammalian endosomal sorting complex required for transport (ESCRT) III protein hSnf7-1 with itself, membranes, and the AAA+ ATPase SKD1. *J Biol Chem* **280**, 12799-12809
16. Zamborlini, A., Usami, Y., Radoshitzky, S. R., Popova, E., Palu, G., and Göttlinger, H. (2006) Release of autoinhibition converts ESCRT-III components into potent inhibitors of HIV-1 budding. *Proc Natl Acad Sci U S A* **103**, 19140-19145
17. Lata, S., Roessle, M., Solomons, J., Jamin, M., Gottlinger, H. G., Svergun, D. I., and Weissenhorn, W. (2008) Structural basis for autoinhibition of ESCRT-III CHMP3. *J Mol Biol* **378**, 818-827
18. Henne, W. M., Buchkovich, N. J., Zhao, Y., and Emr, S. D. (2012) The endosomal sorting complex ESCRT-II mediates the assembly and architecture of ESCRT-III helices. *Cell* **151**, 356-371
19. Bajorek, M., Schubert, H. L., McCullough, J., Langelier, C., Eckert, D. M., Stubblefield, W. M., Uter, N. T., Myszka, D. G., Hill, C. P., and Sundquist, W. I. (2009) Structural basis for ESCRT-III protein autoinhibition. *Nat Struct Mol Biol* **16**, 754-762
20. Im, Y. J., Wollert, T., Boura, E., and Hurley, J. H. (2009) Structure and function of the ESCRT-II-III interface in multivesicular body biogenesis. *Dev Cell* **17**, 234-243
21. Franke, D., and Svergun, D. I. (2009) DAMMIF, a program for rapid ab-initio shape determination in small-angle scattering. *Journal of Applied Crystallography* **42**, 342-346
22. Volkov, V. V., and Svergun, D. I. (2003) Uniqueness of ab initio shape determination in small-angle scattering. *Journal of Applied Crystallography* **36**, 860-864
23. Pires, R., Hartlieb, B., Signor, L., Schoehn, G., Lata, S., Roessle, M., Moriscot, C., Popov, S., Hinz, A., Jamin, M., Boyer, V., Sadoul, R., Forest, E., Svergun, D. I., Göttlinger, H. G., and Weissenhorn, W. (2009) A crescent-shaped ALIX dimer targets ESCRT-III CHMP4 filaments. *Structure* **17**, 843-856
24. Fabrikant, G., Lata, S., Riches, J. D., Briggs, J. A., Weissenhorn, W., and Kozlov, M. M. (2009) Computational model of membrane fission catalyzed by ESCRT-III. *PLoS Comput Biol* **5**, e1000575
25. Putnam, C. D., Hammel, M., Hura, G. L., and Tainer, J. A. (2007) X-ray solution scattering (SAXS) combined with crystallography and computation: defining accurate

- macromolecular structures, conformations and assemblies in solution. *Q Rev Biophys* **40**, 191-285
26. Witte, K., Schuh, A. L., Hegermann, J., Sarkeshik, A., Mayers, J. R., Schwarze, K., Yates, J. R., Eimer, S., and Audhya, A. (2011) TFG-1 function in protein secretion and oncogenesis. *Nat Cell Biol* **13**, 550-558
 27. Eng, J., McCormack, A., and Yates, J. (1994) An approach to correlate tandem mass spectral data of peptides with amino acid sequences in a protein database. *Journal of the American Society for Mass Spectrometry* **5**, 976-989
 28. Xu, T., Venable, J. D., Park, S. K., Cociorva, D., Lu, B., Liao, L., Wohlschlegel, J., Hewel, J., and Yates Iii, J. R. ProLuCID, a fast and sensitive tandem mass spectra-based protein identification program. 10 Ed., AMER SOC BIOCHEMISTRY MOLECULAR BIOLOGY INC 9650 ROCKVILLE PIKE, BETHESDA, MD 20814-3996 USA
 29. Cheeseman, I. M., Niessen, S., Anderson, S., Hyndman, F., Yates, J. R., Oegema, K., and Desai, A. (2004) A conserved protein network controls assembly of the outer kinetochore and its ability to sustain tension. *Genes Dev* **18**, 2255-2268
 30. Tan, S. (2001) A modular polycistronic expression system for overexpressing protein complexes in Escherichia coli. *Protein Expr Purif* **21**, 224-234
 31. Wyatt, P. J. (1993) LIGHT-SCATTERING AND THE ABSOLUTE CHARACTERIZATION OF MACROMOLECULES. *Analytica Chimica Acta* **272**, 1-40
 32. Konarev, P. V., Volkov, V. V., Sokolova, A. V., Koch, M. H. J., and Svergun, D. I. (2003) PRIMUS: a Windows PC-based system for small-angle scattering data analysis. *J Appl Crystallogr* **36**, 1277-1282
 33. Volkov, V. V. a. S., D.I. (2003) Uniqueness of ab-initio shape determination in small-angle scattering. *J Appl Crystallogr* **36**, 860-864
 34. Sievers, F., Wilm, A., Dineen, D., Gibson, T. J., Karplus, K., Li, W., Lopez, R., McWilliam, H., Remmert, M., Söding, J., Thompson, J. D., and Higgins, D. G. (2011) Fast, scalable generation of high-quality protein multiple sequence alignments using Clustal Omega. *Mol Syst Biol* **7**, 539

Chapter 4

Mechanisms of ESCRT-III Spiral Filament Assembly

This chapter represents a manuscript in preparation for publication:

Qing-Tao Shen, Amber L. Schuh, Yuqing Zheng, Julie C. Mitchell, Marisa S. Otegui, Paul Ahlquist, Qiang Cui, and Anjon Audhya

ABSTRACT

The scission of biological membranes is facilitated by a variety of protein complexes that bind and manipulate lipid bilayers. Helical ESCRT-III (endosomal sorting complex required for transport-III) filaments have been proposed to mediate membrane scission during the ostensibly disparate processes of multivesicular endosome biogenesis, cytokinesis, and retroviral budding. However, the mechanisms by which ESCRT-III subunits assemble into a polymer remain unknown. Using cryogenic electron microscopy (cryo-EM), we found that the full-length ESCRT-III subunit Vps32/CHMP4 spontaneously forms single-stranded, spiral filaments in vitreous ice. The resolution afforded by cryo-EM combined with molecular dynamics simulations revealed that individual Vps32/CHMP4 monomers within a filament are flexible and able to accommodate a range of bending angles. By contrast, the interface between monomers is stable and refractory to changes in conformation. We additionally found that the carboxyl-terminus of Vps32/CHMP4 plays a key role in restricting the lateral association of filaments. Taken together, our findings highlight new mechanisms by which ESCRT-III filaments assemble to generate a unique polymer capable of membrane remodeling in multiple cellular contexts.

INTRODUCTION

Membrane bending and fission are required for numerous biological processes including organelle biogenesis, the formation of vesicular transport carriers, and cellular division (1,2). Components of the ESCRT (endosomal complex required for transport) machinery facilitate scission events in cases where membrane budding is oriented away from the cytoplasm (3). Specifically, ESCRT-III polymers have been implicated directly in the topological transition necessary for bilayers to rupture and reseal (4,5). *In vivo*, membrane associated ESCRT-III has been suggested to be composed primarily of polymerized Vps32 (also known as CHMP4 in mammals) subunits, which are nucleated by a complex of ESCRT-II and Vps20/CHMP6 at multivesicular endosomes and through undefined mechanisms during abscission and viral budding (6-8). Structures of Vps32 filaments have shown them to resemble rings and circular arrays *in vitro* and *in vivo* (8-11). However, the limited resolution of these structures has not guided the field toward a potential assembly pathway. Our goal was to identify mechanisms by which ESCRT polymers adopt their spiral-like conformation using a combination of electron microscopy (EM)-based approaches and molecular dynamics.

RESULTS and DISCUSSION

We first identified a full-length isoform of Vps32 that was amenable to homopolymerization *in vitro*, without prerequisite truncations or mutations. In contrast to orthologues examined previously (**Figure 4.S1**), we found that recombinant *C. elegans* Vps32 formed both monomers and oligomers in solution at low concentration (**Figure 4.S2**). Examination by negative staining EM revealed the presence of ring-like structures and circular arrays, as observed previously (**Figures 4.S3A and 4.S3B**) (8-11). However, in contrast to prior work, all polymers exhibited a thickness of ~4 nm, indicating that Vps32 assembles only as individual filaments and fails to associate laterally (**Figures 4.S3D**). Although filament assembly occurred in a concentration-independent manner, their conformations varied from predominantly ring-like assemblies at 1 μ M to mostly spirals at concentrations above 10 μ M (**Figures 4.S3 E and 4.S3F**).

Although facile and rapid, negative staining procedures involve the deposition of heavy atoms and sometimes include a desiccation step (11), which can result in artifacts, including structural rearrangements (12). Moreover, the presence of stain impedes high-resolution structure determination. To circumvent these issues, we quickly froze Vps32 and examined it using a low electron-dose EM imaging mode. Under these more native conditions, we found that Vps32 formed mostly spirals, irrespective of concentration, and only rarely were ring-like structures observed (**Figures 4.1A and 4.S4A-C**). Additionally, the width of filaments was highly uniform, exhibiting a thickness of 4.2 nm (**Figure 4.1B**), similar to that observed *in situ* for overexpressed human Vps32 following quick-freeze deep-etch EM (9). Given that the helical core domains of ESCRT-III monomers are ~3-4 nm wide, as determined previously by crystallographic studies (13,14), our results demonstrate that Vps32 subunits assemble in a head-

to-tail manner with partial overlap to generate single-stranded filaments that do not self-associate.

In contrast to their homogenous widths, the lengths of Vps32 filaments varied, averaging ~110 nm for ring-like structures to ~1.6 μm for spirals (**Figure 4.S5**). To determine the size of repeating units within each filament, we used a fast Fourier transform (FFT) algorithm. Our analysis revealed a clear layer line at 3.2 nm (**Figure 4.1B**). Based on these data, the largest filaments observed (~2.5 μm) harbor approximately 800 repeating units. These data suggest that Vps32 polymerization is highly cooperative and highlight a key distinction between it and other ESCRT-III subunits, which fail to oligomerize at similarly low concentrations (10).

We also found that the spirals were intrinsically limited in their upper and lower diameters. Instead of growing beyond a certain size (~150 nm in diameter), spirals appeared to alter their trajectories when reaching a maximal radius, leading to the generation of paired circular arrays (**Figures 4.1C and 4.S4B**). At a minimal radius, filament assembly was halted. These findings indicate that Vps32 polymers spontaneously self-assemble only within a specific range of curvatures.

To improve resolution of Vps32 filaments, we treated paired spirals as single particles and generated two-dimensional class averages. Individual filaments, composed of one clockwise spiral and one counterclockwise spiral, were segmented using successive boxed areas with 90% overlap, following filament trajectory (**Figure 4.S6**). Results from this analysis revealed the presence of distinct densities separated by narrow linkers (**Figure 4.2A**). The distance between the centers of each density was 3.2 nm, in agreement with our FFT analysis. Importantly, we found that the individual densities were not typically arrayed in a linear fashion, but instead

exhibited curvature. By overlaying multiple highly represented class averages, we found that the bent region corresponds to the linker between densities (**Figure 4.2A**).

We used our class-averaged map to build an isosurface profile, and docked onto it previously solved structures for CHMP3 (helices $\alpha 1$ - $\alpha 4$), a pseudo-atomic model of Vps32 based on CHMP3 and another crystal structure of CHMP4B/Vps32 (helices $\alpha 1$ and $\alpha 2$) (**Figures 4.2B, 4.S7 and 4.S8**) (14,15). In both cases, only one orientation was compatible, in which a single ESCRT-III monomer spanned a pair of EM densities (**Figure 4.S9**). The dimer interface consisted of the extended helical hairpin loop from one monomer and the asymmetric 4-helix bundle from another, which filled the large EM densities (**Figure 4.S10**). Molecular dynamics simulations further confirmed the stability of this architecture and indicated that the interface between monomers is stable and unlikely to tolerate dynamic changes in organization (**Figures 4.2C**). In contrast, the flexible linkers between densities contained the tightly packed central portions of helices $\alpha 1$ and $\alpha 2$. Collectively, our data suggest that the helical hairpin of Vps32 must be pliable to accommodate changes in filament curvature during assembly.

To investigate Vps32 flexibility, we conducted molecular dynamics simulations on its helical core and helices $\alpha 1$ - $\alpha 4$ of CHMP3 (**Figure 4.S8**) (14,15). Our studies demonstrated that helices $\alpha 1$ and $\alpha 2$ bend extensively in a single plane near their center, which we refer to as the hinge region, with angles ranging from 0° - 25° (**Figures 4.3A and 4.S11**). To characterize the free energy distribution for these conformations, we calculated the potential of mean force (PMF) as a function of the bending angle in explicit solvent. This analysis revealed a free energy minimum at an angle of 9° , relative to the published crystal structures (**Figure 4.3B**). Based on our analysis of vitrified Vps32 spirals, we found that the bending angle between monomers

averaged $9.4 \pm 0.7^\circ$ at their center, consistent with reaching a minimal free energy state (**Figures 4.3C and 4.3D**). By contrast, the outer portion of the spirals exhibited an average bending angle of $3.8 \pm 0.8^\circ$, which corresponds to an elevated energy state (**Figure 4.3D**).

To directly test the importance of the helical hairpin ‘hinge’ in spiral assembly, we used MD simulations to identify mutations within this region that are predicted to impair bending. We focused our attention on a specific valine residue (V44) and found that substitution with tryptophan at this position rigidified the hairpin (**Figures 4.S12A and 4.S12B**). Purified Vps32^{V44W} behaved identically to the wild-type protein in hydrodynamic studies (**Figure 4.S12C**). However, upon analysis using negative staining EM, we found that spiral arrays and ring structures no longer assembled. Instead, Vps32^{V44W} formed more linear filaments, consistent with a critical role for the hinge region in mediating spiral assembly (**Figure 4.S12D**).

Although thermodynamic parameters predict that the hinge region should maintain a bending angle close to 9° , the spirals of wild-type Vps32 are not tightly packed. Instead, filaments are consistently separated from one another (on average 6.84 ± 2.16 nm from their centers), suggesting the presence of a steric barrier that restricts lateral interactions (**Figures 4.4A and 4.S13**). Based on our EM density map, it is difficult to place the carboxyl-terminal helices ($\alpha 5$ and $\alpha 6$) of Vps32 within the polymer. Instead, we regularly observe weak densities that extend away from the filament, suggesting the presence of an additional flexible region within Vps32 monomers that could act as a spacer (**Figure 4.2A**). Although deletion of helices $\alpha 5$ and $\alpha 6$ leads to protein aggregation, an isoform of Vps32 lacking $\alpha 6$ alone exhibited similar hydrodynamic properties as the wild-type protein (**Figure 4.S14A**). When examined by negative staining EM or cryo-EM, the truncated protein continued to form ring structures and spirals

(**Figures 4.S14B and 4.S14C**). However, spacing between filaments within the spirals was reduced to 4.81 ± 1.29 nm, indicating that the carboxyl-terminus of Vps32 plays an important role in preventing lateral associations between individual single-stranded polymers (**Figure 4.4B**).

Although all ESCRT-III subunits are predicted to share a similar overall structure (16,17), their lack of redundancy indicates that they operate by distinct mechanisms. During multivesicular endosome biogenesis, the ESCRT-III subunit Vps20, together with ESCRT-II, appears to function as a recruitment factor to facilitate Vps32 polymerization specifically at regions of elevated membrane curvature (e.g. nascent vesicle bud necks; (7)). By contrast, alternative regulators of Vps32 spatial distribution must operate during cytokinetic abscission and the retroviral budding, as Vps20 is largely dispensable for these events (13,18,19). Our findings provide mechanisms by which circular arrays of Vps32 form, irrespective of their site of action. Additionally, we demonstrate that an inherent property of these spirals is their ability to harness free energy during formation. We propose that the coordinated release of this free energy, together with the independent actions of downstream ESCRT-III subunits and potentially the Vps4 AAA ATPase (20-22), promotes membrane constriction, which ultimately facilitates scission (**Figure 4.S15**).

MATERIALS AND METHODS

Protein Sequence Alignment

Protein sequences including *C. elegans* Vps32 (NP_495337.1), *S. cerevisiae* Snf7p (NP_013125.1), *H. sapiens* CHMP4A (NP_054888.2), *H. sapiens* CHMP4B (NP_789782.1), *H. sapiens* CHMP4C (NP_689497.1), *A. thaliana* Vps32.2 (NP_001078468.1) and *H. sapiens* CHMP3 (NP_057163.1) were downloaded from PubMed in FASTA format. COBALT was used to align the sequences (23).

Protein Purification

Recombinant protein expression was performed using BL21-T1R (DE3) *E. coli*. Wild-type and mutant isoforms of *C. elegans* Vps32 were cloned into pGEX6P-1, which encodes a cleavable, amino-terminal GST tag. Initial purifications from bacterial extracts were conducted using glutathione agarose beads. Bound proteins were supplemented with Prescission protease to remove the tag, and eluted Vps32 isoforms were applied to a S200 size exclusion column equilibrated in cryo-EM buffer (50 mM Hepes (pH 7.6), 100 mM NaCl, and 1 mM DTT). 1 mL fractions were collected, and the Stokes radius of each protein or protein complex was calculated from its elution volume based on the elution profiles of characterized globular standards. To determine the sedimentation values for each fraction eluted from the S200 column, samples were applied to 4 mL glycerol gradients (10-30%), which were fractionated by hand (200 μ L each). Sedimentation values were calculated by comparing the position of the peak with that of characterized standards run on a separate gradient in parallel.

Electron Microscopy

Wild-type and mutant isoforms of Vps32 (3 μ L) were negatively stained using a 1% (wt/vol) uranyl formate solution on glow-discharged continuous carbon coated copper grids (25 mA for 120 s; PELCO easiGlowTM) or directly frozen on Quantifoil grids (25 mA for 120 s; PELCO easiGlowTM) using a vitrification device (Vitrobot Mark IV; FEI). Both negatively stained and vitrified samples were examined under an electron microscope (Tecnai G2 F30; FEI) with a field emission gun operated at 300 kV and recorded on a charge-coupled device (CCD) camera (UltraScan1000XP, 2k x 2k; Gatan). The negatively stained samples were captured at magnifications of 23,000x, 39,000x or 59,000x. The frozen hydrated samples were examined in low-dose mode to avoid irradiation damage. Magnifications were set at 39,000x or 59,000x, with final pixel sizes of 2.8 \AA or 1.8 \AA , respectively. The defocus ranged from -2 μ m to -5 μ m. Cryo-EM images were selected for further trajectory and 2D class average analysis. A subset of negatively stained Vps32 samples were examined using electron tomography. Samples were placed on an FEI Tomography holder with maximum tilt angles of +/- 60°. Data were collected using FEI Xplore 3D software at a magnification of 59,000x, with the defocus set at -3 μ m. Tilting step sizes were set at 4° between 0° and 50°, and 2° between 50° and 60°. The tomography data were saved in a single .mrc format.

Trajectory Analysis

Vps32 single-stranded filaments could not be treated as traditional helical assemblies, since they lack helical symmetry and exhibit high curvature. Available software (e.g. EMAN, SPIDER, IMAGIC, Xmipp and IHRSR) was insufficient to analyze these structures. We therefore developed a new user-friendly Graphic-User-Interface (GUI) in MATLAB for trajectory

tracking. The GUI interface incorporates a wide range of functions, including the ability to invert, scale and threshold images, adjust contrast, and color points. The GUI can accept grayscale image files in either .mrc or .tif format. By manually marking several points along any filament, the script tracks the path of filaments using two iterations of Bezier interpolation. First, a number of user-defined points are inserted between neighboring marks on filaments. An equipartition script subsequently divides the path evenly, after calculating the total filament length. A second round of Bezier interpolation repeats this process and provides more evenly spaced points. If necessary, a straightening script can be used prior to the second interpolation.

Filament Straightening

Due to the inherently inaccurate process of marking filaments manually, small deviations may arise after the first round of Bezier interpolation. To address this problem, we developed a peak finding script for automated correction. At each interpolated point, the normal direction is defined, and the image is rotated to vertical using this point as its center. The area between this point and the next is boxed with a rectangular region, the dimensions of which are determined by filament thickness and pixel size. A one-dimensional projection of this boxed area is calculated and the maximum defined. Since the previously identified interpolated points were already close to the peak, searching is limited to a small area. The coordinate of this new peak position then replaces the prior one with improved accuracy. The above peak finding script is also used to straighten curved filaments to define the spacing between neighboring polymers. A relatively larger boxed area (larger than the estimated filament space) is used to cover adjacent filaments. Serial rotated rectangles are stacked in a new image, and both the straightened and neighboring

filaments are easily defined. The GUI system follows the trajectories of neighboring filaments, calculates the distance at specific points and averages them over their lengths.

Two-dimensional Class Average Analysis

Considering that Vps32 single-stranded filaments are highly curved with a narrow width (4.2 nm), cryo-EM images were taken at a magnification of 59,000x for two-dimensional class average analysis. Due to their high curvature, the Helixboxer program in EMAN (24), which is widely utilized to characterize helical structures, is not practical for analysis of Vps32 filaments. Instead, we used a similar 90% overlap strategy to box regions of the Vps32 filaments, following trajectory analysis. To do so, Vps32 filament trajectory was interpolated linearly. The interpolated points were spaced at 0.9 nm intervals and subsequently used as the centers of individual boxed regions. The Batchboxer program in EMAM then defined specific regions with the box size of 9 nm (24). Image stacks were subjected to reference-free two-dimensional alignment and classification using IMAGIC software (Image Science Software GmbH). In total, 8,286 particles were classified into 50 unique, but highly related classes. The center density maps in each class were selected using the EMAN Boxer program and averaged in IMAGIC (25) to define an isosurface. The averaged isosurface was used to replace all three densities in a single box manually, following 3.2 nm intervals without bending. One representative straight Vps32 filament was boxed using EMAN Helixboxer and a fast Fourier transform (FFT) algorithm was performed in the same software package. A one-dimensional projection profile was processed using a script we wrote in MATLAB.

Electron Tomography

Tomography data acquired in the .mrc format were converted into a .st format with a bin size of 2 using the IMOD software package (26). Regions of interest were centered and aligned in a fiducial-less mode. Three-dimensional models were subjected to a low-pass filter to increase contrast. Model building was conducted using the IMOD software package and only distinct trajectories were marked at different tilting angles. The spacing between neighboring filaments in models was calculated using the straightening script (described above), taking advantage of a similar strategy to that used in measuring raw images.

Docking of Atomic Structures into the EM-defined Isosurface

Although ESCRT-III subunits are predicted to contain more than 5 alpha helices, helices $\alpha 1$ - $\alpha 4$ form a stable core, while $\alpha 5$ is likely flexible and can be displaced during filament polymerization (11,27). Therefore, we docked helices $\alpha 1$ - $\alpha 4$ of the human CHMP3 crystal structure (PDB: 2GD5) and a model of a homologous region within *C. elegans* Vps32 into the EM isosurface, which was defined by two-dimensional class average analysis. The co-existence of curved rings and spirals suggested a head-to-tail assembly mode. The monomeric state of purified Vps32, combined with the average length and width of repeating units within the filament, preclude the dimeric CHMP3 or similar structures (88x43x36 Å in size) as the docking unit. Our electron tomography data also precluded the possibility of Vps32 assembling laterally to fit into one density map, since the filament diameter failed to increase at high (+/- 60°) tilt angles, as compared to the untilted view. Based on these findings, docking is restricted to a head-to-tail assembly without lateral association. Therefore, we allowed each Vps32 molecule to span two EM densities, placing helix $\alpha 1$ at the bottom to enable membrane binding as indicated

previously. In this configuration, the asymmetric helical bundle portion of one molecule will interact with the helical hairpin of a neighboring molecule. The detailed protein interface, as predicted by molecular dynamics simulations, is shown.

Helix Wheel Analysis

Portions of each alpha helix in both human CHMP3 and *C. elegans* Vps32 were analyzed using the on-line EMBOSS explore server for helix wheel analysis (<http://emboss.bioinformatics.nl/cgi-bin/emboss/pepwheel>). The organization of helical bundles was assembled according to the topologies observed in crystal or simulated atomic structures.

Molecular Dynamic (MD) Simulation Protocols

Classical MD simulations are used to probe the structural flexibility of both human CHMP3 and *C. elegans* Vps32 monomers as well as the binding interface of dimers. All MD simulations are run with the AMBER molecular dynamic package on GPUs (28,29). The ff99SBnmr1 force field (30) is used to describe the system because recent benchmark calculations showed that this force field provides reliable structural properties with both explicit and implicit solvent simulations (31). Both explicit solvent and implicit solvent MD simulations are carried out to confirm the robustness of the results; the length of the simulation ranges from 300 to 600 ns for explicit solvent simulations and from 400 ns to 3 μ s for implicit solvent simulations. For explicit solvent simulations, the TIP3P water model (32) is used to solvate the protein with periodic boundary conditions. The system size is approximately 33,000 atoms for monomer simulations and 83,000 atoms for dimer simulations. The system is neutralized with counter-ions and electrostatic interactions are calculated with the particle mesh Ewald (PME) method using a grid spacing of approximately 1.0 Å. The non-bonded cutoff for van der Waals interactions is 10 Å.

The SHAKE algorithm (33) is applied to all bonds involving hydrogen, allowing an integration time step of 2 fs. Simulations are run with the NVT ensemble at 300 K using the weak-coupling algorithm (34). For implicit solvent simulations, the GB7 generalized Born model (35) is used. Non-bonded interactions are calculated without any cutoff. A salt concentration of 0.15 M is applied, using a modified generalized Born model based on the Debye-Hückel limiting law for ionic screening of electrostatic interactions (36). The temperature of 300 K is controlled through Langevin dynamics with a collision frequency of 20 ps⁻¹.

Initial Monomer Structure Preparation and Flexibility Analysis using Molecular Dynamics Simulations

Among core ESCRT-III proteins, only human CHMP3⁸⁻²²² and CHMP4B¹⁹⁻⁹⁷ possess solved crystal structures. Even though primary sequences of ESCRT-III proteins are not highly conserved, their overall structures are predicted to be similar, each with two long alpha helices ($\alpha 1$ and $\alpha 2$) and three short helices connected by loops ($\alpha 3$ - $\alpha 5$). CHMP4B has higher sequence homology with *C. elegans* Vps32 while CHMP3 has more helices resolved in the crystal. We used the I-TASSER server (37,38) to build the structural model of *C. elegans* Vps32. Seven other Vps32 models are also built with Modeller (39) using different strategies, but each leads to a less stable structure during subsequent MD simulations. The structure building process of I-TASSER used the crystal structures of both CHMP4B helices ($\alpha 1$ and $\alpha 2$) and CHMP3 ($\alpha 1$ - $\alpha 4$). The final Vps32 structure is of similar conformation to CHMP3 and shows a stable root-mean-square-difference (RMSD) of approximately 3 Å during 3 μ s of GB7 simulation, supporting the validity of the I-TASSER model. This structure, together with CHMP3 crystal structure, is chosen as the starting configurations for further molecular dynamic simulations on their

flexibilities. To quantify the structural flexibility of the protein, MD trajectories are analyzed with a principal component analysis (PCA) using the ProDy package (40). The bending angle of the helical hairpin ($\alpha 1$ and $\alpha 2$) is defined as the dihedral angle spanned by the two ends of helix $\alpha 1$ with respect to the hinge in the middle of the structure. The hinge region is predicted using the DynDom protein domain motion analysis program with structures from the MD trajectories (41). The bending potential of mean force (PMF) is directly inverted from the bending angle distribution, $P(\theta)$, from the MD trajectories: $W(\theta) = -k_B T \ln P(\theta)$, where k_B is the Boltzmann constant and T the absolute temperature (300 K).

MD Dimeric Interface Simulation and its Stability Analysis

Our EM docking results indicate that the 4-helix bundle in one Vps32 monomer interacts with an adjacent monomer (through its helical hairpin) to assemble into single-stranded filaments. A Vps32 molecule is split into a ‘head’ region (amino acids 12-33 and 77-137) and ‘tail’ region (amino acids 34-76) for interface prediction. The head region is set as the reference in ZDOCK calculations for predicting the position of the tail regions (42). No residue was specifically selected or blocked in either the head or tail portions during the prediction. The top 500 predicted positions of the tail are shown as grey dots in Fig. S9. One highly probable position of the tail, in which helix $\alpha 2$ of one Vps32 monomer interacts with helix $\alpha 2$ from the neighboring head region (from another Vps32 monomer), is shown explicitly. Next, to identify the interface shared by two interacting ESCRT-III molecules and explore the structural stability of the interface, we subjected the crystal structure of CHMP3 (helices $\alpha 1$ - $\alpha 4$) to two different protein docking servers: ZDOCK (42) and HADDOCK (43,44). With ZDOCK, one set of calculations does not include any specific constraints while the other two sets include spatial restraints to

impose proximity between R46-E129, K54/R69-E129/E133 respectively across the interface. For HADDOCK, the same sets of restraints are included, and ensemble docking using conformational ensemble collected from MD simulations of CHMP3 is also attempted. 635 top-ranked dimer models from these calculations are screened according to the EM density map and whether the dimer exhibits a uniform interface that potentially binds to a lipid bilayer. Further refinement of selected dimer models with MD simulations leads to a stable complex in which the two monomers are arranged in a head to tail manner with helix $\alpha 2$ contributing most to the binding interface. This complex is predicted by ZDOCK without any constraints and has an initial rank of 25 among the top 200 predictions, as is shown in **Figure 4.S9**. This dimer complex remains structurally stable in both implicit and explicit solvent simulations. For example, the dimer interface is featured with a modest RMSD of approximately 1 Å during the 350 ns of explicit solvent simulations (**Figure 4.2C**).

Structural Analysis

The structural analysis including surface electrostatic distribution and structural superimposition was fulfilled in the UCSF Chimera package (45). The PCA results were visualized in VMD (46).

ACKNOWLEDGEMENTS

This work was supported by a grant from the NIH (GM088151 to AA). YZ is supported by a grant from the NSF (NSF-DMS-1160360 to JCM and QC).

EXPERIMENTAL CONTRIBUTIONS

A.S. performed necessary molecular biology, purified proteins, and protein hydrodynamic studies. Q.T. performed and analyzed EM experiments. Y.Z. performed molecular dynamic simulation studies.

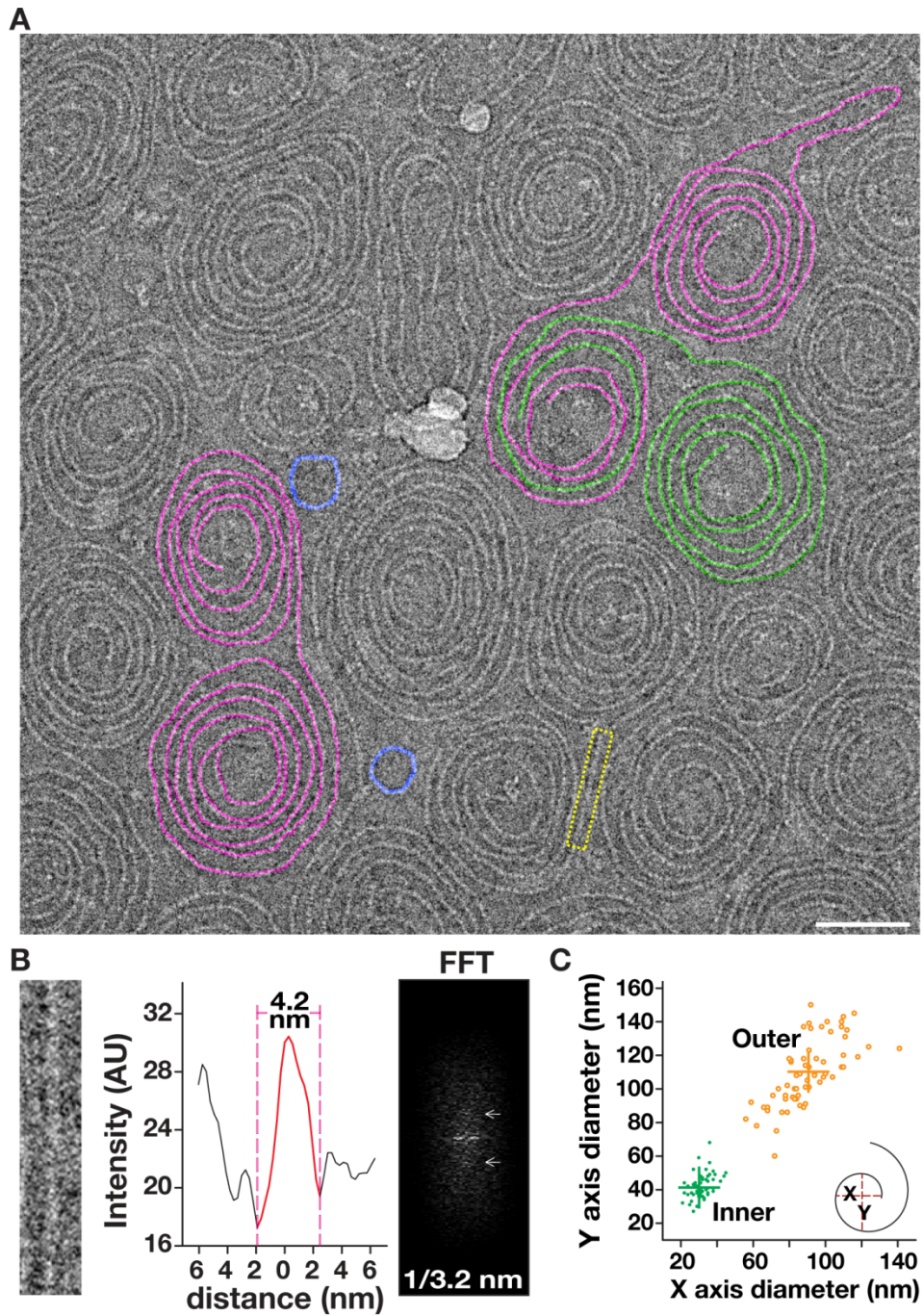


Figure 4.1. Vps32 polymerizes to form curved, single-stranded filaments.

Figure 4.1. Vps32 polymerizes to form curved, single-stranded filaments.

(Figure 4.1A) Representative cryo-EM image (inverted) of Vps32. Select spiral pairs (purple), hybrid spirals (purple/green), and ring structures (blue) are highlighted. Scale bar, 50 nm.

(Figure 4.1B) A straight filament (yellow, boxed region in panel B) was chosen for FFT analysis and width measurement. Layer lines in the FFT analysis are highlighted with arrows. **(Figure**

4.1C) Distribution of spiral diameters. Both inner and outer diameters of spiral filaments were measured in two axes (X and Y).

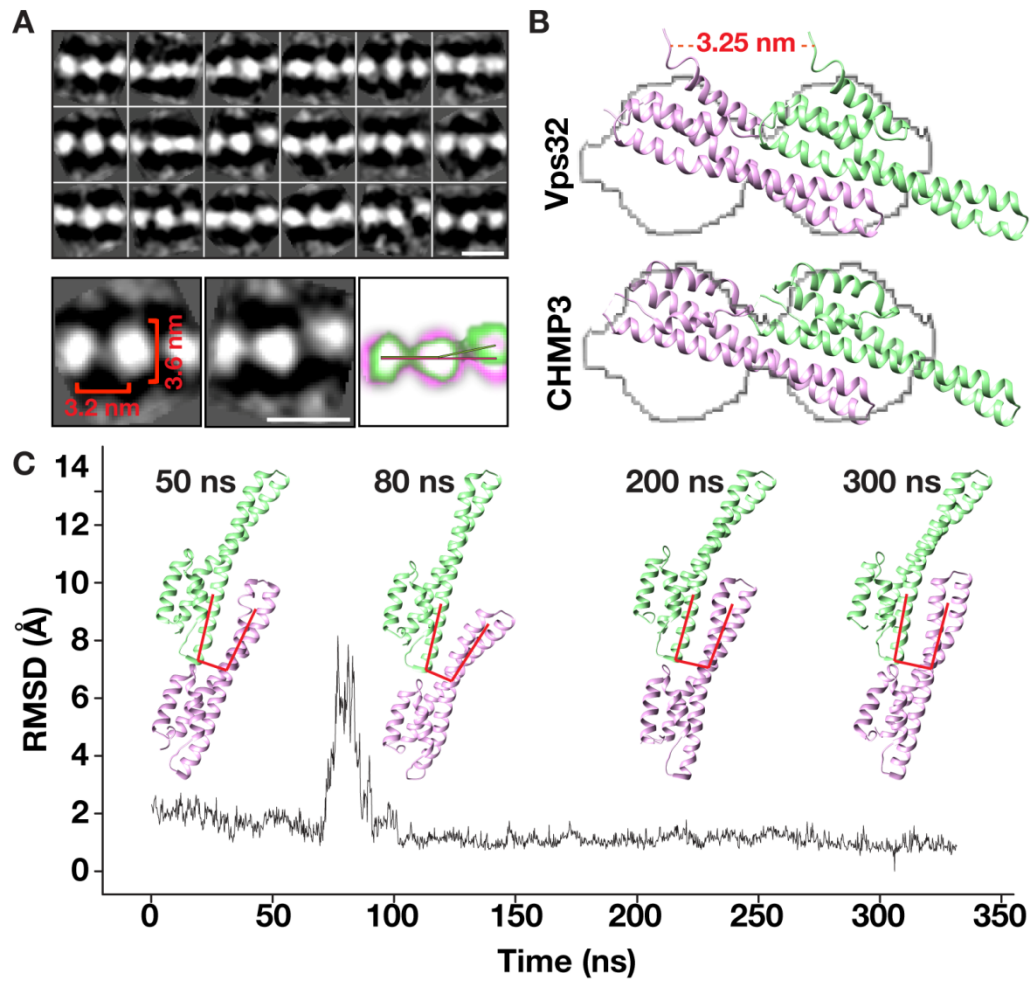


Figure 4.2. Stable interactions between neighboring $\alpha 2$ helices drive head-to-tail assembly of Vps32 filaments.

Figure 4.2. Stable interactions between neighboring $\alpha 2$ helices drive head-to-tail assembly of Vps32 filaments.

(Figure 4.2A) Two-dimensional class average analysis of vitrified Vps32 polymers.

Representative class averages are overlaid to highlight flexibility observed in filaments. The dimensions of EM densities are indicated. Scale bars, 5 nm. **(Figure 4.2B)** Docking of Vps32 (top, pseudoatomic model) and CHMP3 (bottom, based on structure 2GD5) into an averaged EM isosurface. **(Figure 4.2C)** Molecular dynamics simulations demonstrate the stability of the interface between CHMP3 monomers. Individual structure clusters at different time points are shown.

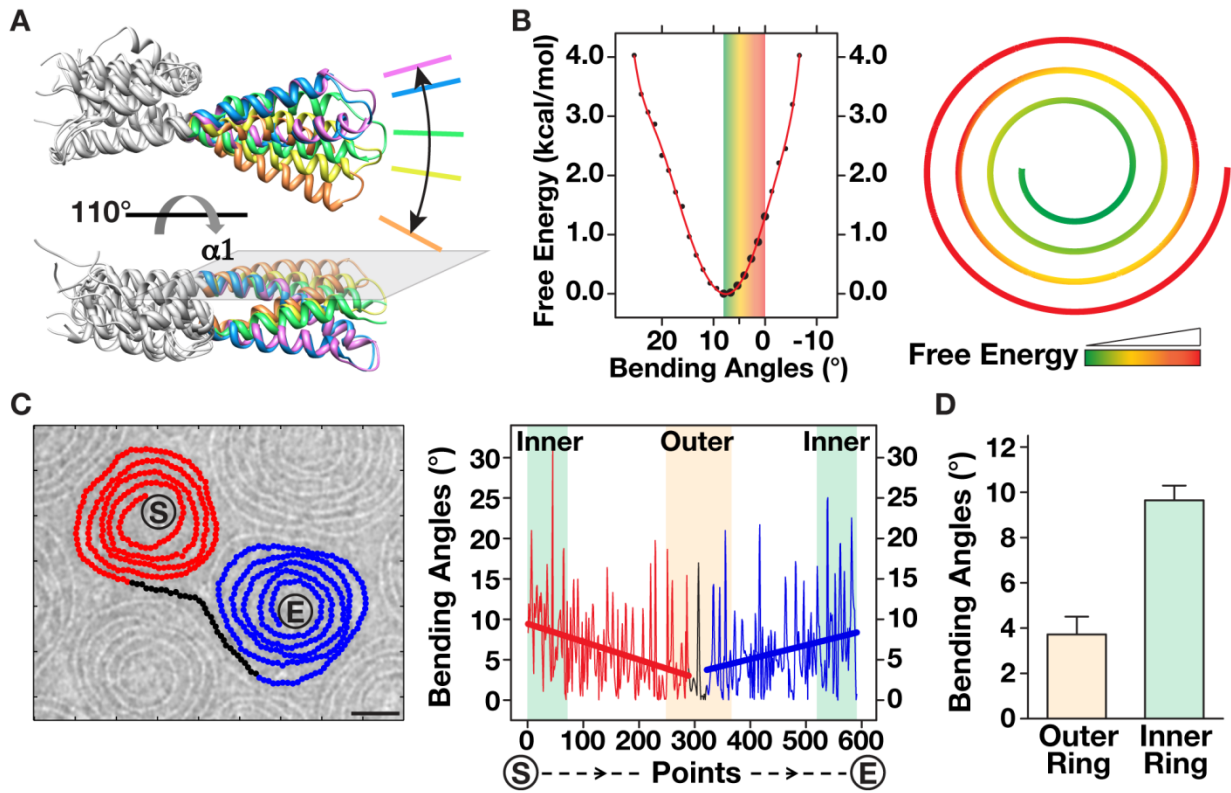


Figure 4.3. Spiral assembly of Vps32 filaments harnesses intrinsic free energy.

Figure 4.3. Spiral assembly of Vps32 filaments harnesses intrinsic free energy.

(**Figure 4.3A**) Two views showing a molecular dynamics simulation of a Vps32 monomer. Bending of the helical hairpin is restricted to a single plane. (**Figure 4.3B**) The free energy analysis of Vps32 at different bending angles. A model showing the changes in free energy throughout the spiral is provided (right). (**Figure 4.3C**) Bending angle analysis of a vitrified Vps32 spiral pair. The filament trajectory is labeled (red, black and blue) and plotted (right). Linear trendlines that were fitted to each portion of the graph are shown. Sites of initiation (S) and termination (E) of the spiral are indicated. Scale bar, 25 nm. (**Figure 4.3D**) Summary of bending angles within spirals (n=25 spiral pairs). Error bars represent mean +/- SEM.

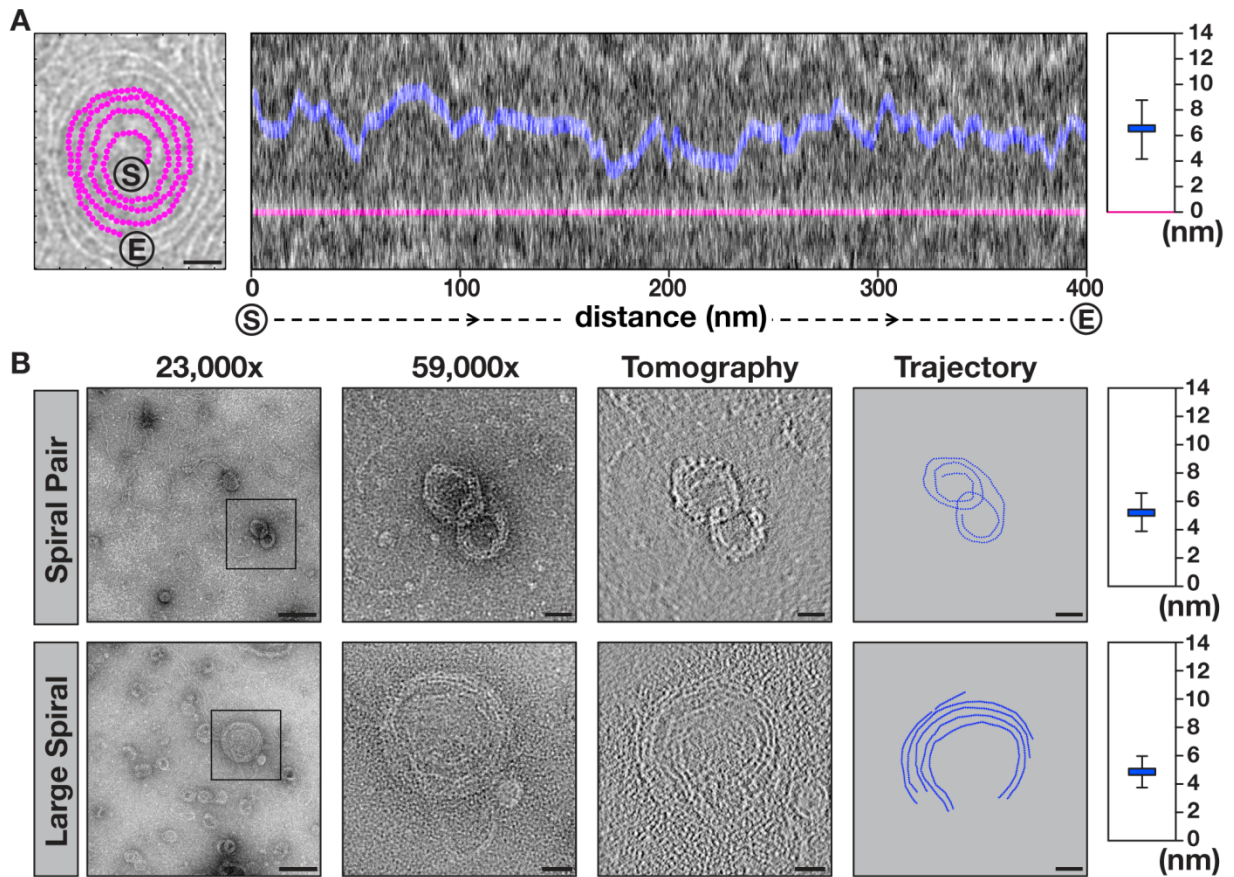


Figure 4.4. The carboxyl-terminus of Vps32 inhibits the lateral association of filaments within spirals.

Figure 4.4. The carboxyl-terminus of Vps32 inhibits the lateral association of filaments within spirals.

(**Figure 4.4A**) Analysis of the spacing between filaments in Vps32 spirals. A representative cryo-preserved Vps32 spiral with its trajectory highlighted in purple is shown (left). Scale bar, 25 nm. A portion of this spiral was straightened and its distance to the adjacent filament within the same structure was calculated along its entire length (middle). The average distance between the centers of each filament is plotted (right). Error bars represent mean +/- SEM. (**Figure 4.4B**) Analysis of the spacing between filaments in a negatively stained spiral composed of a truncated form of Vps32 (amino acids 1-190) was conducted using electron tomography. Representative raw images, tomograms and trajectories are shown for a spiral pair (top) and a large-diameter spiral (bottom). The average distance between the centers of each filament is plotted (right) using 5 independent tomographic datasets. Scale bars, 50 nm (23,000x magnification) and 20 nm (59,000x magnification, tomogram, and trajectory). **, $p < 0.001$ compared to wild-type (one-tail t test). Error bars represent mean +/- SEM.

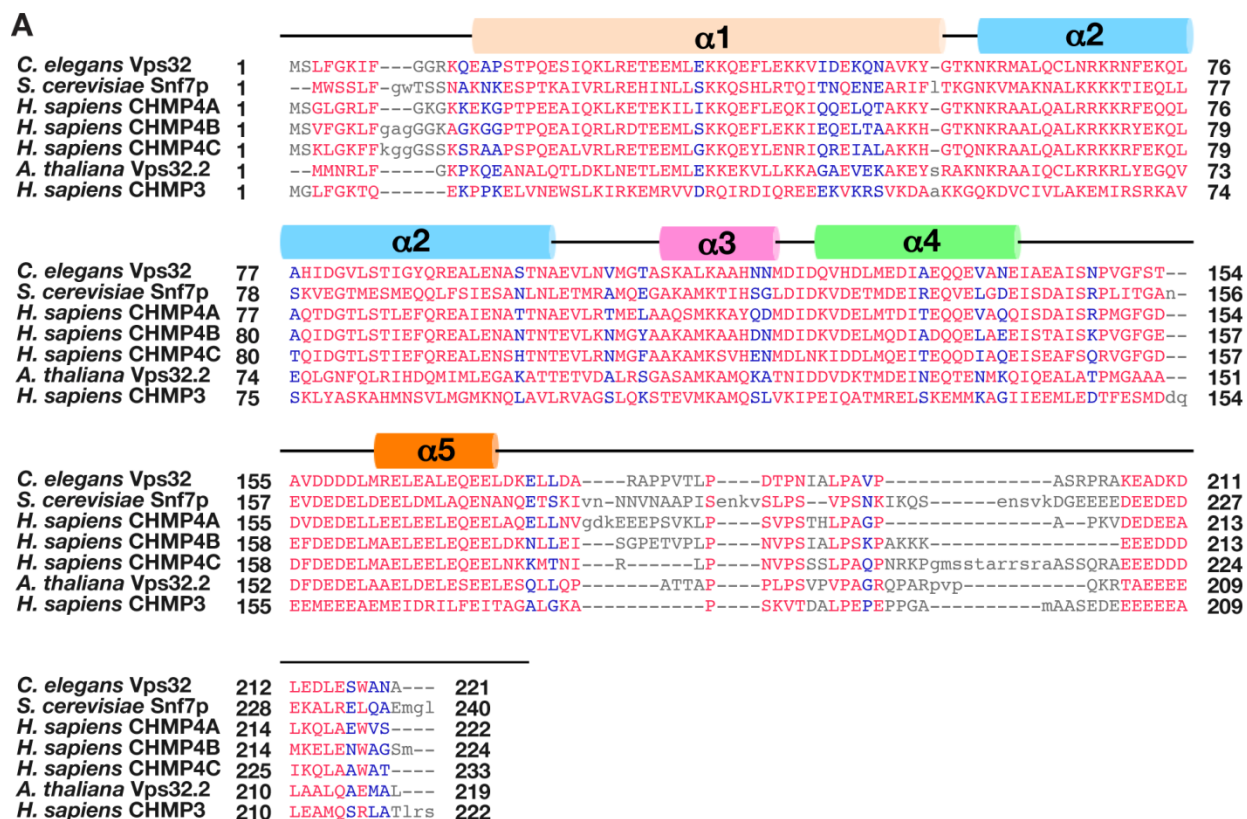


Figure 4.S1. *C. elegans* Vps32 is evolutionarily conserved.

Figure 4.S1. *C. elegans* Vps32 is evolutionarily conserved.

Sequence alignment of several ESCRT-III subunits from different species. The positions of helices $\alpha 1$ - $\alpha 5$ are labeled.

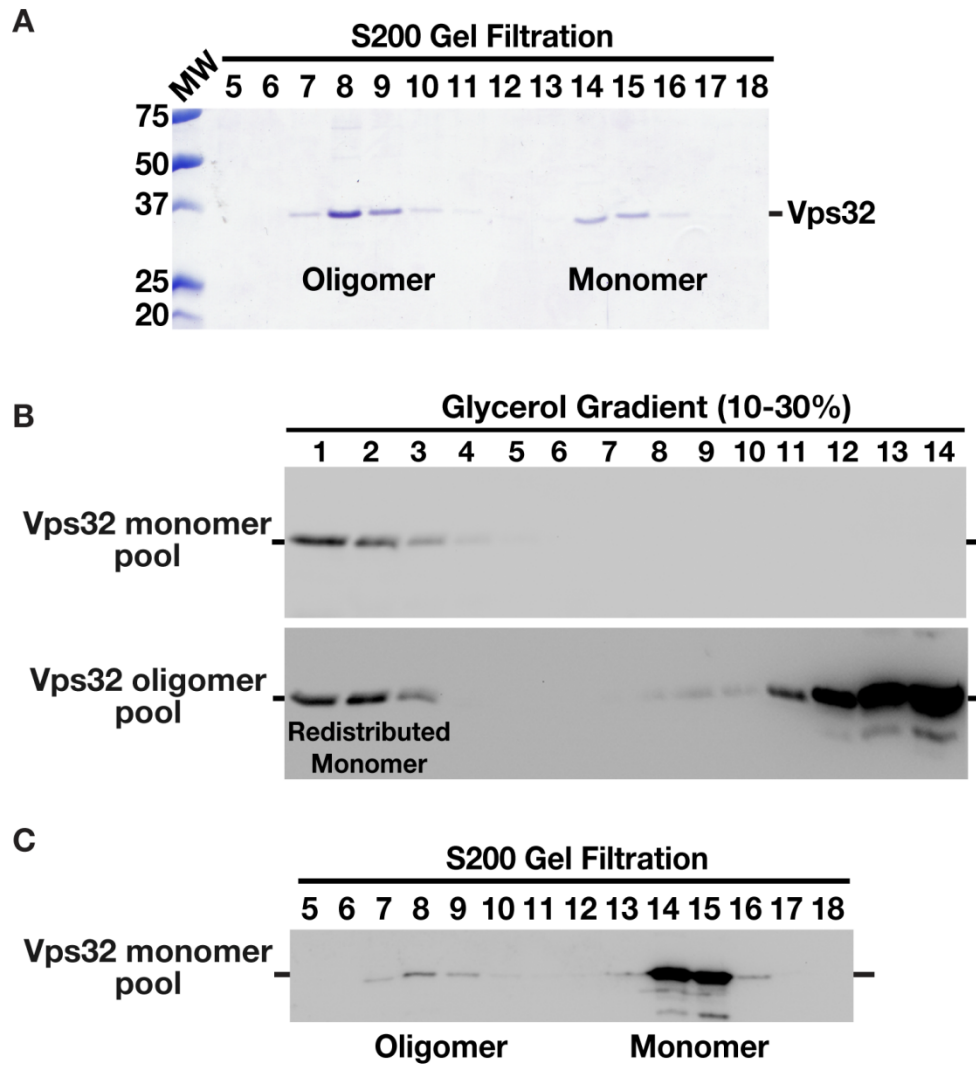


Figure 4.S2. *C. elegans* Vps32 forms an exchangeable pool of monomers and oligomers in solution.

Figure 4.S2. *C. elegans* Vps32 forms an exchangeable pool of monomers and oligomers in solution.

(**Figure 4.S2A**) Coomassie stained fractions of purified, recombinant *C. elegans* Vps32 following size exclusion chromatography and SDS-PAGE analysis. The monomer and oligomer peaks exhibit Stokes radii of 3.8 nm and 9.1 nm, respectively. (**Figure 4.S2B**) Immunoblot analysis showing the distributions of recombinant Vps32 following fractionation over a glycerol gradient. Both the monomer pool (fractions 14 and 15 recovered after size exclusion chromatography, top) and the oligomer pool (fractions 7 and 8 recovered after size exclusion chromatography, bottom) were separated by velocity sedimentation. A redistributed monomer peak is highlighted (bottom). The monomer pool exhibits an approximate sedimentation value of 2.1 S. Based on our hydrodynamic studies, the native molecular weight of Vps32 (monomer pool) is ~33 kD (47), similar to its predicted molecular mass of 25 kD, as determined by amino acid composition. (**Figure 4.S2C**) Immunoblot analysis demonstrating that a fraction of the monomer pool is redistributed to the oligomer pool following a second round of size exclusion chromatography. The monomer and oligomer peaks continue to exhibit Stokes radii of 3.8 nm and 9.1 nm, respectively.

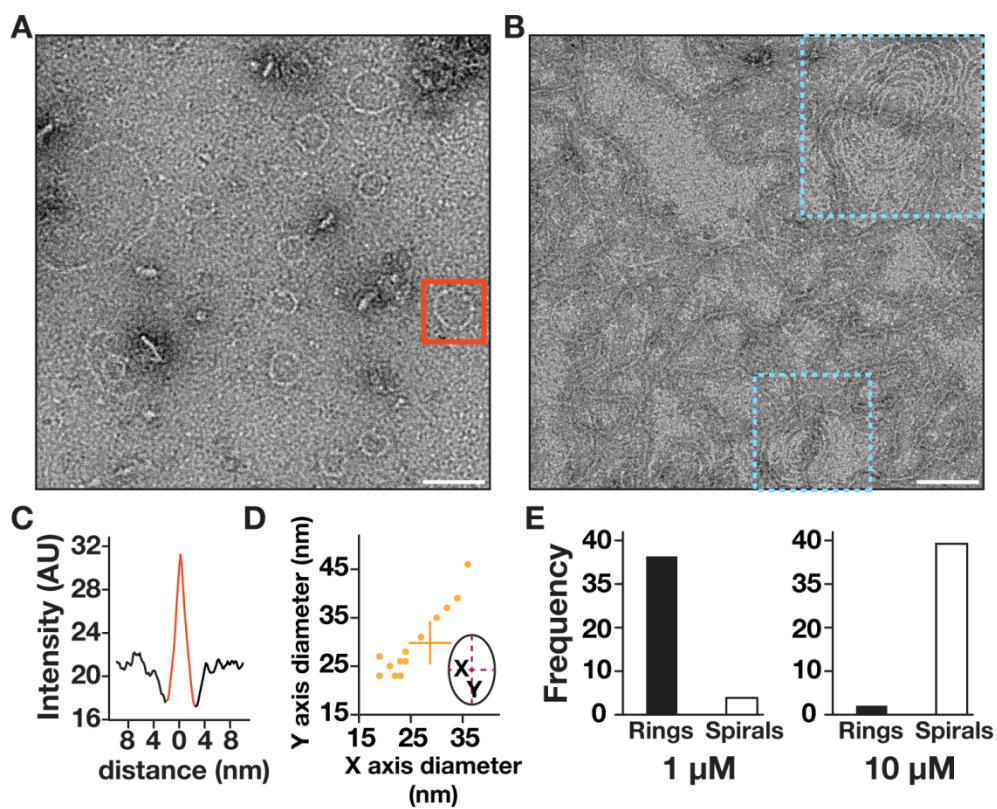


Figure 4.S3. Vps32 polymers form single-stranded, circular filaments following negative straining electron microscopy.

Figure 4.S3. Vps32 polymers form single-stranded, circular filaments following negative straining electron microscopy.

(Figure 4.S3A) A representative EM image of purified, recombinant *C. elegans* Vps32 (1 μ M).

Scale bar, 50 nm. **(Figure 4.S3B)** A representative EM image of purified, recombinant *C.*

elegans Vps32 (10 μ M). Vps32 spirals are highlighted (blue boxed regions). Scale bar, 100 nm.

(Figure 4.S3C) A canonical ring structure (red, boxed region in panel A) was chosen for further analysis to determine the width of Vps32 filaments. **(Figure 4.S3D)** Distribution of ring

structure diameters. Both inner and outer diameters of ring-like filaments were measured in two

axes (X and Y). **(Figure 4.S3E)** Frequency distribution of ring structures and spiral polymers at

different Vps32 concentrations. Only closed filaments were deemed as rings.

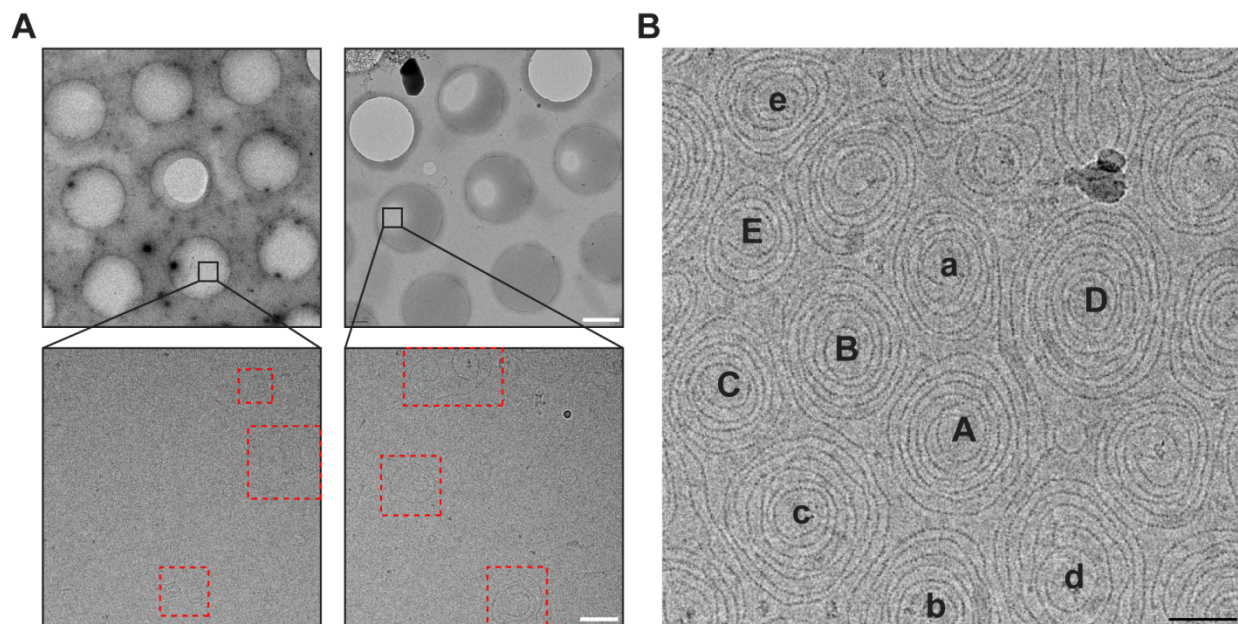


Figure 4.S4. Vps32 polymers form spiral filaments in vitreous ice.

Figure 4.S4. Vps32 polymers form spiral filaments in vitreous ice.

(Figure 4.S4A) Visibility of Vps32 spirals depends on the ice thickness. Although circular Vps32 filaments are present under thick ice (left) and thin ice (right), contrast is improved in the presence of thin ice. Representative filaments are highlighted (red boxed regions). Scale bars, 1 μm (top) and 100 nm (bottom). **(Figure 4.S4B)** Higher magnification of Vps32 spiral pairs following cryo-EM. Select spiral pairs are marked with the corresponding capital and lowercase letters. Scale bar, 50 nm.

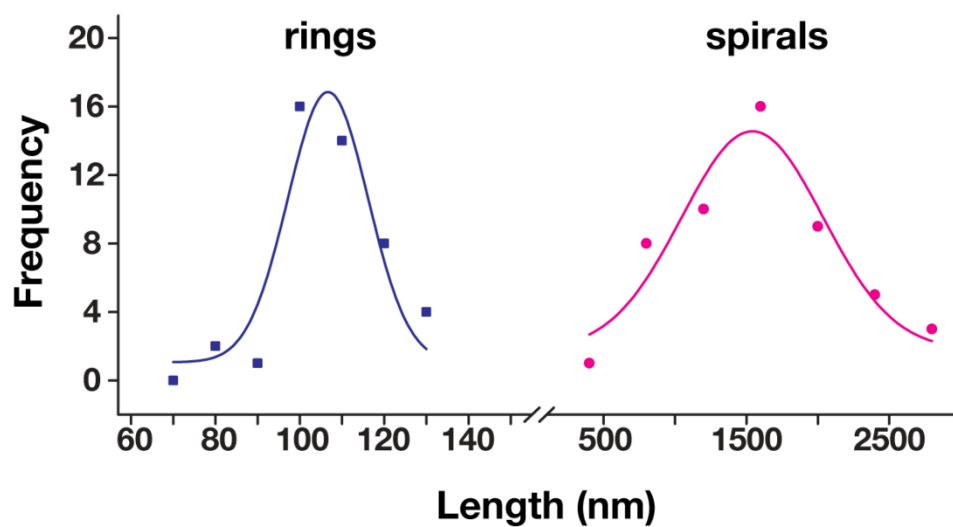


Figure 4.S5. Vitrified Vps32 polymers exhibit a range of lengths.

Figure 4.S5. Vitrified Vps32 polymers exhibit a range of lengths.

A histogram showing the distribution of lengths observed for vitrified Vps32 rings (n=45) and spirals (n=52) is provided.

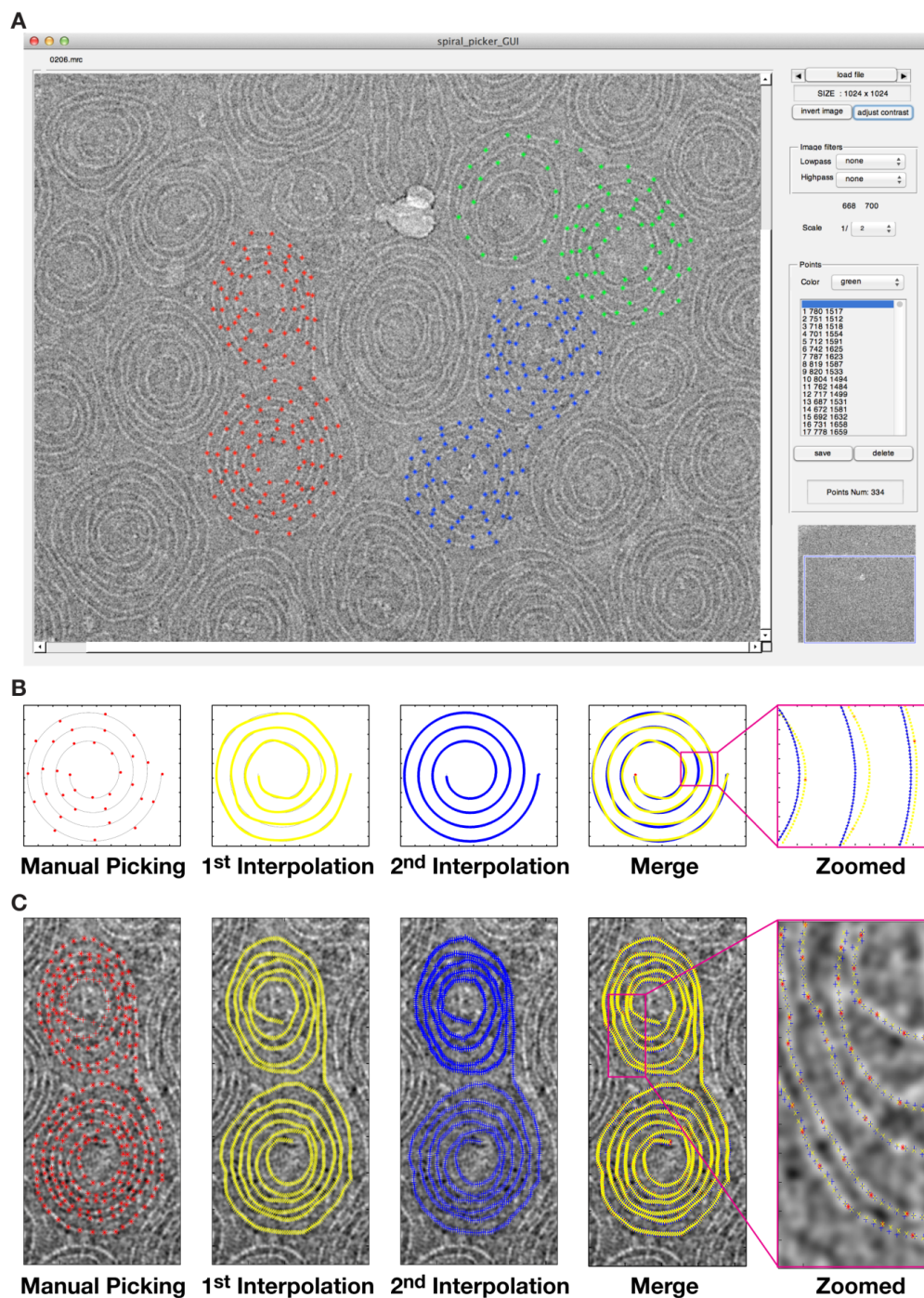


Figure 4.S6. Creation of a GUI system to track filament trajectories.

Figure 4.S6. Creation of a GUI system to track filament trajectories.

(**Figure 4.S6A**) Screen-shot of GUI interface highlighting its multifunctionality. (**Figure 4.S6B**)

Testing of the GUI system. A simulated spiral was marked aberrantly (manually) and analyzed.

Following two rounds of interpolation, an accurate trajectory was identified, as observed in the

merged panels (right). (**Figure 4.S6C**) An experimental spiral was marked, and the trajectory

was defined following two rounds of interpolation.

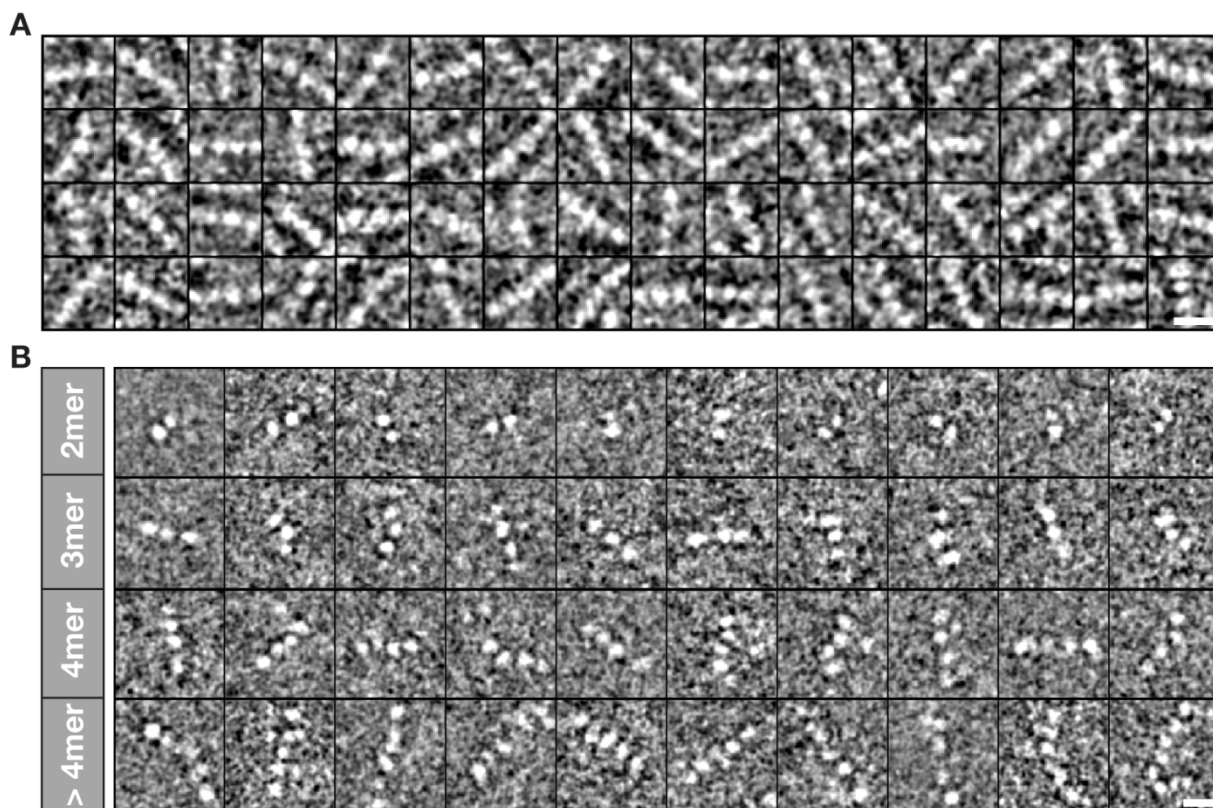


Figure 4.S7. Vps32 filaments are composed of distinct, globular densities joined by thin connections.

Figure 4.S7. Vps32 filaments are composed of distinct, globular densities joined by thin connections.

(Figure 4.S7A) A montage of raw boxed datasets (inverted and filtered) used for two-dimensional class average analysis of Vps32 polymers. Scale bar, 5 nm. **(Figure 4.S7B)** Raw EM density maps for representative Vps32 polymers of particular lengths. All particles shown were selected from inverted cryo-EM images. Scale bar, 5 nm.

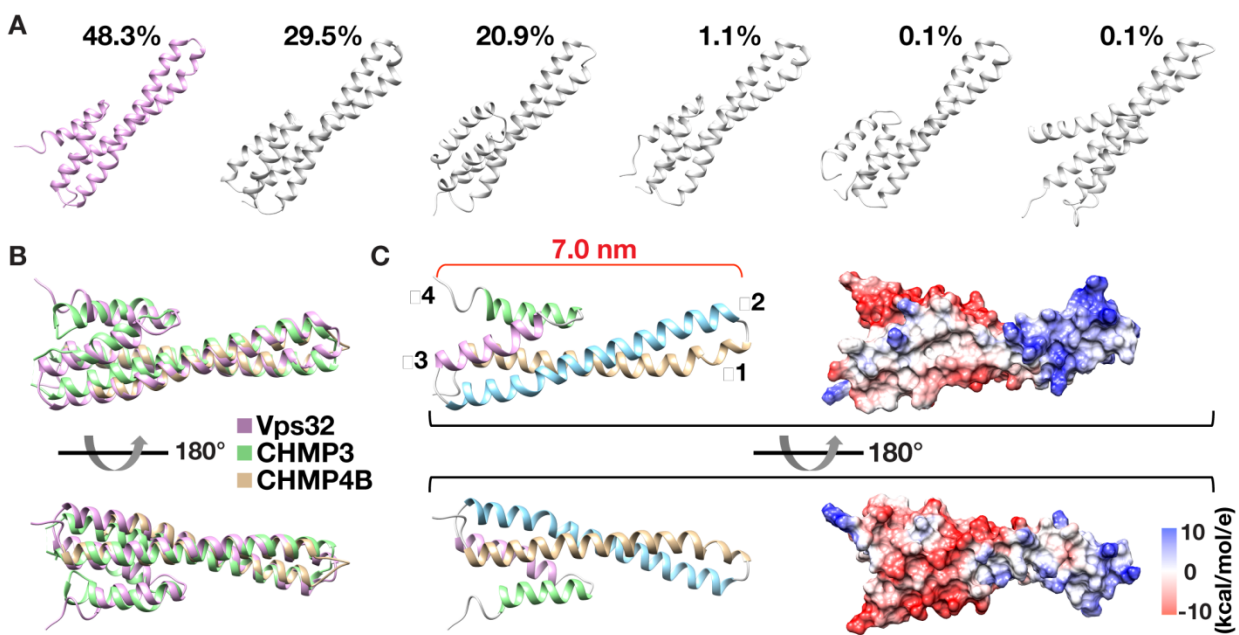


Figure 4.S8. A pseudo-atomic model of *C. elegans* Vps32 exhibits a similar conformation to human CHMP3 and CHMP4B.

Figure 4.S8. A pseudo-atomic model of *C. elegans* Vps32 exhibits a similar conformation to human CHMP3 and CHMP4B.

(Figure 4.S8A) Representative pseudo-atomic structures of Vps32 obtained from molecular dynamics simulations. Structures shown were obtained from cluster analysis of the molecular dynamics trajectories, and their frequencies in the population are indicated. A highly represented structure (purple) was selected as the initial model for further analysis. The initial structure (helices $\alpha 1$ and $\alpha 2$) was built using I-TASSER and is influenced by crystal structures for both CHMP4B and CHMP3, while helices $\alpha 3$ and $\alpha 4$ are modeled on the corresponding helices in CHMP3. **(Figure 4.S8B)** Superimposed structures of *C. elegans* Vps32, human CHMP3 and human CHMP4B are shown, highlighting similarities in the helical hairpin of all proteins.

(Figure 4.S8C) The simulated structure of *C. elegans* Vps32 (helices $\alpha 1$ - $\alpha 4$) exhibits a length of ~ 7 nm. Based on these data, its surface electrostatic distribution is shown (two different views).

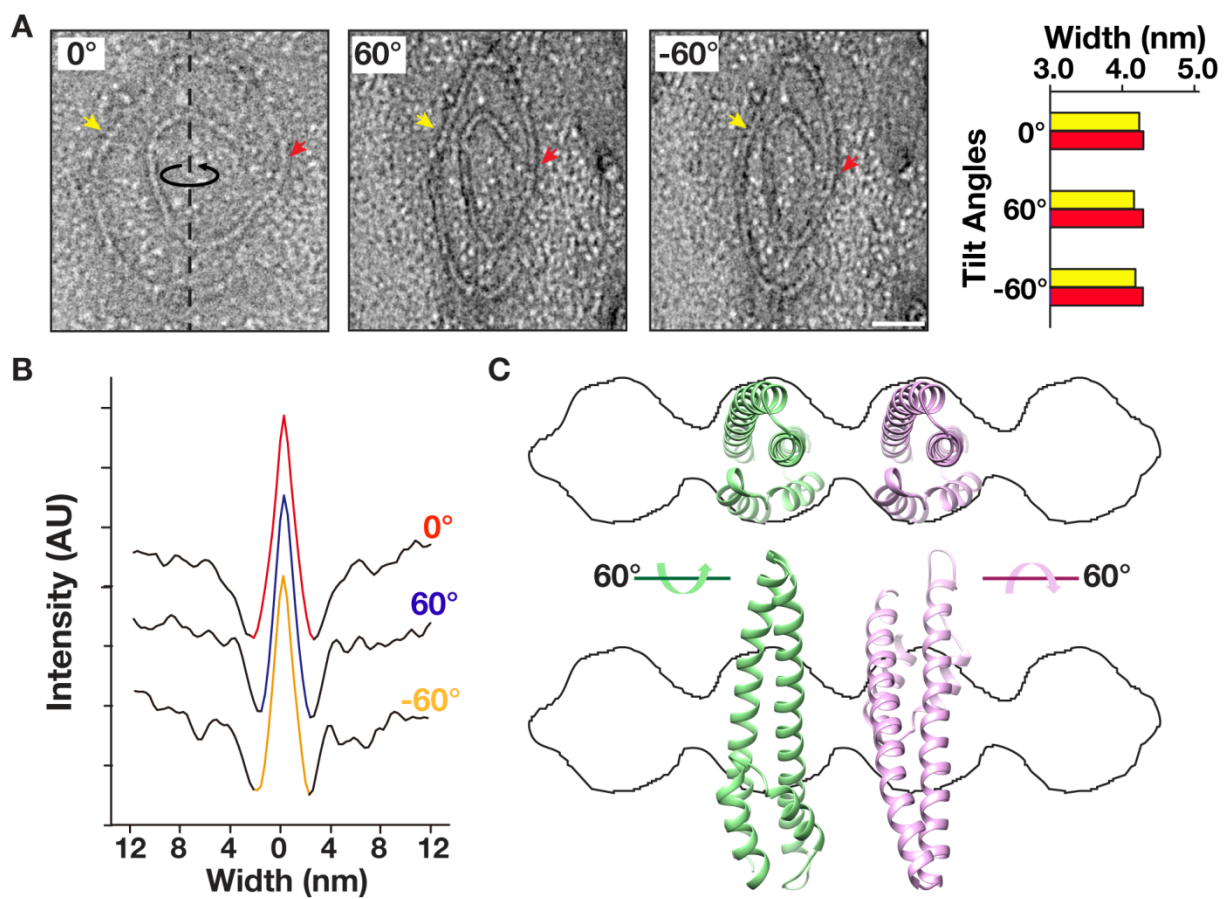


Figure 4.S9. Only a single orientation of Vps32 is compatible with the EM density map.

Figure 4.S9. Only a single orientation of Vps32 is compatible with the EM density map.

(Figure 4.S9A) A representative negatively stained spiral filament and its respective +/- 60° tilted views are shown. Arrowheads highlight portions of the filament that are parallel to the tilting axis, and widths at these locations are indicated for all tilt angles (right). Scale bar, 25 nm.

(Figure 4.S9B) The average thicknesses of single-stranded filaments at different tilting angles.

Curved filaments were first straightened and subsequently projected vertically to determine filament width. **(Figure 4.S9C)** The alternative orientation of Vps32 that docks into the isosurface map at one angle fails to be compatible with the density map at other tilt angles.

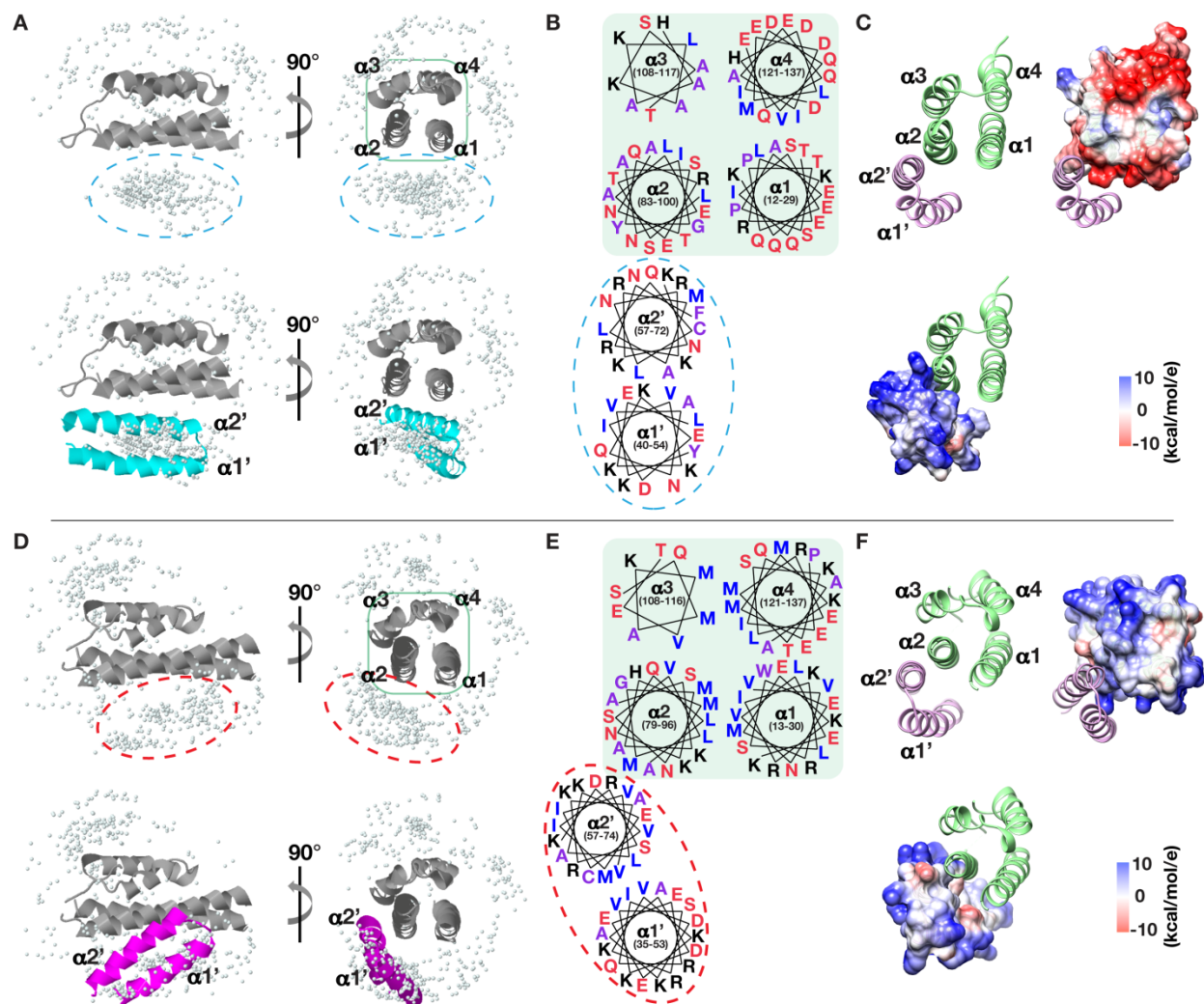


Figure 4.S10. Identification of a common interface between monomers within ESCRT-III filaments.

Figure 4.S10. Identification of a common interface between monomers within ESCRT-III filaments.

(**Figures 4.S10A-4.S10C**) Homotypic association between Vps32 subunits is predicted to be mediated by their $\alpha 2$ helices. (**Figure 4.S10A**) The ZDOCK server was used to determine the relative positions of the helical hairpin from one Vps32 monomer and the asymmetric 4-helix bundle of a neighboring Vps32 subunit. The reference 4-helix bundle is shown as a ribbon cartoon and the top 500 predicted positions of the helical hairpin (from an adjacent Vps32 subunit) are shown as grey dots (upper panel). One highly probable position of the helical hairpin (cyan) is shown explicitly (lower panel). (**Figure 4.S10B**) Helical wheel analysis of the interface described in panel A. Basic (black), acidic (red), hydrophobic (blue), and neutral (purple) residues are shown. (**Figure 4.S10C**) The Vps32 dimer interface is mediated by electrostatic interactions, which mainly arise from the positively charged residues within helix $\alpha 2'$ from one monomer and the negatively charged residues in helix $\alpha 2$ of a neighboring Vps32 subunit. (**Figures 4.S10D-4.S10F**) Homotypic association between CHMP3 subunits is also predicted to be mediated by their $\alpha 2$ helices, as described in panels A-C. (**Figures 4.S10F**) The CHMP3 dimer interface is dominated by hydrophobic interactions, with additional contributions by positively and negatively charged amino acids in the neighboring $\alpha 2$ helices (as described for Vps32).

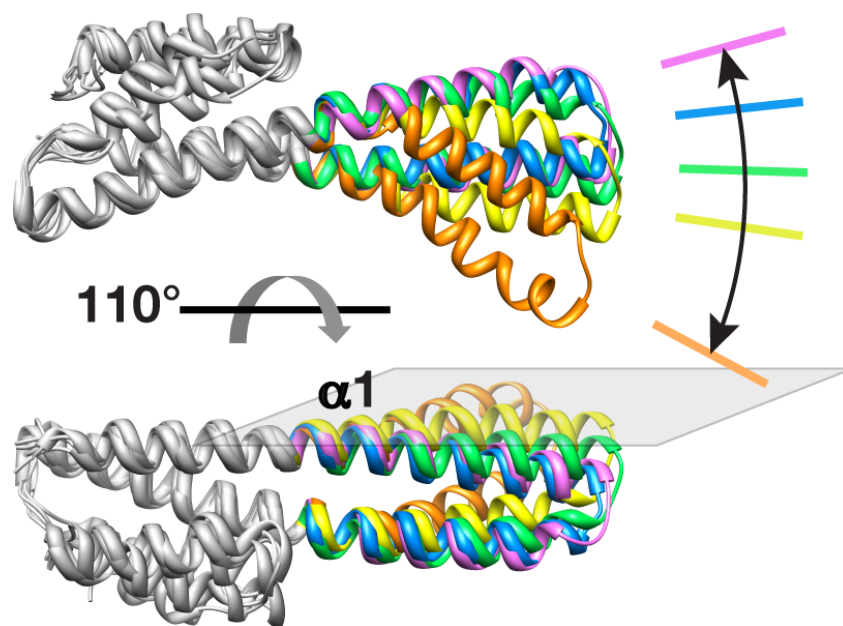


Figure 4.S11. Human CHMP3 exhibits similar flexibility as compared to *C. elegans* Vps32.

Figure 4.S11. Human CHMP3 exhibits similar flexibility as compared to *C. elegans* Vps32.

Two views showing a molecular dynamics simulation of a CHMP3 monomer. Bending of the helical hairpin is restricted to a single plane.

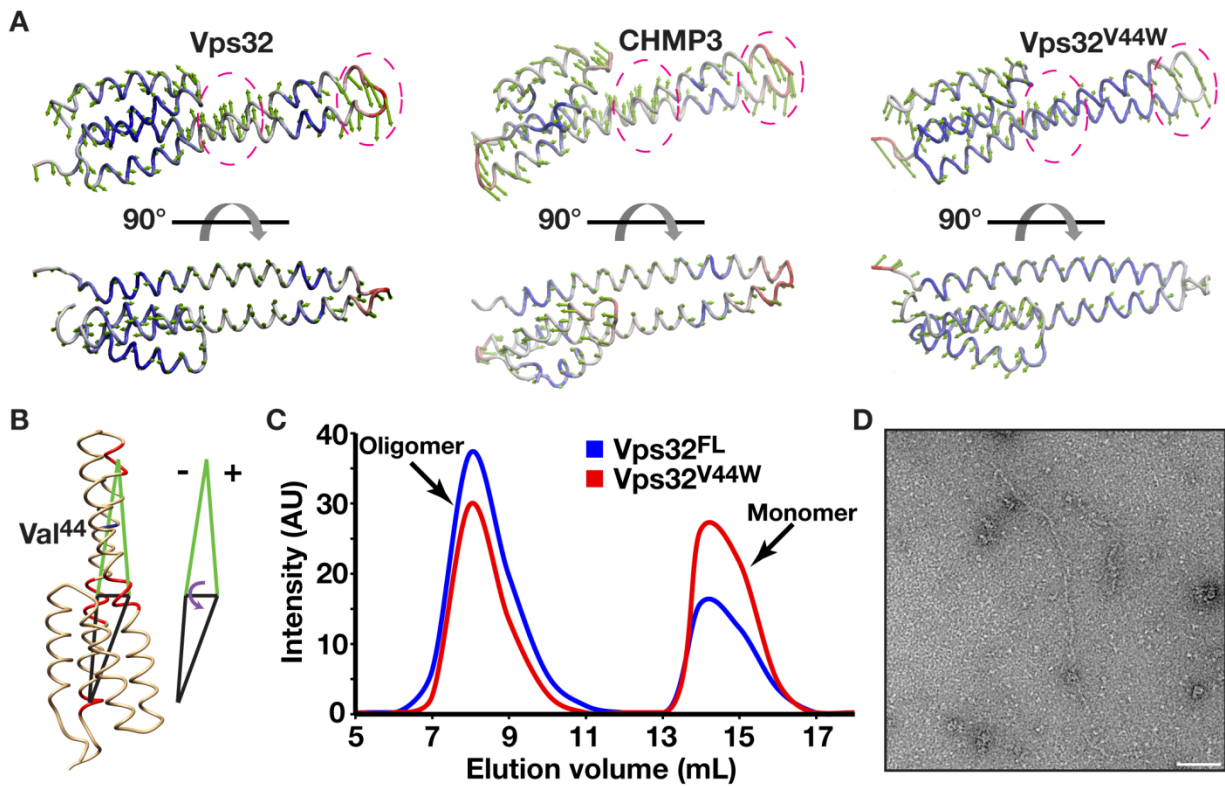


Figure 4.S12. Increasing the rigidity of the Vps32 helical hairpin inhibits spiral filament assembly.

Figure 4.S12. Increasing the rigidity of the Vps32 helical hairpin inhibits spiral filament assembly.

(**Figure 4.S12A**) Principle component analysis was used to compare the flexibilities of wild-type *C. elegans* Vps32, human CHMP3 and a mutant isoform of Vps32 (Vps32^{V44W}), predicted to exhibit a more rigid architecture. The same root-mean-square deviation at 2 Å is applied to all structures. Green arrows indicate the direction of movement, and the length of the arrows indicates the magnitude of motion. The degree of structural flexibility is highlighted with different colors, with red indicating regions of high flexibility and blue indicating region of low flexibility. The hinge region and the tip of the helical hairpin are circled for comparison. Bending takes place in only a single plane. (**Figure 4.S12B**) The bending angle can be defined as the change in a specific dihedral angle in Vps32. The dihedral is composed of three motifs (residues 18-21, 29-33 and 52-55) in helix α_1 , and a single motif (residues 79-82) in helix α_2 . The position of Valine 44 is highlighted. (**Figure 4.S12C**) A comparison of the elution profiles of wild-type (blue) and mutant (V44W, red) Vps32 following gel filtration chromatography indicates only minor differences in their hydrodynamic properties. (**Figures 4.S12D**) Representative negatively stained EM image of purified, recombinant Vps32^{V44W}, which continues to form filaments, but fails to assemble into spirals or ring structures. Scale bar, 50 nm.

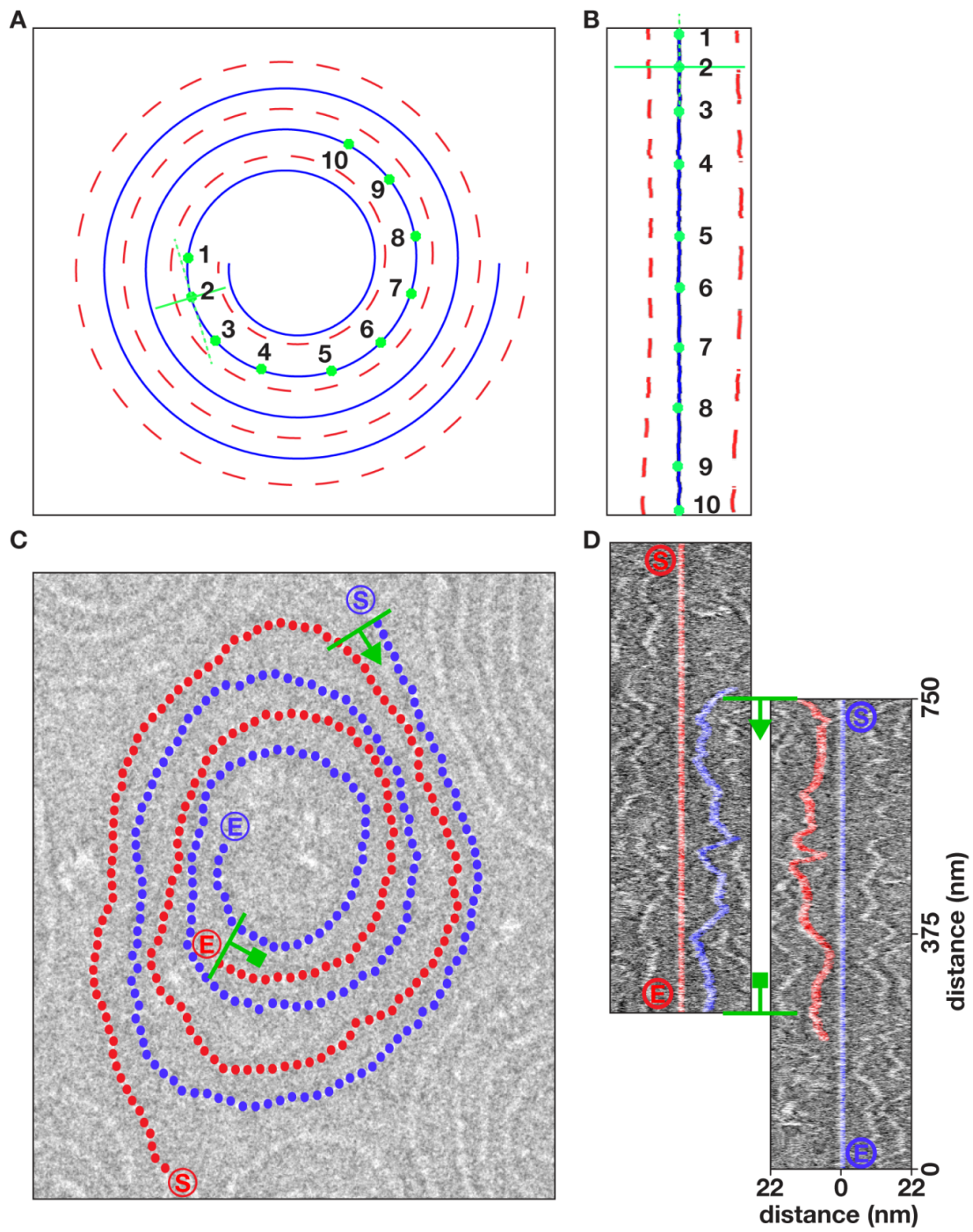


Figure 4.S13. An unbiased approach to determining the distance between adjacent filaments within Vps32 spirals.

Figure 4.S13. An unbiased approach to determining the distance between adjacent filaments within Vps32 spirals.

(**Figures 4.S13A and 4.S13B**) A filament-straightening tool was developed and used to determine the distance between the paths of two simulated spirals (a continuous blue spiral and a dashed red spiral). Accuracy was established by demonstrating that the distance calculated from individual points on one path (green) to juxtaposed dashed lines were identical before and after filament straightening. (**Figures 4.S13C and 4.S13D**) The distance-measuring tool was used on an acquired image of Vps32 spirals. Two distinct filaments in Panel C were straightened and the relative distance to of the adjacent filament was determined along its entire length. Axial symmetry in marked areas (green) further revealed the accuracy of the algorithm.

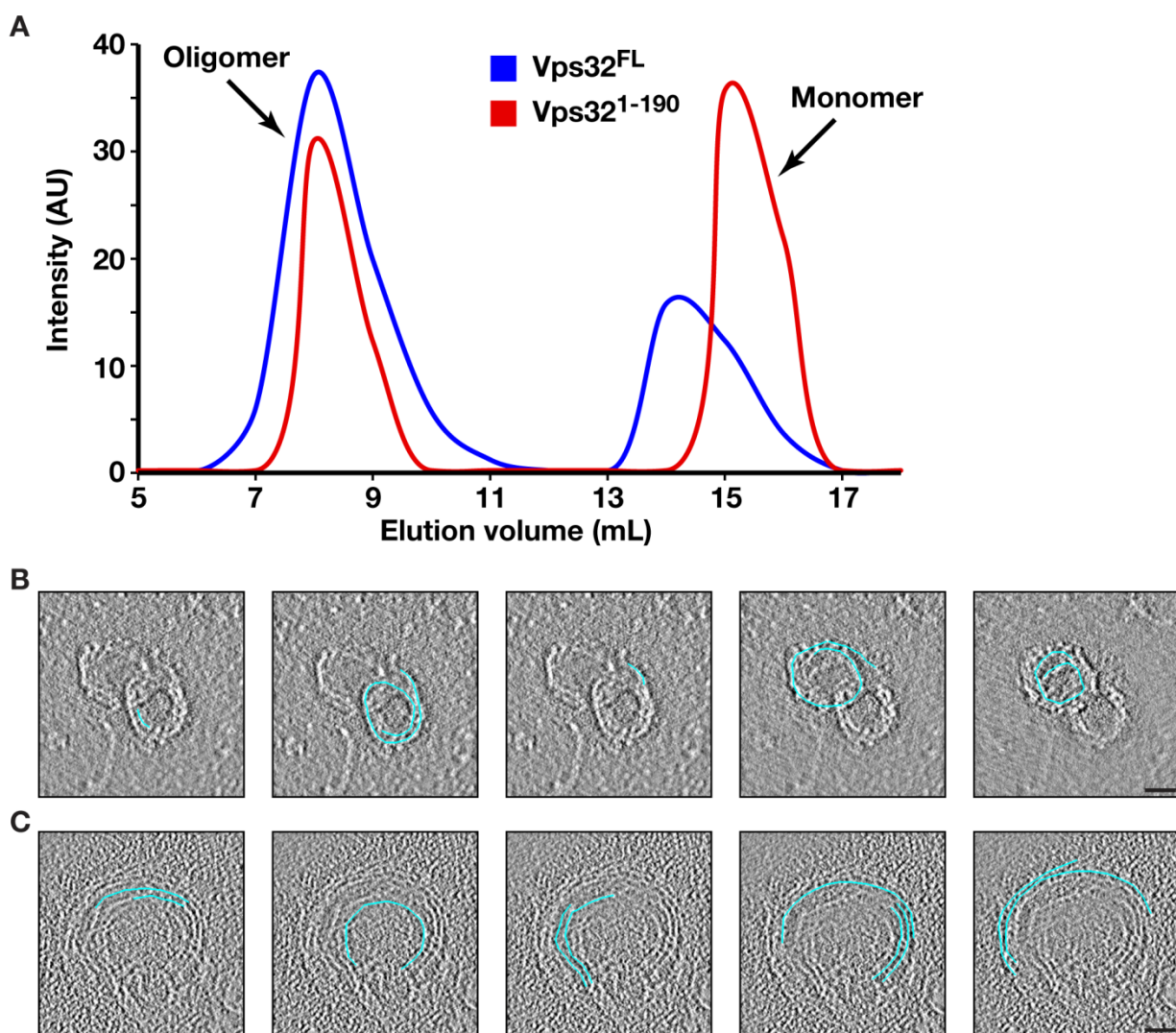


Figure 4.S14. The carboxyl-terminus of Vps32 functions as a spacer between filaments within spirals.

Figure 4.S14. The carboxyl-terminus of Vps32 functions as a spacer between filaments within spirals.

(**Figure 4.S14A**) A comparison of the elution profiles of wild-type Vps32 (blue) and a truncated form of Vps32 (Vps32¹⁻¹⁹⁰, red) following gel filtration chromatography indicates that both assemble as oligomers and monomers in solution. (**Figures 4.S14B and Figures 4.S14C**) The trajectories of the spirals composed of truncated Vps32 (Vps32¹⁻¹⁹⁰) were derived from tomography datasets. The trajectories of filaments within the spirals are drawn (blue) at different tilting angles. Only distinct paths are shown at each tilting angle.

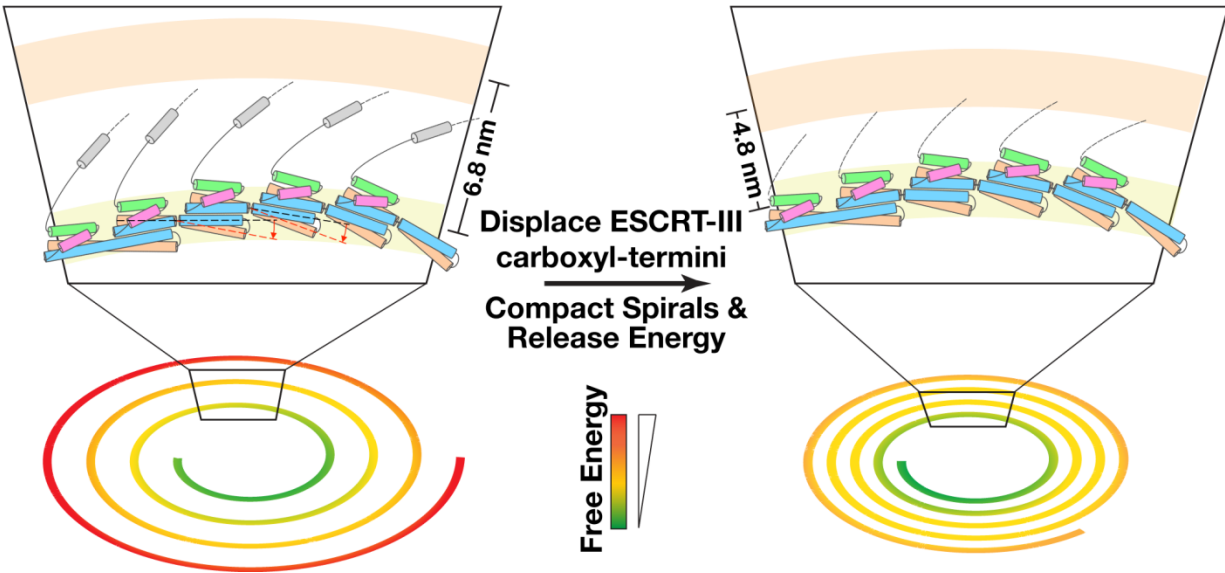


Figure 4.S15. A speculative model illustrating ESCRT-III spiral constriction during membrane scission.

Figure 4.S15. A speculative model illustrating ESCRT-III spiral constriction during membrane scission.

Based on our findings, we propose that displacement of the carboxyl-terminal helices in ESCRT-III subunits away from the interface between individual filaments within spirals would release free energy that contributes to membrane scission.

REFERENCES

1. Hurley, J. H., and Hanson, P. I. (2010) Membrane budding and scission by the ESCRT machinery: it's all in the neck. *Nat Rev Mol Cell Biol* **11**, 556-566
2. Schmid, S. L., and Frolov, V. A. (2011) Dynamin: functional design of a membrane fission catalyst. *Annu Rev Cell Dev Biol* **27**, 79-105
3. Henne, W. M., Buchkovich, N. J., and Emr, S. D. (2011) The ESCRT pathway. *Dev Cell* **21**, 77-91
4. Fabrikant, G., Lata, S., Riches, J. D., Briggs, J. A., Weissenhorn, W., and Kozlov, M. M. (2009) Computational model of membrane fission catalyzed by ESCRT-III. *PLoS Comput Biol* **5**, e1000575
5. Guizetti, J., and Gerlich, D. W. (2012) ESCRT-III polymers in membrane neck constriction. *Trends Cell Biol* **22**, 133-140
6. Teis, D., Saksena, S., and Emr, S. D. (2008) Ordered assembly of the ESCRT-III complex on endosomes is required to sequester cargo during MVB formation. *Dev Cell* **15**, 578-589
7. Fyfe, I., Schuh, A. L., Edwardson, J. M., and Audhya, A. (2011) Association of the endosomal sorting complex ESCRT-II with the Vps20 subunit of ESCRT-III generates a curvature-sensitive complex capable of nucleating ESCRT-III filaments. *J Biol Chem* **286**, 34262-34270
8. Pires, R., Hartlieb, B., Signor, L., Schoehn, G., Lata, S., Roessle, M., Moriscot, C., Popov, S., Hinz, A., Jamin, M., Boyer, V., Sadoul, R., Forest, E., Svergun, D. I., Göttlinger, H. G., and Weissenhorn, W. (2009) A crescent-shaped ALIX dimer targets ESCRT-III CHMP4 filaments. *Structure* **17**, 843-856
9. Hanson, P. I., Roth, R., Lin, Y., and Heuser, J. E. (2008) Plasma membrane deformation by circular arrays of ESCRT-III protein filaments. *J Cell Biol* **180**, 389-402
10. Ghazi-Tabatabai, S., Saksena, S., Short, J. M., Pobbati, A. V., Veprintsev, D. B., Crowther, R. A., Emr, S. D., Egelman, E. H., and Williams, R. L. (2008) Structure and disassembly of filaments formed by the ESCRT-III subunit Vps24. *Structure* **16**, 1345-1356
11. Henne, W. M., Buchkovich, N. J., Zhao, Y., and Emr, S. D. (2012) The endosomal sorting complex ESCRT-II mediates the assembly and architecture of ESCRT-III helices. *Cell* **151**, 356-371

12. Ohi, M., Li, Y., Cheng, Y., and Walz, T. (2004) Negative Staining and Image Classification - Powerful Tools in Modern Electron Microscopy. *Biol Proced Online* **6**, 23-34
13. Bajorek, M., Schubert, H. L., McCullough, J., Langelier, C., Eckert, D. M., Stubblefield, W. M., Uter, N. T., Myszka, D. G., Hill, C. P., and Sundquist, W. I. (2009) Structural basis for ESCRT-III protein autoinhibition. *Nat Struct Mol Biol* **16**, 754-762
14. Muzioł, T., Pineda-Molina, E., Ravelli, R. B., Zamborlini, A., Usami, Y., Göttlinger, H., and Weissenhorn, W. (2006) Structural basis for budding by the ESCRT-III factor CHMP3. *Dev Cell* **10**, 821-830
15. Martinelli, N., Hartlieb, B., Usami, Y., Sabin, C., Dordor, A., Miguet, N., Avilov, S. V., Ribeiro, E. A., Göttlinger, H., and Weissenhorn, W. (2012) CC2D1A is a regulator of ESCRT-III CHMP4B. *J Mol Biol* **419**, 75-88
16. Shim, S., Kimpler, L. A., and Hanson, P. I. (2007) Structure/function analysis of four core ESCRT-III proteins reveals common regulatory role for extreme C-terminal domain. *Traffic* **8**, 1068-1079
17. Babst, M., Katzmann, D. J., Estepa-Sabal, E. J., Meerloo, T., and Emr, S. D. (2002) Escrt-III: an endosome-associated heterooligomeric protein complex required for mvb sorting. *Dev Cell* **3**, 271-282
18. Morita, E., Sandrin, V., McCullough, J., Katsuyama, A., Baci Hamilton, I., and Sundquist, W. I. (2011) ESCRT-III protein requirements for HIV-1 budding. *Cell Host Microbe* **9**, 235-242
19. Morita, E., Colf, L. A., Karren, M. A., Sandrin, V., Rodesch, C. K., and Sundquist, W. I. (2010) Human ESCRT-III and VPS4 proteins are required for centrosome and spindle maintenance. *Proc Natl Acad Sci U S A* **107**, 12889-12894
20. Lata, S., Schoehn, G., Jain, A., Pires, R., Piehler, J., Gottlinger, H. G., and Weissenhorn, W. (2008) Helical structures of ESCRT-III are disassembled by VPS4. *Science* **321**, 1354-1357
21. McCullough, J., Colf, L. A., and Sundquist, W. I. (2013) Membrane fission reactions of the mammalian ESCRT pathway. *Annu Rev Biochem* **82**, 663-692
22. Mayers, J. R., and Audhya, A. (2012) Vesicle formation within endosomes: An ESCRT marks the spot. *Commun Integr Biol* **5**, 50-56
23. Papadopoulos, J. S., and Agarwala, R. (2007) COBALT: constraint-based alignment tool for multiple protein sequences. *Bioinformatics* **23**, 1073-1079

24. Ludtke, S. J., Baldwin, P. R., and Chiu, W. (1999) EMAN: semiautomated software for high-resolution single-particle reconstructions. *J Struct Biol* **128**, 82-97
25. van Heel, M., Harauz, G., Orlova, E. V., Schmidt, R., and Schatz, M. (1996) A new generation of the IMAGIC image processing system. *J Struct Biol* **116**, 17-24
26. Kremer, J. R., Mastronarde, D. N., and McIntosh, J. R. (1996) Computer visualization of three-dimensional image data using IMOD. *J Struct Biol* **116**, 71-76
27. Rózycki, B., Kim, Y. C., and Hummer, G. (2011) SAXS ensemble refinement of ESCRT-III CHMP3 conformational transitions. *Structure* **19**, 109-116
28. Götz, A. W., Williamson, M. J., Xu, D., Poole, D., Le Grand, S., and Walker, R. C. (2012) Routine Microsecond Molecular Dynamics Simulations with AMBER on GPUs. 1. Generalized Born. *J Chem Theory Comput* **8**, 1542-1555
29. Salomon-Ferrer, R., Götz, A. W., Poole, D., Le Grand, S., and Walker, R. C. (2013) Routine Microsecond Molecular Dynamics Simulations with AMBER on GPUs. 2. Explicit Solvent Particle Mesh Ewald. *Journal of Chemical Theory and Computation* **9**, 3878-3888
30. Li, D. W., and Brüschweiler, R. (2010) NMR-based protein potentials. *Angew Chem Int Ed Engl* **49**, 6778-6780
31. Beauchamp, K. A., Lin, Y. S., Das, R., and Pande, V. S. (2012) Are Protein Force Fields Getting Better? A Systematic Benchmark on 524 Diverse NMR Measurements. *J Chem Theory Comput* **8**, 1409-1414
32. Price, D. J., and Brooks, C. L. (2004) A modified TIP3P water potential for simulation with Ewald summation. *J Chem Phys* **121**, 10096-10103
33. Ryckaert, J.-P., Ciccotti, G., and Berendsen, H. J. C. (1977) Numerical integration of the cartesian equations of motion of a system with constraints: molecular dynamics of n-alkanes. *Journal of Computational Physics* **23**, 327-341
34. Berendsen, H. J. C., Postma, J. P. M., van Gunsteren, W. F., DiNola, A., and Haak, J. R. (1984) Molecular dynamics with coupling to an external bath. *The Journal of Chemical Physics* **81**, 3684-3690
35. Mongan, J., Simmerling, C., McCammon, J. A., Case, D. A., and Onufriev, A. (2007) Generalized Born model with a simple, robust molecular volume correction. *J Chem Theory Comput* **3**, 156-169
36. Srinivasan, J., Trevathan, M. W., Beroza, P., and Case, D. A. (1999) Application of a pairwise generalized Born model to proteins and nucleic acids: inclusion of salt effects. *Theoretical Chemistry Accounts* **101**, 426-434

37. Zhang, Y. (2008) I-TASSER server for protein 3D structure prediction. *BMC Bioinformatics* **9**, 40
38. Roy, A., Kucukural, A., and Zhang, Y. (2010) I-TASSER: a unified platform for automated protein structure and function prediction. *Nat Protoc* **5**, 725-738
39. Eswar, N., Webb, B., Marti-Renom, M. A., Madhusudhan, M. S., Eramian, D., Shen, M. Y., Pieper, U., and Sali, A. (2006) Comparative protein structure modeling using Modeller. *Curr Protoc Bioinformatics* **Chapter 5**, Unit 5.6
40. Bakan, A., Meireles, L. M., and Bahar, I. (2011) ProDy: protein dynamics inferred from theory and experiments. *Bioinformatics* **27**, 1575-1577
41. Hayward, S., and Lee, R. A. (2002) Improvements in the analysis of domain motions in proteins from conformational change: DynDom version 1.50. *J Mol Graph Model* **21**, 181-183
42. Chen, R., Li, L., and Weng, Z. (2003) ZDOCK: an initial-stage protein-docking algorithm. *Proteins* **52**, 80-87
43. Dominguez, C., Boelens, R., and Bonvin, A. M. (2003) HADDOCK: a protein-protein docking approach based on biochemical or biophysical information. *J Am Chem Soc* **125**, 1731-1737
44. de Vries, S. J., van Dijk, A. D., Krzeminski, M., van Dijk, M., Thureau, A., Hsu, V., Wassenaar, T., and Bonvin, A. M. (2007) HADDOCK versus HADDOCK: new features and performance of HADDOCK2.0 on the CAPRI targets. *Proteins* **69**, 726-733
45. Pettersen, E. F., Goddard, T. D., Huang, C. C., Couch, G. S., Greenblatt, D. M., Meng, E. C., and Ferrin, T. E. (2004) UCSF Chimera--a visualization system for exploratory research and analysis. *J Comput Chem* **25**, 1605-1612
46. Humphrey, W., Dalke, A., and Schulten, K. (1996) VMD: visual molecular dynamics. *J Mol Graph* **14**, 33-38, 27-38
47. Siegel, L. M., and Monty, K. J. (1966) Determination of molecular weights and frictional ratios of proteins in impure systems by use of gel filtration and density gradient centrifugation. Application to crude preparations of sulfite and hydroxylamine reductases. *Biochim Biophys Acta* **112**, 346-362

Chapter 5

Discussion and Future Directions

In the past decade, the ESCRT field has undergone an impressive scientific endeavor in an attempt to understand how this group of proteins functions in complex membrane remodeling activities. The ESCRT machinery is pivotal in membrane scission activity for MVE biogenesis and cytokinesis. Also, select viruses hijack ESCRT components for viral budding. One of the most striking features of the ESCRT machinery is the range in diameters it can accommodate to achieve membrane scission events. These diameters span from ~40-50 nm for nascent vesicle formation to ~200 nm to suit the large intracellular bridge during cytokinesis. Appreciating the diversity of cellular processes the ESCRT machinery functions in underscores the intricate mechanism utilized by these proteins. Furthermore, ESCRT-III proteins are conserved from archaea to mammals reaffirming the importance these proteins have in membrane remodeling events required at a very broad spectrum of life.

Since the ESCRT machinery is important for cellular homeostasis, dysfunction in this pathway comes at a cost. Specifically related to human health, mutations in ESCRT proteins have just begun to be linked to cancer and neurodegenerative diseases. As these links become clearer, understanding mechanistic details of the ESCRT machinery will be essential. It will only be through these insights that therapies will be developed to circumvent the underlying defects in ESCRT proteins. In this chapter, I will discuss how my work has added mechanistic details to better understand how the ESCRT-III complex functions in MVE biogenesis. I will also address some future directions based upon my findings.

A supercomplex of ESCRT-II and Vps20 senses membrane curvature... what is next?

The ESCRT complexes have membrane binding properties that have been well characterized *in vitro* (1-4). However, assembly of a functional ESCRT-III complex would need to be tightly controlled at a membrane surface to prevent premature scission activity. Curvature sensing proteins have been shown to provide spatiotemporal regulation across biology (5), which is a point of control that could help to address the tight regulation needed for ESCRT-III assembly. In Chapter Two, we demonstrate that a supercomplex of ESCRT-II and Vps20 has an increased affinity for lipid bilayers of elevated curvature. This conclusion was achieved through the use of liposome co-floatation assays and fluorescence-based liposome interaction studies (See **Figures 2.1 and 2.2**). To visualize this interaction, we utilized AFM and observed particle redistribution of proteins to the edges of the bilayer when ESCRT-II and Vps20 were both present (See **Figure 2.3**). Our AFM studies also found this supercomplex to direct ESCRT-III filament assembly to edges of the bilayer and that filament formation was sufficient to drive remodeling of lipid bilayers (See **Figure 2.4 and 2.5**).

From these data, we generated a model where ESCRT-II and Vps20 would bind to a vesicle bud neck, generating an ESCRT-III filament along that curved surface. The binding energy generated from polymerization of ESCRT-III would overcome the energy barrier for membrane fusion to occur (See Figure 2.5D). This model presents the first description of the spatiotemporal regulation within the ESCRT machinery as premature scission is prevented from occurring by the requirement of ESCRT-III assembly to be dependent upon curvature of the membrane.

This raises the important question of what specific proteins initiate membrane curvature to target ESCRT-III assembly. An *in vitro* reconstitution assay utilizing GUVs has shown that ESCRT-I and ESCRT-II together are able to induce membrane deformation (6). However, a caveat to this assay is the highly dynamic nature of GUVs, which includes their ability to undergo spontaneous membrane deformation, independent of proteins. Therefore, we favor a model where ESCRT-II and Vps20 are directly responsible for inducing membrane deformation. Our data has shown that ESCRT-II/Vps20 binding is proportional to the square of the membrane curvature suggesting this supercomplex is mechanosensitive. This would allow ESCRT-II/Vps20 to induce curvature as its binding affinity increased. Such a model would also help to rationalize why ESCRT-II and Vps20 are largely dispensable for cytokinesis and viral budding (7-9). In these two processes, membrane deformation is induced by proteins outside of the ESCRT machinery.

Future experiments will be necessary to understand how initial membrane deformation occurs for MVE biogenesis. It will be worthwhile to investigate if ESCRT-II, Vps20 and/or the supercomplex are able to penetrate the membrane as a potential mechanism to induce membrane bending. A possible experiment to begin to address this would be to conduct a tryptophan fluorescence quenching assay, which would utilize brominated phospholipids within liposomes. If any of these proteins demonstrated penetration into the bilayer, the positions of the bromines on the acyl chain could be used to determine the depth of insertion (10).

Conformational variation within the ESCRT-III subunits

The core ESCRT-III subunits are sequentially recruited during MVE biogenesis where each subunit has a unique function. Vps20 nucleates a filament of Vps32, Vps24 caps the filament, and Vps2 is the final subunit recruited where it plays a role in recruiting Vps4 for disassembly (11). The ESCRT-III subunits have been predicted to have the same structural architecture, which resides in a closed autoinhibited state within the cytoplasm. Studies have suggested that interaction with membranes and the upstream interacting ESCRT subunit would relieve autoinhibition (12-17). These structural similarities make it difficult to rationalize how each subunit has a specific role.

In Chapter 3 we demonstrate that two ESCRT-III proteins are in different conformations in solution. We show that Vps24 is in a closed, autoinhibited state, consistent with the previously reported SAXS models for human Vps24 (15). However, a unique finding was the observation that Vps20 was in an extended conformation that overlays with the crystal structure of human Vps24, which is presumed to resemble an activated ESCRT-III subunit (**Figure 3.3 and 3.7**). Additionally, we demonstrated that Vps20 is able to interact with ESCRT-II in solution. Based on these data, we favor a model where ESCRT-II directly interacts with an open conformation of Vps20 generating the supercomplex described in Chapter Two. This model would argue against ESCRT-II and membrane binding as triggers to release Vps20's autoinhibition since it is already in an open conformation. Future experiments will be necessary to determine how Vps32 recruitment and filament formation is regulated if Vps20 functions in an open conformation. Instead of the dramatic changes from a closed to open conformation previously hypothesized for Vps20, a more subtle structural change could occur, optimizing its

ability to engage Vps32. A study that showed conformational changes within Vps20 upon binding to membranes and ESCRT-II utilized environmentally sensitive fluorescent probes within Vps20 (17). A limitation of these probes is that the size of the spectral change does not correlate with the magnitude of conformational change. Therefore, these conformational changes observed in this study (17) will need closer characterization. Since both crystallographic and NMR techniques have been unsuccessful for full length Vps20 conformational changes could potentially be observed using a single molecule FRET system.

We also used SAXS on the late acting ESCRT-III subunit Did2 and discovered that it was in an extended conformation, similar to Vps20 (**Figure 5.1**). Did2 had a R_g and D_{max} of 30.0 and 96.0 Å, respectively. A major advantage to using SAXS for these experiments is that models are generated in solution without manipulation to the protein with fluorescent probes or tags. Therefore, SAXS will be an important technique to determine conformational states of additional late acting ESCRT-III subunits as the ESCRT field begins to tease out how these differences in conformation relate to function.

Characterization of the Vps32 filament

Circular arrays of ESCRT-III filaments have been identified both *in vitro* and *in vivo* but due to the low resolution nature of these structures a mechanism of assembly has not been identified yet (16,18,19). Chapter Four characterizes the spiral filament assembly of Vps32 using cryo-EM techniques (**Figure 4.1A**), which allowed for better resolution of filamentous structures. Also, this study utilized recombinant *C. elegans* Vps32 that did not require mutations, truncations, or high concentrations to observe homopolymerization, unlike several other studies that observed ESCRT-III filaments (16,18). We also show that Vps32 subunits

have flexibility within the center of the helical hairpin. Based on energy simulations, the lowest energy state corresponded to the bending angles of monomers at the center of a spiral and as the spiral extended outward the bending angles were in an elevated energy state (**Figure 4.3**).

Furthermore, removal of helix 6 from Vps32 reduced the spacing between filaments within the spiral (**Figure 4.4**). Together these data suggests that inherent properties within individual Vps32 monomers govern the overall architecture of a spiral and through the formation of this spiral energy can be stored. We propose a model where the release of individual Vps32 subunits from a spiral produces free energy that could be harnessed to accommodate membrane remodeling.

Additional experiments will be necessary to better understand how such filaments function *in vivo*. Experiments conducted in *S. cerevisiae* could be used to help address this area. Specifically, trafficking of MVE cargo could be observed in a Vps32 deletion strain of *S. cerevisiae* (20) expressing a mutant that inhibits spiral formation *in vitro* (a compliment of the Vps32^{V44W} mutant characterized in Chapter Four). Experiments such as these can be used to validate the findings in Chapter Four. Also, it will be important to study these filaments in the presence of additional ESCRT components and membranes. Specifically, Vps24 has been suggested to cap Vps32 filaments, so characterization of a capped filament by cryo-EM will be useful. Furthermore, membrane binding could largely impact filament formation, so modeling this aspect into the overall structures of a filament of Vps32 will be crucial to better understand the potential energetics such filaments would have within a cell.

Final Perspectives

This body of work represents the first experiments to identify a curvature sensing mechanism within the ESCRT machinery. This property provides regulation as to where membrane remodeling events would occur. This work has revealed that ESCRT-III subunits exist in different conformations, a finding that requires a reevaluation of the closed/open structural change that is currently accepted within the ESCRT field. Furthermore, characterization of the Vps32 filament has demonstrated the complexity utilized within the ESCRT-III complex to achieve membrane scission activity.

Through careful characterization of the ESCRT proteins, it is my hope the field will expand to understand how human health is impacted when this pathway goes awry. Perhaps inhibitors can be identified to block viral proteins from hijacking the membrane scission activity of the ESCRT proteins, reducing viral budding. Maybe one day effective treatments will be available for neurodegenerative diseases caused by mutations in ESCRT proteins. Regardless of the road ahead, the past decade has been an exciting time for the ESCRT field and the future looks even brighter as we begin to better understand this elegant group of proteins.

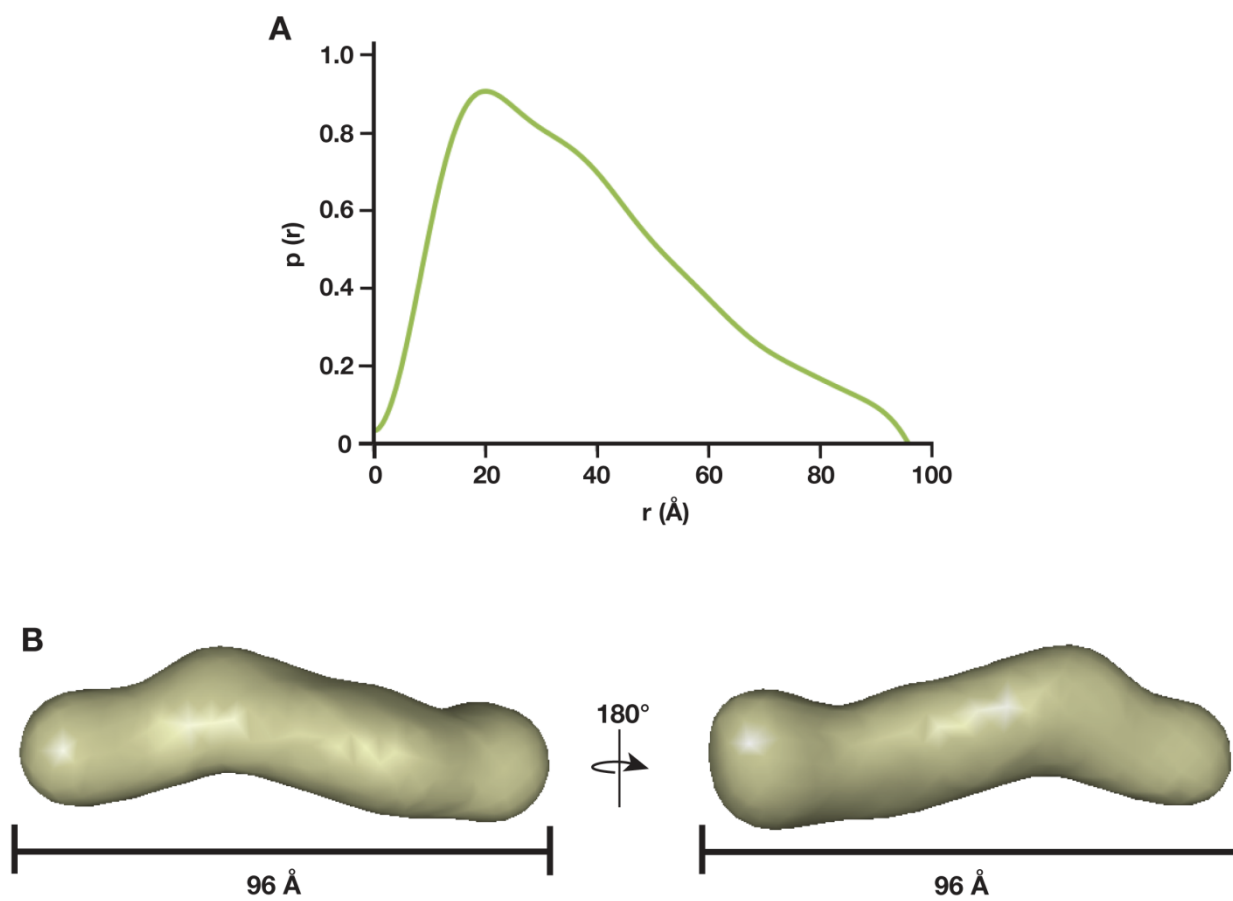


Figure 5.1: SAXS analysis of Did2

Figure 5.1: SAXS analysis of Did2

(**Figure 5.1A**) Pair distance distribution function plot generated from 6mg/mL Did2 data determined a D_{max} of 96 Å. (**Figure 3.3C**) *Ab initio* structure of Did2. Fifteen structures were generated using the program DAMMIF and averaged with DAMAVER, resulting in a NSD value of 0.81. Methods are consistent with SAXS methods described in Chapter Three.

REFERENCES

1. Stahelin, R. V., Long, F., Diraviyam, K., Bruzik, K. S., Murray, D., and Cho, W. (2002) Phosphatidylinositol 3-phosphate induces the membrane penetration of the FYVE domains of Vps27p and Hrs. *J Biol Chem* **277**, 26379-26388
2. Kostelansky, M. S., Schluter, C., Tam, Y. Y., Lee, S., Ghirlando, R., Beach, B., Conibear, E., and Hurley, J. H. (2007) Molecular architecture and functional model of the complete yeast ESCRT-I heterotetramer. *Cell* **129**, 485-498
3. Teo, H., Gill, D. J., Sun, J., Perisic, O., Veprintsev, D. B., Vallis, Y., Emr, S. D., and Williams, R. L. (2006) ESCRT-I core and ESCRT-II GLUE domain structures reveal role for GLUE in linking to ESCRT-I and membranes. *Cell* **125**, 99-111
4. Slagsvold, T., Aasland, R., Hirano, S., Bache, K. G., Raiborg, C., Trambaiolo, D., Wakatsuki, S., and Stenmark, H. (2005) Eap45 in mammalian ESCRT-II binds ubiquitin via a phosphoinositide-interacting GLUE domain. *J Biol Chem* **280**, 19600-19606
5. Antonny, B. (2011) Mechanisms of membrane curvature sensing. *Annu Rev Biochem* **80**, 101-123
6. Wollert, T., and Hurley, J. H. (2010) Molecular mechanism of multivesicular body biogenesis by ESCRT complexes. *Nature* **464**, 864-869
7. Langelier, C., von Schwedler, U. K., Fisher, R. D., De Domenico, I., White, P. L., Hill, C. P., Kaplan, J., Ward, D., and Sundquist, W. I. (2006) Human ESCRT-II complex and its role in human immunodeficiency virus type 1 release. *J Virol* **80**, 9465-9480
8. Carlton, J. G., and Martin-Serrano, J. (2007) Parallels between cytokinesis and retroviral budding: a role for the ESCRT machinery. *Science* **316**, 1908-1912
9. Morita, E., Sandrin, V., Chung, H. Y., Morham, S. G., Gygi, S. P., Rodesch, C. K., and Sundquist, W. I. (2007) Human ESCRT and ALIX proteins interact with proteins of the midbody and function in cytokinesis. *EMBO J* **26**, 4215-4227
10. Bolen, E. J., and Holloway, P. W. (1990) Quenching of tryptophan fluorescence by brominated phospholipid. *Biochemistry* **29**, 9638-9643
11. Teis, D., Saksena, S., and Emr, S. D. (2008) Ordered assembly of the ESCRT-III complex on endosomes is required to sequester cargo during MVB formation. *Dev Cell* **15**, 578-589
12. Lin, Y., Kimpler, L. A., Naismith, T. V., Lauer, J. M., and Hanson, P. I. (2005) Interaction of the mammalian endosomal sorting complex required for transport (ESCRT) III protein hSnf7-1 with itself, membranes, and the AAA+ ATPase SKD1. *J Biol Chem* **280**, 12799-12809

13. Shim, S., Kimpler, L. A., and Hanson, P. I. (2007) Structure/function analysis of four core ESCRT-III proteins reveals common regulatory role for extreme C-terminal domain. *Traffic* **8**, 1068-1079
14. Zamborlini, A., Usami, Y., Radoshitzky, S. R., Popova, E., Palu, G., and Göttlinger, H. (2006) Release of autoinhibition converts ESCRT-III components into potent inhibitors of HIV-1 budding. *Proc Natl Acad Sci U S A* **103**, 19140-19145
15. Lata, S., Roessle, M., Solomons, J., Jamin, M., Gottlinger, H. G., Svergun, D. I., and Weissenhorn, W. (2008) Structural basis for autoinhibition of ESCRT-III CHMP3. *J Mol Biol* **378**, 818-827
16. Henne, W. M., Buchkovich, N. J., Zhao, Y., and Emr, S. D. (2012) The endosomal sorting complex ESCRT-II mediates the assembly and architecture of ESCRT-III helices. *Cell* **151**, 356-371
17. Saksena, S., Wahlman, J., Teis, D., Johnson, A. E., and Emr, S. D. (2009) Functional reconstitution of ESCRT-III assembly and disassembly. *Cell* **136**, 97-109
18. Hanson, P. I., Roth, R., Lin, Y., and Heuser, J. E. (2008) Plasma membrane deformation by circular arrays of ESCRT-III protein filaments. *J Cell Biol* **180**, 389-402
19. Ghazi-Tabatabai, S., Saksena, S., Short, J. M., Pobbati, A. V., Veprintsev, D. B., Crowther, R. A., Emr, S. D., Egelman, E. H., and Williams, R. L. (2008) Structure and disassembly of filaments formed by the ESCRT-III subunit Vps24. *Structure* **16**, 1345-1356
20. Lottridge, J. M., Flannery, A. R., Vincelli, J. L., and Stevens, T. H. (2006) Vta1p and Vps46p regulate the membrane association and ATPase activity of Vps4p at the yeast multivesicular body. *Proc Natl Acad Sci U S A* **103**, 6202-6207

Appendix A

Mechanisms by which TFG Functions in Protein Secretion and Oncogenesis

The work presented in this chapter has been published:

Witte K*, Schuh AL*, Hegermann J, Sarkeshik A, Mayers JR, Schwarze K, Yates JR 3rd,
Eimer S, Audhya A.
(2011) *Nat Cell Biol.* 5:550-558.

*Denotes Equal Contribution

ABSTRACT

Export of proteins from the endoplasmic reticulum (ER) in COPII-coated vesicles occurs at defined sites, which contain the scaffolding protein Sec16. We identify TFG-1, a new conserved regulator of protein secretion that interacts directly with SEC-16 and controls the export of cargoes from the ER in *C. elegans*. Hydrodynamic studies indicate that TFG-1 forms hexamers, which enable SEC-16 and COPII coat components to co-assemble into large molecular weight complexes. Consistent with these findings, TFG-1 depletion leads to a dramatic decline in both SEC-16 and COPII levels at ER exit sites. The amino-terminus of human TFG, which mediates its self-association and its interaction with Sec16, was identified as a fusion partner of two protein kinases, creating a pair of oncogenes. We propose that fusion of these kinases to TFG relocalizes their activities to ER exit sites, where they prematurely phosphorylate substrates during ER export. Our findings provide a mechanism by which translocations involving TFG can result in cellular transformation and oncogenesis.

INTRODUCTION

The trafficking of most secretory cargoes begins with their export from the endoplasmic reticulum (ER) (1,2). In metazoans, cargoes are packaged into vesicles that emerge at defined sites on the ER and ultimately fuse with the ER-Golgi intermediate compartment (ERGIC). This process relies on the efficient recruitment of a set of soluble factors known as the COPII coat, which is composed of two multimeric protein complexes (Sec23/24 and Sec13/31) (3,4). A number of rare diseases have been directly linked to perturbations in COPII function, including Craniolenticulosutural dysplasia, in which a mutation in Sec23A leads to impaired collagen export from the ER (5,6). Although COPII coated vesicle formation has been reconstituted with purified coat proteins on synthetic membranes (7), regulators of COPII assembly remain largely unexplored.

Of the known COPII interacting proteins, two membrane-associated proteins, the small GTPase Sar1 and the putative scaffolding protein Sec16, are among the best characterized (8). When activated by the Sec12 exchange factor, Sar1 recruits the Sec23/24 complex, which forms an adaptor layer for Sec13/31 lattice assembly, completing the COPII coat (9,10). Sec23 also functions as a Sar1 activating protein, which is ultimately stimulated by Sec31, leading to coat disassembly following vesicle budding (11). In contrast to Sar1, which has only been shown to associate directly with Sec23, Sec16 interacts with all components of the COPII coat, potentially serving as a scaffold for their recruitment (12-15). Furthermore, Sec16 has been postulated to stabilize the COPII coat to prevent premature disassembly following activation of the Sec23 GAP (16). Surprisingly, few other proteins have been implicated in the regulation of COPII recruitment. Considering the necessity for controlling secretory flux during cell differentiation

and development, additional factors that govern this process likely exist, and some may function via direct regulation of Sar1 or Sec16. Here, we report the identification of a new, conserved regulator of ER export, which interacts directly with Sec16 and controls COPII subunit accumulation at ER exit sites.

RESULTS

Identification of SEC-16 interacting proteins in *C. elegans*

Based upon the sequence of human Sec16A, we identified a Sec16 homolog in *C. elegans* encoded by the open reading frame ZK512.5, which we named *sec-16*. The homology was largely restricted to the central conserved domain (CCD) found in all Sec16 isoforms (**Figure A.1a**). We generated a polyclonal antiserum directed against SEC-16, which recognized a band at the appropriate molecular weight (~135 kD) following immunoblot analysis of *C. elegans* embryo extract (**Figure A.S1a**). Antibodies were used to immunoprecipitate SEC-16 and associated proteins from detergent-solubilized embryo extracts (**Figures A.S1b and A.S1c**). We then conducted solution mass spectrometry to identify 19 proteins that were specifically and reproducibly isolated by SEC-16 antibodies. Since Sec16 is required for ER export and viability in other organisms, we reasoned that proteins that function with Sec16 would likely be essential in *C. elegans*. We depleted each of the 19 proteins using RNA interference (RNAi) and found that 7 gene products were necessary for embryo production (**Figure A.1b**). Among these were SEC-16, four different COPII subunits (SEC-23, SEC-24.2, SEC-13, and SEC-31), the Sar1 specific GEF SEC-12, and a protein not previously implicated in protein trafficking named TFG-1.

We focused our attention on the novel interaction between SEC-16 and TFG-1. We generated a polyclonal antiserum directed against the full length TFG-1 protein, which was affinity purified. Immunoblot analysis of whole worms using TFG-1 antibodies revealed at least two closely migrating bands immediately below the 75 kD molecular weight marker, significantly larger than the predicted size of 49.8 kD (**Figure A.S1d**). Similarly, recombinant

TFG-1 also exhibited a slow migration on SDS-PAGE (see **Figure A.1f**). Analysis of a SEC-16 immunoprecipitate using TFG-1 antibodies confirmed their interaction initially identified using solution mass spectrometry (**Figure A.1c**), and TFG-1 immunoprecipitation led to an enrichment of SEC-16 (**Figure A.1d**). To determine whether the interaction was direct, we generated recombinant forms of both TFG-1 and SEC-16 and measured their association *in vitro*. We found that a GST-fusion to full length SEC-16, but not GST alone, was capable of binding to recombinant TFG-1 (**Figure A.1e**). To further characterize their interaction, we generated polyhistidine-tagged recombinant forms of full length TFG-1 and two truncations of TFG-1 encoding the amino-terminus (amino acids 1-195) and carboxyl-terminus (amino acids 196-486), and measured their ability to interact with endogenous SEC-16. In a similar fashion to the full-length recombinant protein, the amino-terminal portion of TFG-1 was able to bind to SEC-16, while the carboxyl-terminus did not (**Figure A.1f**). Together, these data confirm a direct biochemical association between SEC-16 and TFG-1.

TFG-1 localizes to ER exit sites with SEC-16

To determine whether SEC-16 interacts with TFG-1 at ER exit sites, we conducted a series of immunofluorescence studies. We first chose to examine the *C. elegans* reproductive system, which is both enriched for TFG-1 (**Figure A.S1e**) and contains large proximal oocytes that are amenable to high magnification confocal microscopy. The TFG-1 antibodies stained punctate structures throughout the cytoplasm of oocytes, 85% of which co-localized with SEC-16 on ER exit sites (**Figure A.2a**). In many cases, we observed that the TFG-1 staining extended beyond the puncta labeled with SEC-16 (**Figure A.2a**, see 6x zoom). Using immuno-gold electron microscopy (EM), we further defined the localization of TFG-1 in proximal oocytes to a

cloud-like region at ER exit sites that spread to the ERGIC (**Figure A.2b**). The high concentration of labeling observed suggested that TFG-1 may form some type of matrix in this region, which would correspond well to the elevated electron density seen there by EM. Furthermore, dual immuno-gold labeling with polyclonal TFG-1 and monoclonal SEC-13 antibodies indicated that both proteins localize to an identical area next to ER exit sites, although the SEC-13 labeling was more discrete (**Figure A.2c**). Based on these data, we conclude that TFG-1 localizes to ER exit sites with both SEC-16 and COPII machinery.

In parallel with these studies, the architecture of ER exit sites was also examined using EM and three-dimensional reconstruction. Our data demonstrate that ER exit sites, which harbor SEC-13, range in size from 70-150 nm, and always contain coated buds emerging from smooth ER that are directed toward ERGIC and Golgi membranes (**Figures A.2d and A.S1f-A.S1h**). Electron tomography was used to confirm these findings and provide a high-resolution depiction of COPII vesicle biogenesis in the early secretory pathway (**Figure A.3a**). Consistent with these observations and our data showing that TFG-1 localizes specifically to ER exit sites, we failed to observe co-localization between TFG-1 and the glucuronyl transferase SQV-8, a marker of the cis/medial Golgi (**Figures A.S1i**). Instead, TFG-1 appeared directly adjacent to SQV-8 labeled structures, further illustrating that in *C. elegans*, ER exit sites are closely juxtaposed to the Golgi, forming an integrated secretion unit.

We next examined the distal region of the *C. elegans* germline, which constitutes a stem cell niche that constitutively requires membrane biosynthesis and secretion to generate partitions between rapidly dividing nuclei (17). EM studies revealed that ER exit sites in this region of the gonad were morphologically similar to those seen in the proximal gonad (**Figure A.3b**).

Immunofluorescence analysis of exit sites in the distal region of the *C. elegans* germline revealed a distribution of intensities for both SEC-16 and TFG-1 (**Figures A.3c and A.3d**). However, the ratio of the fluorescence intensities between SEC-16 and TFG-1 largely did not vary among different ER exit sites, indicating that in wild-type animals, levels of SEC-16 correlated with those of TFG-1, regardless of whether they were high or low (Supplementary Information, **Figure A.S2a**).

To determine localization dependencies between TFG-1 and SEC-16, we depleted each protein using RNAi and examined the localization of the other. Depletion of TFG-1 did not result in a significant decline in the number of SEC-16 labeled ER exit sites (**Figure A.S2b**). However, the distribution of SEC-16 intensities was dramatically altered under these conditions (**Figure A.3d**). The number of exit sites harboring a high level of SEC-16 declined significantly (approximately 30-fold), while the number of low intensity sites increased approximately 2-fold. As the stability of SEC-16 was not diminished following depletion of TFG-1 (**Figure A.3e**), these data suggest that TFG-1 controls the abundance of SEC-16 at ER exit sites. Depletion of SEC-16 led to nearly complete loss of puncta labeled by TFG-1, and the few structures that were observed appeared abnormally large, concentrated within small regions of the germline and did not co-stain for the COPII component SEC-13 (**Figure A.3c** and our unpublished data). Based on these studies, we conclude that TFG-1 requires SEC-16 for its localization, while SEC-16 requires TFG-1 to accumulate normally on ER exit sites.

TFG-1 self-associates to form hexamers that regulate proper SEC-16 complex assembly

Based on size exclusion chromatography, both endogenous SEC-16 and TFG-1 exhibit similar elution profiles, which correspond to globular complexes larger than 800 kD (**Figure**

A.4a). Since TFG-1 was amenable to recombinant expression, we measured its Stokes radius (107.8 Å) and sedimentation value (7.0 S) in the absence of SEC-16 (**Figure A.4b**). Based on these data, we calculated the native molecular weight of TFG-1 to be ~318 kD, nearly identical to the predicted molecular weight of a TFG-1 hexamer. Furthermore, we found that the amino-terminus assembled into an octamer, while the carboxyl-terminus formed a dimer (**Figures A.4c and A.4d**). These data suggest that the amino-terminus of TFG-1 mediates its oligomerization, while the carboxyl-terminus may play a role in restricting the full-length protein to forming hexamers in solution. Since levels of TFG-1 and SEC-16 at ER exit sites co-vary in control animals and loss of TFG-1 leads to diminished accumulation of SEC-16 on ER exit sites, such hexamers of TFG-1 likely play an important role in proper SEC-16 complex assembly. Consistent with this idea, depletion of TFG-1 caused a reduction in the Stokes radius of SEC-16 (by ~70 Å) isolated from whole animals (**Figure A.4e**). Concomitantly, loss of TFG-1 also affected the assembly of complexes containing COPII coat proteins. Analysis of native SEC-13 by size exclusion chromatography demonstrated that the COPII subunit is a component of a large molecular weight complex (Stokes radius of 128.1 Å), similar in size to SEC-16 and TFG-1 (**Figure A.4e**). In addition, SEC-13 was found in a 54.3 Å complex, which likely corresponds to the elongated SEC-13/SEC-31 heterotetramer that was described previously (10), and as a globular monomer (Stokes radius of 23.9 Å). However, following TFG-1 depletion, the majority of SEC-13 was found in a monomeric state (Stokes radius of 24.2 Å), although we continued to detect the COPII subunit in high molecular weight fractions as well. Taken together, we conclude that the normal assembly of large complexes containing SEC-16 and COPII subunits is facilitated by TFG-1 hexamers.

TFG-1 is required for protein secretion

The *C. elegans* germline is a complex tissue whose structure depends on continuous membrane synthesis and secretion. In contrast to individual cells grown in culture, the surface area of compartments within the germline must be rapidly replenished in a relatively short timescale to support ongoing embryo production. In the absence of secretion, oocyte and embryo biogenesis cease, and compartments within the germline fail to segregate nuclei that are dividing in the distal stem cell niche (our unpublished data). Thus, the germline offers an ideal setting to study the requirements for membrane and protein secretion.

Using RNAi, we have shown that TFG-1 is required for normal SEC-16 accumulation on a subset of ER exit sites. Since SEC-16 is one of two proteins required to recruit COPII components, we examined the fate of COPII localization in animals with and without TFG-1. In control animals, the COPII subunit SEC-13 is found in close apposition to SEC-16 labeled exit sites, as well as on the nuclear envelopes of proliferating germ nuclei (**Figure A.5a**). Following depletion of TFG-1, the intensities of both SEC-13 and SEC-16 on punctate structures within the germline declined dramatically, while localization of SEC-13 to the nuclear envelope was largely unaltered (**Figure A.5a**). By measuring the fluorescence intensities of SEC-13 and SEC-16 in control and TFG-1 depleted animals, we found that their ratio was not altered significantly, indicating that the remaining SEC-16 on ER exit sites can continue to recruit COPII components in the absence of TFG-1, albeit to lower levels (**Figure A.5b**).

To determine whether the substantially reduced levels of SEC-16 and SEC-13 were sufficient to support protein secretion following TFG-1 depletion, we examined a number of different secreted integral membrane proteins. The v-SNARE synaptobrevin (SNB-1), which

contains a single transmembrane domain, is synthesized on the rough ER and transported via the Golgi and endosomes to the plasma membrane in the *C. elegans* germline (18). Under steady state conditions in the distal region of the germline, the majority of a GFP fusion to SNB-1 (GFP:SNB-1) co-localizes with a mCherry fusion to the PH domain of rat PLC1d1 (mCherry:PH), which binds to phosphatidylinositol 4,5-bisphosphate generated specifically on the plasma membrane (**Figure A.5c**). However, in TFG-1 depleted animals, GFP:SNB-1 is not secreted to the plasma membrane and instead accumulates in the ER (**Figure A.5c**). Similarly, we found that several other transmembrane proteins, including the *C. elegans* caveolin-like protein CAV-1 and the glucuronyl transferase SQV-8, which normally traffic to other organelles following synthesis, accumulate in the ER in the absence of TFG-1 (**Figures A.S2c and A.S2d**).

The loss of ER exit site function in mammalian cells causes a perturbation in Golgi morphology. To examine the effect of TFG-1 depletion on the *C. elegans* Golgi network, we took advantage of serial section EM and three-dimensional reconstruction. In control animals, ER exit sites were juxtaposed to well-organized stacks of membranes corresponding to the ERGIC and Golgi cisternae (**Figure A.5d**, left). Vesicles that were 48.2 ± 1.2 nm ($n=15$) in diameter were observed throughout the region between the ER and ERGIC. In contrast, subsequent to TFG-1 depletion, ERGIC and Golgi membranes appeared smaller and more poorly stacked, and the ER became fragmented (**Figure A.5d**, right). In addition, fewer Golgi networks were observed in serial sections of germline cells. However, consistent with our findings that reduced levels of SEC-16 at ER exit sites can continue to recruit COPII following depletion of TFG-1, we identified vesicles that were 48.8 ± 0.7 nm ($n=39$) in diameter between the ER and the ERGIC. Although the sizes of vesicles were not affected by TFG-1 depletion, their

distribution was altered. The majority of vesicles observed accumulated close to the ER and failed to migrate toward the ERGIC and Golgi membranes. These data suggest that TFG-1 is required for the efficient, directed movement of COPII vesicles away from the ER, but not for their initial formation.

To further characterize perturbations in Golgi organization that occurred following inhibition of TFG-1, we generated animals that stably express a GFP fusion to the RAB-6 small GTPase, which mediates retrograde transport from the Golgi to the ER. Since RAB-6 has also been shown to cycle between the Golgi and early endosomes (19), we co-expressed a mCherry fusion to the early endosome marker RAB-5, to allow us to distinguish endosome-associated RAB-6 from Golgi-associated RAB-6. In control animals, RAB-5 and RAB-6 exhibited distinct localizations in the distal region of the germline, with RAB-6 localizing to the Golgi and RAB-5 enriched on many small puncta underlying the plasma membrane (**Figure A.S2e**). Following depletion of either SEC-16 or TFG-1, RAB-6 localization was altered, accumulating on fewer, large punctate structures in the germline. The puncta containing RAB-6 also harbored RAB-5, suggesting that RAB-6 localization was shifted from the Golgi to enlarged early endosomes (**Figure A.S2e**). These data are again consistent with the idea that TFG-1 depletion leads to a defect in normal Golgi assembly.

Human TFG localizes to ER exit sites and interacts with Sec16

Using the amino acid sequence of *C. elegans* TFG-1, we were able to identify a single human homolog, previously annotated TFG (for TRK-fused gene; **Figure A.S3a**). To explore whether human TFG plays a similar role to its *C. elegans* counterpart, we generated a GFP fusion to the full-length protein and transiently expressed it in HeLa cells. A mCherry fusion to

Sec16B was co-transfected to label ER exit sites. Analysis of cells expressing both markers indicated that greater than 90% of GFP:TFG labeled puncta also contained mCherry:Sec16B (**Figure A.6a**). These data indicate that similar to *C. elegans* TFG-1, human TFG functions at ER exit sites.

Our co-localization studies are consistent with two potential models for Sec16B and TFG accumulation on ER exit sites. Both proteins may associate in the cytoplasm prior to loading onto exit sites or they may be targeted in distinct steps. To determine whether TFG and Sec16B co-assemble prior to accumulating on ER exit sites, we examined their individual dynamics using fluorescence recovery after photobleaching (FRAP). Similar to GFP:Sec16A (20), we found that only a fraction (56.8 +/- 6.3%) of the fluorescence of mCherry:Sec16B recovered following photobleaching, with a half-time of 5.68 +/- 0.34 seconds. In contrast, a smaller proportion of GFP:TFG recovered (33.6 +/- 5.1%), which exhibited a longer half-time of 8.22 +/- 0.64 seconds (**Figures A.6b and A.6c**). These data indicate that Sec16B and TFG are not loaded onto exit sites simultaneously, and instead suggest that they assemble onto ER exit sites via distinct mechanisms.

To further explore whether the characteristics of *C. elegans* TFG-1 are conserved, we conducted a series of hydrodynamic measurements of human TFG. Similar to our findings with the *C. elegans* homolog, endogenous human TFG exhibited a large Stokes radius corresponding to a globular complex of greater than 700 kD (**Figure A.6d**). We further found that the amino-terminus of TFG (amino acids 1-193) forms an octamer, like its *C. elegans* counterpart, with a native molecular weight of 172 kD (**Figures A.6e and A.6f**). Thus, human TFG and *C. elegans* TFG-1 share multiple physical properties, which suggest they share a common function *in vivo*.

Consistent with these findings, depletion of TFG caused a substantial delay in the secretion of VSVG(ts045)-GFP, a type I transmembrane protein widely used in studying the mammalian secretory pathway (**Figure A.S3b**).

In *C. elegans*, TFG-1 coimmunoprecipitates with SEC-16. To determine whether human TFG similarly binds to Sec16, we first generated a stable HeLa cell line expressing mCherry:Sec16B. We transiently transfected these cells with either a GFP fusion to full length TFG or to the amino-terminus of TFG, and conducted immunoprecipitations using mCherry antibodies. We found that endogenous TFG was recovered under these conditions (**Figure A.6g**). Additionally, we found that both GFP-tagged isoforms were able to bind to mCherry:Sec16B (**Figure A.6g**). These data support the idea that the amino-terminus of TFG interacts with Sec16 in an evolutionarily conserved manner.

Fusion of the TFG amino-terminus to the NTRK1 kinase domain redirects its localization

TFG was initially identified as part of a gene fusion with the receptor tyrosine kinase NTRK1 (also called TrkA), resulting in the formation of an oncogene that is capable of transforming cells and causing papillary thyroid cancer (21). Further studies have shown that TFG is also a fusion partner of the receptor tyrosine kinase ALK in some anaplastic large cell lymphomas (22). In both instances, the amino-terminus of TFG is fused to the other gene, resulting in an oncogenic product. One possible mechanism by which fusion to TFG might cause these kinases to transform cells is through their mislocalization to ER exit sites that contain Sec16. To investigate this idea further, we first expressed the amino-terminus of TFG as a GFP fusion in HeLa cells to determine where it accumulates. Consistent with our finding that this

domain of TFG interacts with Sec16, the amino-terminus of TFG was largely targeted to ER exit sites (**Figure A.7a**).

The portion of NTRK1 that is fused to TFG in some papillary thyroid tumors includes its kinase and transmembrane domains (21). On its own, this region of NTRK1 (which lacks a signal sequence) accumulates mostly in the cytoplasm, although a fraction of the protein also appears to associate with the nuclear envelope (**Figures A.7b**). However, when linked to the amino-terminus of TFG, the majority of the oncogenic fusion protein is targeted to ER exit sites (**Figures A.7c and A.7d**). These data demonstrate that the amino-terminus of TFG is sufficient to redirect the localization of the NTRK1 kinase domain.

Mistargeting of the NTRK1 kinase domain to ER exit sites causes the hyperactivation of downstream NTRK1 effectors and cell transformation

NTRK1 is primarily expressed in the nervous system where it functions as a high affinity receptor for nerve growth factor (NGF) (23). The binding of NGF to NTRK1 leads to its dimerization and autophosphorylation, ultimately causing the activation of several downstream signaling cascades, including the Ras/Raf/MEK/ERK pathway, to promote cell survival and growth (24). Unlike normal NTRK1, the oncogenic TFG-NTRK1 fusion protein is constitutively active and causes cell transformation (25). Consistent with this finding, expression of GFP-TFG-NTRK1 in the telomerase immortalized hTERT-RPE1 cell line caused an increase in the levels of phospho-ERK1/2, as compared to control cells, which exhibit a low level of basal ERK1/2 activity (**Figure A.7e**). To determine whether dimerization of the kinase domain is sufficient to initiate signaling downstream of NTRK1, we linked the constitutive dimer GST to NTRK1 and expressed it as a GFP fusion in hTERT-RPE1 cells. Under these conditions, levels

of phospho-ERK1/2 increased by only 2-fold as compared to control cells (**Figure A.7e**). These data indicate that dimerization of the NTRK1 kinase domain alone is not adequate to cause the hyperactivation of its downstream effectors as is observed following TFG-NTRK1 expression.

As suggested earlier, an alternative mechanism by which fusion to TFG may cause constitutive NTRK1 kinase activity is through mislocalization of NTRK1 to ER exit sites. Therefore, we tested the effect of targeting the NTRK1 kinase domain to exit sites independently of TFG. We fused a region of Sec16B (amino acids 1-791), which localizes to ER exit sites similarly to the full length protein, to NTRK1 and expressed it as a GFP fusion in hTERT-RPE1 cells (GFP:Sec16B-NTRK). Hydrodynamic analysis of a portion of this region in Sec16B (amino acids 34-234) indicated that it oligomerizes *in vitro* (**Figure A.S4a**). As we predicted, GFP-Sec16B-NTRK1 localized to ER exit sites (**Figure A.S4b**). Moreover, expression of this fusion protein resulted in hyperactivation of ERK1/2, similar to the effect following GFP-TFG-NTRK1 expression (**Figure A.7e**). We conclude that targeting of the NTRK1 kinase domain to ER exit sites is necessary for its constitutive activity in cells.

To test whether the ER exit site-targeting of NTRK1 was sufficient to transform cells, we generated NIH3T3 cell lines expressing either GFP, GFP:GST-NTRK1, GFP:TFG-NTRK1, or GFP:Sec16B-NTRK1. These cells were plated onto a monolayer of control, contact-inhibited NIH3T3 cells and examined for colony formation after 2 weeks. Cells expressing the ER exit site-targeted forms of NTRK1 produced at least 8-fold more colonies than the dimerized form of NTRK1 (**Figure A.S4c**). Consistent with our previous results, these data suggest that localization of NTRK1 to ER exit sites strongly contributes its ability to transform cells.

DISCUSSION

Using biochemical and genetics approaches, we have demonstrated that TFG-1 localizes to ER exit sites and is required for protein secretion in the *C. elegans* germline. Additionally, we have found that TFG-1 localizes to ER exit sites in several other tissues, including the intestine, hypodermis, and muscle (**Figures A.S4d-A.S4f**), suggesting a common function in all tissues. Immunofluorescence studies further indicate that TFG-1 does not localize to other membrane compartments, including the Golgi, early endosomes, late endosomes, and mitochondria (our unpublished data). However, TFG-1 has been implicated previously in the regulation of apoptosis in *C. elegans*. Following TFG-1 depletion, the number of apoptotic corpses seen during embryogenesis increases as compared to wild type, while overexpression of TFG-1 diminishes the number of corpses (26). Although a direct role for TFG-1 in these processes has yet to be defined, both phenotypes could result from modulations in the secretory pathway, since membrane deposition must be appropriately regulated during the clearance of apoptotic cells. For example, the loss of corpses observed following overexpression of TFG-1 may be an indirect consequence of an increase in secretory flow, which could accelerate the clearance of apoptotic bodies. Consistent with this idea, overexpression of human TFG has been shown to partially rescue the trafficking defect of mutant F508del-CFTR, which aberrantly accumulates in the ER in cystic fibrosis patients (27,28). Since levels of TFG-1 at ER exit sites appear to correlate with levels of SEC-16 and COPII, additional TFG-1 may increase COPII recruitment and stimulate secretion from the ER.

Based on our data, we speculate that TFG-1 in *C. elegans* and TFG in mammalian cells generate a matrix at ER exit sites that facilitates proper SEC-16 complex assembly and COPII

vesicle transport from the ER. In the absence of TFG family members, ER exit sites still form, but Sec16 levels on these sites decline, diminishing COPII recruitment and thereby dramatically slowing ER export. Therefore, a polymerized TFG matrix at ER exit sites may serve as a molecular sink, which helps to retain COPII components locally and facilitate efficient vesicle formation and egress. The increased membrane flux mediated by TFG-1 may also function to maintain proper Golgi organization in tissues under a high secretory demand, such as the *C. elegans* germline. Together, our findings reveal a novel component of the early secretory pathway that regulates anterograde trafficking from the ER.

Not all ER exit sites are created equally

In cultured cells of *Drosophila* and human origin, the levels of endogenous Sec16 on individual ER exit sites appear similar (29,30). In contrast, *C. elegans* SEC-16 levels vary considerably between different exit sites in the stem cell niche of the germline. Unlike other tissues, this region of the *C. elegans* gonad requires rapid and constitutive secretion to maintain partitions between continually dividing germ nuclei. One mechanism to accommodate such a demanding condition would be to increase COPII levels at ER exit sites and thereby enhance secretory flux (31). Previous work has shown that exit sites adapt to chronic increases in cargo load through accumulation of additional COPII subunits and Sec16 (32), a phenotype similar to that we observe in the distal *C. elegans* germline. Our data further indicate that increased levels of SEC-16 correlate with increased levels of the COPII subunit SEC-13, supporting a previously proposed model in which SEC-16 acts as a scaffold for COPII assembly (33). Such an arrangement of the early secretory pathway would allow for rapid changes in secretory flux via

the modulation of a single factor, Sec16, and may be especially important during development and the differentiation of certain cell types.

TFG is a proto-oncogene that functions at ER exit sites

Human TFG has been implicated in several types of cancer, including thyroid papillary carcinoma, anaplastic large cell lymphoma and extraskeletal myxoid chondrosarcoma (34). In each case, the amino-terminal portion of TFG is fused to a different gene, creating oncogenic fusions capable of transforming cells. This region of TFG has been shown to possess multiple functions that are required for transforming activity (35). Based on our findings, the amino terminus of TFG forms octamers, and fusion of this domain to another protein would likely force that protein to multimerize. In support of this idea, previous studies suggest that the TFG-NTRK1 fusion protein, which joins the TFG amino-terminus with the NTRK1 kinase domain, forms homo-oligomeric complexes (35). Although dimerization of the NTRK1 kinase domain is necessary for its activity, mutations in TFG that do not affect multimerization of the TFG-NTRK1 fusion protein can inhibit its transforming activity, suggesting additional functions for the TFG amino terminus (23,35). Our findings indicate that this region of TFG is sufficient to target the NTRK1 kinase domain to ER exit sites and that localization of multimerized NTRK1 plays a key role in its ability to initiate downstream signaling cascades that cause cell transformation, including the pathway leading to ERK1/2 activation. This finding provides a key insight into the mechanism by which TFG functions as a proto-oncogene. By concentrating constitutive NTRK1 kinase activity at ER exit sites, multiple effectors may be prematurely activated that lead to cell transformation. Additionally, the matrix formed by TFG and Sec16 may further enable transformed cells to sustain a high secretory activity, which could further

augment the oncogenic process. Notably, stimulation of ERK2 at ER exit sites may cause hyperphosphorylation of Sec16, and lead to formation of new exit sites that would recruit additional TFG-NTRK1 (36). Such a feed-forward mechanism may play an important role during oncogenesis. In the future, it will be interesting to determine whether TFG and/or Sec16 levels are upregulated in human cancers.

MATERIALS and METHODS

Antibodies

C. elegans SEC-16, TFG-1, and CYP-33E1 antibodies were raised in rabbits by immunization with GST fusions to either a fragment of SEC-16 (amino acids 813-1014), full length TFG-1, or a fragment of CYP-33E1 (amino acids 244-392) produced in *E. coli*. The antibodies were affinity purified from serum by binding to columns of the same antigens following removal of the GST tags by cleavage with PreScission protease. To produce SEC-13 specific monoclonal antibodies, 10 mice were each immunized with 50 µg of purified GST-SEC-13 fusion protein in PBS using complete Freund's adjuvant. Six booster injections were given thereafter every 4th week with the same amount of antigen in incomplete Freund's adjuvant. 30 days after the last injection, hybridoma fusions were generated and subsequently screened by ELISA according to standard protocols. Mouse monoclonal SEC-13 antibodies were purified via Protein-A Sepharose beads according to the manufacturer's protocol. Antibodies directed against human TFG were purchased from Bethyl Laboratories (A302-341A and A302-343A). Antibodies against ERK1/2 and phospho-ERK1/2 were obtained from Millipore (06-182) and Invitrogen (44680G), respectively. CAR-1, SQV-8, GFP and mCherry antibodies have been described elsewhere (37-39).

Immunofluorescence, Live Imaging, and Electron Microscopy

Images were acquired on a swept field confocal microscope (Nikon Ti-E) equipped with a Roper CoolSnap HQ2 CCD camera using a Nikon 60X, 1.4NA Planapo oil objective lens. Acquisition parameters were controlled by Nikon Elements software, and image analysis was conducted using Metamorph software. Immunofluorescence of fixed gonads was performed as described

previously (38) using directly labeled rabbit antibodies at a concentration of 1 mg/mL. Briefly, 60-120 Z sections at 0.2 mm steps were acquired (depending on sample thickness). The fluorescence intensity of each ER exit site was always confined to a maximum of seven Z planes, which were used to generate a maximum intensity projection. In some cases, an ER exit site from one Z section interfered with the analysis of another ER exit site in a different Z section. These ER exit sites were not analyzed further. To calculate the fluorescence intensity of proteins that localize to ER exit sites, the total intensity in a box containing the ER exit site (from a maximum intensity projection) was measured and the camera background was subtracted. For live imaging of *C. elegans* gonads, animals were anesthetized and mounted on an agarose pad. HeLa cells were grown on 35-mm glass bottom dishes maintained at 37°C for time-lapse imaging. Photobleaching was performed using a 405-nm laser, which was coupled into a Nikon Photo Activation Illuminator Unit to create a single diffraction limited spot. In photobleaching experiments, ten Z sections at 0.2 mm steps were acquired at 5 sec intervals. Analysis was limited to ER site sites that were visible in at least five Z sections during the entire timecourse. The signal at the first post-bleach time point was subtracted from all post-bleach measurements, and the percentage of fluorescence recovered at each time point was calculated by dividing by the difference between the pre-bleach and first post-bleach measurements. Kaleidagraph software was used to fit the data and calculate the maximal fractional recovery and the half-time for recovery. To determine the percent co-localization between two proteins, ER exit sites were analyzed individually using Nikon Elements software. The VSVG(ts045)-GFP trafficking assay was conducted as described previously, with modifications as noted in the legend for Figure S3b (40).

For high pressure freezing, a 100 mm deep aluminum platelet (Microscopy Services) was filled with 20 adult worms in a suspension of *E. coli* and frozen using a BalTec HPM 10. Freeze substitution was carried out in a Leica EM AFS at -90°C for 100 hours in 0.1% tannic acid, followed by 7 hours in 2% osmium tetroxide as described previously (41). For electron microscopy studies, 50 nm longitudinal sections of *C. elegans* were cut using a Leica UC6 ultramicrotome. Ribbons of sections were transferred onto Formvar-coated copper slot grids. The grids were placed in drops of 4% uranyl acetate, washed with water, and dried. They were then transferred onto lead citrate (42) and rinsed again with water. Micrographs were taken with a Proscan CCD HSS in a Zeiss EM 902A electron microscope operated in bright field mode. For 3D reconstructions, serial sections of ER exit sites were imaged, and files were aligned linearly using the software Reconstruct (43). For electron tomography, 250-300 nm EPON sections were transferred onto Formvar-coated copper slot grids and stained similarly as described for thin sections. 10 nm gold beads were applied to both sides. An orthogonal tilt series was acquired on a JEOL JEM 2100 at 200 kV from -55° to 55° (1° increments). Reconstruction was done using IMOD software (<http://bio3d.colorado.edu/imod>). Immuno-electron microscopy was conducted as described previously (41).

Worm Strains, RNA interference and Cell Culture

All *C. elegans* strains were derived from the Bristol strain N2. The generation of animals expressing fluorescent fusions with CAV-1, SNB-1 and the PH domain of rat PLC1d were described previously (18,39). Double stranded RNA (dsRNA) was synthesized as described previously (38) from templates prepared by using primers listed in the Methods section to amplify N2 genomic DNA. For most RNAi experiments, early L4 stage hermaphrodites were

soaked in dsRNA for 24 hours at 20°C within a humidified chamber. Animals were allowed to recover for 48 hours prior to analysis. For partial depletions, late L4 stage worms were soaked in dsRNA for 24 hours, followed by a 22 hour recovery period, and then analyzed. For large-scale depletion of TFG-1 necessary for gel filtration studies, L4 animals were fed bacteria expressing dsRNA directed against TFG-1 for 72 hours, prior to harvesting and extract preparation. HeLa and NIH3T3 cells were maintained in DMEM supplemented with 10% FBS (HeLa) or 10% FCS (NIH3T3), penicillin/streptomycin, and L-glutamine at 37°C in the presence of 5% CO₂.

hTERT-RPE1 cells were grown similarly, with the exception that DMEM/F-12 media was used. Transfections were conducted using Lipofectamine 2000 (Invitrogen), and cells were selected using puromycin (1 mg/mL for HeLa cells and 12.5 mg/mL for hTERT-RPE1 cells). Colony formation assays on monolayers of contact-inhibited NIH3T3 cells were performed as described previously (44).

Primers, dsRNAs, and plasmids used in this study

To generate dsRNAs directed against TFG-1, the following primer sets were used:

(AATTAACCCTCACTAAAGGCTGCTGTGGTGGAGCATATC and
TAATACGACTCACTATAGGATCTCTCGGCTCCAAAACAA),

(AATTAACCCTCACTAAAGGCTTAATCTGCTCGACTTGCT and
TAATACGACTCACTATAGGATGGTGCATTCAAACGGAGC), and

(AATTAACCCTCACTAAAGGTTACTGCTGATACGGCGACT and
TAATACGACTCACTATAGGCAGCAGCAGCAATTCGGAGC). Each dsRNA produced using these primer sets yielded similar results. To generate dsRNAs directed against SEC-16, the following primer sets were used:

(AATTAACCCTCACTAAAGGGCGGTCTGCGAGTTTAGATT and TAATACGACTCACTATAGGCAAGCGGATGCAAGAAGAAT), (AATTAACCCTCACTAAAGGGCAAACCTGTAATTTAAAAT and TAATACGACTCACTATAGGCTTCTGGTTTCGATATGAGT), and (AATTAACCCTCACTAAAGGCTCCACTTCTAGCACTTCGC and TAATACGACTCACTATAGGGTAACGATCAACAACATAAC). Each dsRNA produced using these primer sets yielded similar results. In all cases, primers were used to amplify genomic DNA, and PCR products were cleaned (DNA clean and concentrator kit, Zymo Research). The PCR products were then used as templates for T3 and T7 transcription reactions (Megascript T3 and T7 kits, Ambion). Transcription reactions were cleaned individually (Megaclear kit, Ambion), mixed, and annealed by incubating at 68°C for 10 minutes, followed by 37°C for 30 minutes. dsRNAs were aliquoted and stored at -80°C until use. For siRNA experiments, Lipofectamine 2000 was used for all transfections and used according to the manufacturers recommendations. The following oligonucleotide was used to efficiently deplete TFG: 5'-CUUCUCAGCCUACUAAUUA-3'. The control siRNA used was directed against the ER exit site component TANGO1 (5'-GCAAUAACCUCAACUCUAUUU-3'), which was shown previously not to affect the trafficking of VSVG-GFP (45). To generate polyhistidine fusion constructs, DNAs were cloned by restriction digest into pRSETA, which encodes a 6x histidine tag on the amino-terminus. To generate GST fusion constructs, DNAs were cloned by restriction digest into pGEX6P-1, which encodes a GST tag on the amino-terminus, followed by a PreScission protease cleavage site. A *C. elegans* cDNA library was used as a template for

cloning recombinant expression constructs by PCR, and cDNAs for human TFG and NTRK1 were purchased from Open Biosystems.

Mass Spectrometry Analysis and Biochemistry

Gravid adult hermaphrodites were grown synchronously in liquid culture, and embryos were isolated in buffer containing 0.6 N NaOH and 20% bleach. Extracts were generated in lysis buffer (50 mM Hepes, 1 mM EDTA, 1 mM MgCl₂, 100 mM KCl and 10% glycerol) and used for immunoprecipitations as described previously (37). For mass spectrometry, proteins were precipitated using TCA. The TCA pellets were solubilized and treated with Endoproteinase Lys-C (0.1 µg/µL), followed by Trypsin (0.5 µg/µL). Following digestion, the proteins were pressure-loaded onto a fused silica capillary desalting column containing 3 cm of 5-µm strong cation exchange (SCX) followed by 3 cm of 5-µm C18 (reverse phase or RP material) pressure packed into a deactivated 250-µm inner diameter (i.d.) capillary. The resulting split-column was placed inline with a Hewlett Packard Agilent 1100 Quaternary Pump (Version 1.4; Palo Alto, CA) and analyzed using a customized 4-step separation method (90, 120, 120, and 150 minutes respectively) (46). For each step, one full-scan mass spectrum (400-2000 m/z) occurred followed by 5 data-dependent MS/MS spectra at a 35% normalized collision energy. The spectra were searched with the SEQUEST™ algorithm (47) against the WormBase *C. elegans* (version 2.11 created on 01-10-2010) database.

For immunoprecipitations, HeLa or hTERT-RPE-1 cells were grown in 15 cm plates, and extracts were generated in lysis buffer, which were subjected to centrifugation at 100,000 x g prior to use. Recombinant protein expression was performed using BL21 (DE3) *E. coli*, and purifications were conducted using either glutathione agarose beads (for GST fusions) or nickel

affinity resin (for polyhistidine-tagged proteins). For samples applied to a Superose 6 gel filtration column, the Stokes radius of each protein or protein complex was calculated from its elution volume based on the elution profiles of characterized standards. Glycerol gradients (10-30%) were poured using a Gradient Master and fractionated from the top by hand.

Sedimentation values were calculated by comparing the position of the peak with that of characterized standards run on a separate gradient in parallel. For gel filtration chromatography, 1 mL samples were loaded onto a Superose 6 column, and 1 mL fractions were subsequently collected. In all cases, 1/100 of the fractions were separated by SDS-PAGE and stained with Coomassie. For glycerol gradients, a 4 mL gradient (10-30% glycerol) was generated using a Gradient Master, and 100 mL fractions were collected by hand from the top of the gradient. In all cases, 1/10 of the fractions were separated by SDS-PAGE and stained with Coomassie. To determine the native molecular weight of proteins, the following equation was used: $M = \frac{6\pi\eta N a^3 s}{(1 - \nu\rho)}$, where M is the native molecular weight, η is the viscosity of the medium, N is Avogadro's number, a is the Stokes radius, s is the sedimentation value, ν is the partial specific volume, and ρ is the density of the medium (48). Immunoblotting of extracts and immunoprecipitates were performed as described previously (37). To determine whether endogenous SEC-16 could interact with various fragments of recombinant TFG-1, extracts were generated from animals freshly harvested from fifteen 10-cm plates that were subsequently subjected to sonication in lysis buffer containing 1% Triton X-100. Extracts were clarified by centrifugation (100,000 x g) prior to incubation with proteins bound to nickel affinity resin. To determine the level of TFG-1 depletion following RNAi, both control and dsRNA treated animals (60 each) were hand-picked and placed into eppendorf tubes containing 100 mL of lysis

buffer. Samples were sonicated in a water bath sonicator set to 80°C in the presence of 1x sample buffer for 10 min, after which they were boiled for 10 min at 100°C prior to separation by SDS-PAGE.

Statistical Analysis

Statistical significance was evaluated by performing a two-tailed Student's t test.

ACKNOWLEDGEMENTS

This work was supported in part by a grant from the NIH (1R01GM088151-01A1) to AA and P41RR011823 to JRY. We thank Dr. Beth Weaver (UW-Madison) and Dr. Paul Bertics (UW-Madison) for use of tissue culture facilities, Dr. Robert Landick (UW Madison) for use of a Gradient Master, Dr. Karen Oegema (UC San Diego) for marker strains and antibodies, Dr. Edwin Chapman (UW-Madison) for use of Metamorph software, and Dr. Sabine Koenig for help with RNAi. We also thank Dr. David Stephens (University of Bristol, UK), Dr. Patricia Kiley (UW-Madison), and members of the Audhya lab for critically reading this manuscript.

CONTRIBUTIONS

Conceived and designed experiments: KW, ALS, SE, AA. Performed experiments and analyzed data: KW, ALS, AS, JH, JRM, KS, SE, AA. Contributed reagents/materials/analysis tools: SE, JRY, AA. Wrote the paper: AA.

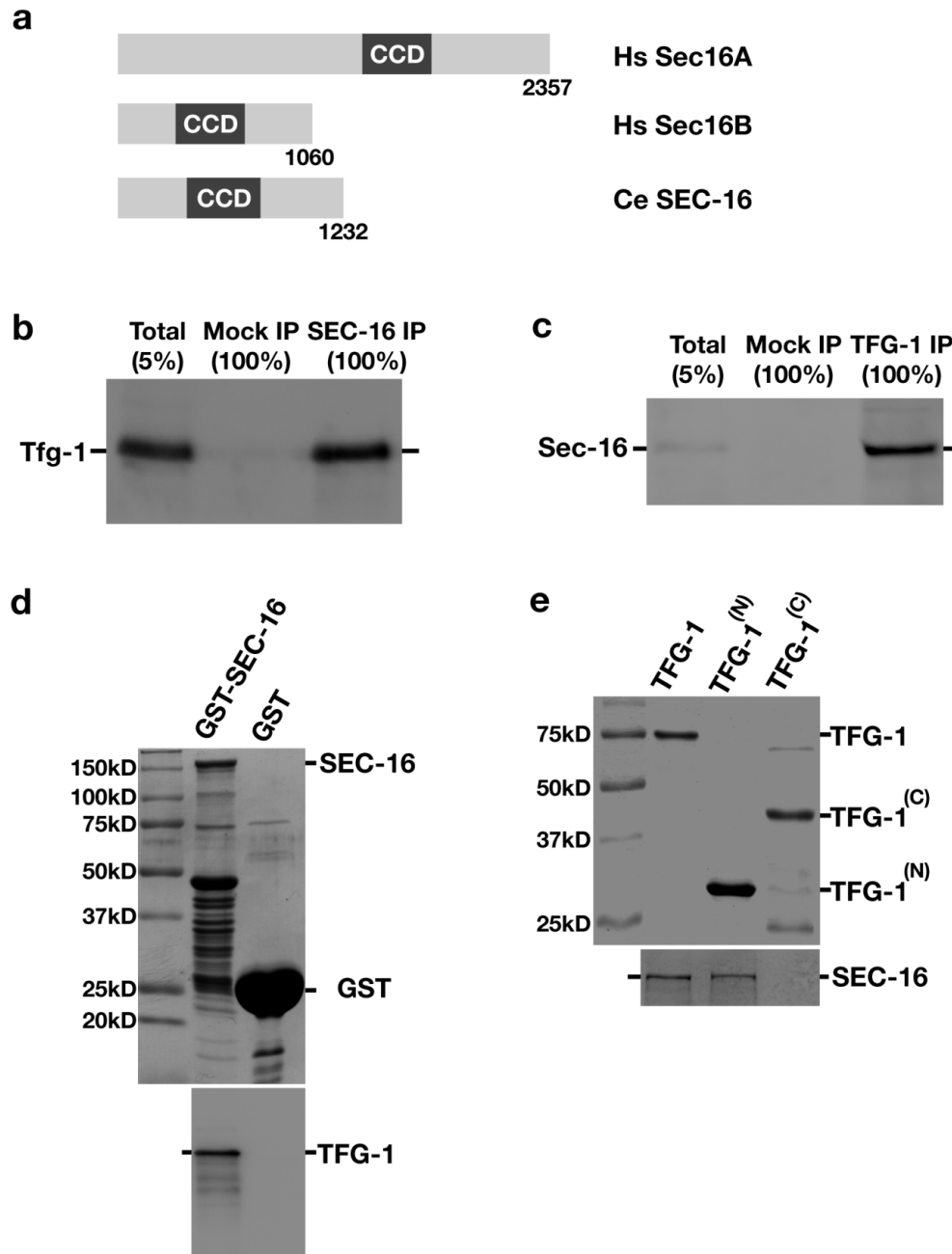


Figure A.1: *C. elegans* TFG-1 interacts with the ER exit site component SEC-16.

Figure A.1: *C. elegans* TFG-1 interacts with the ER exit site component SEC-16.

(**Figure A.1a**) Schematic representation of human and *C. elegans* Sec16 isoforms. The central conserved domain (CCD) is highlighted in each protein. (**Figure A.1b**) SEC-16 was immunoprecipitated from *C. elegans* embryo extract and blotted with α -TFG-1 antibodies (n=3). A mock IP was conducted in parallel using rabbit IgG. (**Figure A.1c**) TFG-1 was immunoprecipitated from *C. elegans* embryo extract and blotted with α -SEC-16 antibodies (n=3). A mock IP was conducted in parallel using rabbit IgG. (**Figure A.1d**) GST alone and GST-tagged full length SEC-16 were immobilized on glutathione agarose beads, which were incubated with an extract generated from *E. coli* expressing recombinant TFG-1. Following a series of washes, proteins were eluted using reduced glutathione, separated by SDS-PAGE, and either stained using Coomassie (top) or immunoblotted using TFG-1 antibodies (bottom). (**Figure A.1e**) Polyhistidine-tagged full length and truncated forms of TFG-1, either encoding amino acids 1-195 (TFG-1^(N)) or 196-486 (TFG-1^(C)), were purified from *E. coli* onto nickel affinity resin and incubated with freshly prepared whole worm extract (n=3). Imidazole eluted proteins were separated by SDS-PAGE, stained with Coomassie (top), and blotted with α -SEC-16 antibodies (bottom). For each figure, uncropped scans of all gels and immunoblots are provided in **Figure A.S6**.

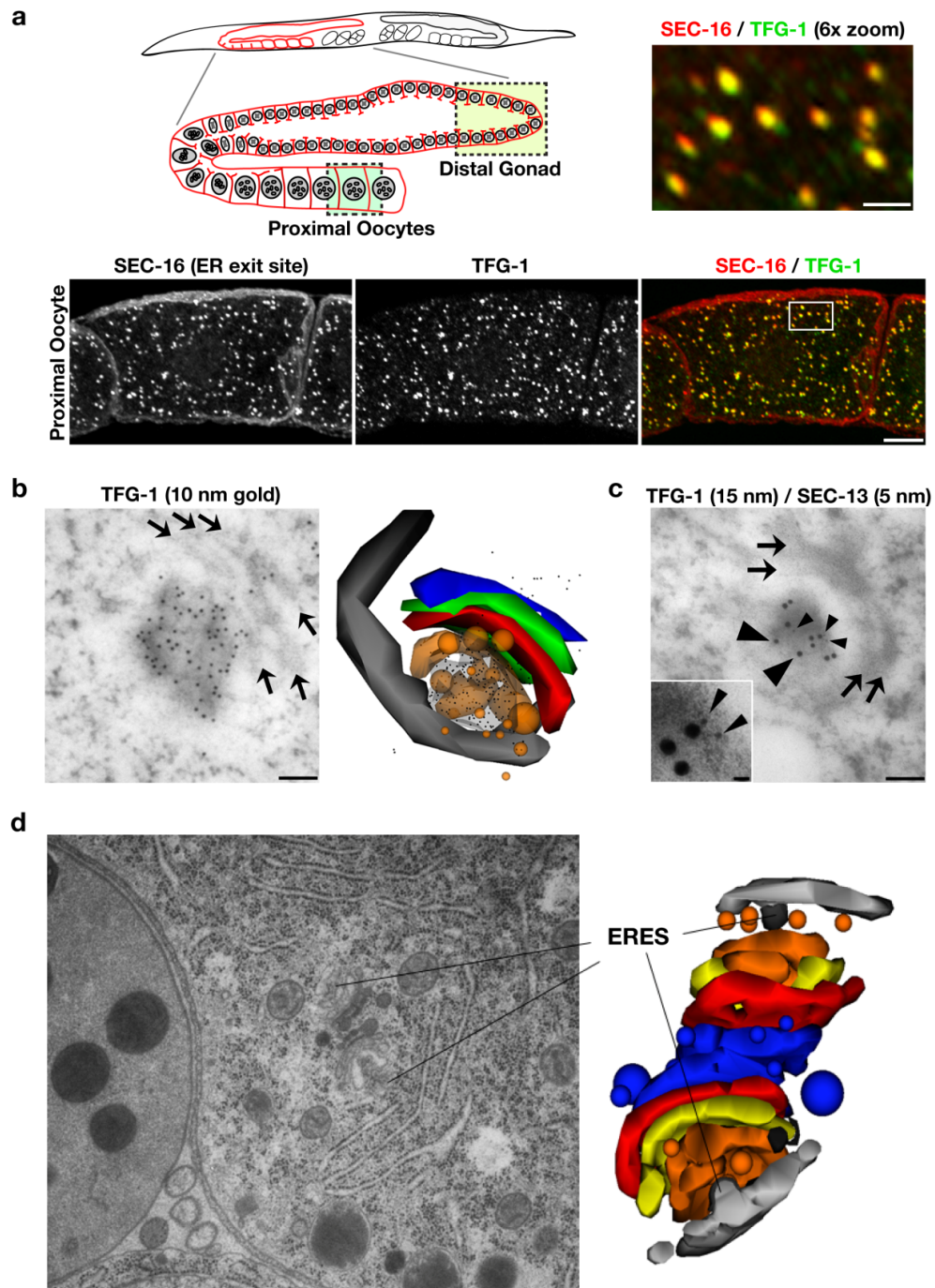


Figure A.2: TFG-1 localizes to ER exit sites that are juxtaposed to the Golgi.

Figure A.2: TFG-1 localizes to ER exit sites that are juxtaposed to the Golgi.

(**Figure A.2a**) Dissected *C. elegans* gonads were fixed and stained using Cy2-labeled α -TFG-1 and Cy3-labeled α -SEC-16 antibodies (n=8). Both individual and merged images of proximal oocytes with TFG-1 in green and SEC-16 in red are shown (Bar, 10 μ m). The upper right image is the boxed area in the panel below magnified 6x (Bar, 2 μ m). Also shown is a schematic of the *C. elegans* reproductive system, which includes a syncytial stem cell niche in the distal gonad (boxed region in light green) and proximal oocytes that have undergone cellularization (boxed region in dark green). (**Figures A.2b and A.2c**) Lowicryl sections of *C. elegans* oocytes were stained with antibodies against TFG-1 or a combination of TFG-1 and SEC-13 antibodies. Arrows highlight Golgi cisternae. Large arrowheads point out 15 nm gold particles associated with immunoreactive TFG-1, and small arrowheads highlight 5 nm gold particles associated with SEC-13. Bars, 100 nm. An inset is provided in panel c to clearly show the distribution of 5 nm particles at higher magnification (Inset bar, 15 nm). In addition, a three-dimensional reconstruction of TFG-1 immunolocalization is shown. The image was generated using the software Reconstruct from serial 50 nm thin sections. Vesicles were reconstructed using the sphere setting, and all other components (ER, ERGIC, coats, Golgi stacks) were generated using the Boissonnat surface setting. Light grey: ER; dark grey: COPII coat; orange: ER-derived transport vesicles and ERGIC; red, green and blue: Golgi cisternae; from cis to trans, respectively. (**Figure A.2d**) An electron micrograph illustrating two ER exit sites and adjacent Golgi complexes in the proximal most oocyte of an animal following high pressure freezing and freeze substitution (Bar, 500 nm). On the right is a three-dimensional reconstruction of the same pair of Golgi complexes and associated ER exit sites. The ER exit sites are surrounded by vesicles that fuse to form the ERGIC. Light grey: ER; dark grey: COPII coat; orange: ER-

derived transport vesicles and ERGIC; yellow, red and blue: Golgi cisternae; from cis to trans, respectively.

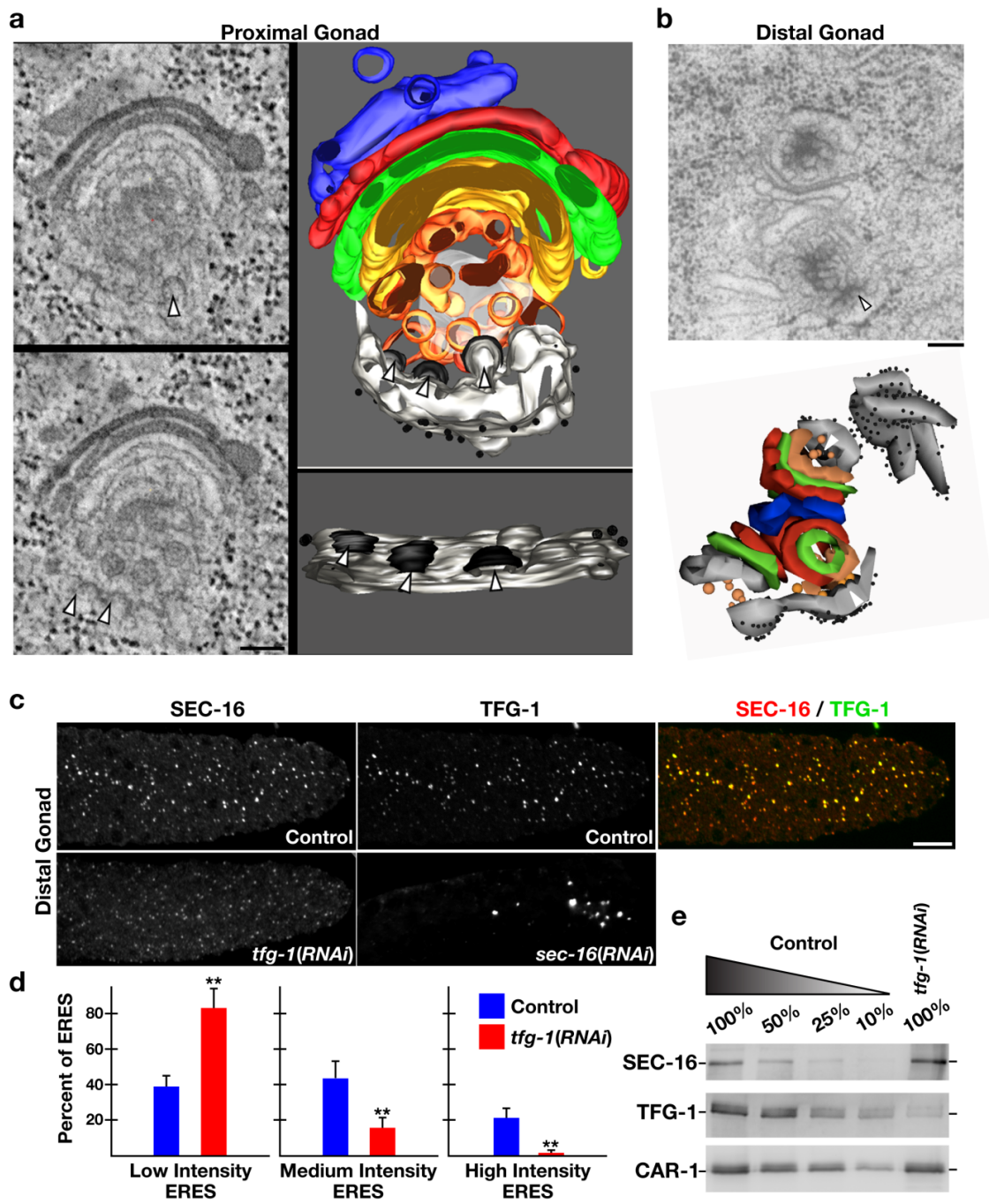


Figure A.3: TFG-1 regulates SEC-16 levels on ER exit sites.

Figure A.3: TFG-1 regulates SEC-16 levels on ER exit sites.

(Figure A.3a) In the proximal gonad, a 300 nm section of the early secretory pathway (ER exit sites, ERGIC, and Golgi) was analyzed by electron tomography. ER exit sites are highlighted by arrowheads. On the left are individual sections from the tomographic stack. On the right are two orthogonal views of the tomogram following three-dimensional reconstruction. Light grey: ER; black: COPII coat; orange and yellow: ER-derived transport vesicles and ERGIC; green, red, blue: Golgi cisternae; diffuse grey: not further resolvable matrix. Bar, 100 nm. **(Figure A.3b)**

An electron micrograph illustrating ER exit sites and adjacent Golgi complexes in the distal gonad following high pressure freezing and freeze substitution. An arrowhead highlights the presence of budding vesicle from smooth ER (Bar, 100 nm). Below is a three-dimensional construction of the same Golgi complexes and associated ER exit sites. **(Figure A.3c)** Dissected gonads from control, TFG-1 depleted, and SEC-16 depleted animals were fixed and stained using Cy2-labeled α -TFG-1 and Cy3-labeled α -SEC-16 antibodies. Individual and merged images of the distal gonad with TFG-1 in green and SEC-16 in red are shown (Bar, 10 μ m).

(Figure A.3d) Fluorescence intensity of SEC-16 in the distal gonad was measured in control and TFG-1 depleted animals, and intensities were segregated into low, medium and high thresholds. To establish individual thresholds, a histogram of fluorescence intensities was equally divided into three regions, and the number of ER exit sites within each area was calculated. The bar graph indicates the percentage of all ER exit sites that fall into a specific threshold. For each condition, at least 1000 unique ER exit sites were examined. Error bars represent mean \pm SEM; 10 different animals. ****p < 0.01** compared with control, calculated using a paired *t* test.

(Figure A.3e) Western blots of extracts prepared from animals depleted of TFG-1 by RNAi

(n=3). Serial dilutions of extracts prepared from control animals were loaded to quantify depletion levels. Blotting with α -CAR-1 antibodies was performed to control loading.

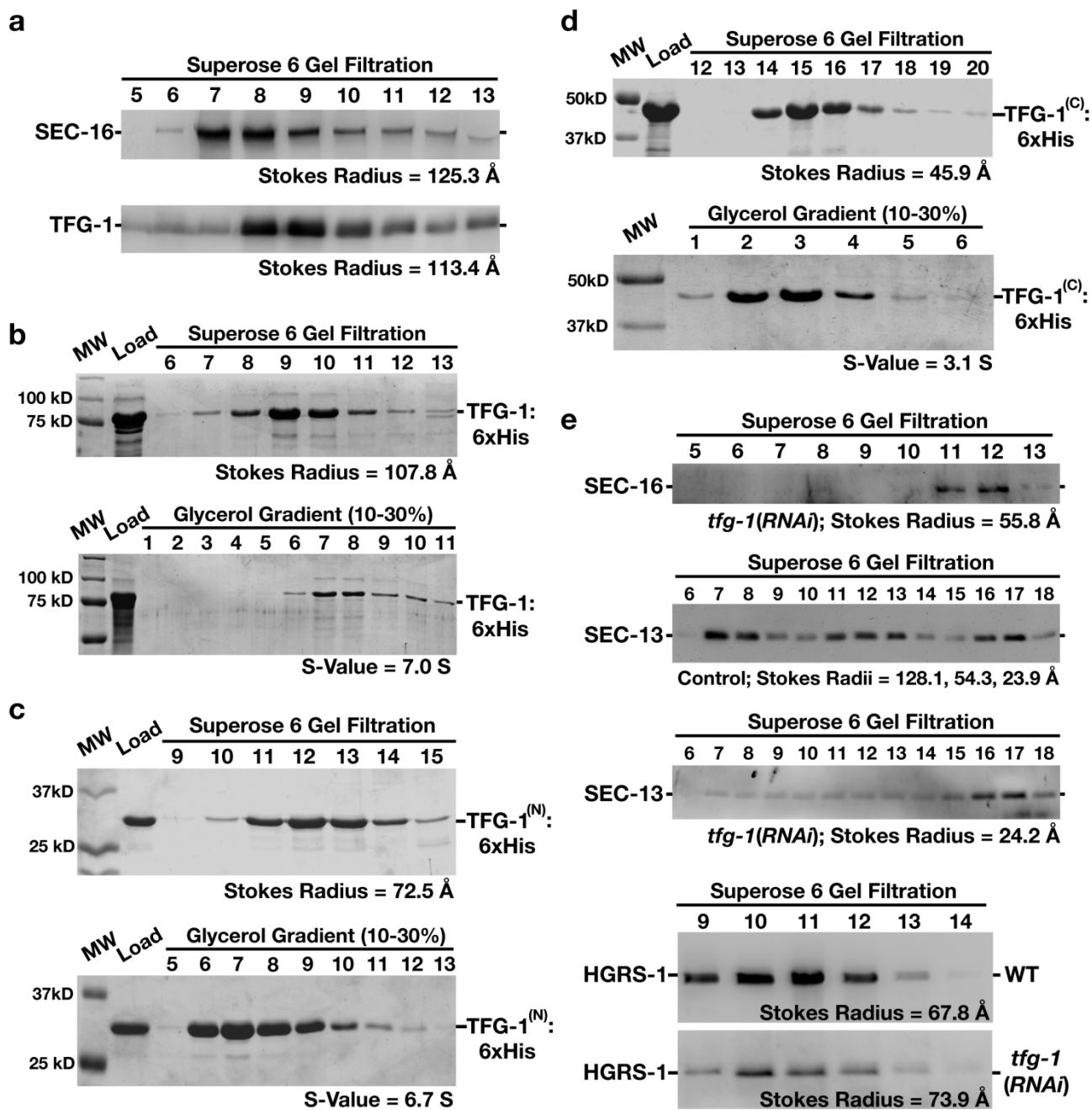


Figure A.4: The amino-terminus of TFG-1 mediates its oligomerization.

Figure A.4: The amino-terminus of TFG-1 mediates its oligomerization.

The results presented in each panel are representative of at least three individual experiments performed. In all cases, the intensities of each band were measured to identify the peak elution fraction, which was used to calculate either a Stokes radius or sedimentation value, depending on the experiment. **(Figure A.4a)** Western blots using SEC-16 antibodies (top) or TFG-1 antibodies (bottom) of *C. elegans* embryo extract fractionated on a Superose 6 gel filtration column. The peaks corresponding to SEC-16 and TFG-1 partially overlap. A Stokes radius was calculated for each protein based on comparison with the elution profiles of known standards. **(Figures A.4b-A.4d)** Recombinant polyhistidine-tagged TFG-1 or fragments of TFG-1 described in Figure 1f were expressed and purified from *E. coli* extracts using nickel resin. A Coomassie stained gel of the peak elution fractions after fractionation of the recombinant proteins on a Superose 6 gel filtration column are shown (top). Proteins were fractionated on a 10-30% glycerol gradient (bottom), and S-values were calculated based on the location of characterized standards run on a parallel gradient. **(Figure A.4e)** Western blots of control and TFG-1 depleted *C. elegans* whole worm extracts fractionated on a Superose 6 gel filtration column and probed with SEC-16 antibodies (top) or SEC-13 antibodies (middle panels). Fractionation of HGRS-1, a component of the ESCRT-0 complex, was examined in both control and TFG-1 depleted conditions (bottom panels), to ensure gel filtration profiles were directly comparable. Stokes radii were calculated for each protein based on comparison with the elution profiles of known standards.

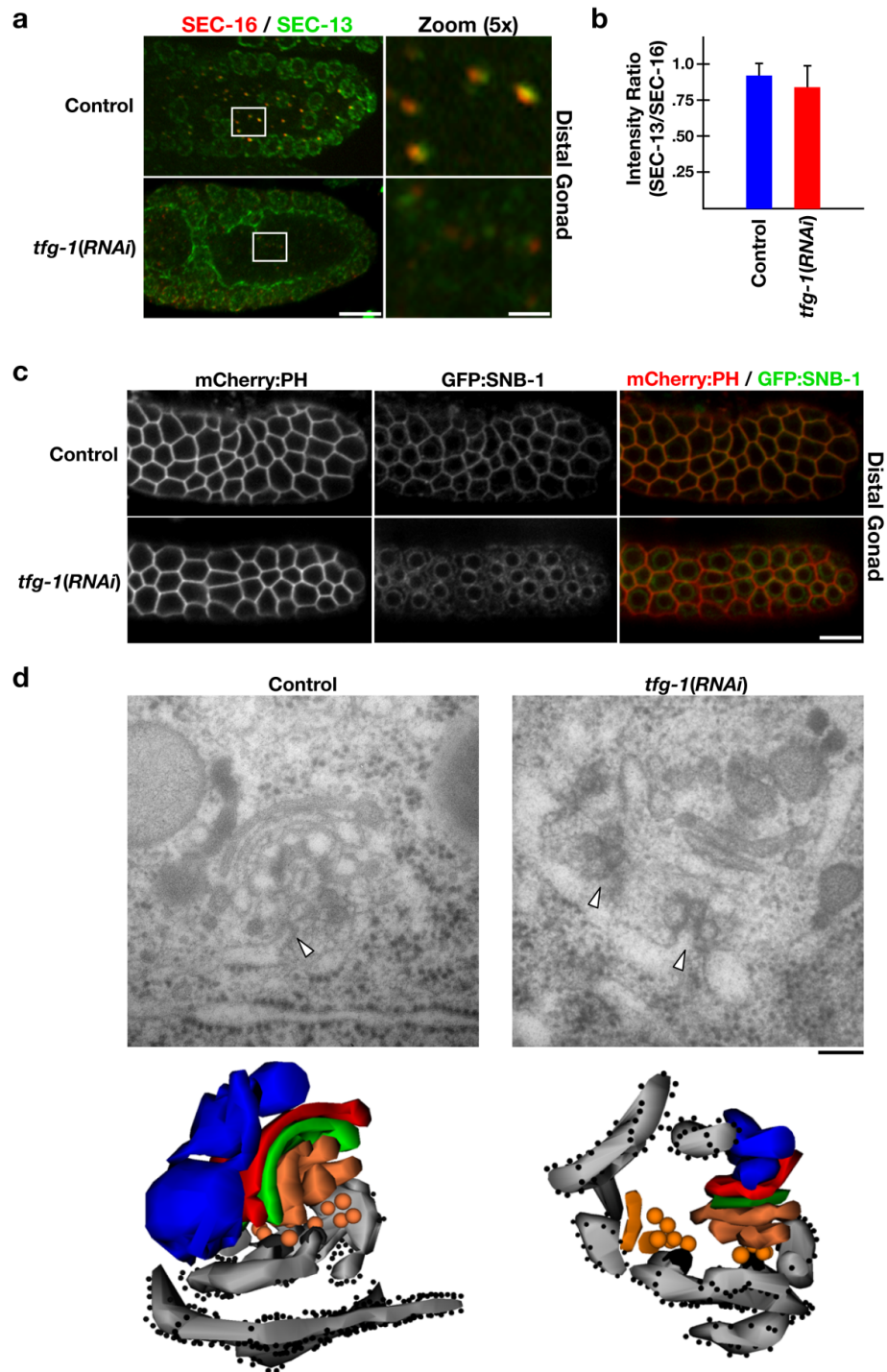


Figure A.5: TFG-1 is required for COPII recruitment and protein secretion.

Figure A.5: TFG-1 is required for COPII recruitment and protein secretion.

(**Figure A.5a**) Dissected *C. elegans* gonads were fixed and stained using Cy2-labeled α -SEC-13 and Cy3-labeled α -SEC-16 antibodies (n=15). Merged images of the distal gonad with SEC-13 in green and SEC-16 in red are shown on the left (Bar, 10 μ m). Panels to the right are magnified 5x views of the boxed area in the adjacent panel (Bar, 2 μ m). (**Figure A.5b**) Bar graph showing the average ratio of SEC-13 to SEC-16 fluorescence intensities in control and TFG-1 depleted animals. For each condition, at least 250 unique ER exit sites in the distal gonad were examined. Error bars represent mean \pm SEM; 6 different animals. No statistically significant difference was observed, based on a calculation using a paired *t* test. (**Figure A.5c**) Swept field confocal optics were used to image anesthetized control (n=15) and TFG-1 depleted (n=15) adult animals expressing GFP:SNB-1 and mCherry:PH. Scale bar, 10 μ m. (**Figure A.5d**) Electron micrographs illustrating the early secretory pathway in the proximal most oocyte of control (left) and TFG-1 depleted (right) animals following high pressure freezing and freeze substitution (Bar, 100 nm). Arrowheads highlight ER exit sites. Below each micrograph is a three-dimensional reconstruction of the same regions. Light grey: ER; dark grey: COPII coat; orange: ER-derived transport vesicles and ERGIC; green, red and blue: Golgi cisternae; from cis to trans, respectively.

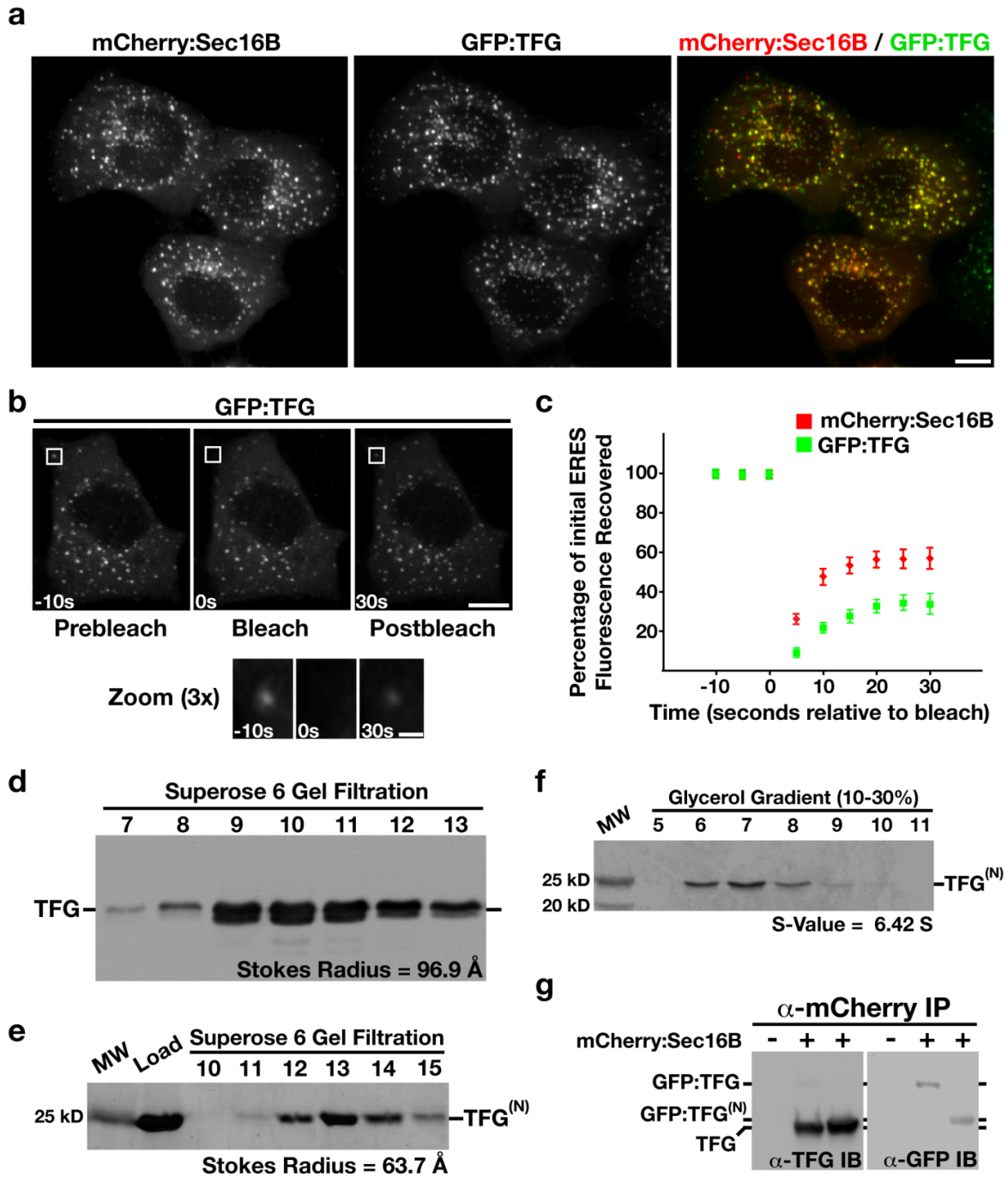


Figure A.6: Human TFG functions at ER exit sites and binds to Sec16.

Figure A.6: Human TFG functions at ER exit sites and binds to Sec16.

(**Figure A.6a**) Swept field confocal optics were used to image HeLa cells that had been transiently transfected with GFP:TFG and mCherry:Sec16B (n=42). Representative color overlays of mCherry:Sec16B (red) and GFP:TFG (green) are shown. Scale bar, 10 μ m. (**Figure A.6b**) Swept field confocal optics were used to monitor the recovery of GFP:TFG after photobleaching (n=15). A 3x magnified view of the boxed region where GFP:TFG was bleached is shown below. Times are in seconds relative to the bleach. Scale bars, 10 μ m (top) and 1 μ m (bottom). (**Figure A.6c**) Graph showing the average percentage of GFP:TFG and mCherry:Sec16B fluorescence recovered as a function of time in seconds relative to the bleach (error bars represent means \pm SEM for each time point; n=15 different cells for each fluorescent fusion protein). (**Figure A.6d**) Western blots of HeLa cell extract fractionated on a Superose 6 gel filtration column (n=3). A Stokes radius was calculated for human TFG based on comparison with the elution profiles of known standards. (**Figures A.6e and A.6f**) A GST-tagged, truncated form of human TFG, amino acids 1-193 was expressed and purified from *E. coli* extracts using glutathione agarose (n=3), and the GST tag was subsequently cleaved using Precision Protease prior to loading onto a gel filtration column or glycerol gradient. A Coomassie stained gel of the peak elution fractions after fractionation of the recombinant protein, referred to as TFG^(N), on a Superose 6 gel filtration column are shown (**Figure A.6e**). The protein was also fractionated on a 10-30% glycerol gradient (**Figure A.6f**), and an S-value was calculated based on the location of characterized standards run on a parallel gradient (n=3). (**Figure A.6g**) Antibodies directed against mCherry were used to immunoprecipitate mCherry:Sec16B from HeLa cells transiently transfected with GFP:TFG or a GFP fusion to the

amino-terminus of TFG referred to as GFP:TFG^(N) (n=3). Isolated proteins were separated by SDS-PAGE and blotted with a-TFG (left) and a-GFP antibodies (right).

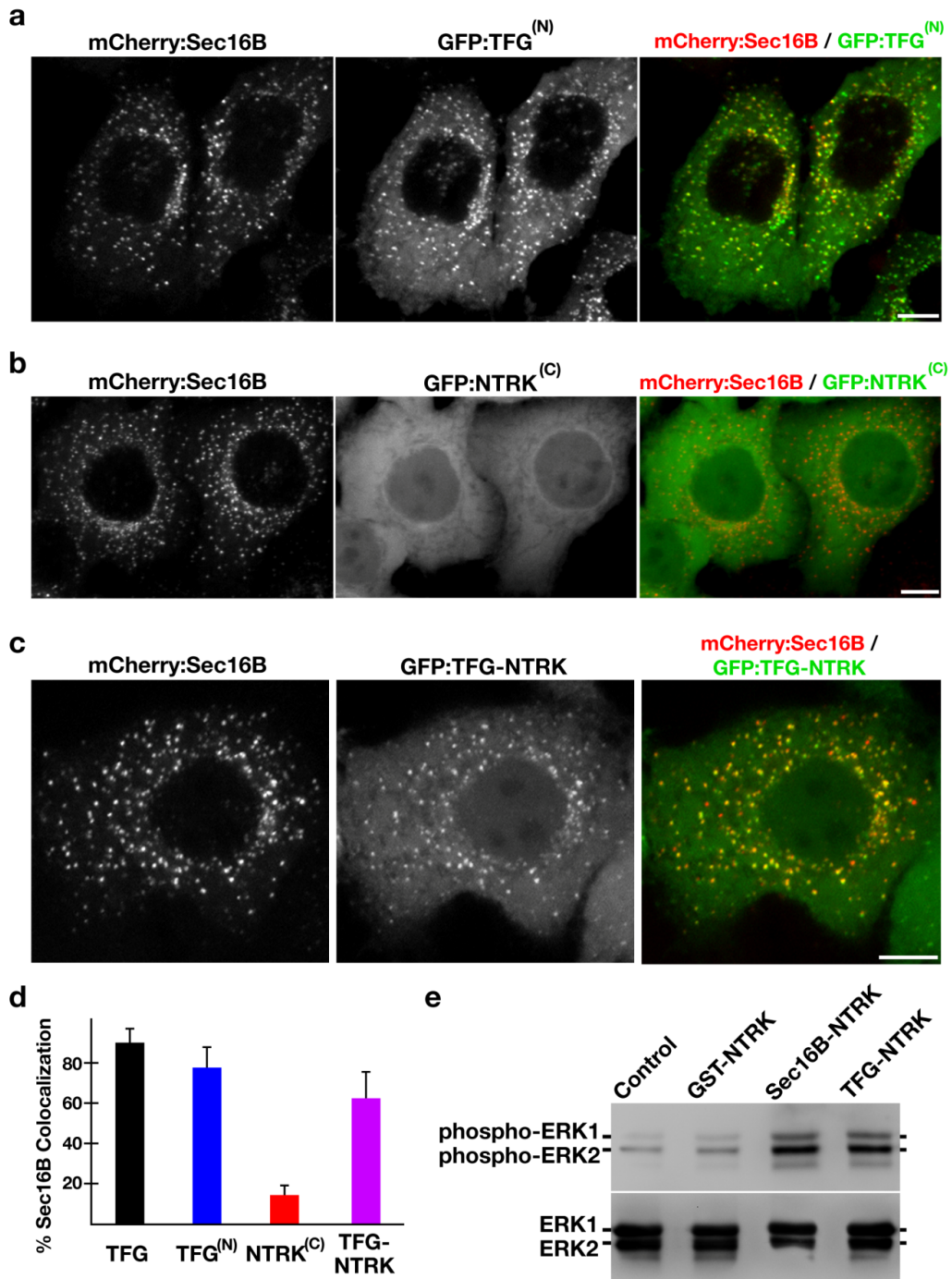


Figure A.7: Targeting of the NTRK1 kinase domain to ER exit sites is sufficient to activate NTRK1-mediated downstream signaling.

Figure A.7: Targeting of the NTRK1 kinase domain to ER exit sites is sufficient to activate NTRK1-mediated downstream signaling.

(**Figures A.7a-c**) Swept field confocal optics were used to image HeLa cells that had been transiently transfected with mCherry:Sec16B and GFP fusions to either the amino terminus of TFG referred to as GFP:TFG^(N) (n=18), the transmembrane and kinase domains of NTRK1 referred to as GFP:NTRK^(C) (n=15), or a TFG^(N)-NTRK1^(C) fusion (n=28). Representative color overlays of mCherry:Sec16B (red) and GFP fusions (green) are shown. Scale bar, 10 μ m.

(**Figure A.7d**) Bar graph showing the percent co-localization between the GFP fusions described above and mCherry:Sec16B (error bars represent means \pm SEM for each condition; n=15 different cells for each condition and at least 800 unique ER exit sites were examined). (**Figure**

A.7e) Extracts from hTERT-RPE1 cells stably transfected with GFP alone (Control) or various GFP fusions to the NTRK1 transmembrane and kinase domains (as indicated) were separated by SDS-PAGE and blotted using a phospho-specific ERK1/2 antibody (top) and a pan-ERK1/2 antibody (bottom).

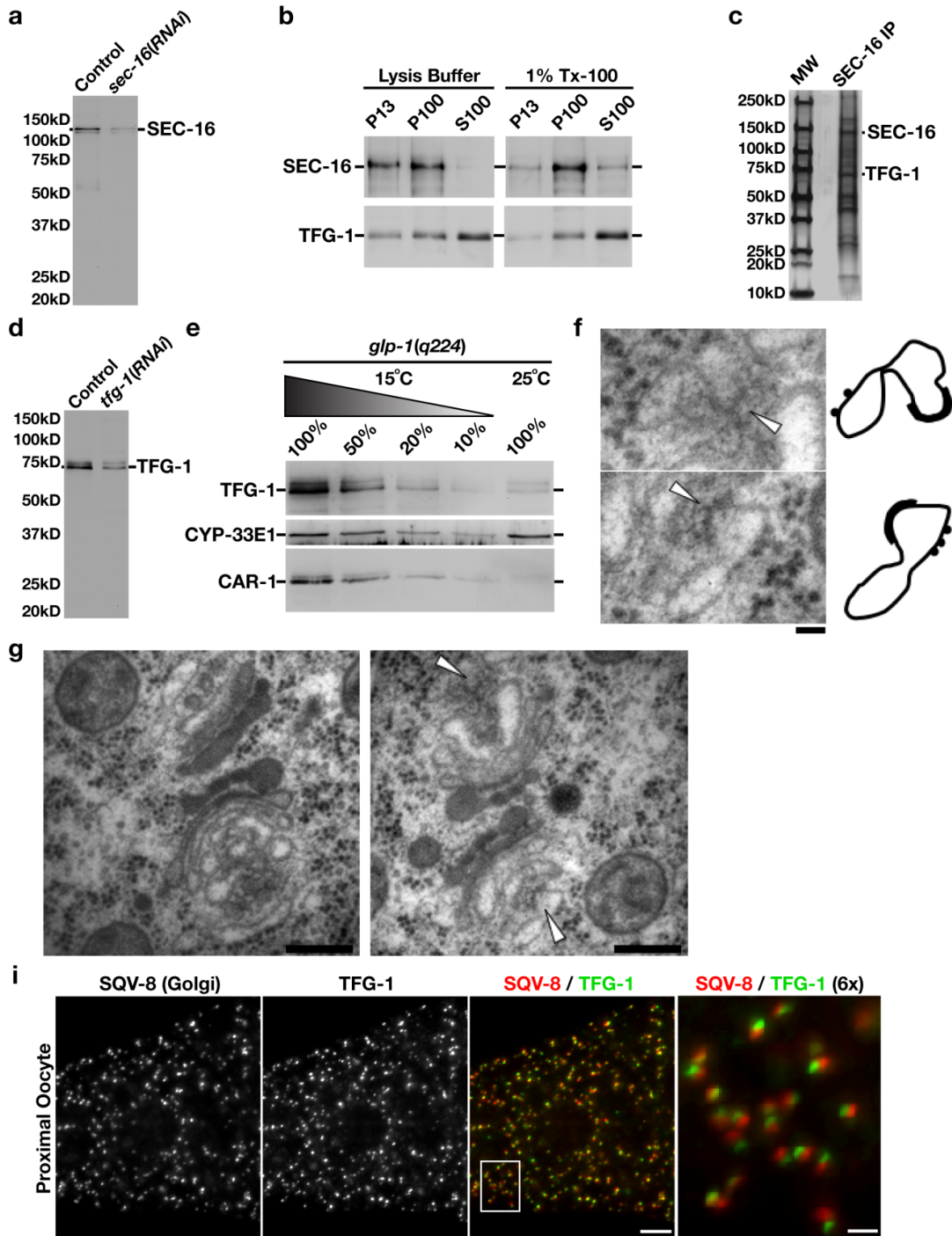


Figure A.S1 TFG-1 functions with SEC-16 at ER exit sites.

Figure A.S1 TFG-1 functions with SEC-16 at ER exit sites.

(**Figure A.S1a**) *C. elegans* embryo extract was separated by SDS-PAGE and immunoblotted using SEC-16 antibodies. (**Figure A.S1b**) *C. elegans* embryo extract was subjected to differential centrifugation in the presence or absence of 1% Tx-100. The 13,000 x g pellet (P13), 100,000 x g pellet (P100), and 100,000 x g supernatant (S100) were recovered and immunoblotted using α -SEC-16 (top) or α -TFG-1 (bottom) antibodies. The P13 fraction is enriched with ER and plasma membrane proteins, while the P100 fraction contains Golgi and endosome membranes (our unpublished data). (**Figure A.S1c**) SEC-16 was immunoprecipitated from detergent-solubilized *C. elegans* embryo extract, and purified proteins were resolved by SDS-PAGE, followed by silver staining. Bands corresponding to the molecular weights of SEC-16 and TFG-1 are highlighted. (**Figure A.S1d**) *C. elegans* embryo extract was separated by SDS-PAGE and immunoblotted using TFG-1 antibodies. (**Figure A.S1e**) L1 stage larvae harboring the temperature sensitive *glp-1(q224)* mutation were grown at 15°C or 25°C immediately after hatching. At 25°C, in the absence of GLP-1 function, larvae fail to generate a germline (49). Extracts were made from 30 animals grown at each temperature and immunoblotted using α -TFG-1 (top), α -CYP-33E1 (middle; not expressed in the germline), or α -CAR-1 (bottom; expressed only in the germline). Serial dilutions of extracts prepared from animals grown at 15°C were loaded to quantify levels of TFG-1 remaining in animals without a germline. (**Figure A.S1f**) Higher magnifications of the ER exit sites shown in panel g with arrowheads marking ER exit sites. On the right are sketches illustrating the ER exit sites (drawn to scale), ribosomes (black dots) and COPII coats (thick black lines). Bar, 50 nm. (**Figure A.S1g**) Higher magnifications of two EM sections from the reconstructed series shown in **Figure A.2d**. Arrowheads highlight ER exit sites. Bars, 200 nm. (**Figure A.S1h**) Dissected gonads were

fixed and stained using Cy2-labeled α -TFG-1 and Cy3-labeled α -SQV-8 (Golgi) antibodies (n=3). Both individual and merged images of proximal oocytes with TFG-1 in green and SQV-8 in red are shown (Bar, 10mm). The panel on the right is the boxed region magnified 6x relative to the adjacent images (Bar, 2 μ m).

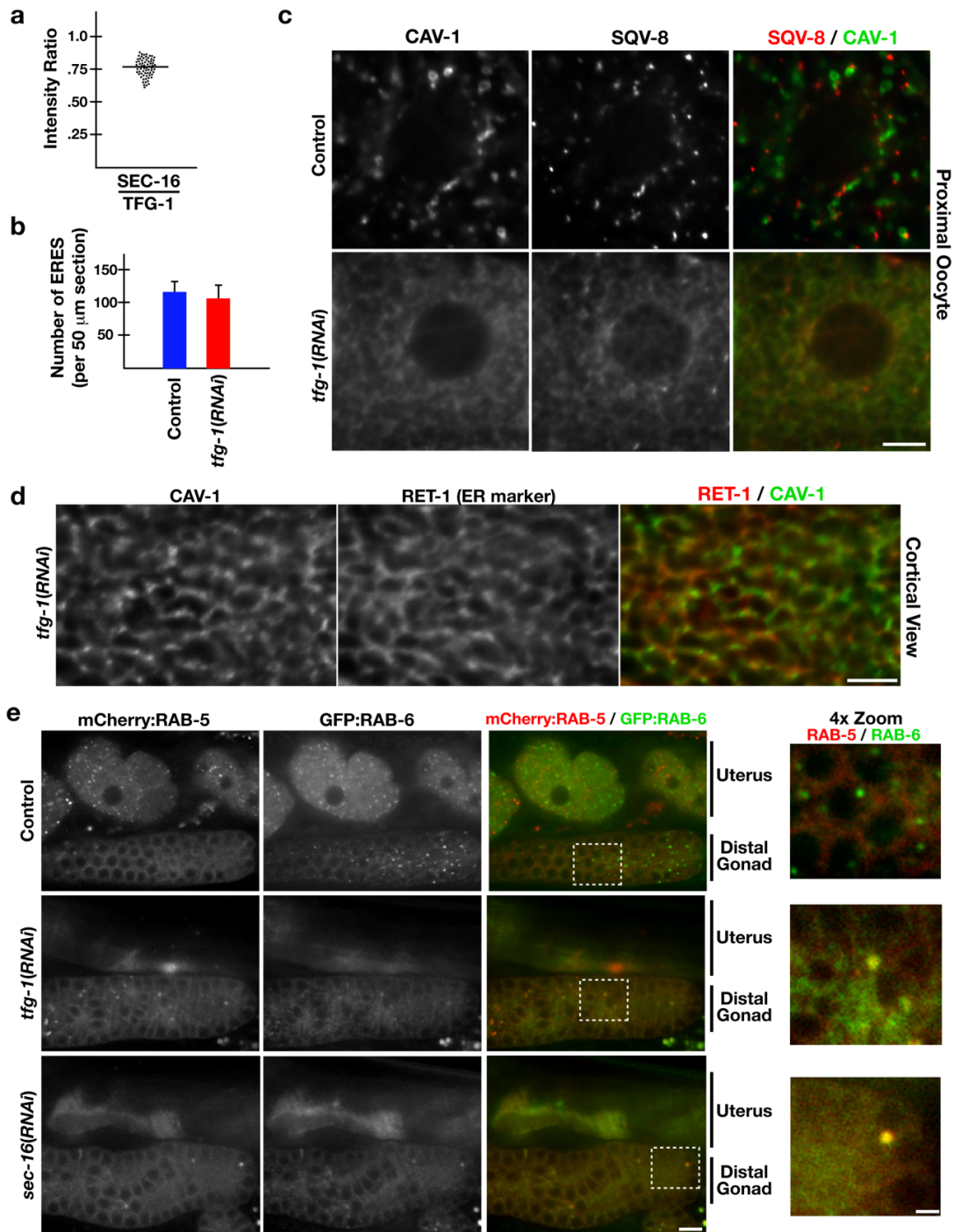


Figure A.S2 TFG-1 is required for secretion and normal localization of RAB-6.

Figure A.S2 TFG-1 is required for secretion and normal localization of RAB-6.

(**Figure A.S2a**) Fluorescence intensities of SEC-16 and TFG-1 in the distal gonad were measured in control animals, and at each ER exit site, a ratio was calculated. Each point in the scatter plot indicates a ratio between the intensities. Although more than 600 ER exit sites were analyzed, only a small (random) selection of ratios is shown due to space limitations. A line indicating the average intensity ratio for all analyzed ER exit sites is shown. (**Figure A.S2b**) Dissected *C. elegans* gonads from control and TFG-1 depleted animals were fixed and stained using Cy3-labeled α -SEC-16 antibodies (n=15 animals each). The number of ER exit sites (puncta harboring SEC-16) was counted for a 50 μ m section from the distal-most region of the germline (in the medial confocal plane of each gonad). Error bars represent mean \pm SEM; 15 different animals for each condition. No statistically significant difference was observed, based on a calculation using a paired *t* test. (**Figure A.S2c**) Dissected *C. elegans* gonads from control and TFG-1 depleted animals expressing GFP:CAV-1 were fixed and stained using Cy2-labeled α -GFP and Cy3-labeled α -SQV-8 antibodies (n=12). Merged images of the proximal oocytes with GFP:CAV-1 in green and SQV-8 in red are shown. Scale bar, 10 μ m. (**Figure A.S2d**) Dissected *C. elegans* gonads from TFG-1 depleted animals expressing GFP:CAV-1 were fixed and stained using Cy2-labeled α -GFP and Cy3-labeled α -RET-1 (reticulon) antibodies, which label ER tubules (n=8). Merged images of the proximal oocytes with GFP:CAV-1 in green and RET-1 in red are shown. Scale bar, 10 μ m. (**Figure A.S2e**) Live control (top), TFG-1 depleted (middle), and SEC-16 depleted (bottom) animals stably expressing GFP:RAB-6 and mCherry:RAB-5 were anesthetized and mounted onto agarose pads for imaging (n=15 each). Both the distal gonad and uterus are indicated in each series of panels. In the absence of TFG-1 or SEC-16, animals

become sterile, as indicated by the lack of embryos in the uterus. Bar, 10 μm . On the right are 4x zoomed images of the boxed regions shown in the merged panels to the left. Bar, 2.5 μm .

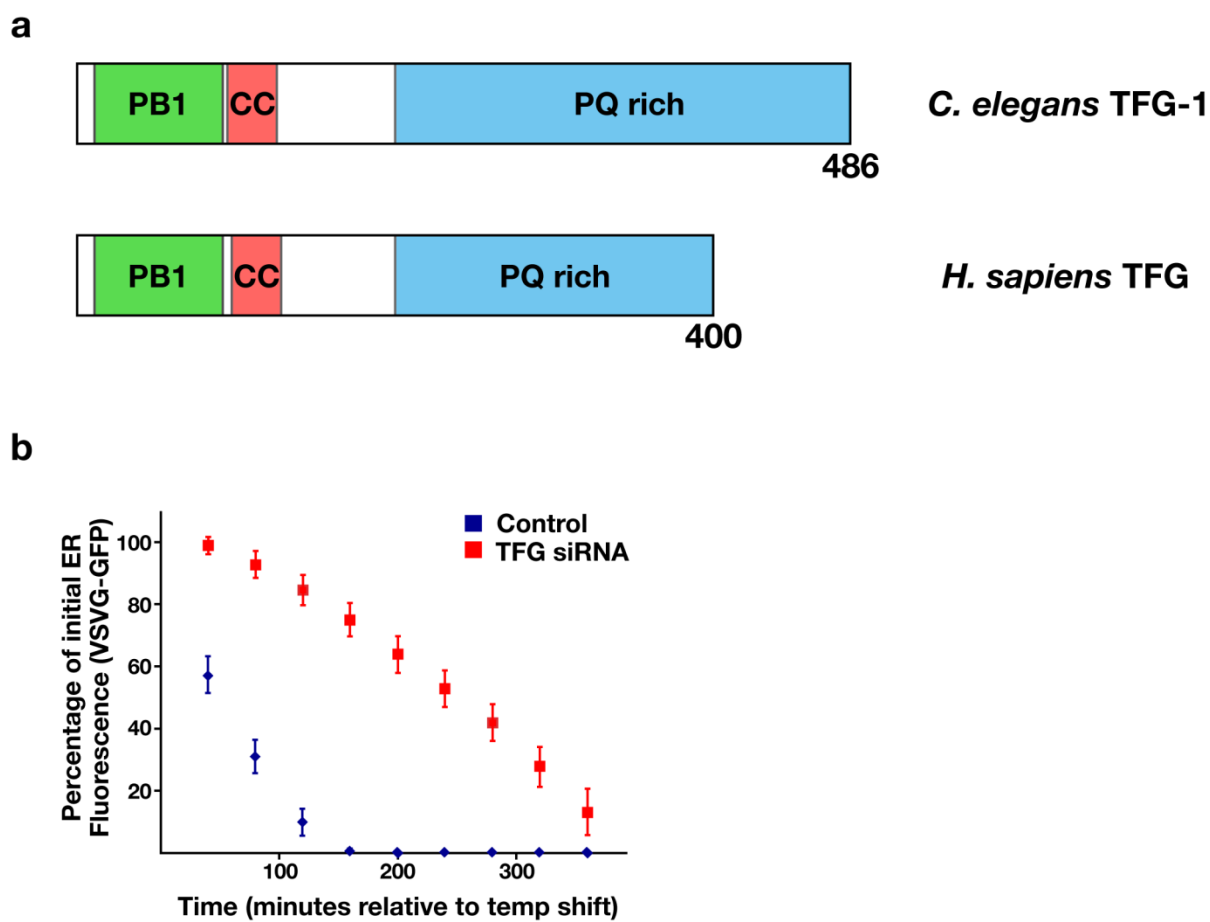


Figure A.S3 Human TFG is a conserved protein required for VSVG(ts045)-GFP secretion.

Figure A.S3 Human TFG is a conserved protein required for VSVG(ts045)-GFP secretion.

(Figure A.S3a) Cartoon illustrating the conserved domains found in TFG isoforms. Based on previous studies, the PB1 domain may function in protein-protein interactions (50). The specific roles of the conserved coiled-coil domain (CC) and the proline/glutamine enriched domain (PQ) remain largely undefined. **(Figure A.S3b)** HeLa cells were co-transfected with a plasmid encoding VSVG(ts045) GFP and either control or TFG siRNA (see Methods for more information). After 36 hours, cells were shifted to 40°C for 16 hours, and then shifted to 32°C for imaging (3 confocal Z sections acquired at 6 min intervals). Fluorescence intensity (total integrated intensity minus camera background) of VSVG(ts045)-GFP in the ER was measured at every time point (n=10 for each condition). The percentage of the initial fluorescence intensity is shown over time. Error bars represent mean +/- SEM; 10 different cells.

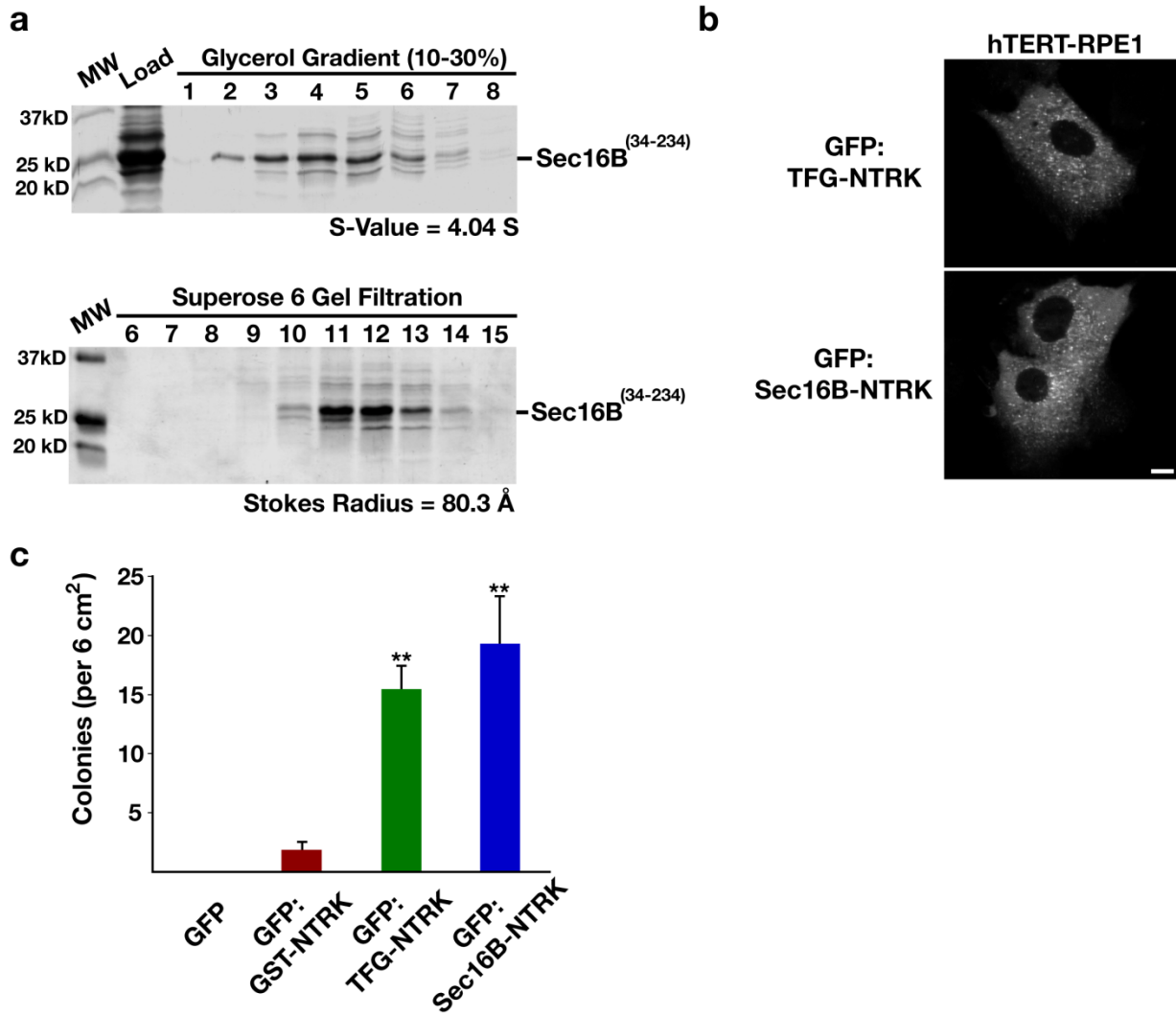


Figure A.S4 The region of Sec16B necessary for its targeting to ER exit sites forms a homo oligomer and targeting of NTRK1 to ER exit sites is necessary for cell transformation.

Figure A.S4 The region of Sec16B necessary for its targeting to ER exit sites forms a homo oligomer and targeting of NTRK1 to ER exit sites is necessary for cell transformation.

(**Figure A.S4a**) The results presented in both panels are representative of at least three individual experiments performed. Recombinant polyhistidine-tagged Sec16B (amino acids 34-234) was expressed and purified from *E.coli* extracts using nickel resin. The protein was fractionated on a 10-30% glycerol gradient (top), and an S-value was calculated based on the location of characterized standards run on a parallel gradient. A Coomassie stained gel of the peak elution fractions after fractionation of the protein on a Superose 6 gel filtration column is shown (bottom). In both cases, the intensities of the bands corresponding to the amino-terminus of Sec16B (amino acids 34-234) were measured to identify the peak elution fraction, which was used to calculate either a Stokes radius or sedimentation value, depending on the experiment.

(**Figure A.S4b**) Swept field confocal optics was used to image hTERT-RPE1 cells that had been stably transfected with either GFP:TFG^(N)-NTRK^(C) or GFP:Sec16B⁽¹⁻⁷⁹¹⁾-NTRK^(C) (n=13 each). Scale bar, 10 μ m. (**Figure A.S4c**) The bar graph shows the number of colonies (at least 0.01 cm² in diameter) that grew in a 6 cm² region of individual tissue culture plates seeded with NIH3T3 cells transfected with either GFP, GFP:GST-NTRK1, GFP:TFG-NTRK1, or GFP:Sec16B-NTRK1. In each case, 500 cells, as calculated using a hemocytometer, were seeded onto a monolayer of control NIH3T3 cells. Colony formation was scored after 14 days. Error bars represent mean \pm SEM; 3 different experiments. **p < 0.01 compared with results obtained using cells expressing GFP:GST NTRK1, calculated using a paired *t* test.

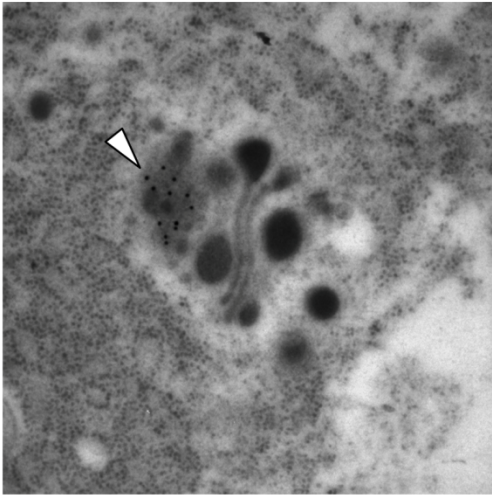
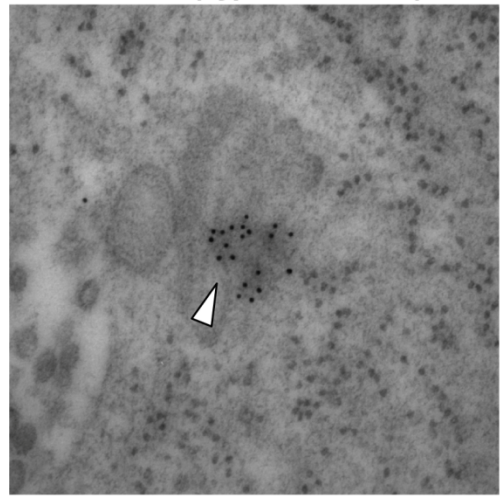
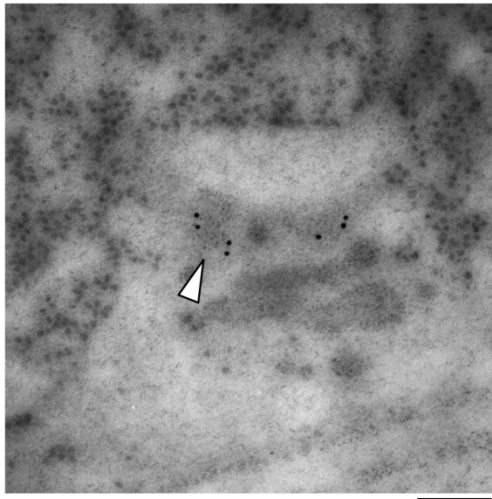
a TFG-1 (intestinal cell)**b** TFG-1 (hypodermal cell)**c** TFG-1 (muscle cell)

Figure A.S5 TFG-1 localizes to ER exit sites in several distinct tissues.

Figure A.S5 TFG-1 localizes to ER exit sites in several distinct tissues.

(**Figures A.5a-A.5c**) Immunogold-electron microscopy was used to define the localization of *C. elegans* TFG-1 in the intestine (**Figure A.5a**), hypodermis (**Figure A.5b**) and muscle (**Figure A.5c**) tissues. Immunoreactive gold particles bound to Tfg-1 are highlighted by arrowheads. In each case, Tfg-1 is found in a cloud-like region that spreads from ER exit sites to the ERGIC/Golgi membranes. Bars, 100 nm.

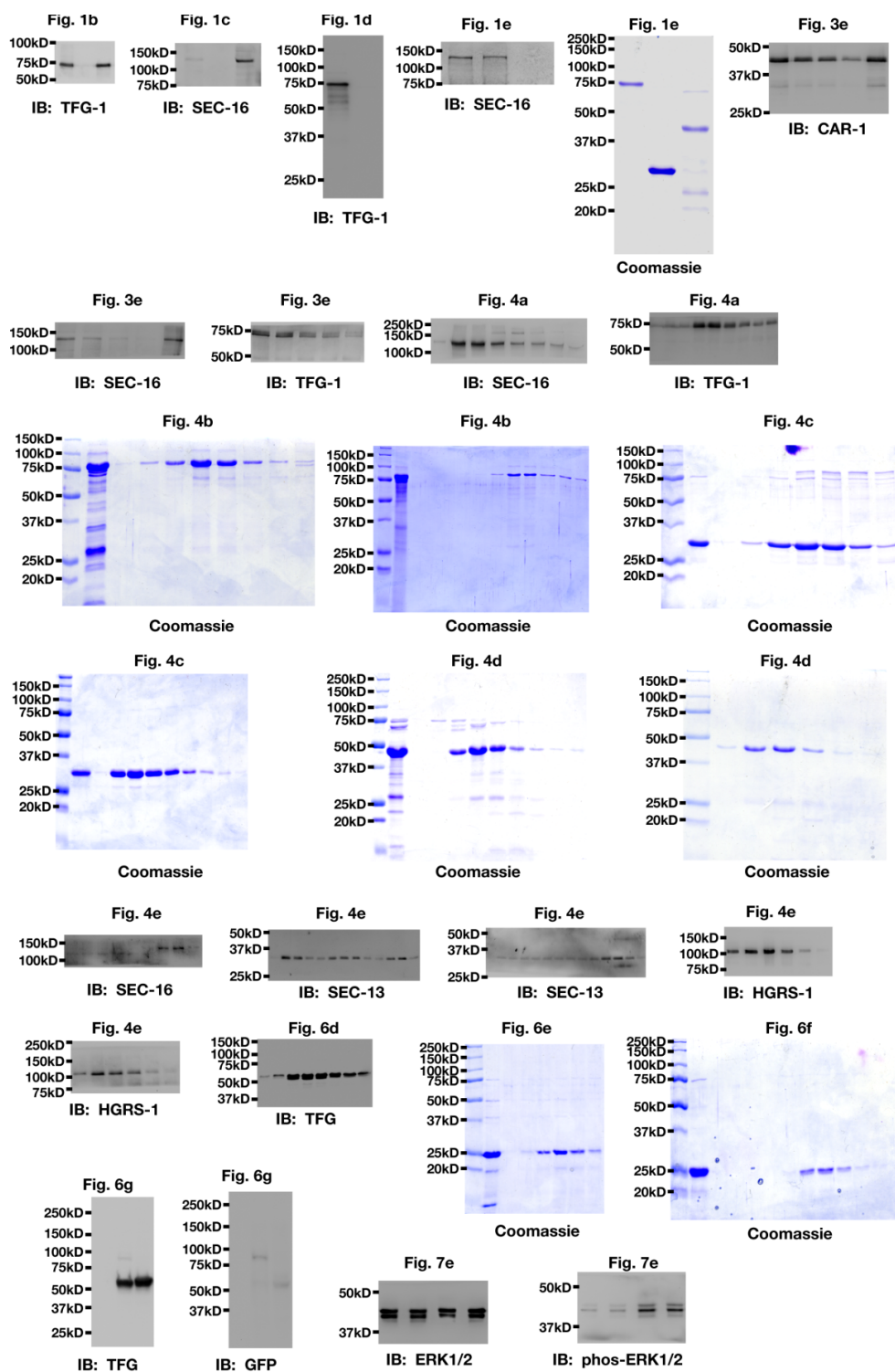


Figure A.S6 Full scan data of immunoblots and Coomassie stained gels.

Figure A.S6 Full scan data of immunoblots and Coomassie stained gels.

In several cases, the nitrocellulose used for immunoblot was cut into strips to minimize the amount of antibody necessary for analysis. Scans of entire nitrocellulose strips are shown.

Protein	% Sequence Coverage	RNAi Phenotype	Predicted Size (kD)
SEC-13/NPP-20 (Y77E11A.13)	55.6	Sterile	34.7
SEC-16 (ZK512.5)	53.2	Sterile	134.9
TFG-1 (Y63D3A.5)	20.2	Sterile	49.7
SEC-31 (T01G1.3)	19.4	Sterile	119.6
SEC-23 (Y113G7A.3)	15.2	Sterile	89.7
SEC-12 (K02B12.3)	14.4	Sterile	46.1
SEC-24.2 (ZC518.2)	9.8	Sterile	109.4

Table A.S1 Essential SEC-16 interacting proteins identified by mass spectrometry.

Table A.S1 Essential SEC-16 interacting proteins identified by mass spectrometry.

Table showing the seven proteins identified by solution mass spectrometry following immunoprecipitation of SEC-16 from *C. elegans* embryo extract (n=3), which also result in sterility following their depletion. The percent sequence coverage and molecular weight of each protein are also shown.

REFERENCES

1. Lee, M. C., Miller, E. A., Goldberg, J., Orci, L., and Schekman, R. (2004) Bi-directional protein transport between the ER and Golgi. *Annu Rev Cell Dev Biol* **20**, 87-123
2. Bonifacino, J. S., and Glick, B. S. (2004) The mechanisms of vesicle budding and fusion. *Cell* **116**, 153-166
3. Bickford, L. C., Mossessova, E., and Goldberg, J. (2004) A structural view of the COPII vesicle coat. *Curr Opin Struct Biol* **14**, 147-153
4. Dancourt, J., and Barlowe, C. (2010) Protein sorting receptors in the early secretory pathway. *Annu Rev Biochem* **79**, 777-802
5. Boyadjiev, S. A., Fromme, J. C., Ben, J., Chong, S. S., Nauta, C., Hur, D. J., Zhang, G., Hamamoto, S., Schekman, R., Ravazzola, M., Orci, L., and Eyaid, W. (2006) Cranio-lenticulo-sutural dysplasia is caused by a SEC23A mutation leading to abnormal endoplasmic-reticulum-to-Golgi trafficking. *Nat Genet* **38**, 1192-1197
6. Lang, M. R., Lapierre, L. A., Frotscher, M., Goldenring, J. R., and Knapik, E. W. (2006) Secretory COPII coat component Sec23a is essential for craniofacial chondrocyte maturation. *Nat Genet* **38**, 1198-1203
7. Matsuoka, K., Orci, L., Amherdt, M., Bednarek, S. Y., Hamamoto, S., Schekman, R., and Yeung, T. (1998) COPII-coated vesicle formation reconstituted with purified coat proteins and chemically defined liposomes. *Cell* **93**, 263-275
8. Miller, E. A., and Barlowe, C. (2010) Regulation of coat assembly--sorting things out at the ER. *Curr Opin Cell Biol* **22**, 447-453
9. Yoshihisa, T., Barlowe, C., and Schekman, R. (1993) Requirement for a GTPase-activating protein in vesicle budding from the endoplasmic reticulum. *Science* **259**, 1466-1468
10. Stagg, S. M., Gürkan, C., Fowler, D. M., LaPointe, P., Foss, T. R., Potter, C. S., Carragher, B., and Balch, W. E. (2006) Structure of the Sec13/31 COPII coat cage. *Nature* **439**, 234-238
11. Bi, X., Mancias, J. D., and Goldberg, J. (2007) Insights into COPII coat nucleation from the structure of Sec23.Sar1 complexed with the active fragment of Sec31. *Dev Cell* **13**, 635-645
12. Espenshade, P., Gimeno, R. E., Holzmacher, E., Teung, P., and Kaiser, C. A. (1995) Yeast SEC16 gene encodes a multidomain vesicle coat protein that interacts with Sec23p. *J Cell Biol* **131**, 311-324

13. Gimeno, R. E., Espenshade, P., and Kaiser, C. A. (1996) COPII coat subunit interactions: Sec24p and Sec23p bind to adjacent regions of Sec16p. *Mol Biol Cell* **7**, 1815-1823
14. Shaywitz, D. A., Espenshade, P. J., Gimeno, R. E., and Kaiser, C. A. (1997) COPII subunit interactions in the assembly of the vesicle coat. *J Biol Chem* **272**, 25413-25416
15. Whittle, J. R., and Schwartz, T. U. (2010) Structure of the Sec13-Sec16 edge element, a template for assembly of the COPII vesicle coat. *J Cell Biol* **190**, 347-361
16. Supek, F., Madden, D. T., Hamamoto, S., Orci, L., and Schekman, R. (2002) Sec16p potentiates the action of COPII proteins to bud transport vesicles. *J Cell Biol* **158**, 1029-1038
17. Li, L., and Xie, T. (2005) Stem cell niche: structure and function. *Annu Rev Cell Dev Biol* **21**, 605-631
18. Shi, A., Chen, C. C., Banerjee, R., Glodowski, D., Audhya, A., Rongo, C., and Grant, B. D. (2010) EHBP-1 functions with RAB-10 during endocytic recycling in *Caenorhabditis elegans*. *Mol Biol Cell* **21**, 2930-2943
19. Mallard, F., Tang, B. L., Galli, T., Tenza, D., Saint-Pol, A., Yue, X., Antony, C., Hong, W., Goud, B., and Johannes, L. (2002) Early/recycling endosomes-to-TGN transport involves two SNARE complexes and a Rab6 isoform. *J Cell Biol* **156**, 653-664
20. Hughes, H., Budnik, A., Schmidt, K., Palmer, K. J., Mantell, J., Noakes, C., Johnson, A., Carter, D. A., Verkade, P., Watson, P., and Stephens, D. J. (2009) Organisation of human ER-exit sites: requirements for the localisation of Sec16 to transitional ER. *J Cell Sci* **122**, 2924-2934
21. Greco, A., Mariani, C., Miranda, C., Lupas, A., Pagliardini, S., Pomati, M., and Pierotti, M. A. (1995) The DNA rearrangement that generates the TRK-T3 oncogene involves a novel gene on chromosome 3 whose product has a potential coiled-coil domain. *Mol Cell Biol* **15**, 6118-6127
22. Hernández, L., Pinyol, M., Hernández, S., Beà, S., Pulford, K., Rosenwald, A., Lamant, L., Falini, B., Ott, G., Mason, D. Y., Delsol, G., and Campo, E. (1999) TRK-fused gene (TFG) is a new partner of ALK in anaplastic large cell lymphoma producing two structurally different TFG-ALK translocations. *Blood* **94**, 3265-3268
23. Schecterson, L. C., and Bothwell, M. (2010) Neurotrophin receptors: Old friends with new partners. *Dev Neurobiol* **70**, 332-338
24. Klesse, L. J., and Parada, L. F. (1999) Trks: signal transduction and intracellular pathways. *Microsc Res Tech* **45**, 210-216

25. Greco, A., Fusetti, L., Miranda, C., Villa, R., Zanotti, S., Pagliardini, S., and Pierotti, M. A. (1998) Role of the TFG N-terminus and coiled-coil domain in the transforming activity of the thyroid TRK-T3 oncogene. *Oncogene* **16**, 809-816
26. Chen, L., McCloskey, T., Joshi, P. M., and Rothman, J. H. (2008) ced-4 and proto-oncogene tfg-1 antagonistically regulate cell size and apoptosis in *C. elegans*. *Curr Biol* **18**, 1025-1033
27. Zhang, F., Kartner, N., and Lukacs, G. L. (1998) Limited proteolysis as a probe for arrested conformational maturation of delta F508 CFTR. *Nat Struct Biol* **5**, 180-183
28. Trzcinska-Daneluti, A. M., Ly, D., Huynh, L., Jiang, C., Fladd, C., and Rotin, D. (2009) High-content functional screen to identify proteins that correct F508del-CFTR function. *Mol Cell Proteomics* **8**, 780-790
29. Watson, P., Townley, A. K., Koka, P., Palmer, K. J., and Stephens, D. J. (2006) Sec16 defines endoplasmic reticulum exit sites and is required for secretory cargo export in mammalian cells. *Traffic* **7**, 1678-1687
30. Ivan, V., de Voer, G., Xanthakis, D., Spoorendonk, K. M., Kondylis, V., and Rabouille, C. (2008) Drosophila Sec16 mediates the biogenesis of tER sites upstream of Sar1 through an arginine-rich motif. *Mol Biol Cell* **19**, 4352-4365
31. Heinzer, S., Wörz, S., Kalla, C., Rohr, K., and Weiss, M. (2008) A model for the self-organization of exit sites in the endoplasmic reticulum. *J Cell Sci* **121**, 55-64
32. Farhan, H., Weiss, M., Tani, K., Kaufman, R. J., and Hauri, H. P. (2008) Adaptation of endoplasmic reticulum exit sites to acute and chronic increases in cargo load. *EMBO J* **27**, 2043-2054
33. Hughes, H., and Stephens, D. J. (2008) Assembly, organization, and function of the COPII coat. *Histochem Cell Biol* **129**, 129-151
34. Greco, A., Miranda, C., and Pierotti, M. A. (2010) Rearrangements of NTRK1 gene in papillary thyroid carcinoma. *Mol Cell Endocrinol* **321**, 44-49
35. Roccato, E., Pagliardini, S., Cleris, L., Canevari, S., Formelli, F., Pierotti, M. A., and Greco, A. (2003) Role of TFG sequences outside the coiled-coil domain in TRK-T3 oncogenic activation. *Oncogene* **22**, 807-818
36. Farhan, H., Wendeler, M. W., Mitrovic, S., Fava, E., Silberberg, Y., Sharan, R., Zerial, M., and Hauri, H. P. (2010) MAPK signaling to the early secretory pathway revealed by kinase/phosphatase functional screening. *J Cell Biol* **189**, 997-1011

37. Cheeseman, I. M., Niessen, S., Anderson, S., Hyndman, F., Yates, J. R., Oegema, K., and Desai, A. (2004) A conserved protein network controls assembly of the outer kinetochore and its ability to sustain tension. *Genes Dev* **18**, 2255-2268
38. Audhya, A., Hyndman, F., McLeod, I. X., Maddox, A. S., Yates, J. R., Desai, A., and Oegema, K. (2005) A complex containing the Sm protein CAR-1 and the RNA helicase CGH-1 is required for embryonic cytokinesis in *Caenorhabditis elegans*. *J Cell Biol* **171**, 267-279
39. Sato, K., Sato, M., Audhya, A., Oegema, K., Schweinsberg, P., and Grant, B. D. (2006) Dynamic regulation of caveolin-1 trafficking in the germ line and embryo of *Caenorhabditis elegans*. *Mol Biol Cell* **17**, 3085-3094
40. Presley, J. F., Cole, N. B., Schroer, T. A., Hirschberg, K., Zaal, K. J., and Lippincott-Schwartz, J. (1997) ER-to-Golgi transport visualized in living cells. *Nature* **389**, 81-85
41. Rostaing, P., Real, E., Siksou, L., Lechaire, J. P., Boudier, T., Boeckers, T. M., Gertler, F., Gundelfinger, E. D., Triller, A., and Marty, S. (2006) Analysis of synaptic ultrastructure without fixative using high-pressure freezing and tomography. *Eur J Neurosci* **24**, 3463-3474
42. REYNOLDS, E. S. (1963) The use of lead citrate at high pH as an electron-opaque stain in electron microscopy. *J Cell Biol* **17**, 208-212
43. Fiala, J. C. (2005) Reconstruct: a free editor for serial section microscopy. *J Microsc* **218**, 52-61
44. Perlaky, L., Valdez, B. C., Busch, R. K., Larson, R. G., Jhiang, S. M., Zhang, W. W., Brattain, M., and Busch, H. (1992) Increased growth of NIH/3T3 cells by transfection with human p120 complementary DNA and inhibition by a p120 antisense construct. *Cancer Res* **52**, 428-436
45. Saito, K., Chen, M., Bard, F., Chen, S., Zhou, H., Woodley, D., Polischuk, R., Schekman, R., and Malhotra, V. (2009) TANGO1 facilitates cargo loading at endoplasmic reticulum exit sites. *Cell* **136**, 891-902
46. Diop, S. B., Bertaux, K., Vasanthi, D., Sarkeshik, A., Goirand, B., Aragnol, D., Tolwinski, N. S., Cole, M. D., Pradel, J., Yates, J. R., Mishra, R. K., Graba, Y., and Saurin, A. J. (2008) Reptin and Pontin function antagonistically with PcG and TrxG complexes to mediate Hox gene control. *EMBO Rep* **9**, 260-266
47. Yates, J. R., Eng, J. K., McCormack, A. L., and Schieltz, D. (1995) Method to correlate tandem mass spectra of modified peptides to amino acid sequences in the protein database. *Anal Chem* **67**, 1426-1436

48. Siegel, L. M., and Monty, K. J. (1966) Determination of molecular weights and frictional ratios of proteins in impure systems by use of gel filtration and density gradient centrifugation. Application to crude preparations of sulfite and hydroxylamine reductases. *Biochim Biophys Acta* **112**, 346-362
49. Maine, E. M., and Kimble, J. (1989) Identification of genes that interact with glp-1, a gene required for inductive cell interactions in *Caenorhabditis elegans*. *Development* **106**, 133-143
50. Moscat, J., Diaz-Meco, M. T., Albert, A., and Campuzano, S. (2006) Cell signaling and function organized by PB1 domain interactions. *Mol Cell* **23**, 631-640

Appendix B

Phosphoinositide Signaling During Membrane Transport in *Saccharomyces cerevisiae*

The work presented in this chapter has been published:

Schuh, A.L and Audhya, A.
(2012) *Subcell Biochem.* 59:35-63.

Abstract

Phosphatidylinositol (PI) is distinct from other phospholipids, possessing a head group that can be modified by phosphorylation at multiple positions to generate unique signaling molecules collectively known as phosphoinositides. The set of kinases and phosphatases that regulate PI metabolism are conserved throughout eukaryotic evolution, and numerous studies have demonstrated that phosphoinositides regulate a diverse spectrum of cellular processes, including vesicle transport, cell proliferation, and cytoskeleton organization. Over the past two decades, nearly all PI derivatives have been shown to interact directly with cellular proteins to affect their localization and/or activity. Additionally, there is growing evidence, which suggests that phosphoinositides may also affect local membrane topology. Here, we focus on the role of phosphoinositides in membrane trafficking and underscore the significant role that yeast has played in the field.

Phosphoinositide metabolism in the yeast *Saccharomyces cerevisiae*

In wild-type *Saccharomyces cerevisiae*, four major phosphorylated derivatives of PI have been identified: PI3P, PI4P, PI3,5P₂ and PI4,5P₂ (**Figure B.1**). A single soluble Class III PI 3-kinase, encoded by *VPS34*, generates the total cellular pool of PI3P, which accumulates mostly in the limiting membranes of endosomes and lysosome-like vacuoles (1-3). Vps34p functions as a subunit of at least two distinct protein complexes, both of which also contain the serine/threonine-protein kinase Vps15p. Myristoylation anchors Vps15p to membranes and assists in the recruitment of cytosolic Vps34p to appropriate intracellular membranes (4,5). Vps15p is considered to be a regulatory subunit within PI 3-kinase complexes and contains HEAT domains responsible for additional protein-protein interactions (6). Despite the essential nature of the Vps15p kinase domain to Vps34p recruitment and activation, direct substrates of Vps15p remain undefined.

The stability of PI3P is regulated by both catabolic and anabolic pathways. Two major routes of PI3P degradation have been characterized. First, PI3P contained in the limiting membrane of endosomes is a substrate for proteolytic enzymes in the vacuole lumen. Inhibition of membrane transport to the vacuole thereby causes an increase in cellular PI3P levels (7). Alternatively, PI3P is subject to dephosphorylation by a group of lipid phosphatases, which include the myotubularin-related enzyme Ymr1p and two synaptojanin-like proteins, Sjl2p and Sjl3p (8,9). Although PI3P synthesis is not essential to yeast cell viability, depletion of all three PI3P phosphatases results in lethality (10). It remains unclear whether elevated PI3P levels are solely responsible for this effect, but the result highlights the importance of regulated phosphoinositide turnover for normal cell proliferation.

PI3P is also a substrate for the Fab1p lipid kinase, which specifically phosphorylates the D5 position in the inositol ring to generate PI3,5P₂. The majority of Fab1p localizes to the limiting membrane of the yeast vacuole, where it functions together with Vac7p, a transmembrane regulatory factor, to generate the total cellular pool of PI3,5P₂ (11-13). In the absence of Vac7p, levels of PI3,5P₂ become undetectable. However, deletion of Fig4p, a PI3,5P₂ 5-phosphatase, can suppress phenotypes exhibited by loss of Vac7p, indicating that Fab1p remains functional in the absence of its regulator (14). Consistent with this finding, mutant isoforms of Fab1p have been characterized, which bypass the requirement for Vac7p in PI3,5P₂ synthesis.

In contrast to the unique functions of Vps34p to generate 3' phosphoinositides and Fab1p to generate PI3,5P₂, three PI 4-kinases have been characterized in yeast and include the type III PI 4-kinase *STT4*, the type IIIb PI 4-kinase *PIK1*, and the type II PI 4-kinase *LSB6*. Both *Stt4p* and *Pik1p* are essential genes in yeast, suggesting they possess non-overlapping functions and generate unique pools of PI4P, which cannot substitute for one another (15). Consistent with this idea, *Stt4p* localizes primarily to the plasma membrane, while the majority of *Pik1p* accumulates on Golgi membranes (16,17). At the cell surface, *Stt4p* appear to coalesce into discrete patches that are enriched in the mother cell. Purification of *Stt4p* has revealed a number of interacting proteins that regulate *Stt4p* function. These include *Sfk1p* and *Efr3p*, two putative transmembrane proteins and *Ypp1p*, a soluble protein containing two tetratricopeptide repeat domains (17-19). Inhibition of each regulator has been shown to decrease PI4P levels at the cell surface and perturb the localization of *Stt4p*. Unlike *Sfk1p*, both *Efr3p* and *Ypp1p* are essential

for yeast cell viability, suggesting they may regulate unique biochemical pathways downstream of Stt4p, but further studies are required to address this issue.

Distinct from plasma membrane synthesis of PI4P, Pik1p generates an essential pool of PI4P on Golgi membranes. Proper targeting of Pik1p to the Golgi requires an interaction with Frq1p, a myristoylated regulator of Pik1p-mediated PI4P synthesis (20). Loss of Frq1p is lethal, but overproduction of Pik1p can bypass the requirement of Frq1p, suggesting that additional mechanisms exist to target Pik1p to Golgi membranes. In addition to its role at the Golgi, Pik1p undergoes nucleo-cytoplasmic shuttling and has been postulated to generate a nuclear pool of PI4P (21,22). Frq1p is not required for Pik1p function in the nucleus, and a specific role for nuclear PI4P has yet to be defined.

Unlike Stt4p and Pik1p, Lsb6p activity is not essential for normal growth of *S. cerevisiae*, and its loss does not impact the total cellular levels of PI4P under standard conditions (23,24). However, overproduction of Lsb6p weakly suppresses the loss of Stt4p, indicating that Lsb6p can function as a PI 4-kinase *in vivo*. Localization studies have placed Lsb6p at the plasma membrane, consistent with its ability to suppress deletion of *STT4*, and the limiting membrane of the vacuole. Additionally, Lsb6p has been shown to regulate endosome motility (25). However, this function of Lsb6p is independent of its lipid kinase activity.

Similar to PI3P, metabolism of PI4P is mediated by a set of lipid phosphatases and a single lipid kinase, the PI4P 5-kinase Mss4p. The plasma membrane pool of PI4P generated by Stt4p is largely regulated by the Sac1p lipid phosphatase (26). Biochemical and localization studies indicate that Sac1p is a type II membrane protein that localizes mainly to the ER under normal growth conditions (26,27). Recent findings indicate that Sac1p hydrolyzes PI4P at sites

of ER-plasma membrane contact, acting from the ER in trans on its plasma membrane substrate (28). The retention of Sac1p in the ER is dependent on the dolichol phosphate mannose synthase Dpm1p, and loss of Dpm1p results in the accumulation of Sac1p in the Golgi (27). In the absence of Sac1p, PI4P levels on the cell surface dramatically increase in an Stt4p-dependent fashion (29).

PI4P generated by Stt4p can also be converted into PI4,5P₂ by the action of Mss4p. Similar to Stt4p, Mss4p is largely restricted to discrete foci on the plasma membrane (17,30). However, patches of Stt4p and Mss4p do not overlap, suggesting that Mss4p can utilize alternative sources of PI4P at the cell surface (17). Consistent with this idea, elimination of Stt4p activity only diminishes PI4,5P₂ levels by ~50% (15). The remaining pool of PI4,5P₂ is synthesized from PI4P initially generated at the Golgi by Pik1p, which is likely transported to the plasma membrane within the membranes of secretory vesicles. Golgi PI4P is further regulated by multiple phosphoinositide phosphatases, including members of the synaptojanin-like family of lipid phosphatases, Sjl2p and Sjl3p, as well as Sac1p (26,27,31).

Although the majority of Mss4p localizes to the plasma membrane, the PI4P 5-kinase also undergoes nucleo-cytoplasmic shuttling similar to Pik1p (32). The factors that mediate nuclear import and export of Mss4p (Kap123p and Bcp1p) are distinct from those that regulate Pik1p nucleo-cytoplasmic transport (Kap95p and Msn5p) (22). Also unlike Pik1p, inhibition of Mss4p nuclear entry fails to affect normal cellular growth, suggesting that nuclear PI4,5P₂ is not essential in yeast (32). Instead, targeting of Mss4p to the nucleus may function to regulate its activity on the cell surface and thereby control cytoplasmic PI4,5P₂ synthesis. Although factors required specifically for cell surface Mss4p patch formation have yet to be defined, plasma

membrane targeting of Mss4p is partially dependent on its phosphorylation by yeast casein kinase I activity (32). Additionally, the small calcium-binding protein calmodulin appears to regulate Mss4p lipid kinase activity, although the mechanistic basis for this affect remains undefined (33). Levels of PI4,5P₂ are further regulated by lipid phosphatases, including the synaptojanin-like proteins Sjl1p and Sjl2p, the ER-localized inositol 5-phosphatase Inp54p, and the phospholipase C isoform Plc1p, which specifically hydrolyzes PI4,5P₂ to generate diacylglycerol (DAG) and IP₃ (34-36).

Through these highly regulated biosynthetic and degradation pathways, individual phosphoinositides are spatially restricted within the cell. PI3P and PI3,5P₂ are enriched in endosomal and vacuolar membranes, while PI4P and PI4,5P₂ are concentrated in the Golgi and plasma membrane (**Figure B.2**). In the following sections, we will highlight mechanisms by which phosphoinositides function to regulate virtually all of the membrane trafficking pathways that have been described in yeast.

Binding Domains and Effector Proteins of PI3P

PI3P carries out its cellular functions by recruiting and/or activating a subset of proteins to specific internal membrane compartments where PI3P is synthesized. These proteins function in signal transduction, vesicle trafficking, and cytoskeletal rearrangements. Despite these differences in function, the majority of proteins known to bind to PI3P share a small subset of domains that interact directly with the phosphoinositide (3,37). We will first highlight roles for PI3P generated at the endosome by PI3K Complex II, which is composed of Vps15p, Vps34p, Vps30p and Vps38p (38). In particular, effectors of PI3P in both anterograde transport from the endosome to the vacuole and retrograde transport from the endosome to the Golgi will be

discussed. Additionally, we will describe alternative roles for PI3P in constitutive and starvation-induced autophagy pathways, which utilize PI3K Complex I, containing Vps15p, Vps34p, Vps30p, and Atg14p (38,39).

The FYVE Domain

The FYVE domain is composed of ~70 conserved residues that specifically bind PI3P. This domain is cysteine rich and coordinates two zinc ions, which are essential for structural integrity and PI3P binding (40-43). Three conserved sequences have been identified in all FYVE domains: the amino-terminal WxxD motif, the central (R/K)(R/K) HHCR motif, and the carboxyl-terminal RVC motif. These three regions are crucial in forming a concave binding pocket for PI3P association. In addition, the FYVE domain contains a hydrophobic protrusion, commonly referred to as the membrane insertion loop (MIL) domain, adjacent to the (R/K)(R/K) HHCR motif (42,43).

The FYVE domain uses a multivalent mechanism to anchor itself to a target membrane, which includes specific interactions with PI3P as well as other lipids. Based upon the calculated electrostatic properties of several FYVE domains, a strong positive potential exists around the MIL domain, which supports interactions with acidic phospholipids (44). Consistent with this finding, studies have shown that the acidic phospholipid phosphatidylserine (PS) specifically enhances the affinity of FYVE domains for lipid bilayers (45). In addition, these nonspecific electrostatic interactions likely help to align the FYVE domain in an optimal position for membrane penetration of the MIL domain (45,46). Insertion of the hydrophobic MIL domain is dependent upon the presence of PI3P, and this process has been shown to significantly increase the affinity between lipid bilayers and FYVE domains (46). Mutagenesis of select hydrophobic

residues within the MIL region drastically reduces the affinity for membrane bound PI3P and disrupts normal function of FYVE domain containing proteins (42,45).

The association of FYVE domains with membranes also appears to be pH dependent. In a neutral buffer (pH 7.0), FYVE domain containing proteins in yeast localize to endosomal and vacuolar membranes. However, when cells are shifted into a mildly basic buffer (pH 8.0), FYVE domain containing proteins largely redistribute to the cytoplasm (47,48). These data support a model in which the two histidine residues within the conserved (R/K)(R/K) HHCR motif must be protonated to form hydrogen bonds with the 3' phosphate of PI3P (49,50).

In total, five FYVE domain containing proteins have been identified in yeast: Vac1p, Fab1p, Vps27p, Pib1p, and Pib2p. Vac1p is required for the transport of vesicles from the Golgi to prevacuolar endosomes (51). Similar to other FYVE domains, the Vac1p FYVE domain binds directly to PI3P and localizes to endosomes when expressed as a GFP fusion. However, in cells lacking PI3P, Vac1p continues to accumulate on membranes, suggesting that the interaction between Vac1p and PI3P does not solely influence its localization (52). Instead, PI3P may regulate Vac1p activity, potentially by influencing its interactions with other proteins. Consistent with this idea, both the Rab-type GTPase Vps21p and the Sec1-like protein Vps45p, interact with Vac1p in a FYVE domain-dependent manner (52,53).

Fab1p, a PI3P 5-kinase, and Vps27p, a component of the ESCRT (endosomal sorting complex required for transport) machinery, have both been implicated in the formation of multivesicular endosomes (MVEs), which are specialized organelles essential for the degradation of many transmembrane proteins (54-57). In this pathway, ubiquitin-modified cargoes are initially sequestered within vesicles that bud into the endosome lumen. Upon MVE fusion with

the vacuole, cargo-laden vesicles are transferred directly into the hydrolytic environment of the vacuole lumen, resulting in protein and vesicle degradation. In the absence of PI3P, neither Vps27p nor Fab1p localize properly, and MVE biogenesis is dramatically inhibited. Unlike the FYVE domain of Vps27p, which localizes to endosomes when expressed as a GFP fusion, the Fab1p FYVE domain associates specifically with the vacuolar limiting membrane (13).

Although it has been shown to bind PI3P directly, these data suggest that the Fab1p FYVE domain may also bind another factor, which directs its accumulation onto the vacuole membrane. The identity of such a factor remains unknown.

In addition to the interaction between PI3P and the FYVE domains of Vps27p and Fab1p, the ESCRT-II subunit Vps36p, which also functions in MVE biogenesis, binds to PI3P through a noncanonical binding pocket within its amino-terminal GLUE (GRAM-like, ubiquitin binding in EAP45) domain (58). The GLUE domain exhibits a split PH (pleckstrin homology) domain fold with two curved beta sheets and a single long alpha helix. A highly basic pocket is delineated by three variable loops within the GLUE domain, a configuration that is distinct from most PH domains that interact with phosphoinositides. Mutations within the basic region inhibit protein sorting into MVEs, indicating association of ESCRT-II with PI3P is critical for function (58,59).

Pib1p may also function in the MVE pathway as an E3 RING-type ubiquitin ligase. Studies indicate that Pib1p localizes to both endosomal and vacuolar membranes, and its distribution is dependent solely on its interaction with PI3P (60). Although specific Pib1p-dependent cargoes have yet to be identified, it is likely that Pib1p functions at the initial stages of cargo selection/modification in the MVE pathway. The role of Pib2p remains unknown, although localization studies indicate that it accumulates on the vacuolar membrane under steady

state conditions (61).

The Phox Homology (PX) Domain

The PX domain is composed of approximately 130 amino acids and is found in proteins that function in vesicle trafficking, protein sorting, and lipid modification (37). Typically, the PX domain folds into a compact structure composed of three beta strands followed by three alpha helices. A conserved RR(F/Y)S(D/E)F motif and three additional basic residues located nearby are proposed to form a binding pocket for PI3P (62-64). In addition, many of the PX domains contain a polyproline motif (PxxP), which is predicted to interact with SH3 domains (65). PX domains also interact with membranes by using a multivalent mechanism, which includes non-specific electrostatic interactions, hydrophobic insertion, and oligomerization. In particular, oligomerization is crucial for increasing the affinity of PX domains that otherwise would be unable to localize to membranes due to low affinities in their monomeric state (66).

In yeast, 15 proteins that harbor a PX domain have been identified, and all have an affinity for PI3P. Using surface plasmon resonance (SPR), four yeast PX domains have been classified as having a high affinity for PI3P, ranging from 0.15 μM to 0.5 μM , while the rest exhibit affinities greater than 100 μM and are classified as low affinity PX domains (67). These affinity measurements suggest that only the four high affinity PX domains are capable of membrane association independently of other binding partners, while the remaining PX domains must require oligomerization or interaction with additional proteins to mediate their localization.

The four yeast proteins with high affinity for PI3P are Mdm1p, Snx3p, Vam7p and Ypt35p. Mdm1p is required for mitochondrial and nuclear inheritance, and although its PX domain has been shown to bind to PI3P with a high affinity, the function of this interaction

remains unknown (67). Snx3p is a member of the sorting nexin family and functions in the retrograde transport of a subset of cargoes from endosomes to the Golgi (68). Importantly, the retrieval of certain transmembrane receptors from late endosomes is required to maintain the proper sorting of hydrolases to the vacuole. One of the best studied receptors is the type I membrane protein Vps10p, which is essential for the normal trafficking of the soluble vacuolar hydrolase carboxypeptidase Y (CPY). At the endosome, CPY dissociates from Vps10p for ultimate delivery to the vacuole, while Vps10p undergoes recycling to the trans Golgi network (TGN), becoming available for another round of CPY transport (69,70). The high affinity of Snx3p for PI3P targets it to tubular endosomes where it can associate with Vps10p and mediate its retrieval. However, mutations in the Snx3p PX domain that inhibit PI3P binding result in the missorting of receptors to the vacuole, inhibiting further transport of CPY and other cargoes (68). These data implicate PI3P in retrograde trafficking from endosomes to the Golgi. Snx3p functions together with the retromer complex, a set of proteins also required for retrograde trafficking from endosomes to the Golgi. Two components of the retromer complex, Vps5p and Vps17p, also contain PX domains, each with a low affinity for PI3P. However, when co-assembled, the multiple low affinity interactions with PI3P maintain an endosomal distribution for the retromer complex, and further highlight a role for PI3P in orchestrating receptor recycling from the endosomal system (71).

The third high affinity PI3P interacting protein Vam7p is a target SNARE (Soluble NSF Attachment Protein Receptor) that functions during the docking and fusion steps of membrane transport to the vacuole (62,72). An intact PX domain is required for this function, implicating PI3P in the late stages of membrane transport to the vacuole. Finally, Ypt35p also binds to PI3P

with high affinity and has been found to localize to endosomal membranes. However, the specific function of Ypt35p remains unknown (67).

Among the other low affinity PI3P-interacting PX domains, Mvp1p, Spo14p, Snx4p, Snx41p, and Atg20p each possess characterized roles in membrane trafficking. Mvp1p is an endosomal protein required for protein sorting to the vacuole. Although its precise role has not been clearly identified, genetic studies indicate that Mvp1p functions with the dynamin-like protein Vps1p in retrograde protein transport from endosomes to the Golgi (73). Spo14p is a phospholipase D isoform that has been implicated in protein secretion (74). During vegetative growth, Spo14p localizes to endosomes, but its specific activity there is poorly characterized, and it would be premature to suggest that PI3P functions directly in the secretory pathway (75). Snx4p (also known as Atg24p), Snx41p, and Atg20p (also known as Snx42p) all are sorting nexins that function in a common complex to sort receptors from early endosomes to the Golgi (76). Even though the binding affinities for individual PX domains within the individual sorting nexins are low, their assembly into a complex leads to PX domain multimerization and an increased affinity for PI3P on endosomes.

In addition, both Snx4p/Atg24p and Atg20p are required for selective autophagy, a constitutive cytoplasm to vacuole targeting (CVT) pathway in which a perivacuolar phagophore assembly site (PAS) initiates the biogenesis of an autophagosome, a double-membrane vesicle (77,78). This pathway depends on a large group of proteins that assist in the elongation of a double-membrane structure known as an isolation membrane that ultimately circularizes to form an autophagosome. The autophagosome then fuses with the vacuole, leading to the degradation of its contents (79). When yeast cells are under starvation, an alternative bulk autophagy

pathway is initiated to break down proteins into amino acids for energy (80). The CVT and bulk autophagy pathways share many of the same proteins, including the PI3K Complex I (Vps15p, Vps34p, Vps30p, and Atg14p). The Atg14p subunit of this complex provides specificity in directing Vps34p to PASs (81). Interactions between PI3P and the PX domains of Snx4p/Atg24p and Atg20p are required for normal CVT pathway function, directly implicating PI3P in the constitutive formation of autophagosomes (77).

Further highlighting a role for phosphoinositides in the CVT pathway are two additional PI3P effectors called Atg21p and Atg27p. Unlike other PI3P binding proteins, neither Atg21p nor Atg27p harbor a PX or FYVE domain. Instead, PI3P binding is mediated by short basic stretches of amino acids, FRRG in Atg21p and KKPAKK in Atg27p (82-85). Mutations in these motifs, which inhibit PI3P binding, block CVT pathway function. In addition, deletion of *VPS34* or *VPS15* has also been shown to block starvation-induced bulk autophagy (82). One phosphoinositide effector potentially responsible for this effect is Atg18p, which also contains an FRRG motif capable of binding to PI3P (86,87). Although the degree to which mutations in the Atg18p PI3P-binding motif affects bulk autophagy remains controversial (84), the participation of PI3P in autophagosome biogenesis is incontrovertible.

In summary, studies in yeast have clearly illustrated the various roles PI3P plays in membrane trafficking, both in directing localization of effector molecules and regulating their activities. Although it is likely that several new PI3P effectors still await characterization, most will likely function at endosomes, vacuoles, or autophagosomes, where PI3P is highly enriched. We predict that many of these new molecules will exhibit a low affinity for PI3P, but together

with other protein-protein interactions, specificity for endosomal/autophagosomal signaling pathways can be achieved.

Effectors of PI3,5P₂ and their roles in membrane trafficking

In yeast, a single PI3P 5-kinase called Fab1p has been identified and is responsible for the generation of PI3,5P₂ (12,88). The Fab1p lipid kinase contains three conserved protein domains: an amino-terminal FYVE domain, a Cpn60/TCP-1 chaperonin family (CCT) domain, and a carboxyl-terminal lipid kinase domain (12,89). PI3,5P₂ is largely generated on the vacuolar limiting membrane, where it has a role in retrograde trafficking from the vacuole and vacuolar homeostasis (90). Deletion of *FAB1* leads to several phenotypes including enlarged vacuoles, defects in MVE biogenesis, a lack of vacuolar acidification and slow temperature sensitive growth (12,54,88,91). Here, we will discuss the effectors of PI3,5P₂ that have been discovered and how they relate to the effects seen upon loss of Fab1p activity.

Two classes of PI3,5P₂ binding domains have been identified. The first is found in a family of seven bladed β -propeller proteins that bind phosphoinositides (PROPPINs), and the second is contained within members of the epsin family. In yeast, three PROPPIN proteins have been identified, including Atg18p, Atg21p and Hsv2p (92). As discussed earlier, both Atg18p and Atg21p harbor a FRRG motif capable of interacting with PI3P. However, SPR studies indicate they can also bind PI3,5P₂ with high affinity (~500 nM) (87). Moreover, loss of Atg18p causes a dramatic increase in vacuole size, similar to the phenotype observed following *FAB1* deletion, suggesting a role downstream of PI3,5P₂ signaling (87). Localization studies indicate that all three proteins associate with both endosomal membranes and the limiting membrane of the vacuole. It is possible that PROPPIN proteins associate with both PI3P and PI3,5P₂ and

exhibit distinct activities depending on the lipid to which they are bound. For example, interactions between PI3P and Atg18p and Atg21p are likely important for constitutive autophagy, which does not depend on Fab1p-mediated PI3,5P₂ production (12,82). In contrast, interaction between PI3,5P₂ and Atg18p is probably required for normal vacuole homeostasis and retrograde trafficking from the vacuole to the Golgi via an endosomal intermediate (87). Notably, in cells lacking Fab1p, the PROPPIN proteins continue to localize to the endosome and vacuolar membranes (93). Nevertheless, PI3,5P₂ binding to these factors may regulate their function as opposed to their localization. Hsv2p is the least well characterized PROPPIN in yeast, but studies indicate that the protein participates in a unique autophagic pathway responsible for the turnover of nuclear membranes (94). It remains unclear whether PI3,5P₂ may function to regulate this activity.

As discussed earlier, Fab1p also regulates the biogenesis of luminal vesicles within endosomes (54). While none of the PROPPIN proteins exhibit a function at the MVE, two other effectors of PI3,5P₂ have been implicated in MVE-mediated protein sorting. Both Ent3p, which contains a phosphoinositide binding motif called the ENTH (epsin N-terminal homology) domain, and Ent5p, which harbors a related ANTH (AP180 N-terminal homology) domain, bind to PI3,5P₂ *in vitro* and require Fab1p activity for localization *in vivo* (95,96). Additionally, the simultaneous loss of Ent3p and Ent5p interferes with the trafficking of integral membrane proteins to the vacuole lumen, similar to the phenotype exhibited by *fab1* mutant cells (96). Moreover, both Ent3p and Ent5p have been implicated in AP-1 (adaptor protein 1)-dependent sorting of chitin synthase, a process previously shown to require Fab1p activity, further suggesting a role for the epsin-like proteins downstream of PI3,5P₂ signaling (97-99).

The phenotypes exhibited by mutant yeast cells lacking Fab1p cannot be explained by the few effector molecules that have been discovered to date. Therefore, it is highly probable that additional PI3,5P₂-binding proteins await characterization. In particular, the proteins that mediate Fab1p-dependent vacuolar acidification remain unknown. Although speculative, the vacuolar ATPase, which is known to regulate the acidification of vacuoles, is a likely candidate for this function. Presumably, there are also other PI3,5P₂ effectors, in addition to Atg18p, which participate in the retrograde transport of proteins from the vacuole to endosomes, since deletion of *ATG18* does not phenocopy the effects of *FAB1* deletion in this pathway (93). The limited production of PI3,5P₂ in yeast cells has hindered progress to identify key effectors of this lipid, but further genetic and biochemical studies will almost certainly uncover new proteins that harbor binding domains specific for PI3,5P₂.

Roles for PI4P in membrane transport

At least two non-redundant pools of PI4P are synthesized in yeast cells, one at the Golgi apparatus and a second at the plasma membrane. Each functions in multiple membrane trafficking pathways, involving both protein and lipid transport. The type III α PI 4-kinase Pik1p regulates PI4P production at the Golgi, and plays critical roles in maintaining secretory protein export to the cell surface, trafficking of cargoes to the vacuole, and endocytic protein transport (15,16,100). The type III α PI 4-kinase controls PI4P synthesis at the plasma membrane and has also been implicated in endocytic trafficking, likely through its regulation of actin cytoskeleton organization (17,101). Additionally, roles for PI4P extend to the endoplasmic reticulum, both in protein secretion from this compartment and aminophospholipid transport (102,103). Here, we

will discuss the various roles of PI4P at different intracellular compartments, specifying effectors that have been identified thus far, which function in membrane transport.

Functions of PI4P synthesized by Pik1p in the Golgi

A function for PI4P in secretion from the Golgi in yeast was initially suggested by studies that focused on the PI transfer protein Sec14p, which is essential for the biogenesis of Golgi transport vesicles (104). In a screen for bypass suppressors of a *sec14* temperature sensitive allele, a mutant isoform of the Sac1p phosphoinositide phosphatase was identified. Loss of Sac1p activity led to an increase in PI4P that was necessary for *sec14* suppression, suggesting a role for this lipid in Golgi secretion. Consistent with this finding, overexpression of the PI 4-kinase *PIK1* partially restored the growth of *sec14* mutant cells at elevated temperature (100). Moreover, loss of Sec14p activity led to diminished production of PI4P, suggesting a role for Sec14p in regulating Pik1p activity. Since subsequent studies have demonstrated that *sac1* mutant cells accumulate PI4P mostly at the cell surface in an Stt4p-dependent manner, the precise nature of Sac1p-mediated Sec14p bypass remains unclear (26,29). However, additional studies further confirmed an essential function for PI4P synthesis at the Golgi. Specifically, multiple *pik1* mutant alleles have been isolated, and each confers a defect in protein transport from the Golgi (16,100). In some cases, Golgi to plasma membrane secretion is specifically inhibited by loss of Pik1p activity, but other *pik1* mutant strains exhibit more severe defects in Golgi function that affect both secretory protein transport and the trafficking of biosynthetic cargoes from the Golgi to endosomes and the vacuole (15,103,105). Additionally, protein glycosylation in the Golgi is adversely affected by the absence of Pik1p activity, suggesting that multiple cisternae require PI4P synthesis for normal assembly and/or function (15).

Several effectors of PI4P that function at the Golgi have been described in yeast. The first were members of the oxysterol binding protein (OSBP) family, which likely function in the transfer of lipids between biological membranes (106). There are a total of 7 OSBPs in yeast, Osh1p-Osh7p, which share a common essential function, and each binds promiscuously to phosphoinositides (107,108). Osh1p, Osh2p and Osh3p each harbor an amino-terminal PH domain, a known phosphoinositide interacting motif. In general, PH domains are composed of approximately 120 amino acids that share a common structure consisting of two perpendicular anti-parallel beta sheets, followed by a carboxyl-terminal amphipathic helix (109). Although diverse in amino acid composition, a single tryptophan located within the helix serves to nucleate the core of the domain. A survey of more than 33 PH domains in yeast revealed that most bind to phosphoinositides with little specificity or affinity, and proteins that harbor PH domains typically require additional interactions for proper intracellular targeting (110). By analyzing GFP fusions to the PH domain-containing OSBPs, Osh1p was shown to localize in part to the Golgi and is potentially involved in sterol transfer with other organelles (111). In contrast, neither Osh2p nor Osh3p discernibly accumulated on Golgi membranes, although the PH domain of Osh2p alone binds to PI4P on the Golgi in a Pik1p-dependent fashion (112). These data highlight the role of additional protein-protein interactions in specifying the distribution of PH domain containing proteins in yeast.

In the case of Osh4p, phosphoinositide binding is mediated by the conserved sterol binding domain, which is found in all OSBPs (106). Studies indicate that Osh4p localizes to the Golgi in a PI4P-dependent fashion and may mediate the movement of sterols to and from this organelle, thereby regulating lipid homeostasis and vesicle biogenesis. Additionally, recent

findings indicate that Osh4p negatively regulates Pik1p activity (113). These data suggest that Osh4p may “sense” PI4P levels on Golgi membranes. For example, if a high concentration of PI4P accumulated on the Golgi, Kes1p recruitment would increase to inhibit Pik1p and slow PI4P synthesis. This type of feedback inhibition may be especially important to regulate secretion in response to changing growth conditions and environmental stress (114).

In addition to members of the OSBP family, the gamma-ear-containing, ADP-ribosylation factor binding protein Gga2p has also been shown to interact with PI4P at the Golgi (115). Gga2p functions as an adaptor for clathrin recruitment and participates in transport between the Golgi and endosomes (116,117). Loss of Gga2p function phenocopied several of the morphological and secretory defects observed in *pik1* mutant cells, including the accumulation of abnormal, cup-shaped membranous structures in the cytoplasm termed “Berkeley bodies.” These data suggest that Gga2p may be the most relevant Pik1p-dependent PI4P effector in Golgi to endosome trafficking (115). PI4P binding is mediated by the VHS (Vps27p/Hrs/STAM) domain of Gga2p, which shares significant similarity to the structure of phosphoinositide-binding ANTH/ENTH domains (115). In general, VHS domains contain approximately 150 amino acids and consist of 8 helices arranged in a superhelix (118). In Gga2p, the loop preceding helix 8 exhibits a pattern of charged and aromatic residues, similar to those found in the ANTH domain of CALM, a clathrin adaptor that interacts with PI4,5P₂ at the plasma membrane (115,119). Mutations within this basic region of Gga2p disrupted its association with PI4P and diminished Gga2p association with the Golgi. However, a GFP fusion to the VHS domain of Gga2p showed that it alone was insufficient to localize to Golgi membranes. Instead, the neighboring Arf1p GTPase-interacting GAT domain was also required.

Therefore, similar to most PH domain containing proteins in yeast, both lipid-protein and protein-protein interactions are required for proper Gga2p localization (115,120).

As noted earlier, protein glycosylation in the secretory pathway is sensitive to impaired Pik1p function, suggesting that PI4P may be required for the proper function or localization of Golgi glycosyltransferases. In many cases, retention of these enzymes in the Golgi requires the function of Vps74p, an oligomeric protein that binds to the cytosolic domains of glycosyltransferases and restricts their transport to other organelles (121,122). Based on crystallographic data, Vps74p harbors four alpha-helices that form a central core, which is surrounded by several additional amphipathic alpha-helices and four beta-strands (121). The recruitment of Vps74p to the Golgi is mediated by PI4P generated by Pik1p (123). In *pik1* mutant cells, Vps74p becomes cytosolic, and glycosyltransferases are no longer retained in the Golgi, thus leading to defects in secretory cargo glycosylation. The PI4P-binding motif within Vps74p is composed of a conserved basic region near the amino-terminus of helix 6, and mutations in this domain inhibit Vps74p-mediated retention of Golgi glycosyltransferases. Although the loss of other PI4P effectors may further contribute to the defects in protein glycosylation observed in *pik1* mutant cells, these data confirm a role for PI4P in this process and further demonstrate that Pik1p-mediated PI4P production is required for retrograde transport of cargoes in the Golgi (123).

Effectors of PI4P in yeast that function during secretory membrane transport have been arguably the most challenging to identify. Genetic studies strongly suggest that Pik1p functions together with multiple components of the secretory pathway, including at least three Rab-type GTPases (Ypt31p, Ypt32p, and Sec4p), two tethering complexes (TRAPP II and exocyst),

components of the actin-myosin network, and the phospholipid flippase Drs2p (16,105). In particular, Rab GTPases are known regulators of membrane trafficking, which have been shown to interface with phosphoinositide signaling during endosomal sorting (124). One attractive model for Golgi secretion involves a cascade of Rab activation, in which the Golgi-localized Ypt32p GTPase recruits the guanine nucleotide exchange factor (GEF) for the subsequent Rab GTPase that acts in the pathway (125). Indeed, the active GTP-bound form of Ypt32p, generated by the GEF activity of the TRAPP II tethering complex, binds directly to Sec2p, which catalyzes GTP exchange on Sec4p that is present on secretory vesicles (126). Active Sec4p can then recruit components of the exocyst complex, which are necessary for vesicle fusion with the plasma membrane (127). The Rab cascade is further regulated by Sec15p, a component of the exocyst complex, which competes with Ypt32p for Sec2p binding (125). The precise mechanism by which Sec15p replaces Ypt32p remains unknown, but recent evidence implicates a role for PI4P in this switch. Specifically, Sec2p was found to interact directly with PI4P generated by Pik1p on Golgi membranes. Three basic patches within the Sec2p GEF were found to be important for PI4P binding *in vitro*, and a mutant isoform of Sec2p containing mutations in these regions failed to localize properly (125). Both Ypt31p and Ypt32p were also found to be important for Sec2p localization, suggesting that a combination of protein-protein and lipid-protein interactions were necessary for proper Sec2p targeting. Consistent with this idea, Sec2p was shown to form a ternary complex with both PI4P and Ypt32p *in vitro*. In contrast, PI4P inhibited the association of Sec2p with Sec15p, suggesting a role for PI4P in stabilizing the association between Sec2p and Ypt32p at the Golgi to drive vesicle formation (125). Subsequent to vesicle budding, Sec2p may catalyze the formation of active, GTP-bound Sec4p, initiating the

recruitment of exocyst subunits including Sec15p, which ultimately displaces Ypt32p. Although this idea is speculative, the data clearly define a novel function for PI4P in secretion from the Golgi and help to explain several of the genetic interactions defined previously using *pik1* mutant cells.

In addition to the role of Rab-type GTPases, vesicle biogenesis from the Golgi also requires the action of Drs2p, a type IV P-type ATPase, which catalyzes the translocation of aminophospholipids from one leaflet of the lipid bilayer to the other. Similar to Pik1p, Drs2p has been implicated in the formation of vesicles destined for the plasma membrane as well as the endosomal/vacuolar system (128-130). Recently, the flippase activity of Drs2p was shown to be dependent on PI4P generated by Pik1p (131). A phosphoinositide binding site within Drs2p was identified and found to exhibit similarity to the PI3P-interacting split PH domain of Vps36p, a component of the ESCRT-II complex. A basic motif within this region (RMKKQR) was critical for PI4P binding *in vitro*, and mutations in this region prohibited complementation in *drs2* mutant cells. Unlike other roles for PI4P in targeting effectors to the Golgi, these data highlight a unique function for this lipid in regulating an enzymatic activity necessary for Golgi vesicle formation.

Since secretory vesicles move from the Golgi to the plasma membrane along actin cables in yeast, it is not surprising that mutations affecting actin cytoskeleton organization are lethal to *pik1* mutant cells (16,132). Further study into this connection has demonstrated that PI4P present in secretory vesicles is critical for vesicle movement mediated by the type V myosin Myo2p. Under normal conditions, directed vesicle movement also requires interactions between Myo2p and the Rab-type GTPases Ypt31p, Ypt32p, and Sec4p. However, by enhancing the

association between Myo2p and PI4P, binding to the Rab-type GTPases becomes dispensable (133). Although Myo2p has not been demonstrated to interact directly with PI4P, these findings strongly suggest that coincidence detection of PI4P and Rab GTPases is important for myosin-dependent transport of secretory vesicles. In the future, it will be critical to understand the mechanism by which Myo2p recognizes vesicles containing PI4P.

While the majority of studies have focused on a role for Pik1p-mediated PI4P production at the trans Golgi network, a cell free assay used to study ER to Golgi transport uncovered a critical role for PI4P in this pathway. Specifically, the presence of PI4P in the cis-Golgi was found to be necessary for COPII vesicle fusion (103). Although vesicle tethering did not require the presence of PI4P, inhibitors of PI4P reduced SNARE complex assembly. Analysis of *pik1* mutant cells further suggested a role for PI4P in anterograde transport between the ER and Golgi. However, a specific effector of PI4P at this early step of the secretory pathway remains unidentified. In a similar fashion, several studies have suggested a potential role for PI4P at the endosome, but confirmation of such a function awaits the characterization of a PI4P-binding protein, which regulates endosomal trafficking (15,16).

Functions of PI4P synthesized by Stt4p at the plasma membrane

Although a significant portion of PI4P generated by Stt4p is rapidly metabolized to PI4,5P₂ (discussed in the next section), the unique phenotypes of *stt4* mutant cells suggest that the plasma membrane pool of PI4P has specific effectors. Consistent with this finding, the Cla4p protein kinase, which is involved in actin cytoskeleton organization, polarized cell growth and cell division, harbors a PH domain that binds to PI4P generated by Stt4p (134,135). In cells lacking Stt4p kinase activity, Cla4p is mislocalized from the cell surface, suggesting that its

interaction with PI4P is critical for its normal targeting. Like other yeast proteins that harbor PH domains, interaction with PI4P alone is insufficient to direct localization of Cla4p. However, together with another interacting protein, the Cdc42p Rho-type GTPase, Cla4p is able to maintain a polarized distribution at the plasma membrane (135). These data again highlight coincident roles for lipid and protein interactions to maintain the cellular distribution of phosphoinositide interacting molecules. Furthermore, these findings illustrate that PI4P directly regulates actin polarity by controlling Cla4p recruitment to the plasma membrane. Notably, in the absence of Stt4p function, directed membrane transport to the bud is disrupted by perturbations in actin organization, resulting in isotropic cell growth (15). Similar phenotypes have been observed in cells lacking Cla4p and a related protein kinase, Ste20p (136). Although Ste20p has not been shown to interact with phosphoinositides, these are the first data demonstrating that PI4P generated by Stt4p exhibits functions in actin organization beyond its role as a precursor to Mss4p-mediated PI4,5P₂ synthesis.

In addition to its role at the plasma membrane, Stt4p has also been implicated in the transport of the phospholipid PS from the ER to the Golgi. Specifically, inhibition of Stt4p kinase activity leads to an accumulation of PS in the ER, which under normal conditions is metabolized to form phosphatidylethanolamine (PE) in the Golgi (102). These data suggest that PI4P generated by Stt4p regulates the movement of phospholipids in the early secretory pathway, although an effector of PI4P in this process remains unknown. Additionally, these findings raise the possibility that PI4P generated by Stt4p at the plasma membrane can be transferred to the ER, potentially at sites of ER-plasma membrane contact. Such a process may be mediated by members of the OSBP family, which all exhibit the capacity to bind phosphoinositides. In

particular, Osh3p appears to be specifically enriched at sites of ER-plasma membrane contact, and this localization is dependent on an interaction between its PH domain and PI4P (28).

Although a model in which OSBPs directly transfer phosphoinositides between organelles is highly speculative, it is supported by studies suggesting that PI4P generated by Stt4p can accumulate in the ER following inactivation of the Sac1p lipid phosphatase (106,123). Further studies are clearly required to confirm or reject this possibility.

Beyond the putative role of OSBPs in lipid transfer, this family of phosphoinositide-binding proteins also regulates PI4P turnover. In mutant cells deficient in OSBP function, PI4P levels rise substantially, similar to the phenotype exhibited by cells lacking Sac1p phosphatase activity (28). Furthermore, OSBPs have been shown to activate the phosphatase activity of Sac1p *in vitro*. Thus, PI4P auto-regulates its stability by recruiting effectors that increase PI4P hydrolysis. This type of feedback inhibition may be necessary to restrict PI4P signaling on the plasma membrane and prevent the mistargeting of PI4P binding proteins required for function downstream of Pik1p at the Golgi.

As mentioned earlier, Osh3p is an effector of PI4P generated on the plasma membrane by Stt4p and localizes to sites of ER-plasma membrane contact (28). Since PI4P accumulates homogeneously on the cell surface, these data suggest that Osh3p distribution is also regulated by additional interactions. Consistent with this idea, two ER membrane proteins that regulate phospholipid biosynthesis, Scs2p and Scs22p, also bind to Osh3p and control its accumulation at sites of ER-plasma membrane contact (28). Notably, Scs2p has been shown to bind PI4P *in vitro*, and mutations that disrupt its ability to associate with phosphoinositides diminish its function in regulating the metabolism of ER phospholipids (137). Together, these data suggest

that PI4P generated by Stt4p plays an important role in generating and/or stabilizing contact sites between the plasma membrane and ER through the recruitment of multiple effector proteins. These contact sites potentially allow for the direct transfer of lipids between these distinct organelles, allowing for rapid changes in membrane content independently of vesicular transport. Further studies are necessary to determine whether inactivation of Stt4p may lead to the disruption of ER-plasma membrane contact and what affect this has on cell growth and viability.

Characterization of *stt4* mutant cells also revealed a role for Stt4p-mediated production of PI4P in vacuolar membrane homeostasis. Following loss of Stt4p activity, vacuoles undergo a dramatic reduction in volume, while their overall surface area does not appear to change significantly (15). One possibility is that PI4P generated at the plasma membrane is required for controlling cellular osmolarity, and defects in PI4P production lead to changes in osmotic pressure within the cell that cause vacuoles to lose volume. Importantly, such an effect is not seen following loss of Mss4p-mediated PI4,5P₂ production, indicating that PI4P does not simply act as a precursor lipid in this pathway. In the future, it will be important to define specific effectors of PI4P, which control cellular osmolarity and/or vacuole size and shape.

Roles for PI4,5P₂ in membrane transport

Although the single yeast PI4P 5-kinase Mss4p undergoes nucleo-cytoplasmic shuttling, studies indicate that the essential cellular pool of PI4,5P₂ is synthesized on the plasma membrane (32). At this location, PI4,5P₂ regulates a number of distinct processes, which include endocytosis, exocytosis, cytokinesis, maintenance of cell polarity, and actin cytoskeleton organization. In several cases, PI4,5P₂ functions as a localization determinant. However, many effectors rely on PI4,5P₂ binding to regulate their activities directly. We will discuss a variety of

mechanisms by which PI4,5P₂ modulates cellular function, with an emphasis on its diverse roles in membrane trafficking.

During endocytosis, a number of different factors must be recruited to the cell surface in a coordinated fashion to drive membrane invagination and scission. In the case of clathrin-mediated endocytosis, adaptor proteins arrive soon after clathrin marks an endocytic site (138). Several of these factors require the presence of PI4,5P₂ to associate with the plasma membrane. For example, the alpha subunit of the mammalian AP-2 adaptor protein complex has been shown to bind PI4,5P₂ through a conserved amino-terminal basic region, and this interaction is required for its localization (139). Although the yeast AP-2 alpha subunit Apl3p exhibits only 30% sequence identity with its human homolog, the basic residues within the amino-terminus are almost entirely conserved, suggesting that Apl3p also binds PI4,5P₂. However, in contrast to human AP-2, the role of the yeast complex is less clear as mutant cells lacking all AP-2 adaptor subunits fail to exhibit significant defects in clathrin-mediated endocytosis (140,141). These data suggest that alternative proteins likely function in a redundant manner to the AP-2 complex in yeast.

The epsins, Ent1p and Ent2p, are adaptor proteins, which may fulfill such a function. Unlike AP-2, epsin function is essential for yeast cell viability, and specifically plays an important role during clathrin-mediated endocytosis (142). Both Ent1p and Ent2p harbor ENTH (epsin N-terminal homology) domains, which bind to PI4,5P₂ (143). In general, ENTH domains are approximately 150 amino acids in length and are composed of 9 alpha helices connected by loops of varying sizes. Based on the structure of the ENTH domain from mammalian epsin, PI4,5P₂ interacts with basic amino acids in loop 1 and helices 3 and 4 (144). The conservation of

this region in Ent1p and Ent2p strongly suggests a common mechanism for phosphoinositide binding. Additionally, genetic studies indicate that the ENTH domain from either Ent1p or Ent2p is sufficient to complement deletions of both genes (145). These data suggest additional functions beyond phosphoinositide binding for this region. Consistent with this idea, the ENTH domain has been found to be a coincident detector of both PI4,5P₂ and GEFs for the Rho-type GTPase Cdc42p, which play an important role in polarized cell growth (145). Thus, a combination of protein-protein and protein-lipid interactions coordinates spatial and temporal regulation of endocytosis with maintenance of cell polarity.

Yeast cells also express two epsin-related proteins, Yap1801p and Yap1802p, which harbor ANTH (AP180 N-terminal homology) domains. The ANTH domain exhibits a similar overall structure to the ENTH domain, containing 9 helices connected by loops (146). Additionally, a PI4,5P₂ binding site within the ANTH domain has been defined (119), and contains the conserved sequence Kx₉Kx(K/R)(H/Y). Although initial studies failed to identify endocytic defects in cells lacking Yap1801p and Yap1802p, subsequent findings indicated that the adaptor proteins possess cargo specific roles in endocytosis (140,147,148). These data further implicate PI4,5P₂ in regulating endocytic trafficking in yeast.

In addition to Yap1801p and Yap1802p, a third ANTH domain containing protein Sla2p has been implicated in endocytosis. Furthermore, Sla2p also functions to regulate actin organization, connecting membrane transport from the cell surface to the underlying cytoskeleton (149). The conserved basic region within the Sla2p ANTH domain was shown to be critical for PI4,5P₂ interaction, and mutations in this region perturbed endocytic function in cells otherwise lacking Sla2p (150). However, loss of the basic region failed to impact

localization of Sla2p, indicating that PI4,5P₂ is not essential for targeting of Sla2p to the plasma membrane. Instead, PI4,5P₂ likely regulates the activity of Sla2p during endocytosis. Since Sla2p binds to components of both the clathrin coat and the actin cytoskeleton, modulations in Sla2p function by PI4,5P₂ may be critical to appropriately couple vesicle formation with actin-dependent vesicle internalization. However, further studies are necessary to pinpoint the precise consequence of PI4,5P₂ interaction with the Sla2p ANTH domain.

The intimate connection between endocytosis and cytoskeletal organization implicates several additional PI4,5P₂ binding proteins, which modulate actin assembly, in membrane trafficking. For example in mammalian cells, the actin severing protein gelsolin is rapidly inactivated in the presence of PI4,5P₂, while PI4,5P₂ binding to the basic motif in WASP family members stimulates actin polymerization mediated by the Arp2/3 complex (151-153). Thus, using several mechanisms, PI4,5P₂ accelerates the formation of actin networks, which play a key role in endocytic vesicle budding. In total, more than 30 actin filament binding proteins have been reported to associate directly with phosphoinositides (154).

Similar to gelsolin, PI4,5P₂ also exhibits an inhibitory effect on the actin depolymerizing factor (ADF)/cofilin known as Cof1p in yeast. In the absence of PI4,5P₂, Cof1p promotes rapid actin dynamics by driving the severing of actin filaments, but its ability to associate with actin and its depolymerizing activity is strongly diminished by PI4,5P₂ (155,156). Based on a series of *cof1* mutant alleles, a highly conserved basic helix in Cof1p, as well as other positively charged residues found throughout the molecule, appear to be important for PI4,5P₂ binding (157). These findings suggest that Cof1p may bind multiple PI4,5P₂ molecules simultaneously. However, work using ADF/cofilin from another organism indicated that PI4,5P₂ binding was mediated by

the carboxyl-terminus of the protein (158). Additional work is necessary to define the precise mechanism by which PI4,5P₂ binds cofilin and inhibits its activity.

Actin polymerization can also be terminated by the function of capping protein, an evolutionarily conserved, heterodimeric complex consisting of alpha and beta subunits, encoded by *CAP1* and *CAP2* in yeast. Through its association with the ends of actin filaments, capping protein inhibits further actin dynamics (159). Both subunits contain highly basic residues that are critical for PI4,5P₂ binding, and association with PI4,5P₂ interferes with the interaction between capping protein and actin, promoting actin dynamics necessary for endocytosis (160). The importance of the interaction between capping protein and PI4,5P₂ is further highlighted by work indicating that a partial loss of function *mss4* allele exhibits synthetic lethality with deletion of either *CAP1* or *CAP2* (161).

Profilin, encoded by *PFY1* in yeast, is another PI4,5P₂ binding protein that interacts specifically with monomeric actin. Under certain cellular conditions, profilin can act as an actin monomer sequestering molecule, inhibiting actin filament assembly (162). Interaction with PI4,5P₂ disrupts the association of profilin with actin, thus inhibiting the effect of profilin on actin polymerization. Several regions of profilin have been implicated in PI4,5P₂ binding, and the interaction appears to be electrostatic in nature (163,164). In a similar fashion, PI4,5P₂ also inhibits the actin monomer sequestering activity of the yeast twinfilin Twf1p (165). Thus, by maintaining free pools of monomeric actin, the presence of PI4,5P₂ generates an environment conducive to actin polymerization and endocytosis.

In several cases, PI4,5P₂ regulates cytoskeletal organization through effectors that do not bind actin directly. For example, the Rho-type GTPase Rho1p is required for polarity of the

actin cytoskeleton in yeast, as well as polarized secretion (166). The Rho1p GEF Rom2p harbors a PH domain that has been shown to interact with PI4,5P₂ (17). Inhibition of Stt4p or Mss4p, which diminish PI4,5P₂ synthesis on the plasma membrane, results in a defect in Rom2p localization and leads to depolarization of the actin cytoskeleton, suggesting that phosphoinositide signaling regulates Rho1p activity. Furthermore, a polybasic sequence within Rho1p, which plays a role in targeting the GTPase to sites of polarized growth independent of its GEFs, has also been shown to interact with PI4,5P₂ (167). Together, these findings demonstrate that phosphoinositide and Rho-type GTPase signaling are tightly coupled.

Mss4p-dependent PI4,5P₂ synthesis is also required for the normal localization of Slm1p and Slm2p, two additional regulators of actin organization in yeast. Both Slm1p and Slm2p contain PH domains capable of interacting with PI4,5P₂, and mutations in the Slm1p PH domain that inhibit phosphoinositide interaction result in the mislocalization of Slm1p to the cytoplasm (161,168). Although the precise mechanism underlying Slm1p and Slm2p regulation of actin cytoskeleton organization remains unknown, these data further highlight the diversity of PI4,5P₂ effectors that control actin polarity. Furthermore, Slm1p and Slm2p also play roles in sphingolipid biosynthesis, which function in several membrane trafficking pathways including endocytosis (169). These data suggest that phosphoinositide and sphingolipid signaling likely intersect, potentially to coordinate vesicle transport with membrane homeostasis.

In addition to its role in endocytosis, the actin cytoskeleton also performs a key function in directed protein secretion and exocytosis. As discussed earlier, PI4P generated on the Golgi by Pik1p plays several important roles in generating secretory vesicles, which move along actin cables to sites of polarized growth. Fusion of vesicles with the plasma membrane requires the

activity of a tethering complex known as the exocyst. Of the 8 exocyst subunits, two have been shown to directly interact with PI4,5P₂ and direct their localization to the plasma membrane, Exo70p and Sec3p (170,171). In the case of Exo70p, PI4,5P₂ binding is mediated by a basic patch of amino acids in the carboxyl-terminus. Similarly, a basic region in the amino-terminus of Sec3p, which has been shown to adopt a PH domain fold, also binds to PI4,5P₂. Consistent with a role for PI4,5P₂ in regulating exocyst localization on the cell surface, inhibition of Mss4p activity led to the accumulation of the exocyst complex in the cytoplasm. Notably, unlike the uniform distribution of PI4,5P₂ on the plasma membrane, the exocyst complex is highly polarized, suggesting additional interactions are necessary for proper exocyst distribution. Indeed, several Rho-type GTPases, which localize in an asymmetric fashion, bind to components of the exocyst, and these interactions also play an important role in recruiting the complex to the plasma membrane (171). Taken together, these data again highlight the importance of dual targeting mechanisms, which combine protein and lipid signals, in determining the localization of phosphoinositide effectors in cells.

Finally, PI4,5P₂ has also been implicated in the final stages of cell division (172) in yeast by regulating several components of the septin complex, which orchestrate membrane remodeling events necessary for cytokinesis. The septins Cdc3p, Cdc10p, Cdc11p, and Cdc12p have been demonstrated to form filaments that can function as a diffusion barrier as cells divide. Studies indicate that each septin harbors a basic motif capable of binding to PI4,5P₂. Mutations in basic residues found in Cdc3p, which mediate PI4,5P₂ binding, cause defects in cell division (172). *In vitro*, PI4,5P₂ promotes septin filament assembly and organization, suggesting that protein-lipid interactions in this case function beyond membrane recruitment (173). Further

work is necessary to understand how phosphoinositide binding may affect septin dynamics during the process of cell division.

Perspectives and Conclusions

The recognized roles of phosphoinositides in membrane transport pathways have grown significantly over the last two decades. Although many more effectors likely await characterization, it has become clear that phosphoinositide signaling plays key roles in the movement of cargoes between virtually all cellular compartments. Two major themes have emerged from the study of PI metabolism. First, the localization of phosphoinositides is highly regulated, and their distributions rarely overlap. Thus, phosphoinositides function as organelle specific labels, enabling membrane compartments to be distinguished from one another and preventing crosstalk between distinct biochemical processes within a common cytoplasm. Second, phosphoinositides infrequently function alone, and instead regulate cellular pathways in concert with other factors. Such a mechanism provides the high specificity necessary for directed membrane transport between organelles. In the future, the diversity of phosphoinositide effectors will likely continue to grow, hopefully shedding additional light on the complex mechanisms by which membrane trafficking is appropriately coordinated.

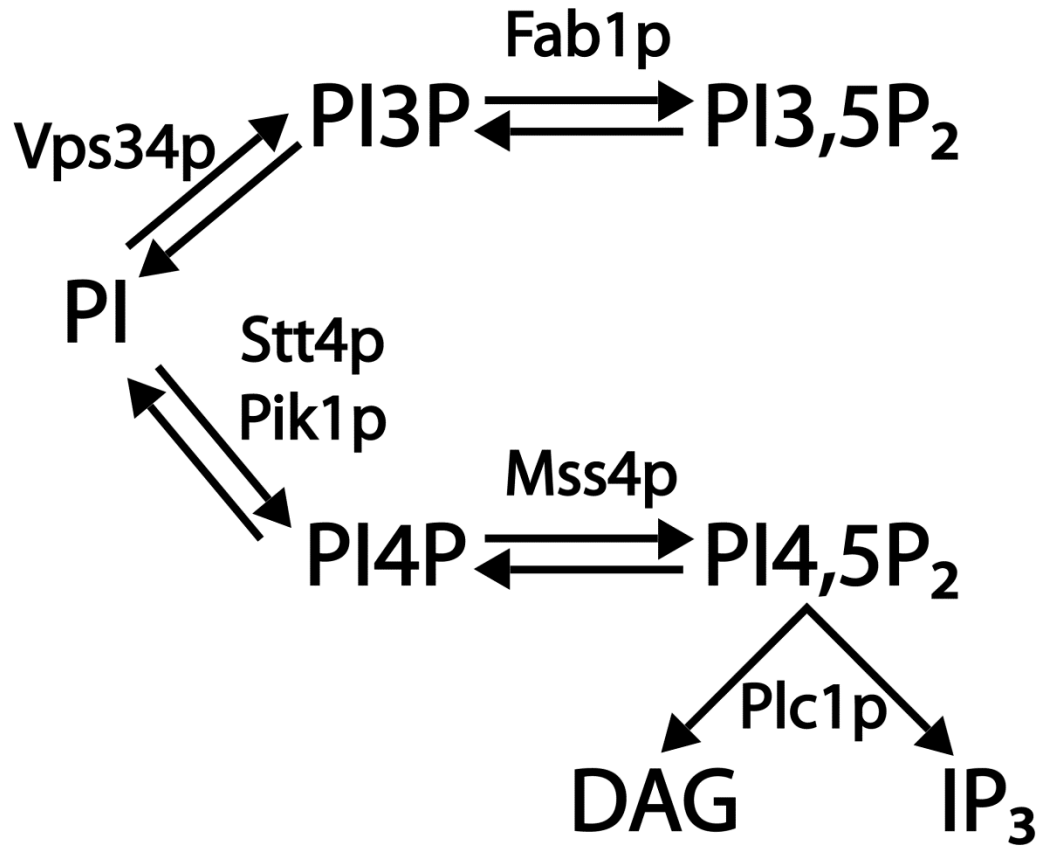


Figure B.1: Phosphoinositide metabolism in yeast.

Figure B.1: Phosphoinositide metabolism in yeast.

The synthesis pathways for the 4 phosphoinositides known to exist in yeast are shown. Major PI kinases are highlighted, as is the phospholipase C isoform Plc1p, which hydrolyzes PI4,5P₂. Not pictured are phosphoinositide phosphatases, which mediate the dephosphorylation of various PI derivatives.

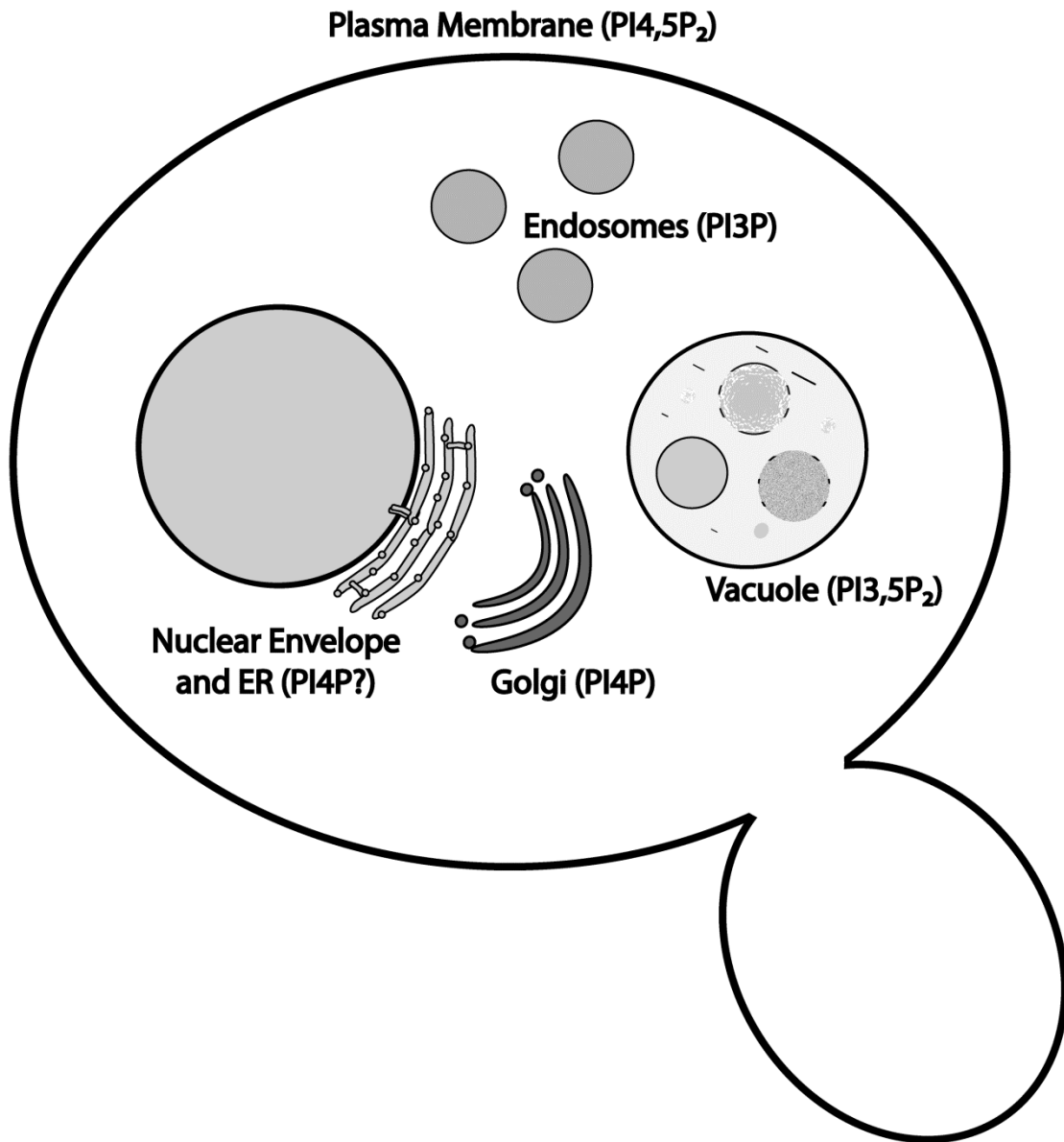


Figure B.2: Distribution of phosphoinositides in yeast.

Figure B.2: Distribution of phosphoinositides in yeast.

A cartoon depicting a yeast cell, with various organelles that harbor phosphoinositides highlighted. The plasma membrane is enriched with PI4,5P₂, the vacuole with PI3,5P₂, endosomes with PI3P, and the Golgi with PI4P. The pool of PI4P synthesized on the plasma membrane is not shown for simplicity.

REFERENCES

1. Schu, P. V., Takegawa, K., Fry, M. J., Stack, J. H., Waterfield, M. D., and Emr, S. D. (1993) Phosphatidylinositol 3-kinase encoded by yeast VPS34 gene essential for protein sorting. *Science* **260**, 88-91
2. Stack, J. H., and Emr, S. D. (1994) Vps34p required for yeast vacuolar protein sorting is a multiple specificity kinase that exhibits both protein kinase and phosphatidylinositol-specific PI 3-kinase activities. *J Biol Chem* **269**, 31552-31562
3. Stenmark, H., and Gillooly, D. J. (2001) Intracellular trafficking and turnover of phosphatidylinositol 3-phosphate. *Semin Cell Dev Biol* **12**, 193-199
4. Herman, P. K., Stack, J. H., DeModena, J. A., and Emr, S. D. (1991) A novel protein kinase homolog essential for protein sorting to the yeast lysosome-like vacuole. *Cell* **64**, 425-437
5. Stack, J. H., Herman, P. K., Schu, P. V., and Emr, S. D. (1993) A membrane-associated complex containing the Vps15 protein kinase and the Vps34 PI 3-kinase is essential for protein sorting to the yeast lysosome-like vacuole. *EMBO J* **12**, 2195-2204
6. Vanhaesebroeck, B., Guillermet-Guibert, J., Graupera, M., and Bilanges, B. (2010) The emerging mechanisms of isoform-specific PI3K signalling. *Nat Rev Mol Cell Biol* **11**, 329-341
7. Wurmser, A. E., and Emr, S. D. (1998) Phosphoinositide signaling and turnover: PtdIns(3)P, a regulator of membrane traffic, is transported to the vacuole and degraded by a process that requires luminal vacuolar hydrolase activities. *EMBO J* **17**, 4930-4942
8. Stolz, L. E., Huynh, C. V., Thorner, J., and York, J. D. (1998) Identification and characterization of an essential family of inositol polyphosphate 5-phosphatases (INP51, INP52 and INP53 gene products) in the yeast *Saccharomyces cerevisiae*. *Genetics* **148**, 1715-1729
9. Parrish, W. R., Stefan, C. J., and Emr, S. D. (2004) Essential role for the myotubularin-related phosphatase Ymr1p and the synaptojanin-like phosphatases Sjl2p and Sjl3p in regulation of phosphatidylinositol 3-phosphate in yeast. *Mol Biol Cell* **15**, 3567-3579
10. Parrish, W. R., Stefan, C. J., and Emr, S. D. (2005) PtdIns(3)P accumulation in triple lipid-phosphatase-deletion mutants triggers lethal hyperactivation of the Rho1p/Pkc1p cell-integrity MAP kinase pathway. *J Cell Sci* **118**, 5589-5601
11. Bonangelino, C. J., Catlett, N. L., and Weisman, L. S. (1997) Vac7p, a novel vacuolar protein, is required for normal vacuole inheritance and morphology. *Mol Cell Biol* **17**, 6847-6858

12. Gary, J. D., Wurmser, A. E., Bonangelino, C. J., Weisman, L. S., and Emr, S. D. (1998) Fab1p is essential for PtdIns(3)P 5-kinase activity and the maintenance of vacuolar size and membrane homeostasis. *J Cell Biol* **143**, 65-79
13. Botelho, R. J., Efe, J. A., Teis, D., and Emr, S. D. (2008) Assembly of a Fab1 phosphoinositide kinase signaling complex requires the Fig4 phosphoinositide phosphatase. *Mol Biol Cell* **19**, 4273-4286
14. Gary, J. D., Sato, T. K., Stefan, C. J., Bonangelino, C. J., Weisman, L. S., and Emr, S. D. (2002) Regulation of Fab1 phosphatidylinositol 3-phosphate 5-kinase pathway by Vac7 protein and Fig4, a polyphosphoinositide phosphatase family member. *Mol Biol Cell* **13**, 1238-1251
15. Audhya, A., Foti, M., and Emr, S. D. (2000) Distinct roles for the yeast phosphatidylinositol 4-kinases, Stt4p and Pik1p, in secretion, cell growth, and organelle membrane dynamics. *Mol Biol Cell* **11**, 2673-2689
16. Walch-Solimena, C., and Novick, P. (1999) The yeast phosphatidylinositol-4-OH kinase pik1 regulates secretion at the Golgi. *Nat Cell Biol* **1**, 523-525
17. Audhya, A., and Emr, S. D. (2002) Stt4 PI 4-kinase localizes to the plasma membrane and functions in the Pkc1-mediated MAP kinase cascade. *Dev Cell* **2**, 593-605
18. Baird, D., Stefan, C., Audhya, A., Weys, S., and Emr, S. D. (2008) Assembly of the PtdIns 4-kinase Stt4 complex at the plasma membrane requires Ypp1 and Efr3. *J Cell Biol* **183**, 1061-1074
19. Zhai, C., Li, K., Markaki, V., Phelan, J. P., Bowers, K., Cooke, F. T., and Panaretou, B. (2008) Ypp1/YGR198w plays an essential role in phosphoinositide signalling at the plasma membrane. *Biochem J* **415**, 455-466
20. Hendricks, K. B., Wang, B. Q., Schnieders, E. A., and Thorner, J. (1999) Yeast homologue of neuronal frequenin is a regulator of phosphatidylinositol-4-OH kinase. *Nat Cell Biol* **1**, 234-241
21. Garcia-Bustos, J. F., Marini, F., Stevenson, I., Frei, C., and Hall, M. N. (1994) PIK1, an essential phosphatidylinositol 4-kinase associated with the yeast nucleus. *EMBO J* **13**, 2352-2361
22. Strahl, T., Hama, H., DeWald, D. B., and Thorner, J. (2005) Yeast phosphatidylinositol 4-kinase, Pik1, has essential roles at the Golgi and in the nucleus. *J Cell Biol* **171**, 967-979
23. Han, G. S., Audhya, A., Markley, D. J., Emr, S. D., and Carman, G. M. (2002) The *Saccharomyces cerevisiae* LSB6 gene encodes phosphatidylinositol 4-kinase activity. *J Biol Chem* **277**, 47709-47718

24. Shelton, S. N., Barylko, B., Binns, D. D., Horazdovsky, B. F., Albanesi, J. P., and Goodman, J. M. (2003) *Saccharomyces cerevisiae* contains a Type II phosphoinositide 4-kinase. *Biochem J* **371**, 533-540
25. Chang, F. S., Han, G. S., Carman, G. M., and Blumer, K. J. (2005) A WASp-binding type II phosphatidylinositol 4-kinase required for actin polymerization-driven endosome motility. *J Cell Biol* **171**, 133-142
26. Foti, M., Audhya, A., and Emr, S. D. (2001) Sac1 lipid phosphatase and Stt4 phosphatidylinositol 4-kinase regulate a pool of phosphatidylinositol 4-phosphate that functions in the control of the actin cytoskeleton and vacuole morphology. *Mol Biol Cell* **12**, 2396-2411
27. Faulhammer, F., Konrad, G., Brankatschk, B., Tahirovic, S., Knödler, A., and Mayinger, P. (2005) Cell growth-dependent coordination of lipid signaling and glycosylation is mediated by interactions between Sac1p and Dpm1p. *J Cell Biol* **168**, 185-191
28. Stefan, C. J., Manford, A. G., Baird, D., Yamada-Hanff, J., Mao, Y., and Emr, S. D. (2011) Osh proteins regulate phosphoinositide metabolism at ER-plasma membrane contact sites. *Cell* **144**, 389-401
29. Roy, A., and Levine, T. P. (2004) Multiple pools of phosphatidylinositol 4-phosphate detected using the pleckstrin homology domain of Osh2p. *J Biol Chem* **279**, 44683-44689
30. Homma, K., Terui, S., Minemura, M., Qadota, H., Anraku, Y., Kanaho, Y., and Ohya, Y. (1998) Phosphatidylinositol-4-phosphate 5-kinase localized on the plasma membrane is essential for yeast cell morphogenesis. *J Biol Chem* **273**, 15779-15786
31. Guo, S., Stolz, L. E., Lemrow, S. M., and York, J. D. (1999) SAC1-like domains of yeast SAC1, INP52, and INP53 and of human synaptojanin encode polyphosphoinositide phosphatases. *J Biol Chem* **274**, 12990-12995
32. Audhya, A., and Emr, S. D. (2003) Regulation of PI4,5P2 synthesis by nuclear-cytoplasmic shuttling of the Mss4 lipid kinase. *EMBO J* **22**, 4223-4236
33. Desrivères, S., Cooke, F. T., Morales-Johansson, H., Parker, P. J., and Hall, M. N. (2002) Calmodulin controls organization of the actin cytoskeleton via regulation of phosphatidylinositol (4,5)-bisphosphate synthesis in *Saccharomyces cerevisiae*. *Biochem J* **366**, 945-951
34. Flick, J. S., and Thorner, J. (1993) Genetic and biochemical characterization of a phosphatidylinositol-specific phospholipase C in *Saccharomyces cerevisiae*. *Mol Cell Biol* **13**, 5861-5876
35. Wiradjaja, F., Ooms, L. M., Whisstock, J. C., McColl, B., Helfenbaum, L., Sambrook, J. F., Gething, M. J., and Mitchell, C. A. (2001) The yeast inositol polyphosphate 5-

- phosphatase Inp54p localizes to the endoplasmic reticulum via a C-terminal hydrophobic anchoring tail: regulation of secretion from the endoplasmic reticulum. *J Biol Chem* **276**, 7643-7653
36. Stefan, C. J., Audhya, A., and Emr, S. D. (2002) The yeast synaptojanin-like proteins control the cellular distribution of phosphatidylinositol (4,5)-bisphosphate. *Mol Biol Cell* **13**, 542-557
 37. Seet, L. F., and Hong, W. (2006) The Phox (PX) domain proteins and membrane traffic. *Biochim Biophys Acta* **1761**, 878-896
 38. Kihara, A., Noda, T., Ishihara, N., and Ohsumi, Y. (2001) Two distinct Vps34 phosphatidylinositol 3-kinase complexes function in autophagy and carboxypeptidase Y sorting in *Saccharomyces cerevisiae*. *J Cell Biol* **152**, 519-530
 39. Kametaka, S., Okano, T., Ohsumi, M., and Ohsumi, Y. (1998) Apg14p and Apg6/Vps30p form a protein complex essential for autophagy in the yeast, *Saccharomyces cerevisiae*. *J Biol Chem* **273**, 22284-22291
 40. Gaullier, J. M., Simonsen, A., D'Arrigo, A., Bremnes, B., Stenmark, H., and Aasland, R. (1998) FYVE fingers bind PtdIns(3)P. *Nature* **394**, 432-433
 41. Burd, C. G., and Emr, S. D. (1998) Phosphatidylinositol(3)-phosphate signaling mediated by specific binding to RING FYVE domains. *Mol Cell* **2**, 157-162
 42. Kutateladze, T. G., Ogburn, K. D., Watson, W. T., de Beer, T., Emr, S. D., Burd, C. G., and Overduin, M. (1999) Phosphatidylinositol 3-phosphate recognition by the FYVE domain. *Mol Cell* **3**, 805-811
 43. Misra, S., and Hurley, J. H. (1999) Crystal structure of a phosphatidylinositol 3-phosphate-specific membrane-targeting motif, the FYVE domain of Vps27p. *Cell* **97**, 657-666
 44. Diraviyam, K., Stahelin, R. V., Cho, W., and Murray, D. (2003) Computer modeling of the membrane interaction of FYVE domains. *J Mol Biol* **328**, 721-736
 45. Stahelin, R. V., Long, F., Diraviyam, K., Bruzik, K. S., Murray, D., and Cho, W. (2002) Phosphatidylinositol 3-phosphate induces the membrane penetration of the FYVE domains of Vps27p and Hrs. *J Biol Chem* **277**, 26379-26388
 46. Kutateladze, T. G., Capelluto, D. G., Ferguson, C. G., Cheever, M. L., Kutateladze, A. G., Prestwich, G. D., and Overduin, M. (2004) Multivalent mechanism of membrane insertion by the FYVE domain. *J Biol Chem* **279**, 3050-3057
 47. Lee, S. A., Eyson, R., Cheever, M. L., Geng, J., Verkhusha, V. V., Burd, C., Overduin, M., and Kutateladze, T. G. (2005) Targeting of the FYVE domain to endosomal

- membranes is regulated by a histidine switch. *Proc Natl Acad Sci U S A* **102**, 13052-13057
48. He, J., Vora, M., Haney, R. M., Filonov, G. S., Musselman, C. A., Burd, C. G., Kutateladze, A. G., Verkhusha, V. V., Stahelin, R. V., and Kutateladze, T. G. (2009) Membrane insertion of the FYVE domain is modulated by pH. *Proteins* **76**, 852-860
 49. Dumas, J. J., Merithew, E., Sudharshan, E., Rajamani, D., Hayes, S., Lawe, D., Corvera, S., and Lambright, D. G. (2001) Multivalent endosome targeting by homodimeric EEA1. *Mol Cell* **8**, 947-958
 50. Kutateladze, T. G. (2006) Phosphatidylinositol 3-phosphate recognition and membrane docking by the FYVE domain. *Biochim Biophys Acta* **1761**, 868-877
 51. Webb, G. C., Zhang, J., Garlow, S. J., Wesp, A., Riezman, H., and Jones, E. W. (1997) Pep7p provides a novel protein that functions in vesicle-mediated transport between the yeast Golgi and endosome. *Mol Biol Cell* **8**, 871-895
 52. Tall, G. G., Hama, H., DeWald, D. B., and Horazdovsky, B. F. (1999) The phosphatidylinositol 3-phosphate binding protein Vac1p interacts with a Rab GTPase and a Sec1p homologue to facilitate vesicle-mediated vacuolar protein sorting. *Mol Biol Cell* **10**, 1873-1889
 53. Peterson, M. R., Burd, C. G., and Emr, S. D. (1999) Vac1p coordinates Rab and phosphatidylinositol 3-kinase signaling in Vps45p-dependent vesicle docking/fusion at the endosome. *Curr Biol* **9**, 159-162
 54. Odorizzi, G., Babst, M., and Emr, S. D. (1998) Fab1p PtdIns(3)P 5-kinase function essential for protein sorting in the multivesicular body. *Cell* **95**, 847-858
 55. Katzmman, D. J., Stefan, C. J., Babst, M., and Emr, S. D. (2003) Vps27 recruits ESCRT machinery to endosomes during MVB sorting. *J Cell Biol* **162**, 413-423
 56. Bilodeau, P. S., Winistorfer, S. C., Kearney, W. R., Robertson, A. D., and Piper, R. C. (2003) Vps27-Hse1 and ESCRT-I complexes cooperate to increase efficiency of sorting ubiquitinated proteins at the endosome. *J Cell Biol* **163**, 237-243
 57. Raiborg, C., and Stenmark, H. (2009) The ESCRT machinery in endosomal sorting of ubiquitylated membrane proteins. *Nature* **458**, 445-452
 58. Teo, H., Gill, D. J., Sun, J., Perisic, O., Veprintsev, D. B., Vallis, Y., Emr, S. D., and Williams, R. L. (2006) ESCRT-I core and ESCRT-II GLUE domain structures reveal role for GLUE in linking to ESCRT-I and membranes. *Cell* **125**, 99-111
 59. Im, Y. J., and Hurley, J. H. (2008) Integrated structural model and membrane targeting mechanism of the human ESCRT-II complex. *Dev Cell* **14**, 902-913

60. Shin, M. E., Ogburn, K. D., Varban, O. A., Gilbert, P. M., and Burd, C. G. (2001) FYVE domain targets Pib1p ubiquitin ligase to endosome and vacuolar membranes. *J Biol Chem* **276**, 41388-41393
61. Huh, W. K., Falvo, J. V., Gerke, L. C., Carroll, A. S., Howson, R. W., Weissman, J. S., and O'Shea, E. K. (2003) Global analysis of protein localization in budding yeast. *Nature* **425**, 686-691
62. Cheever, M. L., Sato, T. K., de Beer, T., Kutateladze, T. G., Emr, S. D., and Overduin, M. (2001) Phox domain interaction with PtdIns(3)P targets the Vam7 t-SNARE to vacuole membranes. *Nat Cell Biol* **3**, 613-618
63. Bravo, J., Karathanassis, D., Pacold, C. M., Pacold, M. E., Ellson, C. D., Anderson, K. E., Butler, P. J., Lavenir, I., Perisic, O., Hawkins, P. T., Stephens, L., and Williams, R. L. (2001) The crystal structure of the PX domain from p40(phox) bound to phosphatidylinositol 3-phosphate. *Mol Cell* **8**, 829-839
64. Sato, T. K., Overduin, M., and Emr, S. D. (2001) Location, location, location: membrane targeting directed by PX domains. *Science* **294**, 1881-1885
65. Xu, Y., Seet, L. F., Hanson, B., and Hong, W. (2001) The Phox homology (PX) domain, a new player in phosphoinositide signalling. *Biochem J* **360**, 513-530
66. Kutateladze, T. G. (2007) Mechanistic similarities in docking of the FYVE and PX domains to phosphatidylinositol 3-phosphate containing membranes. *Prog Lipid Res* **46**, 315-327
67. Yu, J. W., and Lemmon, M. A. (2001) All phox homology (PX) domains from *Saccharomyces cerevisiae* specifically recognize phosphatidylinositol 3-phosphate. *J Biol Chem* **276**, 44179-44184
68. Strohlic, T. I., Setty, T. G., Sitaram, A., and Burd, C. G. (2007) Grd19/Snx3p functions as a cargo-specific adapter for retromer-dependent endocytic recycling. *J Cell Biol* **177**, 115-125
69. Marcusson, E. G., Horazdovsky, B. F., Cereghino, J. L., Gharakhanian, E., and Emr, S. D. (1994) The sorting receptor for yeast vacuolar carboxypeptidase Y is encoded by the VPS10 gene. *Cell* **77**, 579-586
70. Stack, J. H., Horazdovsky, B., and Emr, S. D. (1995) Receptor-mediated protein sorting to the vacuole in yeast: roles for a protein kinase, a lipid kinase and GTP-binding proteins. *Annu Rev Cell Dev Biol* **11**, 1-33
71. Burda, P., Padilla, S. M., Sarkar, S., and Emr, S. D. (2002) Retromer function in endosome-to-Golgi retrograde transport is regulated by the yeast Vps34 PtdIns 3-kinase. *J Cell Sci* **115**, 3889-3900

72. Song, X., Xu, W., Zhang, A., Huang, G., Liang, X., Virbasius, J. V., Czech, M. P., and Zhou, G. W. (2001) Phox homology domains specifically bind phosphatidylinositol phosphates. *Biochemistry* **40**, 8940-8944
73. Ekena, K., and Stevens, T. H. (1995) The *Saccharomyces cerevisiae* MVP1 gene interacts with VPS1 and is required for vacuolar protein sorting. *Mol Cell Biol* **15**, 1671-1678
74. Sreenivas, A., Patton-Vogt, J. L., Bruno, V., Griac, P., and Henry, S. A. (1998) A role for phospholipase D (Pld1p) in growth, secretion, and regulation of membrane lipid synthesis in yeast. *J Biol Chem* **273**, 16635-16638
75. Sciorra, V. A., Rudge, S. A., Wang, J., McLaughlin, S., Engebrecht, J., and Morris, A. J. (2002) Dual role for phosphoinositides in regulation of yeast and mammalian phospholipase D enzymes. *J Cell Biol* **159**, 1039-1049
76. Hettema, E. H., Lewis, M. J., Black, M. W., and Pelham, H. R. (2003) Retromer and the sorting nexins Snx4/41/42 mediate distinct retrieval pathways from yeast endosomes. *EMBO J* **22**, 548-557
77. Nice, D. C., Sato, T. K., Stromhaug, P. E., Emr, S. D., and Klionsky, D. J. (2002) Cooperative binding of the cytoplasm to vacuole targeting pathway proteins, Cvt13 and Cvt20, to phosphatidylinositol 3-phosphate at the pre-autophagosomal structure is required for selective autophagy. *J Biol Chem* **277**, 30198-30207
78. He, C., and Klionsky, D. J. (2009) Regulation mechanisms and signaling pathways of autophagy. *Annu Rev Genet* **43**, 67-93
79. Huang, W. P., and Klionsky, D. J. (2002) Autophagy in yeast: a review of the molecular machinery. *Cell Struct Funct* **27**, 409-420
80. Burman, C., and Ktistakis, N. T. (2010) Regulation of autophagy by phosphatidylinositol 3-phosphate. *FEBS Lett* **584**, 1302-1312
81. Farré, J. C., Krick, R., Subramani, S., and Thumm, M. (2009) Turnover of organelles by autophagy in yeast. *Curr Opin Cell Biol* **21**, 522-530
82. Wurmser, A. E., and Emr, S. D. (2002) Novel PtdIns(3)P-binding protein Etf1 functions as an effector of the Vps34 PtdIns 3-kinase in autophagy. *J Cell Biol* **158**, 761-772
83. Strømhaug, P. E., Reggiori, F., Guan, J., Wang, C. W., and Klionsky, D. J. (2004) Atg21 is a phosphoinositide binding protein required for efficient lipidation and localization of Atg8 during uptake of aminopeptidase I by selective autophagy. *Mol Biol Cell* **15**, 3553-3566

84. Krick, R., Tolstrup, J., Appelles, A., Henke, S., and Thumm, M. (2006) The relevance of the phosphatidylinositolphosphat-binding motif FRRGT of Atg18 and Atg21 for the Cvt pathway and autophagy. *FEBS Lett* **580**, 4632-4638
85. Nair, U., Cao, Y., Xie, Z., and Klionsky, D. J. (2010) Roles of the lipid-binding motifs of Atg18 and Atg21 in the cytoplasm to vacuole targeting pathway and autophagy. *J Biol Chem* **285**, 11476-11488
86. Barth, H., Meiling-Wesse, K., Epple, U. D., and Thumm, M. (2001) Autophagy and the cytoplasm to vacuole targeting pathway both require Aut10p. *FEBS Lett* **508**, 23-28
87. Dove, S. K., Piper, R. C., McEwen, R. K., Yu, J. W., King, M. C., Hughes, D. C., Thuring, J., Holmes, A. B., Cooke, F. T., Michell, R. H., Parker, P. J., and Lemmon, M. A. (2004) Svp1p defines a family of phosphatidylinositol 3,5-bisphosphate effectors. *EMBO J* **23**, 1922-1933
88. Cooke, F. T., Dove, S. K., McEwen, R. K., Painter, G., Holmes, A. B., Hall, M. N., Michell, R. H., and Parker, P. J. (1998) The stress-activated phosphatidylinositol 3-phosphate 5-kinase Fab1p is essential for vacuole function in *S. cerevisiae*. *Curr Biol* **8**, 1219-1222
89. Efe, J. A., Botelho, R. J., and Emr, S. D. (2005) The Fab1 phosphatidylinositol kinase pathway in the regulation of vacuole morphology. *Curr Opin Cell Biol* **17**, 402-408
90. Dove, S. K., and Johnson, Z. E. (2007) Our FABulous VACation: a decade of phosphatidylinositol 3,5-bisphosphate. *Biochem Soc Symp*, 129-139
91. Yamamoto, A., DeWald, D. B., Boronenkov, I. V., Anderson, R. A., Emr, S. D., and Koshland, D. (1995) Novel PI(4)P 5-kinase homologue, Fab1p, essential for normal vacuole function and morphology in yeast. *Mol Biol Cell* **6**, 525-539
92. Michell, R. H., Heath, V. L., Lemmon, M. A., and Dove, S. K. (2006) Phosphatidylinositol 3,5-bisphosphate: metabolism and cellular functions. *Trends Biochem Sci* **31**, 52-63
93. Efe, J. A., Botelho, R. J., and Emr, S. D. (2007) Atg18 regulates organelle morphology and Fab1 kinase activity independent of its membrane recruitment by phosphatidylinositol 3,5-bisphosphate. *Mol Biol Cell* **18**, 4232-4244
94. Krick, R., Henke, S., Tolstrup, J., and Thumm, M. (2008) Dissecting the localization and function of Atg18, Atg21 and Ygr223c. *Autophagy* **4**, 896-910
95. Friant, S., Pécheur, E. I., Eugster, A., Michel, F., Lefkir, Y., Nourrisson, D., and Letourneur, F. (2003) Ent3p Is a PtdIns(3,5)P₂ effector required for protein sorting to the multivesicular body. *Dev Cell* **5**, 499-511

96. Eugster, A., Pécheur, E. I., Michel, F., Winsor, B., Letourneur, F., and Friant, S. (2004) Ent5p is required with Ent3p and Vps27p for ubiquitin-dependent protein sorting into the multivesicular body. *Mol Biol Cell* **15**, 3031-3041
97. Costaguta, G., Duncan, M. C., Fernández, G. E., Huang, G. H., and Payne, G. S. (2006) Distinct roles for TGN/endosome epsin-like adaptors Ent3p and Ent5p. *Mol Biol Cell* **17**, 3907-3920
98. Phelan, J. P., Millson, S. H., Parker, P. J., Piper, P. W., and Cooke, F. T. (2006) Fab1p and AP-1 are required for trafficking of endogenously ubiquitylated cargoes to the vacuole lumen in *S. cerevisiae*. *J Cell Sci* **119**, 4225-4234
99. Copic, A., Starr, T. L., and Schekman, R. (2007) Ent3p and Ent5p exhibit cargo-specific functions in trafficking proteins between the trans-Golgi network and the endosomes in yeast. *Mol Biol Cell* **18**, 1803-1815
100. Hama, H., Schnieders, E. A., Thorner, J., Takemoto, J. Y., and DeWald, D. B. (1999) Direct involvement of phosphatidylinositol 4-phosphate in secretion in the yeast *Saccharomyces cerevisiae*. *J Biol Chem* **274**, 34294-34300
101. Tahirovic, S., Schorr, M., and Mayinger, P. (2005) Regulation of intracellular phosphatidylinositol-4-phosphate by the Sac1 lipid phosphatase. *Traffic* **6**, 116-130
102. Trotter, P. J., Wu, W. I., Pedretti, J., Yates, R., and Voelker, D. R. (1998) A genetic screen for aminophospholipid transport mutants identifies the phosphatidylinositol 4-kinase, STT4p, as an essential component in phosphatidylserine metabolism. *J Biol Chem* **273**, 13189-13196
103. Lorente-Rodríguez, A., and Barlowe, C. (2011) Requirement for Golgi-localized PI(4)P in fusion of COPII vesicles with Golgi compartments. *Mol Biol Cell* **22**, 216-229
104. Kearns, B. G., McGee, T. P., Mayinger, P., Gedvilaite, A., Phillips, S. E., Kagiwada, S., and Bankaitis, V. A. (1997) Essential role for diacylglycerol in protein transport from the yeast Golgi complex. *Nature* **387**, 101-105
105. Sciorra, V. A., Audhya, A., Parsons, A. B., Segev, N., Boone, C., and Emr, S. D. (2005) Synthetic genetic array analysis of the PtdIns 4-kinase Pik1p identifies components in a Golgi-specific Ypt31/rab-GTPase signaling pathway. *Mol Biol Cell* **16**, 776-793
106. Li, X., Rivas, M. P., Fang, M., Marchena, J., Mehrotra, B., Chaudhary, A., Feng, L., Prestwich, G. D., and Bankaitis, V. A. (2002) Analysis of oxysterol binding protein homologue Kes1p function in regulation of Sec14p-dependent protein transport from the yeast Golgi complex. *J Cell Biol* **157**, 63-77
107. Beh, C. T., Cool, L., Phillips, J., and Rine, J. (2001) Overlapping functions of the yeast oxysterol-binding protein homologues. *Genetics* **157**, 1117-1140

108. Schulz, T. A., and Prinz, W. A. (2007) Sterol transport in yeast and the oxysterol binding protein homologue (OSH) family. *Biochim Biophys Acta* **1771**, 769-780
109. Lemmon, M. A. (2008) Membrane recognition by phospholipid-binding domains. *Nat Rev Mol Cell Biol* **9**, 99-111
110. Yu, J. W., Mendrola, J. M., Audhya, A., Singh, S., Keleti, D., DeWald, D. B., Murray, D., Emr, S. D., and Lemmon, M. A. (2004) Genome-wide analysis of membrane targeting by *S. cerevisiae* pleckstrin homology domains. *Mol Cell* **13**, 677-688
111. Levine, T. P., and Munro, S. (2001) Dual targeting of Osh1p, a yeast homologue of oxysterol-binding protein, to both the Golgi and the nucleus-vacuole junction. *Mol Biol Cell* **12**, 1633-1644
112. Levine, T. P., and Munro, S. (2002) Targeting of Golgi-specific pleckstrin homology domains involves both PtdIns 4-kinase-dependent and -independent components. *Curr Biol* **12**, 695-704
113. Fairn, G. D., Curwin, A. J., Stefan, C. J., and McMaster, C. R. (2007) The oxysterol binding protein Kes1p regulates Golgi apparatus phosphatidylinositol-4-phosphate function. *Proc Natl Acad Sci U S A* **104**, 15352-15357
114. Faulhammer, F., Kanjilal-Kolar, S., Knödler, A., Lo, J., Lee, Y., Konrad, G., and Mayinger, P. (2007) Growth control of Golgi phosphoinositides by reciprocal localization of sac1 lipid phosphatase and pik1 4-kinase. *Traffic* **8**, 1554-1567
115. Demmel, L., Gravert, M., Ercan, E., Habermann, B., Müller-Reichert, T., Kukhtina, V., Haucke, V., Baust, T., Sohrmann, M., Kalaidzidis, Y., Klose, C., Beck, M., Peter, M., and Walch-Solimena, C. (2008) The clathrin adaptor Gga2p is a phosphatidylinositol 4-phosphate effector at the Golgi exit. *Mol Biol Cell* **19**, 1991-2002
116. Black, M. W., and Pelham, H. R. (2000) A selective transport route from Golgi to late endosomes that requires the yeast GGA proteins. *J Cell Biol* **151**, 587-600
117. Costaguta, G., Stefan, C. J., Bensen, E. S., Emr, S. D., and Payne, G. S. (2001) Yeast Gga coat proteins function with clathrin in Golgi to endosome transport. *Mol Biol Cell* **12**, 1885-1896
118. Mao, Y., Nickitenko, A., Duan, X., Lloyd, T. E., Wu, M. N., Bellen, H., and Quioco, F. A. (2000) Crystal structure of the VHS and FYVE tandem domains of Hrs, a protein involved in membrane trafficking and signal transduction. *Cell* **100**, 447-456
119. Stahelin, R. V., Long, F., Peter, B. J., Murray, D., De Camilli, P., McMahon, H. T., and Cho, W. (2003) Contrasting membrane interaction mechanisms of AP180 N-terminal homology (ANTH) and epsin N-terminal homology (ENTH) domains. *J Biol Chem* **278**, 28993-28999

120. Zhdankina, O., Strand, N. L., Redmond, J. M., and Boman, A. L. (2001) Yeast GGA proteins interact with GTP-bound Arf and facilitate transport through the Golgi. *Yeast* **18**, 1-18
121. Schmitz, K. R., Liu, J., Li, S., Setty, T. G., Wood, C. S., Burd, C. G., and Ferguson, K. M. (2008) Golgi localization of glycosyltransferases requires a Vps74p oligomer. *Dev Cell* **14**, 523-534
122. Tu, L., Tai, W. C., Chen, L., and Banfield, D. K. (2008) Signal-mediated dynamic retention of glycosyltransferases in the Golgi. *Science* **321**, 404-407
123. Wood, C. S., Schmitz, K. R., Bessman, N. J., Setty, T. G., Ferguson, K. M., and Burd, C. G. (2009) PtdIns4P recognition by Vps74/GOLPH3 links PtdIns 4-kinase signaling to retrograde Golgi trafficking. *J Cell Biol* **187**, 967-975
124. Zerial, M., and McBride, H. (2001) Rab proteins as membrane organizers. *Nat Rev Mol Cell Biol* **2**, 107-117
125. Mizuno-Yamasaki, E., Medkova, M., Coleman, J., and Novick, P. (2010) Phosphatidylinositol 4-phosphate controls both membrane recruitment and a regulatory switch of the Rab GEF Sec2p. *Dev Cell* **18**, 828-840
126. Ortiz, D., Medkova, M., Walch-Solimena, C., and Novick, P. (2002) Ypt32 recruits the Sec4p guanine nucleotide exchange factor, Sec2p, to secretory vesicles; evidence for a Rab cascade in yeast. *J Cell Biol* **157**, 1005-1015
127. Guo, W., Roth, D., Walch-Solimena, C., and Novick, P. (1999) The exocyst is an effector for Sec4p, targeting secretory vesicles to sites of exocytosis. *EMBO J* **18**, 1071-1080
128. Chen, C. Y., Ingram, M. F., Rosal, P. H., and Graham, T. R. (1999) Role for Drs2p, a P-type ATPase and potential aminophospholipid translocase, in yeast late Golgi function. *J Cell Biol* **147**, 1223-1236
129. Hua, Z., Fatheddin, P., and Graham, T. R. (2002) An essential subfamily of Drs2p-related P-type ATPases is required for protein trafficking between Golgi complex and endosomal/vacuolar system. *Mol Biol Cell* **13**, 3162-3177
130. Gall, W. E., Geething, N. C., Hua, Z., Ingram, M. F., Liu, K., Chen, S. I., and Graham, T. R. (2002) Drs2p-dependent formation of exocytic clathrin-coated vesicles in vivo. *Curr Biol* **12**, 1623-1627
131. Natarajan, P., Liu, K., Patil, D. V., Sciorra, V. A., Jackson, C. L., and Graham, T. R. (2009) Regulation of a Golgi flippase by phosphoinositides and an ArfGEF. *Nat Cell Biol* **11**, 1421-1426

132. Pruyne, D., Legesse-Miller, A., Gao, L., Dong, Y., and Bretscher, A. (2004) Mechanisms of polarized growth and organelle segregation in yeast. *Annu Rev Cell Dev Biol* **20**, 559-591
133. Santiago-Tirado, F. H., Legesse-Miller, A., Schott, D., and Bretscher, A. (2011) PI4P and Rab inputs collaborate in myosin-V-dependent transport of secretory compartments in yeast. *Dev Cell* **20**, 47-59
134. Eby, J. J., Holly, S. P., van Drogen, F., Grishin, A. V., Peter, M., Drubin, D. G., and Blumer, K. J. (1998) Actin cytoskeleton organization regulated by the PAK family of protein kinases. *Curr Biol* **8**, 967-970
135. Wild, A. C., Yu, J. W., Lemmon, M. A., and Blumer, K. J. (2004) The p21-activated protein kinase-related kinase Cla4 is a coincidence detector of signaling by Cdc42 and phosphatidylinositol 4-phosphate. *J Biol Chem* **279**, 17101-17110
136. Holly, S. P., and Blumer, K. J. (1999) PAK-family kinases regulate cell and actin polarization throughout the cell cycle of *Saccharomyces cerevisiae*. *J Cell Biol* **147**, 845-856
137. Kagiwada, S., and Hashimoto, M. (2007) The yeast VAP homolog Scs2p has a phosphoinositide-binding ability that is correlated with its activity. *Biochem Biophys Res Commun* **364**, 870-876
138. Liu, J., Sun, Y., Oster, G. F., and Drubin, D. G. (2010) Mechanochemical crosstalk during endocytic vesicle formation. *Curr Opin Cell Biol* **22**, 36-43
139. Collins, B. M., McCoy, A. J., Kent, H. M., Evans, P. R., and Owen, D. J. (2002) Molecular architecture and functional model of the endocytic AP2 complex. *Cell* **109**, 523-535
140. Huang, K. M., D'Hondt, K., Riezman, H., and Lemmon, S. K. (1999) Clathrin functions in the absence of heterotetrameric adaptors and AP180-related proteins in yeast. *EMBO J* **18**, 3897-3908
141. Yeung, B. G., Phan, H. L., and Payne, G. S. (1999) Adaptor complex-independent clathrin function in yeast. *Mol Biol Cell* **10**, 3643-3659
142. Wendland, B., Steece, K. E., and Emr, S. D. (1999) Yeast epsins contain an essential N-terminal ENTH domain, bind clathrin and are required for endocytosis. *EMBO J* **18**, 4383-4393
143. Aguilar, R. C., Watson, H. A., and Wendland, B. (2003) The yeast Epsin Ent1 is recruited to membranes through multiple independent interactions. *J Biol Chem* **278**, 10737-10743

144. Itoh, T., Koshiba, S., Kigawa, T., Kikuchi, A., Yokoyama, S., and Takenawa, T. (2001) Role of the ENTH domain in phosphatidylinositol-4,5-bisphosphate binding and endocytosis. *Science* **291**, 1047-1051
145. Aguilar, R. C., Longhi, S. A., Shaw, J. D., Yeh, L. Y., Kim, S., Schön, A., Freire, E., Hsu, A., McCormick, W. K., Watson, H. A., and Wendland, B. (2006) Epsin N-terminal homology domains perform an essential function regulating Cdc42 through binding Cdc42 GTPase-activating proteins. *Proc Natl Acad Sci U S A* **103**, 4116-4121
146. Legendre-Guillemain, V., Wasiak, S., Hussain, N. K., Angers, A., and McPherson, P. S. (2004) ENTH/ANTH proteins and clathrin-mediated membrane budding. *J Cell Sci* **117**, 9-18
147. Wendland, B., and Emr, S. D. (1998) Pan1p, yeast eps15, functions as a multivalent adaptor that coordinates protein-protein interactions essential for endocytosis. *J Cell Biol* **141**, 71-84
148. Burston, H. E., Maldonado-Báez, L., Davey, M., Montpetit, B., Schluter, C., Wendland, B., and Conibear, E. (2009) Regulators of yeast endocytosis identified by systematic quantitative analysis. *J Cell Biol* **185**, 1097-1110
149. Wesp, A., Hicke, L., Palecek, J., Lombardi, R., Aust, T., Munn, A. L., and Riezman, H. (1997) End4p/Sla2p interacts with actin-associated proteins for endocytosis in *Saccharomyces cerevisiae*. *Mol Biol Cell* **8**, 2291-2306
150. Sun, Y., Kaksonen, M., Madden, D. T., Schekman, R., and Drubin, D. G. (2005) Interaction of Sla2p's ANTH domain with PtdIns(4,5)P₂ is important for actin-dependent endocytic internalization. *Mol Biol Cell* **16**, 717-730
151. Janmey, P. A., and Stossel, T. P. (1987) Modulation of gelsolin function by phosphatidylinositol 4,5-bisphosphate. *Nature* **325**, 362-364
152. Rohatgi, R., Ho, H. Y., and Kirschner, M. W. (2000) Mechanism of N-WASP activation by CDC42 and phosphatidylinositol 4, 5-bisphosphate. *J Cell Biol* **150**, 1299-1310
153. Papayannopoulos, V., Co, C., Prehoda, K. E., Snapper, S., Taunton, J., and Lim, W. A. (2005) A polybasic motif allows N-WASP to act as a sensor of PIP(2) density. *Mol Cell* **17**, 181-191
154. Yin, H. L., and Janmey, P. A. (2003) Phosphoinositide regulation of the actin cytoskeleton. *Annu Rev Physiol* **65**, 761-789
155. Carlier, M. F., Laurent, V., Santolini, J., Melki, R., Didry, D., Xia, G. X., Hong, Y., Chua, N. H., and Pantaloni, D. (1997) Actin depolymerizing factor (ADF/cofilin) enhances the rate of filament turnover: implication in actin-based motility. *J Cell Biol* **136**, 1307-1322

156. Gorbatyuk, V. Y., Nosworthy, N. J., Robson, S. A., Bains, N. P., Maciejewski, M. W., Dos Remedios, C. G., and King, G. F. (2006) Mapping the phosphoinositide-binding site on chick cofilin explains how PIP2 regulates the cofilin-actin interaction. *Mol Cell* **24**, 511-522
157. Ojala, P. J., Paavilainen, V., and Lappalainen, P. (2001) Identification of yeast cofilin residues specific for actin monomer and PIP2 binding. *Biochemistry* **40**, 15562-15569
158. Kusano, K., Abe, H., and Obinata, T. (1999) Detection of a sequence involved in actin-binding and phosphoinositide-binding in the N-terminal side of cofilin. *Mol Cell Biochem* **190**, 133-141
159. Saarikangas, J., Zhao, H., and Lappalainen, P. (2010) Regulation of the actin cytoskeleton-plasma membrane interplay by phosphoinositides. *Physiol Rev* **90**, 259-289
160. Kim, K., McCully, M. E., Bhattacharya, N., Butler, B., Sept, D., and Cooper, J. A. (2007) Structure/function analysis of the interaction of phosphatidylinositol 4,5-bisphosphate with actin-capping protein: implications for how capping protein binds the actin filament. *J Biol Chem* **282**, 5871-5879
161. Audhya, A., Loewith, R., Parsons, A. B., Gao, L., Tabuchi, M., Zhou, H., Boone, C., Hall, M. N., and Emr, S. D. (2004) Genome-wide lethality screen identifies new PI4,5P2 effectors that regulate the actin cytoskeleton. *EMBO J* **23**, 3747-3757
162. Witke, W. (2004) The role of profilin complexes in cell motility and other cellular processes. *Trends Cell Biol* **14**, 461-469
163. Lassing, I., and Lindberg, U. (1985) Specific interaction between phosphatidylinositol 4,5-bisphosphate and profilactin. *Nature* **314**, 472-474
164. Richer, S. M., Stewart, N. K., Tomaszewski, J. W., Stone, M. J., and Oakley, M. G. (2008) NMR investigation of the binding between human profilin I and inositol 1,4,5-triphosphate, the soluble headgroup of phosphatidylinositol 4,5-bisphosphate. *Biochemistry* **47**, 13455-13462
165. Palmgren, S., Ojala, P. J., Wear, M. A., Cooper, J. A., and Lappalainen, P. (2001) Interactions with PIP2, ADP-actin monomers, and capping protein regulate the activity and localization of yeast twinfilin. *J Cell Biol* **155**, 251-260
166. Levin, D. E. (2005) Cell wall integrity signaling in *Saccharomyces cerevisiae*. *Microbiol Mol Biol Rev* **69**, 262-291
167. Yoshida, S., Bartolini, S., and Pellman, D. (2009) Mechanisms for concentrating Rho1 during cytokinesis. *Genes Dev* **23**, 810-823

168. Fadri, M., Daquinag, A., Wang, S., Xue, T., and Kunz, J. (2005) The pleckstrin homology domain proteins Slm1 and Slm2 are required for actin cytoskeleton organization in yeast and bind phosphatidylinositol-4,5-bisphosphate and TORC2. *Mol Biol Cell* **16**, 1883-1900
169. Tabuchi, M., Audhya, A., Parsons, A. B., Boone, C., and Emr, S. D. (2006) The phosphatidylinositol 4,5-bisphosphate and TORC2 binding proteins Slm1 and Slm2 function in sphingolipid regulation. *Mol Cell Biol* **26**, 5861-5875
170. He, B., Xi, F., Zhang, X., Zhang, J., and Guo, W. (2007) Exo70 interacts with phospholipids and mediates the targeting of the exocyst to the plasma membrane. *EMBO J* **26**, 4053-4065
171. Zhang, X., Orlando, K., He, B., Xi, F., Zhang, J., Zajac, A., and Guo, W. (2008) Membrane association and functional regulation of Sec3 by phospholipids and Cdc42. *J Cell Biol* **180**, 145-158
172. Bertin, A., McMurray, M. A., Thai, L., Garcia, G., Votin, V., Grob, P., Allyn, T., Thorner, J., and Nogales, E. (2010) Phosphatidylinositol-4,5-bisphosphate promotes budding yeast septin filament assembly and organization. *J Mol Biol* **404**, 711-731
173. Bertin, A., McMurray, M. A., Grob, P., Park, S. S., Garcia, G., Patanwala, I., Ng, H. L., Alber, T., Thorner, J., and Nogales, E. (2008) *Saccharomyces cerevisiae* septins: supramolecular organization of heterooligomers and the mechanism of filament assembly. *Proc Natl Acad Sci U S A* **105**, 8274-8279